University of Oxford

University Offices, Wellington Square, Oxford OX1 2JD

From the Graduate Studies Office

To: The Bodleian Library

24th November 1999

Name: Mr Daniel Kapitan

College: Jesus College

Title: Laser ablation with copper vapour lasers.

Degree Awarded: D.Phil.

The Board of the Faculty of Physical Sciences has decided, on the application of the candidate, that this thesis should **not** be made available for consultation or photocopying for a period of five years from the date when the thesis is deposited in the Bodleian Library.

25 NOV 1999

OXFORD

LASER ABLATION WITH COPPER VAPOUR LASERS

DANIEL KAPITAN, JESUS COLLEGE, UNIVERSITY OF OXFORD

Thesis submitted for the degree of Doctor of Philosophy at the Faculty of Physical Sciences, Trinity 1999



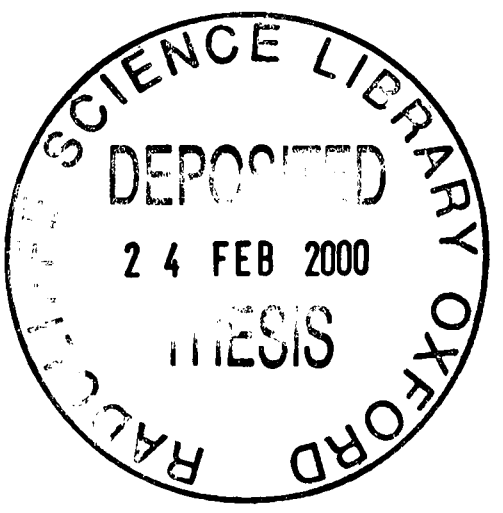
ABSTRACT

The use of copper vapour lasers for laser ablation in laser materials processing applications is studied. To this purpose, the generation of near diffraction-limited beam quality output from a single medium-scale oscillator is demonstrated via matching the total buffer gas pressure to the specific electrical input power loading and the degree of insulation of the plasma tube. The design and characterisation of a Master-Oscillator Power-Amplifier system based on a small-bore oscillator is also described, focusing on pulse stretching techniques to provide efficient seeding required for producing 20-50 W high beam-quality output for laser materials processing purposes. Various experimental studies on the fundamental processes of laser ablation of metals are presented.

The effect of the background gas properties on shock-wave formation in laser generated plasmas is studied using a ballistic pendulum. The experimental findings are found to be accurately described by a modified Sedov-Taylor-Von Neumann theory which accounts for the effect of the piston-mass. The theory is applied to characterise the fluorination process in the shock-wave, in view of oxygen isotope analysis in geochemistry. Atomic emission spectroscopy is shown to provide some measure of the electron temperature and electron density at the plasma core. The experimental results are discussed in view of existing models to describe the extreme Stark-broadening and self-absorption in dense, cool plasmas.

A comparative study of the use of femtosecond and nanosecond pulsed lasers for laser ablation of metals is presented to assess the relative importance of thermal diffusion. Measurement of the recoil momentum due to ejection of molten particulates during ablation in vacuum provides insight into the effect of material properties. Diffusion-limited surface texturing of metals via direct transfer of an optical interference patterns is demonstrated.

This work was supported by the European Community Brite/EuRam programme BE95-1228.



To all those who taught me

Contents

Acknowledgements v

Chapter 1 Introduction 1

1.1 BACKGROUND & CONTEXT 1
I Laser ablation 1
II The copper vapour laser & its applications 3
III Laser materials processing with CVLs 4

1.2 OUTLINE 6
I The Compala project 6
II Thesis outline 7
III Acknowledgements 8

Chapter 2 Single-Unit Medium-Scale Copper Vapour Oscillators 9

2.1 INTRODUCING THE FAMILY OF COPPER VAPOUR LASERS 9
I The elemental CVL 9
II Use of H_2-admixtures 10
III Copper halide & HyBrID lasers 11
IV Kinetically enhanced CVLs 12

2.2 TOWARDS HIGH BEAM-QUALITY CVLS 12
I Radial effects of the copper medium 12
II Formation of output in CVLs 13
III An interlude: defining the diffraction limit 14

2.3 EXPERIMENTS 18
I Description of laser systems 18
II Measurement of ASE seed profiles 19
III Oscillator characterisation 21
IV Addition of H_2 to the neon buffer gas 25

2.4 DISCUSSION 26
I Operation of high magnification unstable resonators 26
II Radial gain distribution in medium-scale CVLs 27
III Degree of thermal insulation and power loading 29

2.5 CONCLUSION 30

CHAPTER 4 SHOCK-WAVE FORMATION DURING PULSED LASER ABLATION 55

4.1 SHOCK-WAVE THEORY 55
I INTRODUCTION 55
II SEDOV-TAYLOR-VON NEUMANN THEORY 58
III MODIFIED STN THEORY 61
IV TEMPORAL HISTORY OF LASER GENERATED SHOCK-WAVES 62
V LASER SUPPORTED DETONATION WAVES 64
VI THE RECOIL PRESSURE INTEGRAL 65

4.2 THE BALLISTIC PENDULUM EXPERIMENT 68
I MEASUREMENT OF MOMENTUM TRANSFER DURING LASER ABLATION 68
II THE BALLISTIC PENDULUM 70
III EXPERIMENTAL SETUP 74
IV RESULTS 75

4.3 DISCUSSION 79
I SHOCK-WAVE FORMATION & EVOLUTION 79
II BEYOND MSTN: SHOCK WAVE STRUCTURE IN GASES 82

4.4 CONCLUSION 85

CHAPTER 5 IN-SITU OXYGEN ISOTOPE ANALYSIS: LASER FLUORINATION MICROPROBES 87

5.1 INTRODUCTION 87
I STABLE ISOTOPE GEOCHEMISTRY 87
II MICROANALYSIS OF OXYGEN ISOTOPES IN NATURE 89
III MASS SPECTROMETRY & MICROANALYTICAL TECHNIQUES 91
IV LASER ABLATION MICROPROBES 92

5.2 SHOCK-WAVE FORMATION & FLUORINATION 94
I INTRODUCTION 94
II UV ABLATION OF WIDE-BANDGAP MATERIALS 94
III THE FLUORINATION PROCESS 95
IV CALCULATIONS 97

5.3 DISCUSSION 98
I EFFECT OF THE BACKGROUND GAS PROPERTIES ON FLUORINATION 98
II FRACTIONATION DUE TO KINETIC & TRANSPORT EFFECTS 101
III COMPARISON OF EXCIMER & UV-CVL LASER MICROPROBES 104

5.4 CONCLUSION 105

CHAPTER 6 CONTINUUM RADIATION FROM COOL, DENSE METALLIC PLASMAS 107

6.1 INTRODUCTION 107
I SPECTROSCOPY AND PLASMA DIAGNOSTICS 107
II THE EARLY CONTINUUM PHASE 108

III OUTLINE 109
6.2 TIME-INTEGRATED OPTICAL SPECTROSCOPY 109
I EXPERIMENTAL SETUP 109
II SPECTRAL IDENTIFICATION 110
III DISCUSSION 115
6.3 TIME-RESOLVED OPTICAL SPECTROSCOPY 119
I SETUP 119
II RESULTS 121
III DISCUSSION 125
6.4 MODELLING OF COOL, DENSE PLASMAS 126
I STRONGLY COUPLED PLASMAS 126
II THE MODIFIED SEMI-EMPIRICAL METHOD 127
III OPACITY BROADENING 129
6.5 CONCLUSION 132
I SUMMARY 132
II FUTURE WORK 133
CHAPTER 7 PULSED LASER ABLATION OF METALS: AN ENERGETICS PICTURE 135
7.1 ABLATION WITH FEMTOSECOND-NANOSECOND LASERS 135
I INTRODUCTION 135
II HEAT DIFFUSION & THERMAL TRANSPORT 136
III ENERGY DEPOSITION PER UNIT VOLUME 137
IV NANOSECOND LASER ABLATION WITHIN COMPALA 141
V DISCUSSION 143
7.2 PRODUCTION OF SUB-MICRON PERIODIC SURFACE STRUCTURES 144
I INTRODUCTION 144
II EXPERIMENTAL SETUP 144
III RESULTS & CALCULATIONS 146
IV DISCUSSION 150
7.3 MOMENTUM TRANSFER DUE TO MELT EJECTION 152
I INTRODUCTION 152
II EXPERIMENTS & RESULTS 153
III DISCUSSION 160
7.4 CONCLUSION 161
CHAPTER 8 CONCLUSION 163
8.1 SUMMARY 163
8.2 FUTURE WORK 164
LIST OF PUBLICATIONS 167
APPENDIX A THE BALLISTIC PENDULUM 169
APPENDIX B 'EINSTEIN'S' SHOCK-CONDITION 173
APPENDIX C HEAT CAPACITIES OF REAL GASES 175

APPENDIX D ELEMENTS OF CLASSICAL PLASMA THEORY 179

APPENDIX E HEAT TRANSPORT DURING PULSED LASER ABLATION 185

BIBLIOGRAPHY 187

Acknowledgements

A genuine 'terimah kasih' to all those who made it happen:

Colin Webb, for his care, support and enthusiasm; for sharing his passion for teaching; but far and foremost to allow me the opportunity and freedom to find my own way as a physicist.

David Coutts, my mentor, whip-cracker, solace and guidance whilst in the lab; and fellow traveller, 'homo mundi scientea' and classical music-fan when off duty. And all of that always done in good humour with a healthy pinch of antipodean cynicism thrown in.

All the people who put up with me working on this project: Tony Andrews, for his invaluable practical advise and for not making me feel stupid when I was; Julian Cashmore, who contributed to the work on spectroscopy; Simon Hooker, for always having a discerning and critical opinion when I needed one; David Heading, for writing Cromwell; Ed Young, for a truly interdisciplinary project. And, of course, the 'army' of technicians without which I would be hopelessly lost. Special mention to George Matthews, for just about everything, and Graham Quelch for his ideas on the pendulum.

The partners in the Compala programme, and in particular Andrew Kearsley and Martyn Knowles at Oxford Lasers Ltd., who taught me how to work professionally, and give me a chance to work and learn at the company. I also hope that this work reflects some of the spirit of Gerard Notenboom (Philips CFT), who was the main proponent of the COMPALA programme, but unfortunately never saw its completion.

The EPSRC for paying my fees, the European Commission for giving me ample financial support, and Queen Beatrix for granting me a Dutch nationality.

The past and present members of the laser group: Adam Whybrew, my prime example of English lower upper class culture; William Wadsworth, a fellow physicist and mad sportsman; Heather Booth, without whom the Laser Group wouldn't have been half as pleasant to work in as it was in the past four years; Andrew McGonigle, for walking along the other side of the fence, and for not getting himself killed on the bike; Dave Spence, for providing critical mass to group-outings; and Laure Montandon-Varoda (Switzerland) and Felix Buchkramer (Germany) whose visits turned the Laser group into a little Europe of our own.

The students who provided a welcome change to working alone in the lab: Rob Hinch (Jesus), Robert Bates (St John's), Matthew McBrien (LHM), and Carol Gardiner (Corpus Christi).

Those who shared the Oxford experience: Michael (Germany), Deya (Mexico), Ian (Trinidad), Bernard (Australia), Sabine (Germany), Bruno (France), Dik (Netherlands) Ruth (Northern Ireland), Ulrika (Sweden), Sharon (Australia), Edmund (Canada), Patricia (Poland), Petra (Hungary), and naturally James & Bryan, my two flatmates at 121 Woodstock who made me more British than I'll ever be.

And of course, ma & pa, for giving me and my two sisters a home away from home.

Chapter 1
Introduction

If you knew what you were doing you'd probably be bored
FRESCO'S DISCOVERY

1.1 Background & Context

I Laser ablation For centuries sun-light has been the primary source for optical radiation of high brightness. The well-known summer ritual of burning leaves or small insects on the playground using a single lens is perhaps the most common example of what effect high concentrations of focused optical radiation can have on (solid) materials. Indeed, before the advent of the laser, the use of large burning lenses with relatively large numerical apertures was the only practical method to achieve high optical power densities for scientific research purposes (see figure 1.1). Given the diameter of the sun ($1.4{\cdot}10^9$ m) and its distance from the earth (around 8 light-minutes), the full-angle divergence of sunlight is of order 10 mrad. Thus, with an average intensity of 0.02 W/cm^2 impinging on the Earth's surface on a clear summer day, the optical intensity at the focus of a lens is of order $200 \cdot (D/f)^2$ W/cm^2. With a lens diameter $D = 16$ inch and focal length $f = 25$ inch, broadband, continuous sunlight can be concentrated to produce optical power densities up to 10^2 W/cm^2, which is sufficient to cause burning of, for example, non-transparent organic substances.

From the early days of the invention of lasers, the capability of pulsed lasers to generate burst of high brightness radiation has triggered the study of laser ablation, a term coined for the various mechanisms via which layers of material can be removed from solid substrates using intense optical radiation. Note that at times this occurred incidentally, such as the phenomenon of optical damage of transparent materials in the field of high power laser physics. An 'urban legend' relates that the common standard to measure absolute laser power used at Bell Labs in the 1960s involved penetrating a number of Gillette razor-blades with the laser beam. Today, optical power densities in the range of $10^8 - 10^{10}$ W/cm^2 are readily available from table-top nanosecond pulsed lasers for materials processing purposes, while more novel femtosecond pulsed lasers can generate up to $10^{13} - 10^{15}$ W/cm^2, and ultimately at the extreme of $10^{20} - 10^{22}$ W/cm^2 generated at large-scale national laser facilities, are increasingly used to the study of laser-material interactions in many different regimes. To illustrate the active field of laser ablation research (Steen 1991, von Allmen & Blatter 1995, Bäuerle 1996, Duley 1996), consider the numerous applications in science and industry including medical applications, art restoration, contamination analysis of nuclear reactors, growth of high T_c superconducting materials in pulsed laser deposition (PLD) (Geohegan 1994), and production of environmentally sound fuel injection nozzles. These application involve many different types processes, such as cutting, drilling, welding, annealing, hardening, surface cleaning and texturing,

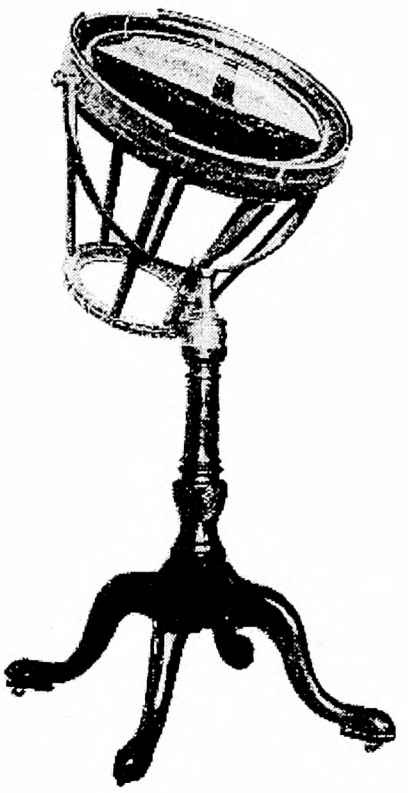


FIGURE 1.1: English burning lens, courtesy of the Museum of the History of Science, Oxford. Known to have been made in 1791 by William Parker & Son, glass manufacturers of Fleet St., London. Shown is the primariy lens with a diameter of 16 inches, while the smaller secondary lens (9 inches) is missing. The use of burning lenses was taken over by the Bunsen burner in the 1850s.

and structuring. Indicative of the explosive growth in this area of research is the number of attendees at Conference On Laser Ablation (COLA), which increased from 75 at the first meeting to well over 200 at the third COLA'97.

The main theme of the present work involves study of laser ablation of metals using copper vapour lasers (CVLs). The primary focus will be to investigate the various aspects of the ablation process, which can roughly be classified to involve i) the generation and manipulation of the laser beam itself; ii) the formation of shock-waves and plasma above the target surface; and iii) the processes occurring in the bulk of the target substrate. To study these phenomena in their entire complexity involves a wide variety of disciplines, varying from laser physics, optics, and fluid dynamics, to plasma physics, material science and thermodynamics. To cover each discipline to significant depth would, therefore, be well beyond the scope of any dissertation. Instead, the general approach and philosophy adopted here has always been to find a balance between, on the one hand, investigations into the specific characteristics of laser ablation of metals with CVLs, while at the same time an attempt has been made to put experimental findings into a wider context and be comprehensive in referencing the vast existing body of reports in similar fields of research. Indeed, many of the methods, experiments, models and theories presented here have either been published earlier, or were derived in close analogy to the work of others.

Before turning to the main body of this thesis, first an introduction of the CVL will be given, followed by an overview of the scope of the use of these devices in laser materials processing applications. Only a short outline of the experimental work will be given in the second section of this introduction, while a more thorough introduction to the various relevant disciplines is deferred to the six main chapters of

this work. While the choice of these six topics may seem somewhat random and unrelated, they do have bearing on the technological goals set within the European Brite/EuRam project which first initiated these studies. Within the practical (and in many aspects commercial) guidelines set by the *COMPALA* workprogramme, the author has attempted to focus on issues and the current interests in the academic community as communicated through the ongoing deluge of journal papers in the field of laser ablation.

II THE COPPER VAPOUR LASER & ITS APPLICATIONS Copper vapour lasers (CVLs) belong to a class of pulsed metal vapour lasers (MVLs) where the active medium consists of a discharge excited metal vapour. While the development on gold vapour lasers (GVLs) (Gorchakov et al. 1994) and barium vapour lasers (BVLs) (Mildren et al. 1995, Mildren et al. 1997*a*, Mildren et al. 1997*b*, Mildren et al. 1997*c*) still receives attention, the latter in particular because most of the atomic transitions are in the visible to allow detailed kinetic studies using Hook spectroscopy, the CVL is by far the most well-developed of all MVLs. Historically, the development of large multi-laser systems for the use of uranium enrichment via atomic vapour laser isotope separation (AVLIS) in the heights of the Cold War led to significant progress of these devices (Little & Sabotinov 1995). However, while data regarding their performance could be communicated freely within the research community, many fundamental aspects and engineering details remained classified until not too long ago. The ability of the CVL to generate high average output (up to 100 W for table-top systems) in the visible (fundamental wavelengths of 510.6 nm green and 578.2 nm yellow) with relatively high wallplug efficiencies ($1 \sim 2\%$), combined with the high pulse repetition frequency (PRF) of the CVL ($1 - 50$ kHz) have resulted in a growing interest for a host of new applications for which to date there exist few other reliable alternative laser sources with these characteristics.

For example, development of large-scale television projection systems require multi–watt average power in the red, green and blue at the line frequency of 15.6 kHz. To this purpose high power blue lasers are in development via frequency doubling of high power CVL-pumped Ti:Sapphire lasers (Wadsworth 1997, Coutts 1998). CVLs have already been established as reliable pump sources for high power dye lasers in the yellow-red region of the spectrum, where the longer pump wavelength compared to excimers greatly enhances the lifetime of the dye medium. These systems are widely used in medical applications such as oncological photodynamic therapy and dermatological removal of port-wine stains (Little & Sabotinov 1995).

Another active field of research involving high power CVL-pumped dye laser systems is in the field of adaptive optics, where the development of sodium laser guide stars has been identified as a crucial method for the next generation ground-based astronomical telescopes. The combination of low pulse energy and high PRF of the CVL as a pump source to give the required high *average* power is key for efficient excitation of the relatively 'thin' mesospheric sodium layer (Booth 1998). The high PRF of the CVL has also been proven to be particularly useful for high-speed imaging and diagnostic techniques of highly turbulent or hostile environment via particle image velocimetry (PIV) techniques (Little & Sabotinov 1995). More recently progress has been made to simultaneously use the high gain of the CVL medium as a narrow-band brightness amplifier to allow observation of small (seeding) particulates against a bright background such as a plasma torch (Buchkremer 1997).

The development of tunable UV laser sources with high PRFs is of particular interest for chemist

and atmospheric physicist interested in the detection of trace species in the troposphere. A portable system based on the frequency doubled 308 nm output generation of a CVL pumped dye lasers (Evans & Webb 1994) has been used on field campaigns for direct monitoring of the OH radical concentration (Brauers et al. 1996, Hofzumahaus et al. 1996). With current nonlinear frequency conversion technology, UV-CVL output at 255.3 nm (doubled green), 289.1 nm (doubled yellow) and 271.2 nm (green plus yellow) can be generated with optical conversion efficiencies up to 48% (Coutts 1995*a*, Coutts & Brown 1995*b*). Recent efforts focus on the use the UV-CVL output to pump Ce^{3+}-ions to obtain tunable UV output from colquiriites (fluoride crystals such as LiCAF and LiSAF) (Coutts 1998, McGonigle et al. 1998).

III LASER MATERIALS PROCESSING WITH CVLS One of the main aims in the field of CVL research has focused towards developing techniques for generating high beam-quality output from these devices. It is only with these advances that the CVL has been able to gradually establish itself in the well established field of laser materials processing, and in particular micromachining of metals (Knowles 1996). To sketch the context of current use of lasers in materials processing application, consider the following three main categories.

First, carbondioxide (CO_2) lasers, and to a lesser some extent other gas laser operating in the infrared such as the carbonmonoxide (CO) laser, and iodine laser, are well established as an efficient cutting tool. With their capability to deliver optical powers up to tens of kilowatts in the far infrared (10.6 μm) at wall-plug efficiencies of around 10%, CO_2 lasers are often used for large volume processing. In heavy industry, for example, cutting and welding of metal sheets with a thickness up to a few centimetres can be achieved with typical resolutions of a few millimetres using CO_2 lasers. The second category consists of laser operating at a shorter infrared wavelengths, of which the fundamental Nd:YAG lasers (1.06 μm) are the most well known. These lasers are now becoming common in the electronics and micromechanical industry, used for cutting, drilling and welding processes of metal sheets of few millimetres thick. Development of high-power diode-pumped Nd:YAG lasers has triggered the use of these lasers as a replacement for CO_2 lasers, aiming to enhance processing accuracies down to fractions of a millimetre. Finally, on the other end of the spectrum, the third class of excimer lasers operating in the ultraviolet (from 308 nm from a XeCl down to 193 nm for ArF) are primarily used in the semiconductor industry to produce Very Large Systems Integration (VLSI) circuits by means of mask-imaging lithographic techniques.

Evidently, in order to push CVL technology into the field of laser materials processing requires identification of the critical parameters and characteristics which set the laser ablation with CVLs apart from alternative laser technologies. Historically, when CVLs were first introduced the 1990s as alternatives to commonly used infrared laser, a number of advantages were put forward. First, the shorter wavelength allowed for efficient coupling into most metals, which exhibit typical reflectivity of $50-60\%$ in the visible, compared to more than 90% in the infrared (Steen 1991). Secondly, the short pulse duration of few tens of nanoseconds resulted in significantly faster energy deposition compared to conventional quasi-cw infrared sources, causing most of the material to be removed via explosive ablation and violent melt-ejection. As a result, the heat affected zone (HAZ) was significantly reduced compared to the relatively slow 'melt-cutting' process of microsecond pulsed lasers. Finally, owing to the high PRF of CVLs, the material removal rates are can be high, which is favourable for the economics of laser materials processing.

Since then, however, major advances have been made in the field of laser physics research at large,

and laser materials processing in particular. For example, at the time of writing of this work, much interest exists within the academic research community evolves regarding the relative advantages of 'femtosecond' (< 1 ps) pulsed lasers versus 'nanosecond' (> 1 ns) pulsed lasers for laser materials processing applications. While it remains to be seen to what extent the use of complex chirped pulse amplified Ti:sapphire femtosecond lasers is practical in an industrial environment, recent reports show significant improvements in further reducing thermal damage and advantages by using such short pulsed, high peak power lasers. Similarly, from a more technological viewpoint, the development of Q-switched frequency doubled Nd:YAG systems capable of delivering 10-20 W average power at 1 kHz, further pushes the need to establish the capabilities of CVL if it is to be accepted for widespread use in industry, as it is no longer the only available nanosecond pulsed laser system operating in the visible.

In the past few years, most of the reports on laser materials processing applications with CVLs have originated from a handful laboratories around the world. Work by Körner et al. (1996) at the University of Erlangen (Germany) has focused on the high fluence regime, using elaborate multi-laser systems with 3 or 4 amplifiers. As a spin-off of the AVLIS programme, experiments on micro-drilling (Chang et al. 1994) and shock-wave dynamics (Chang & Warner 1996) have been conducted at the large-scale CVL facility at Lawrence Livermore National Laboratory (USA). Similarly, research at equivalent Russian institutes continues, reporting on the etching of sapphire (Dolgaev et al. 1996*a*, Dolgaev et al. 1996*b*). Drilling and cutting of transparent materials has also been the main interest of Pini (1996) at the Institute of Quantum Electronics, Florence, Italy. Being the world-leading manufacturer of CVLs, Oxford Lasers Ltd. (UK) have reported on various technological aspects for the application of these lasers to drill and cut a host of materials (Knowles et al. 1994, Knowles 1996, Knowles & Webb 1995). Ventzek et al. (1992*b*) and Lash & Gilgenbach (1993) at the University of Michigan (USA) have also used Oxford Lasers CVLs for machining polymers and metals. Finally, with arguably the highest concentration of CVL experts worldwide to date, Glover et al. (1993) at the Centre for Laser Applications at Macquarie University, Sydney (Australia) were the first to demonstrate efficient processing of polymers with UV-CVLs which has now become a more mature process technology (Glover et al. 1995).

While each of these reports vary in content and methodology, the general approach for laser ablation with CVLs involve direct write, serial processing with tightly focused (or imaged) beams. Owing to the good beam-quality output, the CVL presently maintains a slight advantage over current solid state lasers, which often suffer from severe thermal distortions. As such, processes involving precision cutting and drilling are particularly suited to the CVL for a wide range of materials including sheet metal, ceramics, semiconductors, and diamond. Specific applications of precision hole drilling include production of fuel injector nozzles for the automotive industry, inktjet printer nozzles, and drilling vias for interconnects in multilayer printed circuit boards to reduce packaging sizes. Furthermore, the elevated pulse repetition frequencies of the CVL allow for high turn-over rates, important from an economic perspective for mass-production of such specialised, high-tech components in industry. These issues will be addressed in the final concluding chapter in view of identifying the future prospect of CVL research and development in laser materials processing.

1.2 OUTLINE

I THE COMPALA PROJECT The work presented in this thesis forms an integral part of the Brite/Euram programme BE95-1228, which has the primary goal to investigate the *cost-effective series and mass-production of high-precision metallic microparts and optical structures in moulds by laser submicron-machining (COMPALA).* Laser micromachining techniques are not only expected to replace existing technologies for producing small metallic parts, like punching, sputtering, reactive-ion etching and electrical discharge machining (EDM), but also to improve the quality of the processing, reduce the production costs and to alleviate the environmental impact of processing techniques like EDM. The industrial partners in the programme are Philips (the Netherlands), Bosch (Germany) and Oxford Lasers (United Kingdom), while TNO (Dutch Organisation for Applied Scientific Research) are involved alongside the University of Oxford to provide backup towards knowledge building and development of new process technologies.

application	**current state-of-the-art**	**target COMPALA**
Laser cutting of 0.2 mm metal sheets	cutting width: 100 μm cutting speed: 3 m/min contamination: high	< 25 μm > 3 m/min none
Laser hole driling of 1 mm metal sheets	hole diameter: 100 μm drilling speed: 5 /s wall taper: $> 5°$	50 μm 20 /s $< 2°$
Laser structuring of moulds for product housings and AR lenses	feature size: 10 μm roughness: > 10 μm periodic structures: > 1 μm release angle: $> 7°$	2 μm < 0.5 μm 0.4 μm $< 2°$
Laser micromilling of metal	removal rate: 0.05 mm^3/s roughness: > 5 μm	> 1 mm^3/s < 0.5 μm
Process control techniques	only passive methods	active control using plasma diagnostics
Copper vapour laser development	industrial system not yet available	100 W industrial prototype system
Optical fibre beam delivery CVL	industrial system not yet available feature size: > 30 μm	integrated transmission losses $< 15\%$ < 10 μm

To give an overview of the nature of the project, listed above are its main targets set out at the start, compared to the state of the art at that time. Note that these goals only reflect the industrial and technological aspects of the programme. Only the tasks related to the development of a high beam-quality laser system, and studies on the generation of (sub-)micron periodic surface structures via interferometric techniques, have directly resulted in experimental work which is included in this thesis. The motivation for the majority of the studies will become evident in the following.

II THESIS OUTLINE In the first two chapters a study on the laser physics of CVLs is made, focused on the generation of high beam-quality output required for micromachining applications. Both medium scale single-unit CVLs (chapter 2) and Master-Oscillator Power-Amplifier (MOPA) systems (chapter 3) are considered. The temporal evolution of the radial gain-profile distribution of elemental CVLs are found to be critically dependent on the combination of total buffer gas pressure, the specific electrical input power, and degree of thermal insulation of the plasma bore. These operating conditions are optimised to generate the preferred centrally peaked radial gain profile, and the findings are discussed in view of recent developments in the study of the gas-phase kinetics of discharge excited metal vapour lasers. Pulse stretching techniques are investigated in view of enhancing the beam-quality output of MOPA systems.

In chapter 4 the phenomenon of shock-wave formation is studied by measuring the momentum transfer during the ablation process using a ballistic pendulum. The recoil momentum is measured for different background gas properties, and the observed scaling laws are accurately described the Sedov-Taylor-von Neumann theory which is modified to account for the piston mass formed by the ablated material. The theory is further applied to the development of laser microprobes for chemical mass-spectrometry in the field of stable oxygen isotope geochemistry. As presented in chapter 5, issues pertaining sustaining of exothermic reactions in the shocked, reactive background gas are assessed.

Following on from the shock-wave formation studies, chapter 6 considers the spectroscopy of cool, dense metallic plasmas as associated with the piston mass plasma core. The validity of existing semi-classical and empirical numerical codes to describe the observed Stark broadening in such plasmas is assessed, in comparison with other broadening mechanisms, most importantly regarding the opacity of plasma plume. Drawing from multichannel time-integrated spectroscopic measurements, and time-resolved monitoring of the evolution single atomic lines, semi-quantitative values for the electron temperature T_e and density n_e are calculated to provide an evolutionary picture of these laser generated plasmas.

The effect of thermal diffusion on the ablation process is studied in chapter 7. A comparative literature study is presented on the relative advantages of using short-pulse (< 10 ps) lasers versus nanosecond pulsed lasers for laser ablation, where a distinction between different regimes of laser ablation is made using the concept of power deposition per unit volume u (J/cm^3). Subsequently, experimental results on the controlled production of (sub-)micron surface relief gratings in stainless steel are presented, and assessed in terms of the importance of thermal diffusion relative to other surface effects in the threshold regime. Considering the effect of material properties on the ablation process, ballistic pendulum experiments are conducted in vacuum for a variety of metals to quantify the kinetic balance between modes of material removal.

Finally, in the concluding chapter the primary findings of these studies are distilled, and discussed within a wider context of laser ablation with CVLs. Implications with respect to the various academic, technological and economic incentives which first initiated these studies are discussed, and put in perspective in view of the ongoing developments in this field.

III ACKNOWLEDGEMENTS At this point the author would like to specifically acknowledge the various co-workers who have had a significant contribution to the contents of this thesis.

E.D. YOUNG at the Department of Earth Sciences, University of Oxford, was the prime investigator of the work on the laser fluorination microprobe for stable oxygen isotope geochemical analysis, in collaboration with A.J. ANDREWS and D.W. COUTTS who constructed the UV-CVL system. The author's original contribution as described in chapter 5 pertains to the theoretical analysis and background to the issues of shock-wave formation and the dynamics of the laser ablation plume within the fluorinating background gas.

J.S. CASHMORE performed the time-integrated spectroscopy experiments described in section 6.2. The *CROMWELL* code used in section 6.4 was developed by D.J. HEADING. Furthermore, the following undergraduate students have worked under the author's supervision and contributed to different aspects of the work contained in chapter 6: R. HINCH (Jesus) performed the spectral assignment and identification of the time-integrated spectra; R. BATES (St. Johns) assisted in the construction of the time-resolved experiments; and C. GARDINER (Corpus Christi) conducted the numerical experiments using *CROMWELL*.

The work on the controlled production of sub-micron periodic surface relief gratings as described in section 7.2 was done by D.W. COUTTS, who was responsible for the all the reported experiments as well as the numerical simulations of the heat transport problem. The experiments on single-shot vacuum ablation of different metals (chapter 7, section 3) were performed under my supervision by M.N. MCBRIEN for his 4th year MPhys project. The author's original work pertains to the analysis and theoretical discussion of both experiments within the wider theme of chapter 7 on pulsed laser ablation of metals.

Chapter 2
Single-Unit Medium-Scale Copper Vapour Laser Oscillators

The floggings will continue until morale improves
used by DAVID COUTTS

An overview of the current state-of-the art of the copper vapour laser (CVL) is given. Work on the development of medium-scale CVL oscillators generating high beam-quality output is presented. Performance characteristics of single-unit medium-scale oscillators are determined to optimise the operation with negative branch on-axis unstable resonators with very high magnifications (up to $M = 360$) to yield better than two times diffraction-limited beam output. Relevant design issues regarding the formation of high beam-quality output are studied, and the effects of hydrogen additives to the neon buffer gas, thermal loading and degree of insulation of the laser plasma head are investigated in the light of current understanding of kinetic mechanisms of the copper gain medium.

2.1 Introducing the Family of Copper Vapour Lasers

I The elemental CVL Standard elemental CVLs operate with an insulated ceramic plasma tube, which due to the self-heating process of the excitation discharge on the neon buffer gas (typical pressure in the range of $10 - 100$ mbar) reaches an optimum operating temperature of order 1500° C required for vaporisation of the copper medium. Via electronic excitation an inversion is created between the $3d^{10}\,4p\,^2P^0_{3/2,1/2}$ upper laser levels and the $3d^9\,4s^2\,^2D_{5/3,3/2}$ lower laser levels of the atomic copper vapour (see figure 2.1). The principal difference between the kinetics of the upper and lower laser levels is that the $^2P^0$ possess several strong loss channels, such as deexcitation to the $3d^{10}\,4s\,^2S_{1/2}$ ground-state and upward excitation to higher states, while the metastable ^2D states only decay on timescales of few microseconds. The process of preferential collisional excitation of the $^2P^0$ level by which an inversion is created (Webb 1991), ceases approximately 100 ns after the onset of the discharge pulse due to the falling electron temperature and decrease of the ground-state copper population. On the other hand, the decrease in the electron temperature and ground-state copper density do not affect the kinetics of the ^2D levels as severely, which causes the ^2D population densities to continue to increase beyond the $^2P^0$ densities (Brown et al. 1990). Brown et al. (1990) have emphasised that the termination of the laser pulse is not only due to filling of the lower laser level but also because a reduction in the upper laser level pumping related to the collapse of power input to the plasma during the excitation pulse. Thus, an inversion can not be sustained resulting in the inherent self-terminating character of the CVL medium. In addition,

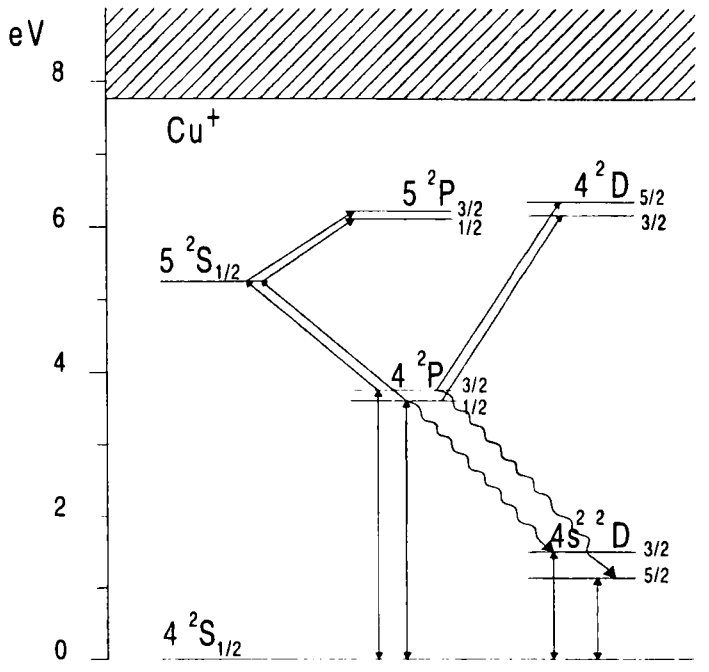


FIGURE 2.1: Simplified Grotrian diagram of atomic copper, showing the transitions relevant to the lasing action.

Astadjov et al. (1985) also measured that depopulation of the $^2P^0$ levels via collisional excitation to higher lying states adds to the self-termination process. Note that it is misleading to state that the CVL self-terminates because of the metastable nature of the ^2D levels, for which radiative dipole transitions to the ground-state are forbidden. Ultimately the maximum repetition rate is limited by the de-excitation rate of the ^2D level, but this constraint will only become important on longer timescales compared to the dominant self-terminating process due to the kinetics of the electronic excitation mechanism.

Apart from elemental CVLs there exists a whole family of other CVLs which continue to be subject of investigation in order to obtain a better understanding of the physics of metal vapour lasers and to improve their performance in general (Little & Sabotinov 1995). Generally, two main modifications have been investigated which significantly alter the kinetics of the gain medium, respectively involving use of H_2-admixtures to the neon buffer gas, and use of copper halides to establish a 'cold' discharge. These different members of the family of CVLs will be introduced below.

II USE OF H_2-ADMIXTURES The use H_2-admixtures has been proven to significantly improve the performance of elemental CVLs (Huang et al. 1986, Withford et al. 1994*b*, Brown et al. 1995, Withford et al. 1995). While a number of mechanisms have been proposed to describe the observed enhancement, including extensive numerical simulations (Chang 1994, Carman et al. 1994, Carman 1995, Carman 1997), to date there remains some controversy as to which process is the most dominant. Most likely the relatively large elastic collision cross section of hydrogen enhances the cooling of the electrons in the interpulse period, thus increasing the depopulation of the metastable ^2D levels. Long running investigations reported by the group at Macquarie University have indeed shown the importance of the importance of the inter-pulse residual electron density (Withford et al. 1994*a*, Withford et al. 1994*b*, Withford 1995, Withford

et al. 1996*a*). Comparative studies on the kinetics of CVLs by Webb & Hogan (1995) further support such an interpretation. On the other hand, the numerical data presented by Chang (1994) indicate that the primary mechanism for the enhanced relaxation is due to a larger thermal diffusion loss from the tube centre to the wall, together with a larger power deposition into the laser tube. Both these effects lead to an increase in the copper ground-state density, thus improving the power output and efficiency of the CVL. The relative effect of trace additives on the impedance matching between the laser discharge and the driving circuit has also been investigated by Withford et al. (1994*b*), but they concluded this effect is minor relative to the enhanced plasma cooling by elastic interactions to reduce the pre-pulse electron densities is the most dominant process.

Indeed it remains difficult to deconvolve the myriad of microscopic kinetic mechanisms and macroscopic effects such as enhanced thermal conductivity and impedance matching. It is clear, however, that regardless of the exact nature of the mechanism the performance of the CVL is enhanced by two factors:

- fast relaxation (cooling) of the electron temperature T_e and the electron density n_e
- fast re-population of the ground-state copper density.

The degree to which these relaxation processes take place during the interpulse period determines the pre-pulse conditions of the medium, and thus significantly influences the gain characteristics and optical output of the CVL. It is important to note that relatively small changes in these relaxation rates can lead to significant cumulative effects in the steady-state operating conditions, as emphasised by Mildren et al. (1995), due to the cyclic operation of the CVL at high pulse repetition frequency (PRF).

III Copper halide & HyBrID lasers

Copper halide lasers, such as CuBr (Sabotinov et al. 1993, Petrash 1995, Sabotinov 1995, Astadjov et al. 1997) and CuCl (Nerheim 1977, Vetter & Nerheim 1977, Sabotinov et al. 1993), constitute a class of copper lasers which operate at lower tube temperatures around 600-800° C. This is possible due to the lower atomisation temperature of the copper halide compound to form the required copper vapour density. These devices are capable of obtaining higher output powers per unit volume and improved wallplug efficiencies compared to elemental CVLs. However, establishing a stable discharge in the CuBr medium requires complicated multiple electrode arrangements, sometimes causing spurious acoustic waves which may have detrimental effect on the formation of optical output during the gain pulse. Moreover, the accumulation of volatile bromide can not exceed partial pressures of few millibars due to its high reactivity, and intricate laser head design incorporating cold zones to collect the bromide are required. Similar to the behaviour of elemental CVLs, copper halide lasers also benefit from the use of H_2 admixtures (Sabotinov et al. 1993). Astadjov et al. (1985) observed reduction of depopulation of the $^2S_{1/2}$ copper ground-state in the excitation pulse, and 20 times more rapid repopulation during the interpulse period in the presence of hydrogen, resulting in a doubling of the average output power.

An alternative approach to establish such a 'cold' running CVL is by introducing HBr to the neon buffer gas of an (uninsulated) elemental copper laser, appropriately named a HyBrID (Hydrogen-Bromide In Discharge) laser (Coutance et al. 1995, Little et al. 1995). The copper HyBrID works via introducing hydrogen bromide (HBr) in the discharge in the presence of metallic copper to form a chemical reaction to produce copper bromide (CuBr) vapour, which then dissociates to form the atomic copper vapour

similar as in copper halide lasers. A major disadvantage of this process is the formation of dendrites on the bottom of the plasma tube, which may cause significant blocking of the laser aperture. The enhanced operation of HyBrID lasers over elemental CVLs is primarily ascribed to the presence of HBr, which provides an important pathway for enhanced plasma cooling via dissociative attachment.

IV KINETICALLY ENHANCED CVLS Most recently the development of the kinetically enhanced CVLs (KE-CVLs) by the Centre for Laser Applications at Macquarie University (Withford et al. 1996*b*, Withford et al. 1996*c*, Withford et al. 1997, Withford et al. 1998*a*, Withford et al. 1998*b*, Withford et al. 1998*c*) has resulted in an increase by a factor of two of the total output power of elemental CVLs adding a mixture of H_2 and HCl to the discharge of a 'hot' copper medium. The philosophy which led to the development of the KE-CVL was based on the idea of decoupling the effect of hydrogen halides additives, such as HBr and HCl, on the enhanced kinetic relaxation of the CVL gain medium, from its role to produce the copper vapour as in HyBrID lasers. The behaviour of KE-CVLs suggests that besides the enhanced cooling established by hydrogen, the process of dissociative attachment of the negative hydrogen halides to the free electrons is the dominant mechanism for decreasing the pre-pulse electron density (Withford et al. 1998*c*). This increase in the electron density decay rate, combined with the efficient reassociation of HCl in the plasma region, have significantly pushed the key limiting factor of PRF scaling, allowing for linear output power scaling with increasing PRF (Withford et al. 1998*b*). At the same time, mutual neutralisation of the ionised copper atoms with the negative hydrogen and halogen species leads to an increased gain on-axis, which is favourable for generation of low divergence output. Otherwise the copper density on-axis would be depleted due to ambi-polar diffusion, resulting in an annular gain profile. With ongoing development of KE-CVL technology, these findings may have important implications in the future for applications of high power CVLs.

In summary, the current state-of-the-art in CVL development has emphasised the importance of two parameters which dominate the laser performance, namely the relaxation rate of the electron temperature and electron density, and the rate at which the ground-state copper density is replenished. These parameters determine the operating range of the device, such as power output, PRF and efficiency. Apart from these factors, there are a host of radial effects which greatly influence the operation of CVLs, in particular when operating with unstable resonators with high magnifications. As stated clearly by e.g. Brown et al. (1989), due to the short inversion time of the CVL there is insufficient time for the establishment of transverse modes in the resonator, and so the radial behaviour of the optical pulse is directly related to the radial kinetics of the upper and lower laser levels. Thus, in order to investigate the operation with high magnification unstable resonators in order to improve the beam quality, these radial effects need to be considered.

2.2 TOWARDS HIGH BEAM-QUALITY CVLS

I RADIAL EFFECTS OF THE COPPER MEDIUM Copper vapour lasers (CVLs) are increasingly used in micromachining applications (Glover et al. 1995, Chang & Warner 1996, Knowles 1996, Körner et al. 1996) because of their unique capability to deliver high average output powers with very high beam-quality. The need for low divergence output from CVLs with a centrally peaked far-field intensity distribution

free of 'hot–spots' is also important for many other applications, such as analytic sampling techniques based on laser ablation (Young et al. 1996, see also chapter 5), non-linear frequency conversion (Coutts et al. 1990, Coutts & Piper 1992, Coutts 1995*a*, Coutts & Brown 1995*b*, Withford & Brown 1995) and pumping of solid-state lasers (Knowles & Webb 1993, Knowles & Brown 1995*b*, Coutts et al. 1998). In order to acquire practical acceptance, single unit (stand-alone) oscillators are required which are capable of delivering 5 to 10 W average power with very high beam quality (better than two times the diffraction limit). It is only practical to attempt to efficiently generate near diffraction-limited output from medium-scale devices (bore diameter $20 - 35$ mm) as it becomes increasingly difficult to obtain such output from CVL oscillators with larger bore diameters since unrealistically large unstable resonator magnifications are required to force the divergence to be within the required limit.

At the same time, it is known that in elemental CVLs the gain during the early part of the cavity build-up period is usually depleted on-axis when the device is operated with nominally pure neon buffer gas. Historically, this led to the design of off-axis resonator geometries (Kearsley et al. 1987) to enhance power extraction and improve the efficiency of the laser. A disadvantage of this technique is that the far-field intensity distribution of the laser output is annular or crescent-shaped, and can be quite asymmetric (Coutts 1994), making it unsuitable for high beam-quality applications requiring radially symmetric, centrally peaked far-field intensity distribution. In general, the observed annular radial gain distribution of elemental CVLs is ascribed to the depletion of gain on-axis, which can be caused by a number of radial effects (Brown et al. 1989, Carman et al. 1994, Withford et al. 1995, Carman 1997). Due to the gas temperature profile of the gain medium, which is hottest on-axis, the copper vapour density is smaller at the tube centre than at the walls (Chang 1994, Mildren et al. 1997*b*). The high electrical conductivity of the copper vapour also leads to an observed skin-effect, in particular for large bore systems, where the delay for the electric field to penetrate to the tube axis results in reduced gain on-axis (Chang 1993). The effect of ion-pumping (radial cataphoresis), where the outward diffusion of ionised (copper) species is not compensated by the inward flux of neutral atoms, also leads to an annular gain distribution (Carman 1997).

While HyBrID lasers (Coutance et al. 1995, Little et al. 1995) and KE-CVLs (Withford et al. 1996*b*, Withford et al. 1996*c*, Withford et al. 1997, Withford et al. 1998*a*, Withford et al. 1998*b*, Withford et al. 1998*c*) generally do not exhibit such an annular gain profile, to allow elemental CVLs to be efficiently operated with on-axis unstable resonators the spatio-temporal gain characteristics need to be modified. Primarily, the addition of H_2 as an admixture to the neon buffer gas has been shown to significantly enhance the gain on-axis (Withford et al. 1994*a*, Withford et al. 1994*b*, Withford et al. 1995, Mildren et al. 1995, Withford et al. 1996*a*). The present work will demonstrate that introduction of H_2 additives alone is not sufficient, and other important mechanisms will be investigated which need to be taken into consideration to optimise the design and performance of medium-scale CVL oscillators for efficient extraction of high beam-quality output using on-axis unstable resonators with high magnification.

II Formation of output in CVLs Owing to the high gain and short pulse duration of the laser medium, CVLs are usually fitted with high-magnification unstable resonators to produce high beam quality output. Optical cavities which have been successfully employed include (both negative and positive branch) on-axis (Chang 1994, Coutts 1995*b*) and off-axis (Coutts 1994, Coutts 1995*b*) unstable resonators,

and self-filtering unstable resonators (SFUR) (Pini et al. 1990). When using single oscillators, a trade-off between output power and beam quality has to be made. The output of CVL oscillators fitted with unstable resonators, is derived from an initial seed of amplified spontaneous emission (ASE) which propagates on repeated round-trips within the unstable resonator (Coutts & Brown 1995*a*). This results in the output beam consisting of a succession of components of increasing quality corresponding to propagation of the seed on successive round trips (4, 6 and possibly 8 passes through the gain medium). For sufficiently high magnification M ($\sim$ 50 upwards), the beam quality of the output of higher order round trips (6 and 8-pass) is essentially diffraction-limited. However, the far-field intensity distribution (divergence) of the 4-pass output is determined by the spatial distribution of the initial seed, and scales inversely with the resonator magnification M (Coutts 1995*b*). For medium-scale oscillators the 4-pass component comprises a significant fraction (often more than 50%) of the total non-ASE output power, particularly when operated at high (10 kHz upwards) pulse repetition frequencies.

By increasing the resonator magnification in order to reduce the divergence of the 4-pass output, the effective feedback from the output coupler ($\propto 1/M^2$) is reduced, eventually precluding efficient power extraction. To allow use of the preferred on-axis unstable resonators with very high (100 upwards) magnifications whilst maintaining efficient power extraction, the gain medium needs to exhibit a centrally peaked ASE seed radial profile. To this purpose the temporal and spatial characteristics of the ASE output have been studied, in order to characterise the features of the gain medium during the transient build-up period. It was found that, apart from the effect of the partial H_2 admixture pressure as investigated by Withford et al. (1995), the relative effect due to the degree of thermal insulation, the level of electrical power loading and the total (neon) buffer gas pressure is also significant on establishing the required centrally peaked radial gain profile. To investigate all these effects, a comparative study on two medium-scale CVL oscillators was conducted, each having a different degree of thermal insulation and operated at varying levels of electrical power loading, total neon buffer gas pressure and H_2 partial pressure content. Efficient extraction of high beam-quality output (maximum brightness) from a single medium-scale CVL oscillator using very high magnification (up to $M = 360$) on-axis unstable resonators, is demonstrated.

III AN INTERLUDE: DEFINING THE DIFFRACTION LIMIT

Before the experimental work is presented in the next section, a small side-step is made at this point to include a discussion on the definition of the 'diffraction limit'. This short topical escapade seems appropriate, following the recent international efforts to define a standarised procedure for evaluating the spatial characteristics and quality of any laser system (ISO/DIS11146 1995). In particular, there still exist some controversy as to which definition is most appropriate for characterising non-Gaussian beams such as generated using unstable resonators with high magnifications (Bollanti et al. 1997, Bélanger et al. 1994). The main issue in this discussion will be outlined below, and will be concluded with an appropriate definition of the diffraction limit for the present work.

Due to the Langrange invariance of geometrical optics, the product of the beam waist diameter and the divergence angle $w_0 \cdot \Theta_0$ for a given laser beam is constant, provided that the propagation through the optical system is free of aberrations and (hard–edged) apertures. This fundamental result allows the definition of a 'beam-quality factor' (BQ-factor), and here an outline is given following the derivation involving theory moments as given by Bélanger et al. (1994). Consider a monochromatic

beam in rectangular coordinates propagating along the z axis. An expression is sought for the BQ-factor along the x, y coordinates which in the most general case may differ due to e.g. astigmatism. Given the result that the product $w_0 \cdot \Theta_0$ is invariant, the BQ-factor should relate to both the near-field intensity distribution as determined by the (complex phasor) field amplitude distribution $E(x)$, and its Fourier transform which describes the far-field intensity distribution in terms of an angular distribution of the plane-wave spectrum $P(s)$ defined as

$$P(s_x) = \int_{-\infty}^{\infty} E(x) \exp(-2\pi i s x)\, dx \tag{2.1}$$

Here the notation of Bélanger et al. (1994) is adopted where $s = \sin(\Theta_x)/\lambda$, and Θ_x is the incidence angle of the plane-wave along the x coordinate.

Now it has been shown explicitly by Bélanger et al. (1994) that the BQ-factor is determined by the product of the variances (second-order moments) of $E(x)$ and $P(s)$, i.e. the spatial spread function $\langle x^2 \rangle$ and the angular spread function $\langle s_x^2 \rangle$ given by (Bélanger et al. 1994)

$$\begin{aligned} \langle x^2 \rangle &= \frac{1}{I} \int_{-\infty}^{\infty} x^2 |E(x)|^2\, dx \\ \langle s_x^2 \rangle &= \frac{1}{I} \int_{-\infty}^{\infty} s_x^2 |P(s_x)|^2\, ds_x \end{aligned} \tag{2.2}$$

where the integrated intensity distribution I is conveniently defined as

$$I \equiv \int_{-\infty}^{\infty} |E(x)|^2\, dx \tag{2.3}$$

The numerical value of the BQ-factor is obtained by normalising to certain theoretical values for the product $\langle x_0^2 \rangle \cdot \langle s_{x0}^2 \rangle$ which is constant throughout the propagation of the laser beam

$$(\text{BQ-factor})_x^2 = \left(\frac{\langle x^2 \rangle \cdot \langle s_x^2 \rangle}{\langle x_0^2 \rangle \cdot \langle s_{x0}^2 \rangle} \right)^{1/2} \tag{2.4}$$

A similar definition holds along the y coordinate. Thus, a BQ-factor of unity is defined as the diffraction limit, and a BQ-factor of 2 is often referred to as two times diffraction limited. In practise, the BQ-factor is often normalised with respect to the theoretical values $\langle x_0^2 \rangle \cdot \langle s_{x0}^2 \rangle$ obtained from the Gaussian beam formalism (Bollanti et al. 1997), since in the paraxial approximation the lowest order transverse mode (TEM_{00}) in stable resonators is accurately described by Gaussian beam. Also, the Gaussian beam has the lowest divergence angle for a given beam waist, i.e. it minimises the product $\langle x_0^2 \rangle \cdot \langle s_{x0}^2 \rangle$.

However, '... these methods may not apply to highly diffractive beams such as those produced by

unstable resonators or passing through hard-edged apertures' (ISO/DIS11146 1995), as is the case for CVLs and excimer lasers. As Bélanger et al. (1994) point out, the presence of sharp discontinuities in the near-field intensity distribution (as for example in a top-hat intensity profile) translates to a Fourier-spectrum of plane-waves whose asymptotic behaviour scales as $1/s$, cf. the $\sin(s)/s$ Airy distribution obtained by Fraunhofer diffraction of a plane-wave. This causes $\langle s_x^2 \rangle$ to diverge, and hence no useful definition for the BQ-factor as in equation (2.4) can be made. In this sense, Gaussian distributions constitute a rather special class of beams since the integrals of the form $\langle x^2 \rangle = \int_{-\infty}^{\infty} x^2 \exp(-x^2)\, dx$ are finite, while more generally $P(s)$ may not be square-integrateable[1]. Particularly for Fraunhofer diffraction the angular spread function (i.e. the far-field intensity distribution) does not converge upon square-integration, and Bélanger et al. (1994) stress that a useful definition of a BQ–factor can only be obtained if evanescent waves of the plane-wave spectrum are ignored. They suggest, for instance, that the integral for $\langle s_x^2 \rangle$ given in equation (2.2) could be limited to $s_0 \equiv 1/\lambda$, which effectively states that sub-wavelength structure in the far-field is ignored. While the existence of sub-wavelength structure in a paraxial focus has recently been measured experimentally by Karman et al. (1998), for many practical purposes and applications of lasers it is of little relevance.

As a result, the definition of the 'diffraction limit' of an optical beam implies a somewhat subjective selection of quantitative and qualitative criteria which refer to some specific practical requirement. Bollanti et al. (1997) suggested that the normalisation constant $\langle x_0^2 \rangle \cdot \langle s_{x0}^2 \rangle$ could be obtained by calculating the direct Fourier transform of the (idealised) near-field distribution as defined by the resonator configuration. In the case of the CVL the presence of the copper shadow and the central hole in the output coupler of the on-axis unstable resonator significantly influence the geometry of the optical near-field intensity distribution. As such, the numerical value for the 'diffraction-limited' BQ-factor $\langle x_0^2 \rangle \cdot \langle s_{x0}^2 \rangle$ calculated in this fashion would be larger than that, say, of a perfect uniform and symmetric top-hat, leading to a false enhancement of the measured BQ-factor. While such an approach would give an accurate measure for the best obtainable BQ-factor for a given resonator configuration, it does not allow for useful comparison between different resonator configurations and involves calculation of the Fourier transform of the (arbitrary) near-field intensity profile which may not be trivial.

A more stringent definition of the diffraction limit will be adopted here instead, where the output of the CVL is assumed to exhibit a cylindrically symmetric top-hat near-field intensity profile with a plane wavefront. Now, the diffraction-limited spot size at focus is defined to be the radius of the central Airy disc (Rayleigh criterion), and one finds from standard optics textbooks (Hecht 1987, pp. 416-421)

$$w_0 = 1.22 \frac{\lambda f_0}{D} \tag{2.5}$$

where w_0 is the radius of the focal spot defined the first zero points as in the Rayleigh criterion, f_0 is the focal length of the lens and D is the effective aperture given by the beam diameter at the lens. The

[1] The $\sin(x)/x$ function, together with e.g. the Lorentzian distribution, belong to a more generic class of Levy-distributions which are generally not square-integrateable. Levy-distributions have recently gained interest to describe various complex natural statistical phenomena such as stock-markets and the flight patterns of pigeons (Casti 1997).

diffraction-limited half-angle divergence Θ_d in this definition is given by

$$\Theta_d = 1.22\frac{\lambda}{D} \quad , \tag{2.6}$$

which substituted in (2.5) yields

$$w_0 = f_0\,\Theta_d \quad . \tag{2.7}$$

In analogy with Gaussian beams, a definition of a Rayleigh range is useful to quantify the depth of field of a given focus. While a universally accepted definition of a Rayleigh range does exist (Siegman 1986), it is here defined as the distance at which the diameter of the geometric shadow calculated using rays optics is equal to the waist w_0 as given in (2.5). In this definition one finds for the Rayleigh range Δz

$$\Delta z = 2.44\,\lambda\left(\frac{f_0}{D}\right)^2 . \tag{2.8}$$

Using the above, a beam with a 25 mm diameter at a focusing lens of 200 mm for $\lambda = 500$ nm, the focal spot radius is 5 μm, while the depth of field on either side is 80 μm. In comparison with the definition of the Rayleigh range z_R for Gaussian beams

$$z_R \equiv \frac{\pi w_0^2}{\lambda} \tag{2.9}$$

a focal spot radius of 5 μm would have $z_R = 0.16$ mm, which is twice the value of the geometric definition given in equation (2.8).

For laser machining purposes, the focusability of the laser is an important parameter and a measure for the actual focused power density is needed. A common technique uses the 'power-in-the-bucket' principle, which measures the transmitted power through a constricting aperture. Note that such a definition of the diffraction limit is very stringent, and often results in a conservative value for the beam quality. To calculate the power-in-the-bucket beam quality, consider the incident power density in the far-field for plane wave diffraction from a circular aperture given by

$$I(r) = I(0)\left[\frac{2J_1\left(\pi Dr/\lambda R\right)}{\pi Dr/\lambda R}\right]^2 \tag{2.10}$$

where R is the distance between the plane of observation and the aperture object plane, r is the constricting aperture diameter and J_1 is the first order Bessel function of the first kind. This equation assumes the far-field condition $R \gg r$, or in the case of a focusing lens $R \approx f_0$. Integration of (2.10) up to the first minimum (the Airy disc) yields 84% of the total power, while 91% of the total power is contained within the extremities of the second Airy ring with a diameter of 1.8 times the Airy disc. Generally, the

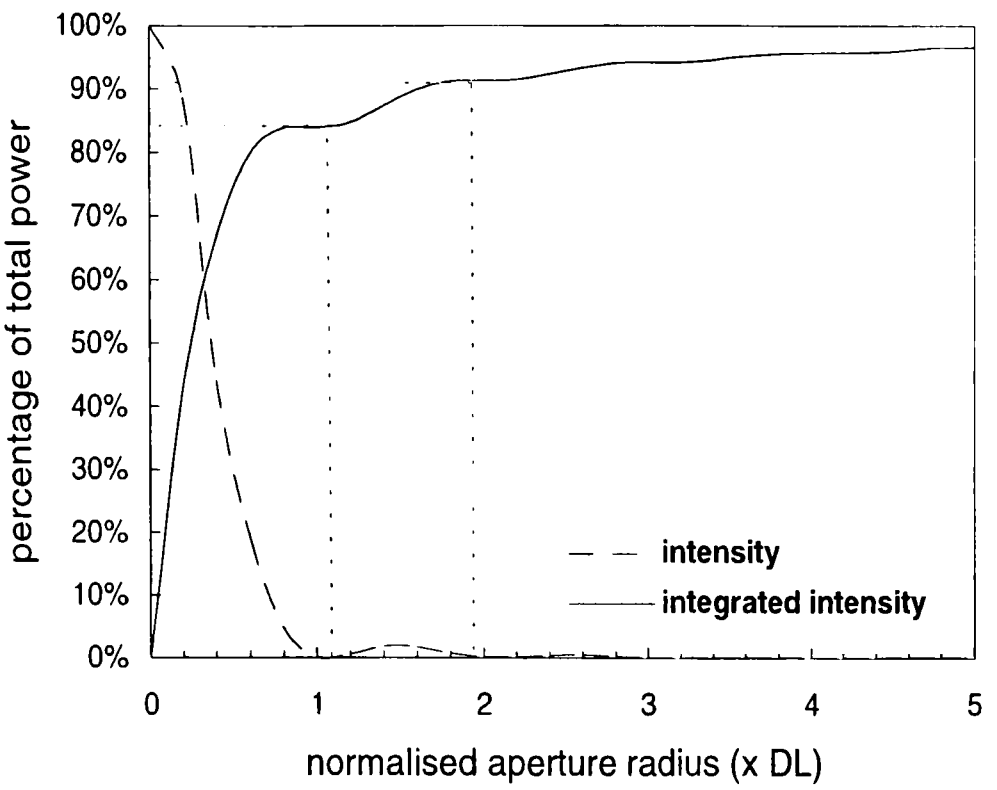


FIGURE 2.2: The Airy diffraction pattern and integrated power-in-the-bucket energy distribution.

fraction of the power-in-the-bucket collected as a function of r is given by

$$\text{power-in-the-bucket} = \frac{\int_0^r 2\pi r I(r)\, dr}{\int_0^\infty 2\pi r I(r)\, dr} \tag{2.11}$$

The result of (2.11) is plotted in figure 2.2. Note that due to the periodic character of the intensity profile, the integrated transmitted power curve exhibits points of inflection corresponding to the minima of the Airy pattern. These features will only be observed for a diffraction limited output beam in absence of any other aberrations, which generally will not be the case.

2.3 EXPERIMENTS

I DESCRIPTION OF LASER SYSTEMS The primary laser system used in the studies on the stand-alone oscillator operation of medium-scale devices was the Oxford Lasers LS 20-10 unit (henceforth referred to as LS), consisting of a longitudinal discharge-pumped 1 m long active region with a 25 mm bore diameter. The alumina plasma tube was wrapped in high-grade alumina fibre insulation (maximum hold-off temperature $\sim$ 1800 °C) which is contained in a silica tube. The typical electrical input power required to achieve near optimum wall temperature was 4.1 - 4.3 W/cc at a PRF of 10 kHz. The excitation circuit comprised a thyratron switched LC-inversion scheme, and a single magnetic pulse compression (MPC) stage. The measured peak voltage on the laser head was 17 kV with a rise-time of 30 ns.

To establish the relative effects of the amount of insulation of the plasma tube on the operating characteristics, a comparison was made with a second, in-house built laser (referred to as IH), which

consisted of a similar but less heavily insulated laser head with a 0.75 m long plasma tube and 25 mm bore diameter. This laser was typically operated at 6.2 7.3 W/cc electrical input power to achieve optimum temperature at 10 kHz, representing a significantly higher power loading. The excitation circuit was similar to that of the LS system, also containing a single MPC stage.

Since the LS system was normally operated with a slow flow of buffer gas, the gas outflow rate was changed while the gas inflow rate was kept constant in order to vary the total neon buffer gas pressure. The pressure was measured with an internal pressure transducer (accuracy 1 mbar), which was calibrated using a mercury manometer showing a straight linear dependence in the range $1 - 1000$ mbar with a correlation coefficient $R^2 = 0.99$ or better. The IH laser was normally run with a sealed-off laser head, with the static gas fill replaced daily. While nominally 'pure' (99.95%) neon was normally used as the buffer gas, both the LS and IH laser contained a small ambient concentration of H_2 impurities outgassed from the insulation and nylon tubing in the gas handling system. (From this point onwards the word 'nominally pure' neon will denote 99.95% grade neon supply, combined with the native concentration of H_2 impurities arising from the gas handling system and the laser head).

II MEASUREMENT OF ASE SEED PROFILES ASE seed profiles were measured for both lasers at various neon buffer gas pressures using an imaging arrangement as described in Coutts & Brown (1995*a*). A spatial filter, consisting of a pair of lenses and a pinhole, ensured only parallel rays emerging from the far end of the plasma tube were collected. Generation of 2-pass ASE output due to spurious feedback was suppressed by placing a black screen at 45° at the far end of the gain medium, and all imaging optics were either placed slightly skew or sufficiently remote to prevent backscatter into the laser. Both the green and yellow component were measured simultaneously, using AR coated achromatic doublet lenses at all times. By scanning a fast photodiode (Thor Labs DET200) across the imaged output beam, time-traces of the ASE seed profiles were recorded on a digital oscilloscope (Tektronix 2430A). For each radial position, the peak value of the initial ASE spike was taken to represent the intensity of the ASE seed at that position.

In figure 2.3 and figure 2.4 the ASE seed radial intensity profiles $I(r)$ are plotted for various pure neon buffer gas pressures for the LS and the IH laser respectively. While there were slight variations in the ASE seed power ($\sim 10\%$) over the range of pressures investigated, it is the spatial distribution of the seed that determines the spatial distribution of the subsequent laser output in the far-field. The areas under the curves have therefore been normalised to give constant seed power integrated over the whole aperture radius R, i.e.

$$\int_0^R 2\pi r I(r)\, dr \equiv 1. \tag{2.12}$$

From the measured radial ASE seed profiles it is evident that at a low buffer gas pressure of 30 mbar of nominally pure neon, the initial gain distribution is highly annular. By increasing the buffer gas pressure the annularity was reduced and the axially depleted gain profile was 'filled-in'. In the case of the LS laser operated at 4.1 W/cc, the ASE seed profile is approximately top-hat at 80 mbar (figure 2.3). By further increasing the buffer gas pressure the gain became more centrally peaked, ultimately approaching Gaussian-like distributions for pressures in excess of 100 mbar.

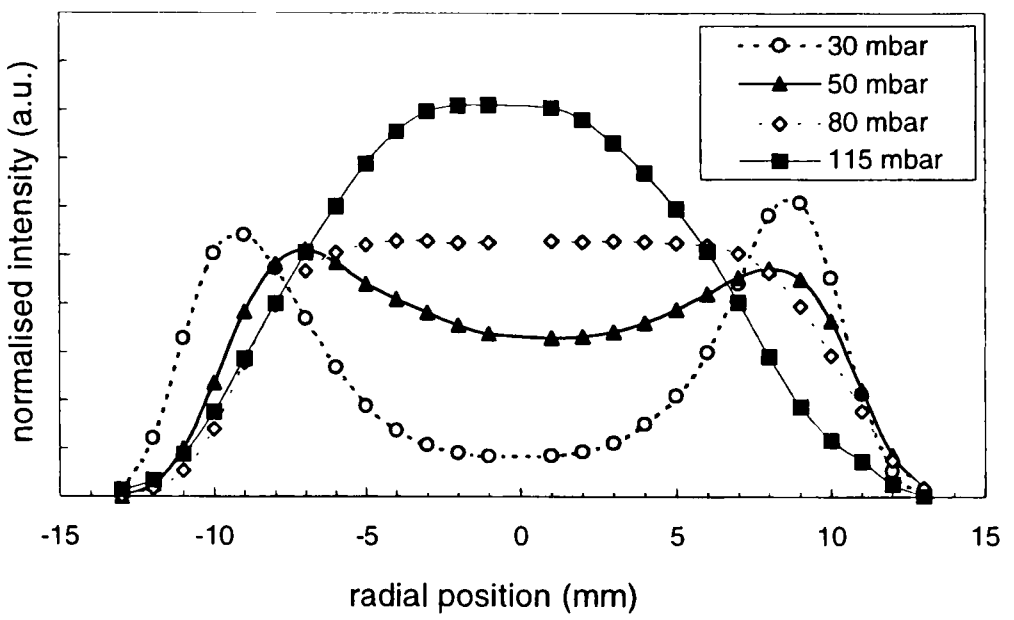


FIGURE 2.3: ASE seed radial profiles from the LS 20-10 laser operated at various nominally pure neon buffer gas pressures with 4.1 W/cc specific electrical input power.

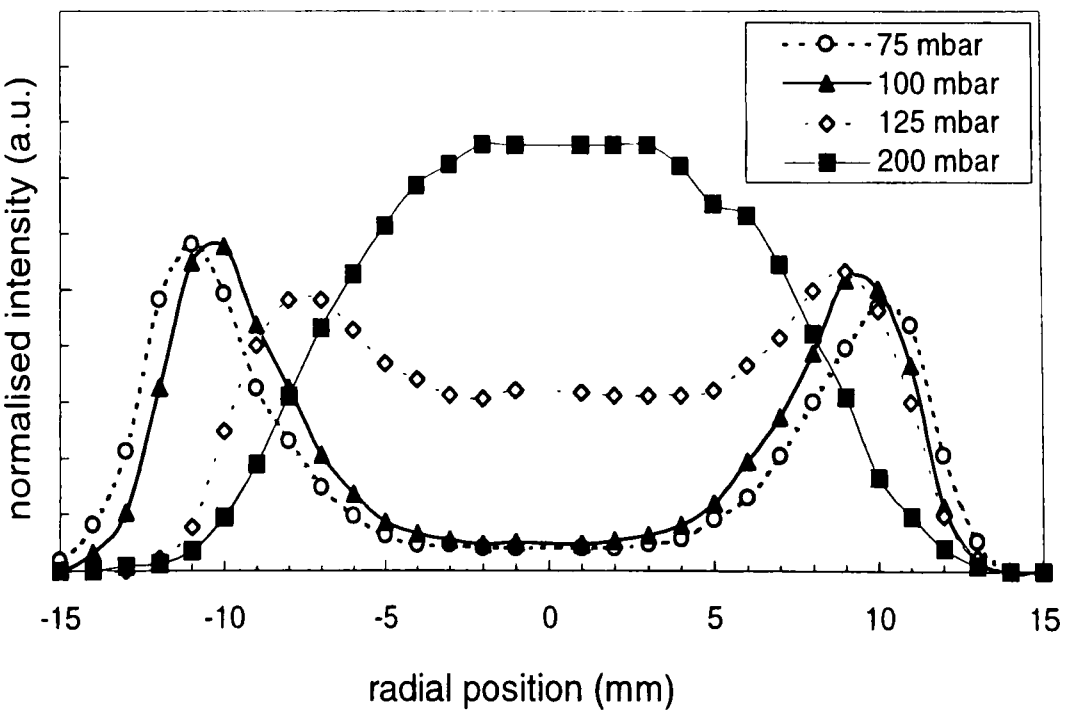


FIGURE 2.4: ASE seed radial profiles from the in-house built laser operated at various nominally pure neon buffer gas pressures with 7.3 W/cc electrical input power, except for 200 mbar where the electrical input power was 6.5 W/cc.

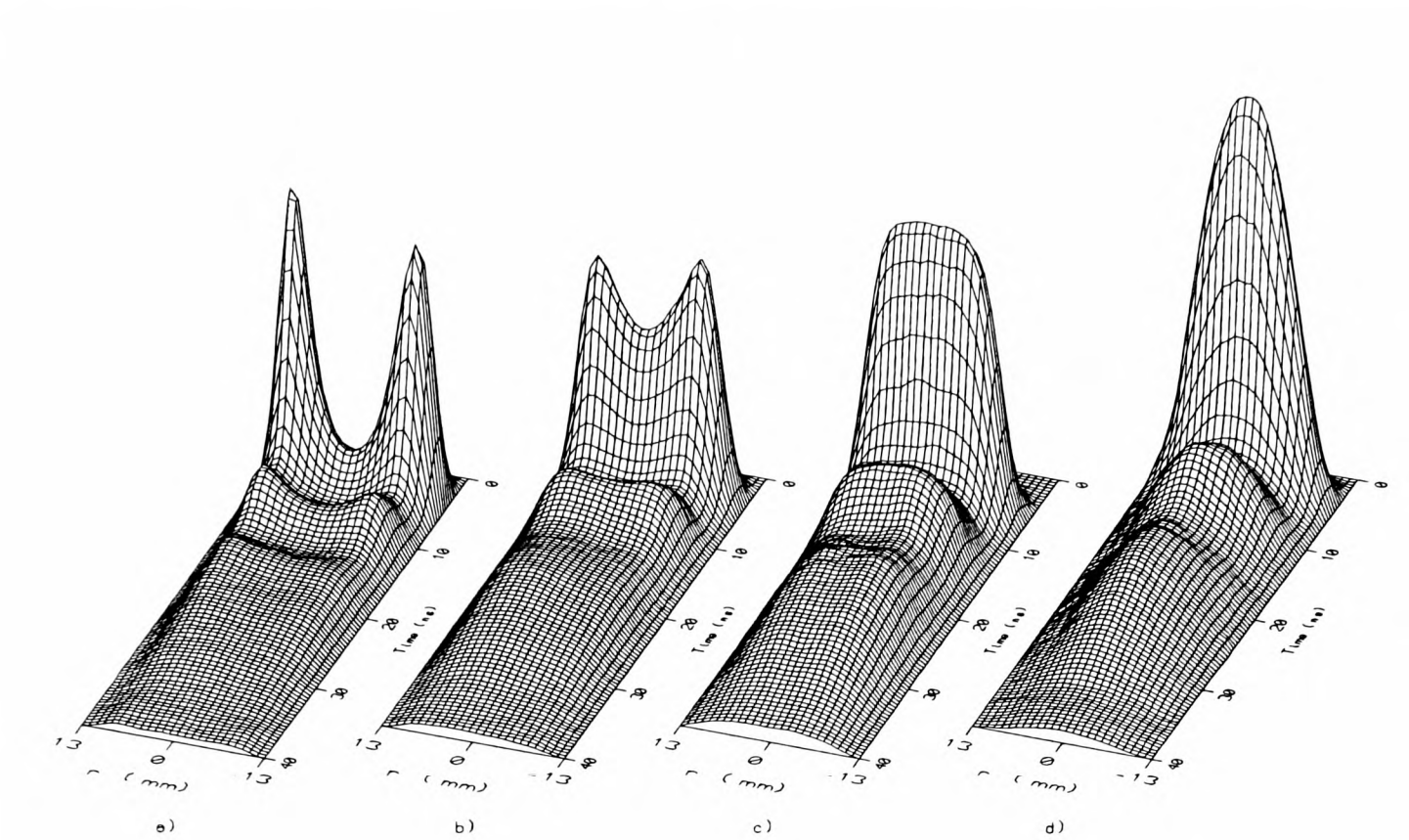


FIGURE 2.5: Time-traces of the optical pulse from the LS 20-10 laser measured across the laser aperture (radius R) at different pressures: a) 30 mbar; b) 50 mbar; c) 80 mbar; d) 115 mbar.

Similar results were obtained with the IH laser operated at 7.3 W/cc, where an increase in the total buffer gas pressure also led to a more centrally peaked gain profile (figure 2.4). However, for the IH laser much higher pressures were required to achieve similar effects. While the LS CVL produced a top-hat profile at 80 mbar, at this pressure the IH system still exhibited an annular profile similar to that of the LS at 30 mbar. To alleviate the annularity, the IH laser required approximately twice the pressure of the LS system.

To illustrate the evolution of the radial gain distribution after the initial ASE spike, the time-traces of the full ASE pulse recorded for the LS system are plotted as a function of radial position at different pressures in figure 2.5. At the low pressure of 30 mbar the annularity of the ASE intensity distribution is found to linger up to 15 ns after the initial ASE spike, and is therefore present for a significant fraction of the total pulse duration of 35 ns. At 50 mbar, while the ASE seed is found to be axially depleted, the radial profile is already significantly filled-in on-axis at around 10 ns after the start of the optical pulse. At higher pressures in excess of 80 mbar, the radial ASE distribution is centrally peaked at all times. For both laser systems it was found that the overall gain duration of the laser medium remains relatively unchanged ($\pm$ 3 ns) with varying buffer gas pressures.

III OSCILLATOR CHARACTERISATION Operation of the LS laser with negative branch on-axis unstable resonators with very high magnifications was characterised. The resonator consisted of a 45° scraper mirror with a 1 mm diameter hole, placed at the common focus of pair of concave mirrors to form a confocal unstable resonator. The concave HR mirror had a radius of curvature of 3.6 m, while the radius of the small concave mirror was chosen to be 10, 25 or 50 mm, giving resonator magnifications M of 360, 144 and 72 respectively. The output power was measured at different operating buffer gas

p (mbar)	plane-plane	M = 72	M = 144	M = 360
30	(19.5)	10.5 (17.5)	8.5 (16.5)	4.5 (15.0)
50	(21.0)	11.0 (17.5)	9.5 (17.0)	6.0 (15.0)
80	(22.0)	12.5 (20.0)	10.5 (19.0)	7.0 (17.0)
115	(23.0)	13.5 (20.5)	11.0 (19.5)	8.5 (18.5)

TABLE I: Output power characteristic of the LS 20-10 laser at various cavity magnifications and nominally pure neon buffer gas pressures with 4.1 W/cc electrical input power. The low divergence component is listed, compared with the total raw output power in brackets, both given in watts.

pressures using a thermopile power meter (Ophir 925), giving a relative accuracy of ±0.5 W. A spatial filter was used to separate the ASE output from the low divergence component in order to measure the low divergence non-ASE component of the output power. The low divergence component was further characterised by imaging the far-field intensity distribution onto a CCD camera (Exitech, 256×256 pixels over 4×4 mm). Additionally, as a hard measure of the beam quality a 'power-in-the-bucket' experiment was performed. In this case a field restricting aperture stop was placed in the far-field image plane, and the power transmitted was measured as a function of aperture diameter.

The output power characteristics of the LS laser are listed in table I. Both the low divergence component and the total raw output power (in brackets) are given at various resonator magnifications and buffer gas pressures with nominally pure neon. Note that raw output power referes to the sum of the ASE output power and the low divergence (non-ASE) output power. As expected, both the low divergence and total raw output power decrease with increasing resonator magnification at constant pressure. For a given configuration, the output power increases with increasing buffer gas pressure. For example, for

P_{in} (W/cc) (kW) p (mbar)	3.9 (1.9)	4.1 (2.0)	4.3 (2.1)	4.5 (2.2)	4.7 (2.3)
40	2.5 (8.0)	3.5 (11.0)	4.5 (14.0)	5.0 (16.0)	5.0 (17.0)
130	-	8.5 (18.5)	10.0 (21.5)	6.0 (19.0)	-
150	5.0 (13.0)	8.0 (18.5)	9.5 (22.0)	8.0 (23.5)	-

TABLE II: Output power characteristic of the LS 20-10 laser at various specific electrical input powers (with the corresponding total input powers cited in brackets) for cavity magnification of 360 at high nominally pure neon buffer gas pressures. The low divergence component is listed, compared with the total raw output power in brackets, both given in watts.

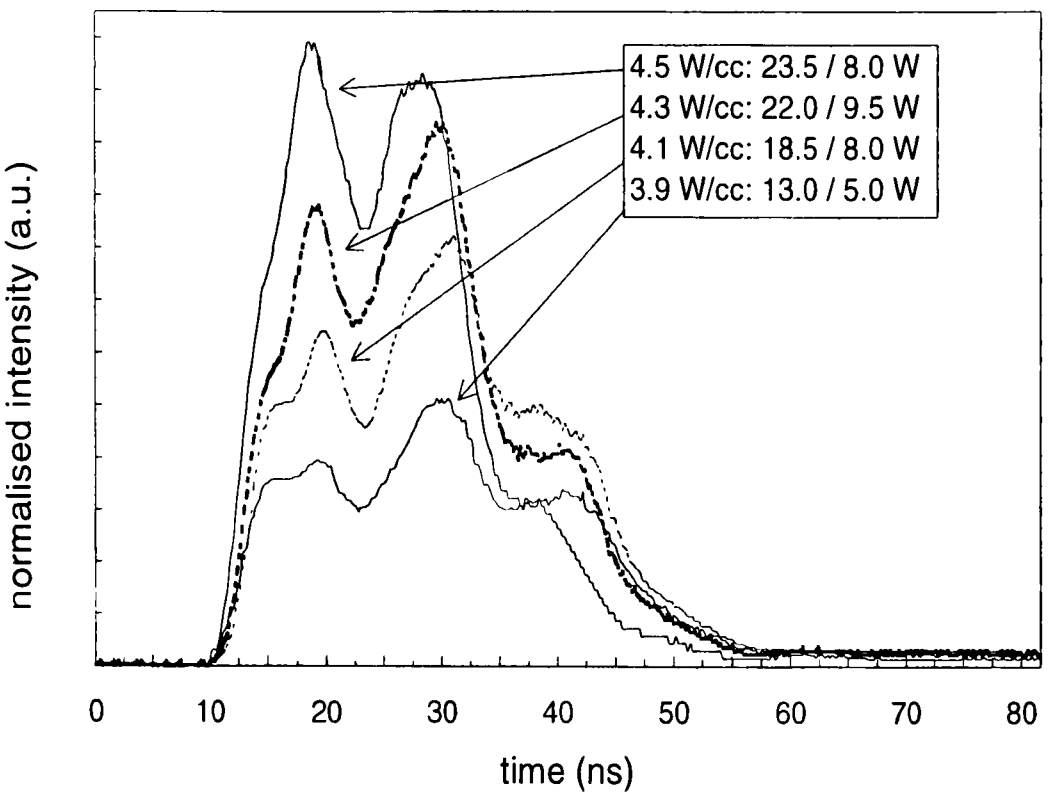


FIGURE 2.6: Optical output of the LS 20-10 laser at different levels of electrical input power, operated with 150 mbar pure neon buffer gas pressure, $M = 360$.

$M = 360$ the non-ASE output power increases from 4.5 W at 30 mbar to 8.5 W at 115 mbar.

In table II the low divergence and total raw optical output powers are listed for varying specific electrical input powers at a resonator magnification of 360 at buffer gas pressures of 40, 130 and 150 mbar. When operated at low pressures and near-optimum electrical input powers (4.1 - 4.3 W/cc), the maximum non-ASE output power obtained remains significantly lower than at elevated buffer gas pressures, while increasing the input power only results in an increase of the ASE output power. At high buffer gas pressures (130 - 150 mbar) optimum operation was for 4.3 W/cc electrical input power, with maximum low divergence output power of 10.0 W obtained at 130 mbar from the $M = 360$ unstable resonator. For 4.5 W/cc input power the LS laser output turned distinctly yellow, indicating that the laser was overheated. Bringing the input power down to 3.9 W/cc resulted in a significant reduction of output power, giving only 13 W of total output.

In figure 2.6 the shape of the optical output traces are plotted for various electrical input powers, for the LS laser operated with $M = 360$ at 150 mbar pure neon buffer gas pressure. The plotted intensity is normalised to reflect the total output power in the optical pulse, while for reference the non-ASE output powers are noted again, taken from the bottom row of table II. From figure 2.6 it is clear, that increasing the electrical input power from 3.9 W/cc up to 4.3 W/cc results in a simultaneous increase in of both the ASE (2-pass) output, and the non-ASE output contained in the 4- and 6-pass component. While a further increase of the electrical input power beyond 4.3 W/cc up to 4.5 W/cc results in an increase in the ASE output, the high-beam quality component is found to reduce. This effect is illustrated in figure 2.6 by the significant reduction of the area contained under the 6-pass output at 4.5 W/cc.

The far-field intensity profile of the low divergence output at near optimum conditions of 115 mbar and 4.1 W/cc electrical input power for the high magnification resonator of 360, is plotted in figure 2.7.

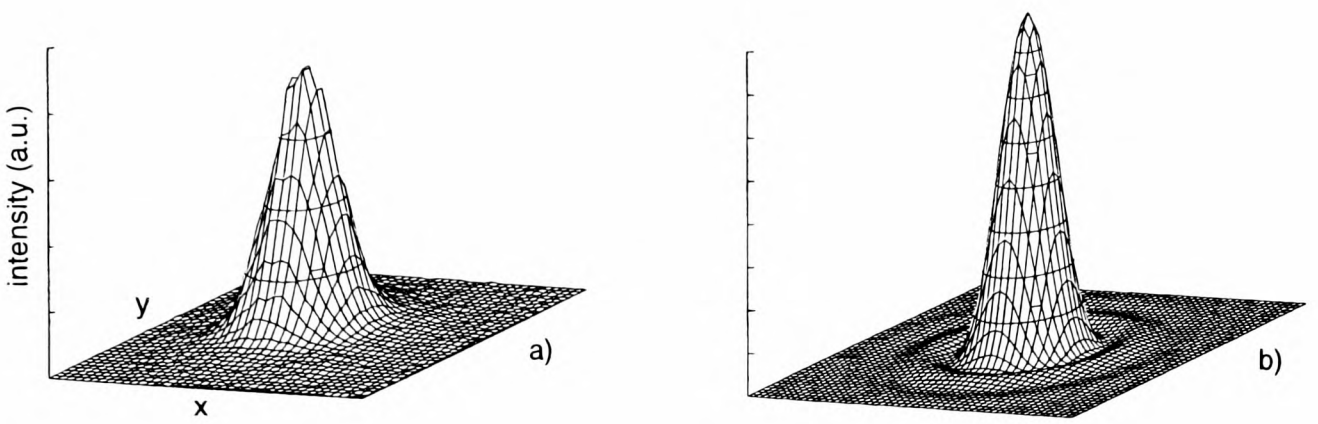


FIGURE 2.7: Far-field intensity profiles: **a)** as measured for the LS 20-10 laser with $M = 360$; compared to **b)** the diffraction limited Airy pattern due to Fraunhofer diffraction through a circular aperture. Full extent of the plotted xy-plane corresponds to 0.1 mrad.

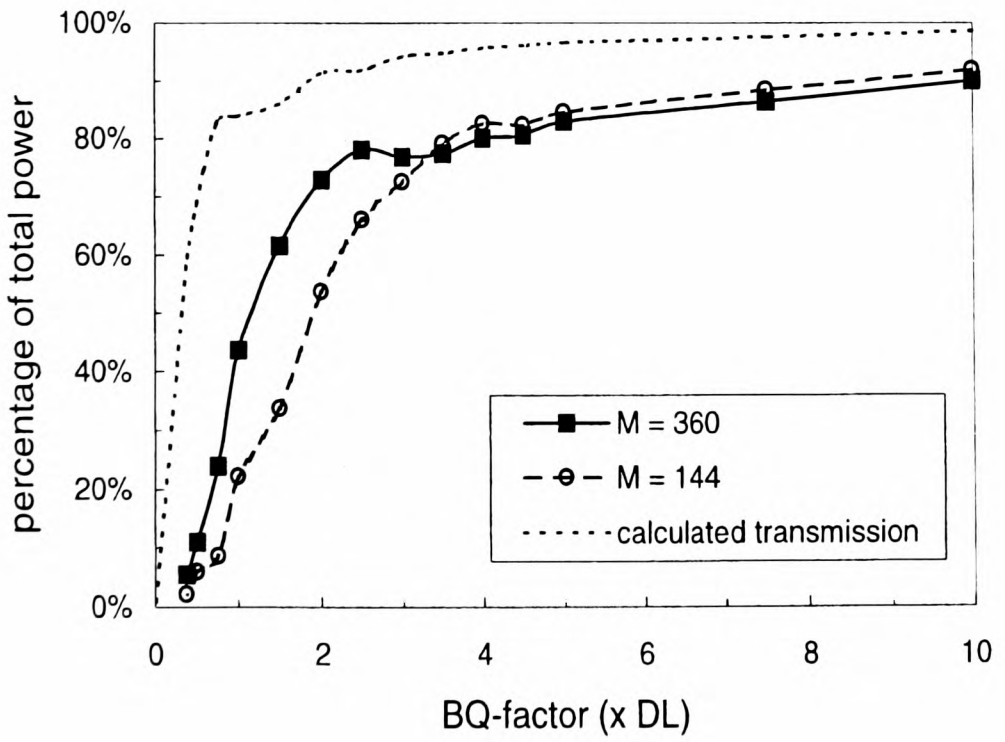


FIGURE 2.8: Power-in-the-bucket measurement of the LS 20-10 laser for high M resonators.

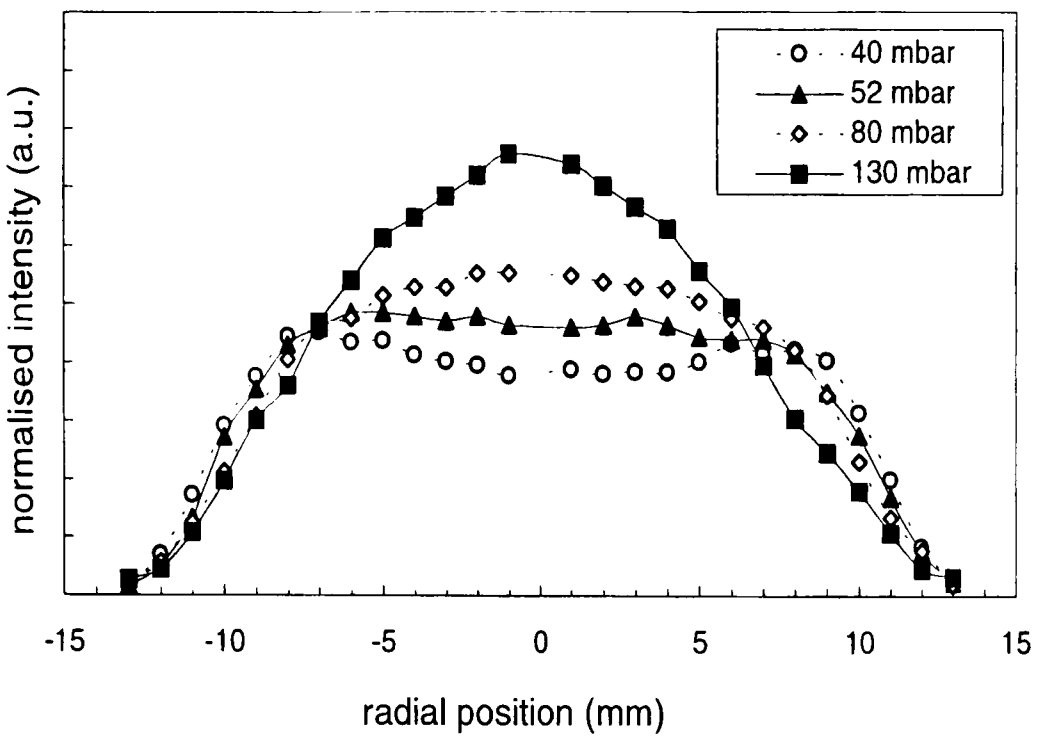


FIGURE 2.9: ASE seed radial profiles from the LS 20-10 laser operated at various neon buffer gas pressures containing 2% H_2 with 4.1 W/cc electrical input power.

The profile is to be compared with the diffraction limited Airy pattern due to Fraunhofer diffraction of a plane wave through a circular aperture of equal diameter as the beam diameter, as discussed earlier in section 2.III. The plotted xy-range in both graphs corresponds to 0.1 mrad full angle divergence. The central lobe is approximately 1.5 times wider than the central Airy disc, extending towards the second Airy ring. Note that the angular diameter of the second Airy ring is equivalent to 1.8 times the diameter of the Airy disc.

In figure 2.8 the result of the power-in-the-bucket measurement is given for resonator magnifications of 144 and 360, again operating at a buffer gas pressure of 115 mbar and 4.1 W/cc electrical input power. The dashed line is the calculated throughput of a circular aperture given by the radially integrated power density in the far-field for plane wave diffraction from a circular aperture. Note also that due to the periodic character of the Bessel function-like distribution, the theoretical curve exhibits points of inflection corresponding to the minima of the Airy pattern illustrated in figure 2.7. The turning point in the power-in-the-bucket curve occurs at 2 times the diffraction limited aperture for the $M = 360$ resonator, which confirms the observation that the central lobe of the far-field intensity distribution extends towards the second Airy ring.

IV ADDITION OF H_2 TO THE NEON BUFFER GAS To establish the merits of increasing the total buffer gas pressure on the laser operation, relative to an increase in the partial H_2 pressure, the LS laser was operated with a neon buffer gas supply containing 2% H_2 with 4.1 W/cc electrical input power. The ASE seed radial profiles were measured, as plotted in figure 2.9.

At constant total pressure the ASE seed profiles were found to be less annular at higher partial pressures of H_2. The unstable resonator total non-ASE output power characteristics obtained with the

H_2 admixture, however, could never reproduce or match the performance achieved by operation with nominally pure neon at elevated pressures. In the pressure range between 60-130 mbar the total raw output power was found to be very low, never exceeding 13.0 W, while the low divergence component was always less than 6.5 W when using a resonator magnification of 360 and operating at 4.1 W/cc electrical input power. By going to a lower magnification of 72, and increasing the input power to 4.5 W/cc, the total raw output power could be increased to 19.5 W when operating at 40 mbar with the H_2 admixture, matching the performance obtained with nominally pure neon. However, the low divergence component in this case never exceeded 7.0 W, which is approximately 50% of the maximum value obtained with nominally pure neon. To ensure that the H_2 concentration of 2% is not too far from the optimum value, a combination of an admixture containing 10% H_2 in neon, and nominally pure neon was used to perform a qualitative scan of a range of H_2 concentrations. It was found that at elevated H_2 concentrations in excess of 2%, the gain duration is considerably shortened, eventually leading to the cessation of lasing action. Efficient operation could only be established by reducing the H_2 concentration towards the 1-2% range, reproducing the results obtained with the 2% gas admixture.

In comparison with the LS laser, the IH laser should by itself contain a lower background H_2 concentration for two reasons. Firstly, the fact that the plasma tube is not heavily insulated means that the alumina fibre runs hotter under normal operating conditions, allowing more thorough outgassing of impurities, such as water vapor, prior to operation. Secondly, the gas handling system was completely made out of copper tubing, which significantly reduces the diffusion of water vapor into the system compared to nylon tubing. To establish the relative merits of an increase in the partial H_2 pressure compared to an overall pressure effect, the IH system was run clean by outgassing impurities by flushing the active medium with a steady flow of pure neon during normal lasing operation for 6 hours. The radial ASE seed profiles were measured for high pressures operating with 6.5 W/cc electrical input power. With a 'dirty' system a centrally peaked profile could be produced at 200 mbar, similar to that plotted in figure 2.4. However, after impurities were flushed out the ASE seed radial profile returned to the highly annular shape even when operated at pressures in excess of 200 mbar, where the seed profile resembled those obtained in the LS laser at low pressures (less than 100 mbar) depicted in figure 2.4.

2.4 DISCUSSION

I OPERATION OF HIGH MAGNIFICATION UNSTABLE RESONATORS The divergence of the output of medium-scale CVL oscillators, where typically only 3-4 round trips (ASE, 4-pass and 6-pass components) can be accommodated during the gain pulse, is critically dependent on the resonator magnification M. To first order, the normalised near-field spatial intensity profile of the ASE seed is reproduced in the far-field intensity distribution of the subsequent 4-pass output, where the divergence scales $\propto 1/M$ (and hence the intensity distribution in the far-field scales by M^2). Thus, a more centrally peaked ASE seed profile generally results in a lower divergence of the 4-pass component.

In order to reduce the divergence of the 4-pass output to less than twice the diffraction limit, cavity magnifications M of order ≥ 300 are required. However, to produce any significant power output at such extremely high magnifications, the gain on-axis needs to be sufficiently high to overcome the high losses

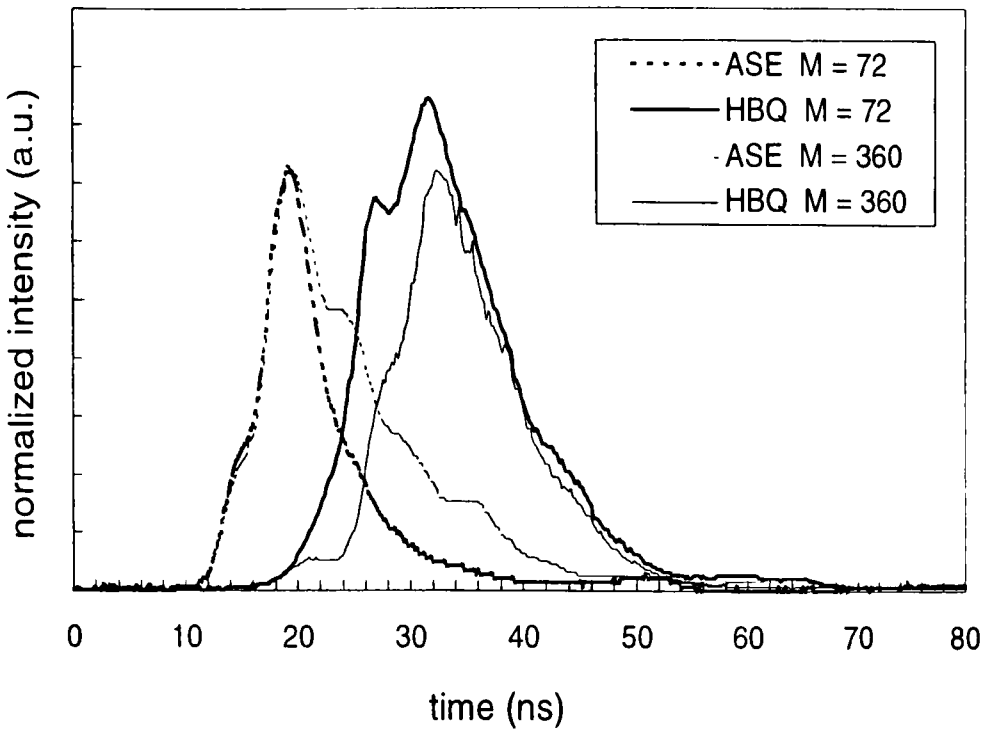


FIGURE 2.10: ASE and high beam-quality (HBQ) components of the optical output of the LS 20-10 laser for different M resonators.

of the unstable resonator and control the ASE. For example, for $M = 360$ the fractional feedback is only $\sim 10^{-5}$. It follows from geometric considerations, that during the first amplifying (3-pass) stage of the seed, only the central part of the gain (within the solid angle subtended by the focus at the scraper mirror and the full aperture of the HR mirror) can contribute the amplification of the small fraction of the seed which is reflected into the resonator. Therefore, not only is a centrally peaked ASE seed needed to generate the required high beam quality of the subsequent 4-pass output, but equally important is the need for the gain to remain sufficiently high on-axis throughout the laser pulse in order to control (saturate) the laser medium to establish efficient power extraction.

This effect is illustrated in figure 2.10, where both the ASE and high beam-quality (HBQ) components of the optical output from the LS laser are plotted against time for two different resonator magnifications. Separation of the ASE and HBQ components was done using a spatial filter, where utmost care needed to be taken to ensure no spurious feedback or parasitic lasing would bias the measured relative contributions. In the case of relatively low $M = 72$, the initial ASE spike is found to decay fast, indicating that the output coupler reflectivity is sufficiently high to saturate the gain medium and efficiently extract power during the higher order round trips. In comparison, when the laser is fitted with the $M = 360$ resonator, the ASE signal is found to extend longer into the optical pulse, thus reducing the output power in the HBQ component, indicating that the effective reflectivity is too low to fully control the gain medium. To verify this observation, a beamsplitter was used to sample 2% of the average intracavity power at the HR. For $M = 72$ resonator the average intracavity *non-ASE* power was 250 mW, while for the $M = 360$ resonator this was reduced to 40 mW.

II RADIAL GAIN DISTRIBUTION IN MEDIUM-SCALE CVLS Present understanding of CVL kinetics

highlights the importance of recombination and relaxation processes during the afterglow and interpulse period (Mildren et al. 1995, Webb & Hogan 1995, Hogan et al. 1995). Kinetic relaxation processes directly affect the pre-pulse conditions in the plasma, which in turn influence the radial gain distribution of the laser medium. As pointed out earlier, a number of pathways have been suggested via which the plasma relaxation process can be enhanced, yet it remains to be experimentally verified as to which mechanism is the most dominant one. For the present discussion it suffices to state that the observed radial variations in the gain medium of medium-scale CVLs is caused by axial depletion of the pre-pulse copper vapour density (Brown et al. 1989, Carman et al. 1994, Withford et al. 1995, Carman 1997).

It has been demonstrated that addition of small partial pressures of H_2 to the neon buffer gas of elemental CVLs modifies the plasma kinetics to result in a more centrally peaked gain profile (Withford et al. 1994*a*, Withford et al. 1994*b*, Mildren et al. 1995, Withford et al. 1995, Withford et al. 1996*a*). In comparison, the present investigation shows that the enhanced beam-quality performance of the LS laser is ascribed to a *simultaneous* increase of the partial hydrogen pressure and the total pressure. Although the concentration of the ambient H_2 content of the LS laser has not been measured directly, there is evidence that it is of order one percent, which is sufficient to change the plasma kinetics. In this respect, it is also important to note that Withford et al. (1996*a*) showed that the optimum H_2 content for a given configuration is not determined by the relative percentage, but rather the absolute partial pressure of H_2.

Again, the importance of establishing a high gain on-axis persisting *throughout* the pulse when using high magnification unstable resonators is emphasised. While an increase of the partial H_2 pressure alone can modify the gain to be centrally peaked, maximum power extraction can only be obtained by operating at elevated buffer gas pressures with relative H_2 concentrations up to 1%. Recall the results for the LS laser, where a centrally peaked ASE seed could be established by just increasing the partial H_2 pressure (see figure 2.9), yet efficient power extraction in the high beam-quality component was only achieved by a simultaneous increase of the total buffer gas pressure up to 150 mbar (see table II). In comparison, results reported by Withford & Brown (1995) for a medium-scale CVL oscillator (plasma tube same size as the LS laser operated at 10 kHz with 6.5 - 6.9 W/cc, $M = 100$ and capable of delivering 25 W with plane-plane resonator using a similar excitation scheme as the LS laser) found the optimum low divergence output of the green component to be 1.6 W for a nominally pure neon buffer gas pressure of 50 mbar, and 5.7 W of green when 2% H_2 is added, the latter figure corresponding to a total HBQ output of 11 W. Also, Withford et al. (1996*a*) have shown that for the same laser by increasing the H_2 concentration up to 5%, whilst maintaining the total buffer gas pressure low at 50 mbar, a more centrally peaked gain profile could only be established at the cost of reduced total power output. In comparison with these reports, the 10 W low divergence output delivered by the LS laser when operated at elevated buffer gas pressures (> 100 mbar) with $M = 360$ does not seem to constitute a major improvement. However, there remains a significant difference in cavity magnifications ($M = 100$ reported by Withford & Brown (1995) and Withford et al. (1996*a*) compared to $M = 360$ for the LS) which indicates that the LS should give between 30% and 60% more non-ASE power when fitted with $M = 100$. Furthermore, addition of H_2 to the neon buffer gas alone without increasing the total buffer gas pressure, did not produce enhancements for the LS laser similar to those observed by Withford & Brown (1995) and Withford et al. (1996*a*), particularly for such high cavity magnifications. This comparison indicates that the present

results truly constitutes another, significantly different near-optimum regime of operation within the full parameter-space of elemental CVL design. Additional comparison of the difference in insulation levels and corresponding electrical input power (3.2 kW vs. 2.1 kW for the LS), as will be discussed below, underline this statement. Understanding of the physical mechanisms by which an increase in the total buffer gas pressure results in such a pronounced improvement in the high beam-quality power extraction efficiency, can not be given at this point and most likely requires extensive numerical simulations (Carman et al. 1994, Carman 1997) to account for the complex dynamics of the gain medium and the optical field.

III DEGREE OF THERMAL INSULATION AND POWER LOADING In addition to the effect of the total buffer gas pressure and the partial H_2 pressure on the radial gain distribution, the need for operation at reduced specific electrical input powers is also underlined in the present investigation (see for example figure 2.6). A high degree of thermal insulation enables a reduction in the power loading of the laser, while the optimum wall temperature can still be achieved, which results in a more 'gentle' excitation discharge. Consequently, the degree of ionisation of the copper vapor is reduced, thus reducing deleterious effects such as radial cataphoresis (radial migration/ion-pumping) in the afterglow period, which ultimately can outweigh other beneficial processes aimed towards enhancing the on-axis gain. As such, the use of more heavily insulated plasma tubes is favored. Comparing the two lasers investigated, the measured ASE seed and radial gain profiles are indeed found to be less annular for the heavily insulated LS laser, operating under similar buffer gas conditions as the IH laser but at reduced specific input powers. An equally important argument for the choice of a high degree of thermal insulation, is the reduction of radial gas temperature gradients, which also translates to variations of the copper vapor density across the plasma tube. The relative importance of the effect of radial cataphoresis versus gas temperature effects can only be determined by comprehensive numerical simulations (Carman et al. 1994, Carman 1997). Finally, note also the added advantage for a high degree of thermal insulation is the improved wall-plug efficiency of the device now requiring less electrical input power.

Results obtained by Withford (1995) underwrite this interpretation regarding the effect of specific input power loading. For a less heavily insulated medium-scale CVL (25 mm bore diameter, 1 m length, requiring 6.1 - 6.5 W/cc electrical input power at 9.2 kHz with similar electrical excitation circuit like the LS laser) Withford (1995) found that the annular ASE seed profile could *not* be alleviated, either by adding up to 5% of hydrogen, or by increasing the neon buffer pressure up to 130 mbar. At the same time, by reducing the electrical input power to 5.5 W/cc and applying supplementary heating to maintain the required wall temperature, a significant increase of the seed intensity on-axis was established using hydrogen additives, resulting in a nearly flat radial ASE seed profile. In addition, Withford (1995) found that the level of power loading significantly affects the total gain duration: at high specific electrical input powers the contribution to the total output power of the 6-pass component was nearly negligible. For the LS laser the 6-pass component comprises a significant fraction of the total raw output power, and contributes to the high beam-quality output as can be concluded from figure 2.10. Similar to findings reported by Withford et al. (1995), the increase in total output power obtained here by increasing the total buffer gas pressure is due to an increase in the power extracted in the HBQ component, while the power of the LBQ component remained relatively unchanged.

2.5 CONCLUSION

In summary it has been shown that in order to allow medium-scale elemental CVL oscillators to be efficiently operated with high magnification on-axis unstable resonators (and hence deliver high beam-quality output), the gain medium needs to exhibit:

- a centrally peaked ASE seed profile, to generate the required low divergence of the 4-pass component;
- a persistently high gain on-axis throughout the optical pulse, to establish efficient power extraction in the high beam-quality output.

While addition of H_2 can enhance the radial ASE profile to meet the first requirement, an increase in the total buffer gas pressure is imperative to establish good efficiency when using very high resonator magnifications ($M \geq 100$). At the same time, to reduce the deleterious effects of radial cataphoresis and provide a more uniform radial gas temperature profile, reduction of the specific electrical input power loading is necessary, thus implying the need for a high degree of thermal insulation of the plasma tube. With these design issues in mind, final optimisation can be achieved by matching the electrical input power to the elevated buffer gas pressure and increased level of thermal insulation.

Specifically, operation of high beam-quality single unit medium-scale elemental CVL oscillators has been characterised and design criteria were determined which achieve a centrally peaked ASE seed profile and persistent high gain on-axis. Efficient extraction of near diffraction-limited beam quality output (divergence less than two times the diffraction-limit) using very high magnification unstable resonators (magnifications up to $M = 360$) was found to require a heavily insulated plasma tube (with low specific electrical input powers of order 4 W/cc), operated at elevated total neon buffer gas pressures (100 - 150 mbar) and with a partial pressure of the background H_2 concentration of order 1% of the total pressure. A single medium-scale CVL oscillator (25 mm bore diameter, 1 m long active region) fitted with an on-axis unstable resonator with $M = 360$, which is the highest reported to date for any laser, when operated at 130 mbar total buffer gas pressure and 4.3 W/cc electrical input power at 10 kHz pulse repetition frequency, was capable of delivering 10 W of high beam-quality output with a divergence of less than 2 times the diffraction-limit at a wall-plug efficiency of 0.5%.

It is important to emphasise these findings can not be directly applied to large-scale devices. In elemental CVLs with bore diameters in excess of $\sim$ 35 mm the occurrence of annular ASE seed and gain profiles is primarily ascribed to the skin-effect of the conducting plasma medium (rather than axial depletion of the ground-state copper density), leading to a significant delay (up to tens of nanoseconds) between the onset of gain near the tube walls and on-axis. Results reported by Chang (1993) for a 40 mm bore diameter CVL showed that this temporal delay can be reduced by increasing the total buffer gas pressure, however, at the same time the output power was found to decrease when using a plane-plane resonator. Chang (1993) determined qualitatively that for these large bore devices the optimum pressure is of order 40 mbar. The present investigation showed that, for a heavily insulated medium-scale CVL both the total raw output power and the low divergence component increase with increasing pressure. The disparity between these results indicates that the dominant physical processes leading towards radial variations of the gain distribution during the build-up time, is significantly different for medium bore diameter ($\emptyset \leq 35$ mm) CVLs versus large bore diameter ($\emptyset \geq 35$ mm) devices.

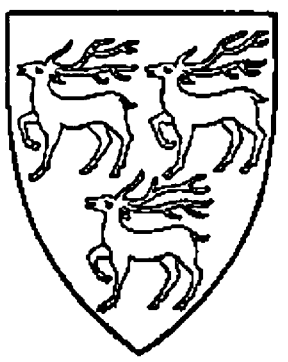
Note also that the pressure scaling effects observed here can not be solely attributed to impedance

matching effects, determined by the conductivity and the inductance of the laser head (Blau 1994). It is generally true that the impedance of the plasma column is increased by increasing the total buffer gas pressure, which may result in a higher optical output power (provided the plasma is not overheated). However, as can be concluded from table II, by increasing the electrical input power alone at a constant pressure of 40 mbar, the low divergence output is only found to increase proportionally with the total raw output power. An increase in the relative contribution of the high beam-quality output is only established by operating at elevated buffer gas pressures, in order to extract approximately 45-65% of the total raw output power in the low divergence component.

LASER ABLATION WITH COPPER VAPOUR LASERS: CHAPTER 3

DANIEL KAPITAN, JESUS COLLEGE, UNIVERSITY OF OXFORD

Thesis submitted for the degree of Doctor of Philosophy at the Faculty of Physical Sciences, Trinity 1999



NOTE:
NOT FOR PUBLIC CONSULTING OR PHOTOCOPYING
FOR A PERIOD OF FIVE YEARS STARTING 1ST JUNE 1999

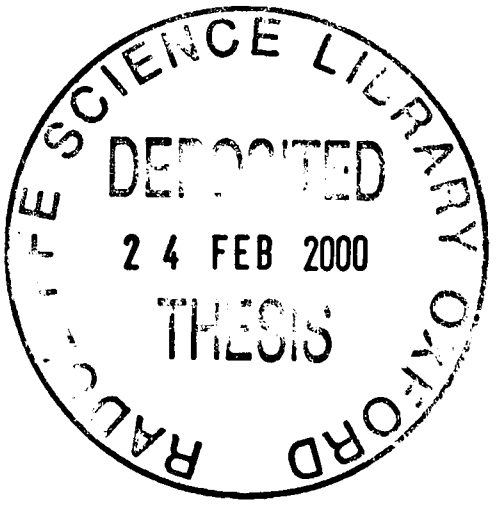
This thesis has been the direct result of studies performed at the Sub-department of Atomic & Laser Physics as part of a three year European Brite/Euram programme BE95-1228. In line with general guidelines set by the European Commission, communication, publication or dissemination of information and/or results from this project, are subject to the conditions of the consortium agreement in view of confidentiality and intellectual property rights, and requires approval of all parties involved.

Considering the highly specific content of some the experimental work described in chapter 3 of this thesis, which has direct bearing on the competitive advantage of the industrial partners in future commercialisation and exploitation of its results, some parts of this thesis have been granted dispensation from the usual requirements set by the University regarding public consulting and photoncopying. Therefore, chapter 3 will not be available for consultation by third parties for a period of 5 years counting from the date of submission. For further information one should inform the Faculty Board, or contact one of the following persons:

Andrew Kearsley
Managing Director
Oxford Lasers Ltd
Abingdon Science Park, Abingdon
tel. 01235 ~~554211~~ 810088.

Prof C.E. Webb
Sub-department of Atomic & Laser Physics
University of Oxford
Parks Road, Oxford OX1 3PU
c.webb1@physics.ox.ac.uk

Daniel Kapitan
p/a Arthur D. Little
PO Box 540
3000 AM Rotterdam
the Netherlands
tel. +31 (0)10 2018811
kapitan.daniel@adlittle.com



Chapter 3
Design of Master-Oscillator Power-Amplifier Systems

Power is nothing without control
PIRELLI ADVERT

The design of CVL Master-Oscillator Power-Amplifier (MOPA) systems is discussed in view of generating tens of watts average power with near diffraction limited beam quality. The main issue pertains to extension of the pulse duration of the master oscillator output, in order to allow control and seeding of the power amplifier with the essentially diffraction limited higher order roundtrips. A system based around a small-scale master oscillator and a medium-scale CVL amplifier is constructed and characterised. A magnetic pulse stretching circuit is characterised to allow extension of the pulse duration of a medium-scale CVL master oscillator for use in larger MOPA systems.

3.1 Introduction

I CVL MOPA systems Master Oscillator Power Amplifier (MOPA) arrangements have been used extensively with a variety of laser systems to obtain high power output from multiple pulsed laser systems, including large-scale glass lasers at national facilities, dye lasers, excimer lasers and table-top solid-state lasers. In a standard MOPA arrangement, the output of the Master Oscillator (MO) is propagated for amplification through one or several Power Amplifier (PA) stages. The properties of the output beam are primarily determined by the resonator configuration of the oscillator, while the amplifier units are commonly not fitted with a resonator. By appropriate choice of the relative timing between the master oscillator and the power amplifiers, the optical seed pulse of the oscillator is made to overlap with the excitation pulse as the seed propagates through the various amplifying gain media. Necessarily, the pulse duration of the oscillator seed needs to be at least as long as the gain duration of the amplifier medium. In order to obtain efficient power extraction, the peak power intensity of the master-oscillator seed also needs also to be sufficiently high to drive the power amplifier in the saturated regime. This issue is of particular importance, for instance, in systems involving pulsed amplification of cw master-oscillator signals where the incoming peak power intensities can be many orders of magnitude smaller than the required saturation intensity (Kapitan 1995). In large-scale multi-stage systems it is of importance that each of the (pre-)amplifiers is operated in the appropriate regime to ensure that the overall efficiency of the MOPA chain is maximised. In the case of high power dye laser systems, for example, this involves optimisation of the distribution of the available pump power over the various stages and matching the

dye concentrations in each amplifier cell (Hnilo & Inez 1987).

Operation of copper vapour lasers (CVLs) in MOPA systems has a number of distinct advantages related to the characteristics of copper medium (Brown & Coutts 1996, Coutts & Brown 1995*b*). Firstly, for high gain devices such as the CVL, saturation of the amplifier medium is readily achieved even at relatively low oscillator input powers. This is particularly useful from the point of view of generation of high beam quality output, as has been reviewed by Brown & Coutts (1996). By employing a MOPA arrangement the design constraints set by the trade-off between using high magnification unstable resonators to establish high beam quality output at the cost of reduced efficient power extraction, can be separated (Brown & Coutts 1996). For example, small-scale oscillators with bore diameters of order 10 mm with high aspect ratios (up to 1 m long) are preferred to generate a high beam quality seed. Despite the relatively low power output, such a small-scale MO can be used to efficiently seed a medium-scale ($\emptyset$ 18 – 25 mm) or large-bore ($\emptyset \geq 25$ mm) PA with relatively long gain lengths (≥ 1 m) to generate tens of watts of average output power (Brown & Coutts 1996). Furthermore, by employing a MOPA arrangement the combined efficiency of the PA units is generally better than would be the case if each PA was operated as a stand-alone oscillator. As the only practical route to generating high beam quality output involves the use of unstable resonators with high magnifications, operation of each of separate oscillator would be relatively inefficient. In a MOPA arrangement only one unit would be operated as an oscillator, while the full output power capability of each PA is extracted to amplify the high beam quality output, often giving output powers greater than the maximum output power when the power amplifier would have been operated as an oscillator with a plane-plane resonator (Brown & Coutts 1996).

In addition, the use of MOPA arrangements allows manipulation of the overall beam quality of the system. The oscillator output can be 'cleaned-up' using a spatial filter with a constricting aperture stop (pinhole) placed at the common focus of a Cassegrian telescope. Only the transmitted oscillator signal will be subsequently amplified, where the MOPA beam quality is now primarily determined by the imaging condition of the spatial filter, similar to the principle of self-filtering unstable resonators (Pini et al. 1990). In theory, this technique can be applied to generate high-power, diffraction-limited output, provided the beam quality and output power of the oscillator output are sufficiently high such that the fraction of the initial seed signal propagated through the spatial filter is sufficient to saturate the amplifier. Practically, the use of 'hard' spatial filters is limited by complications and spurious side effects, such as parasitic lasing due to reflection of the edges of the pinhole. Also, the positioning and structural rigidity of the pinhole becomes increasingly more critical for increasingly tight spatial filters, and issues related to vibrations and turbulence disturbing the beam propagation become more pressing to maintain overall stability and reliability of the MOPA system.

Another important technique for beam-quality manipulation of MOPA systems makes use of the evolutionary character of the beam quality from CVL oscillators, as discussed earlier in chapter 2. By adjusting the relative timing between the oscillator and amplifier, the amplifier can be set to preferentially amplify the diffraction-limited components of the oscillator output (Coutts & Brown 1995*b*). This technique requires the pulse duration of the oscillator to be sufficiently long such that by discarding the ASE and high divergence components of the output, the net pulse duration of the high beam-quality output is as long as the gain duration of the amplifier. This aspect of the design of MOPA systems will be

considered in this chapter.

Besides beam-quality manipulation, the relative timing between the oscillator and amplifier also can be used for delay shutter control of the MOPA output (Körner et al. 1996). Due to the significant population densities of the metastable ^2D lower laser levels (see chapter 2) in the afterglow of the excitation pulse, the copper medium can act as an efficient absorber at the laser transitions. As such, the total output of the MOPA can be switched on and off by alternating the timing of the oscillator pulse relative to the amplifier to be either in sync or delayed by approximately 100 ns. Despite the high pulse repetition frequency (PRF) of typically 10 kHz, the pulse-train format of the MOPA output can be controlled on single-shot basis with sufficiently fast switching electronics. Operation with a wide range of PRFs varying from parametric fractions of the fundamental PRF, burst-mode operation down to sub-Hz single shot operation has been demonstrated (Körner et al. 1996).

II INJECTION-CONTROLLED OSCILLATORS An alternative approach to generate high beam-quality output from multiple CVLs involves injection-controlled oscillators (Warner 1986, Naylor et al. 1986, Naylor et al. 1988, Chang 1995). In an injection-controlled oscillator (ICO) arrangement, the power amplifier is operated as an oscillator which is seeded with the output from the master oscillator. This technique is sometimes referred to as an injection seeded oscillator (ISO), the small difference being that for the ICO the two cavities share a common mirror. The primary advantage of the ICO arrangements is that the master oscillator and injection-controlled oscillator are allowed to have different pulse lengths, since the master-oscillator seed is only required during the build-up period of the ICO. In practice the trailing part of the master-oscillator laser pulse is used for this purpose, as output from higher order roundtrips is often essentially diffraction limited. Thus, the constraint on the master oscillator to produce sufficiently long optical pulse durations relative to the gain duration of the amplifier, is relaxed.

It is important to note that in the ICO arrangement, the two resonators are not locked or mode-matched in any way (as is the case for e.g. cw systems), but that by using highly diffractive unstable resonators the master-oscillator seed is self-filtered to obtain the high beam quality output from the ICO. Due to the high diffraction losses of the ICO unstable resonator, the latter part of the ICO output is essentially operating in free-running mode and generally has different beam propagation properties from the initial master-oscillator seed. As a result, most of the output power from the master oscillator seed is lost, which constitutes a major disadvantage. Furthermore, the optimum operating condition of the ICO is critically dependant on the alignment of the two resonators. Chang (1995) observed that relatively small misalignment can lead to significant spatial and temporal fluctuations in the far-field (multiple spots, beam dither etc.).

Finally, it is known that for a large–scale ICO ($\emptyset$ = 40 mm, 2.7 m long) optimum operation conditions are very sensitive to the relative timing of the MO-ICO when using an on-axis arrangement. Since the ICO needs to sustain free-running oscillator modes like a stand-alone oscillator, radial effects of the gain medium significantly influence its performance for similar reasons as discussed in chapter 2. For large-scale devices, reliable and efficient operation can only be obtained when an off-axis injection scheme is used (Kearsley et al. 1987, Chang 1995), which is not preferred for HBQ applications requiring a symmetric far-field intensity distribution.

III OUTLINE OF EXPERIMENTS Within the framework of the Compala project, the primary objective was to generate 25 – 30 W of output from a CVL with near diffraction-limited beam quality (2 times or better), which could be used routinely for the various studies on laser ablation. To this purpose various design issues regarding the construction and optimisation of dual CVL MOPA systems were addressed. First, the construction and design of a MOPA system based around a small-scale MO will be presented. The design and characterisation of a small-scale master oscillator ('Guzz ') is presented. In combination with a medium-scale Oxford Lasers LS 20-10 device ('Goldie'), a mini-MOPA system as first reported by Brown & Coutts (1996) is constructed and characterised. The primary issue involved optimisation of Guzz to provide a sufficiently long optical pulse length to seed Goldie. To ensure maximum power extraction, best performance was obtained using a double-pass amplifier arrangement (Coutts et al. 1998) of which the operation characteristics will also be presented.

The second part of the experiment addresses the issue of generating an extended optical pulse from the medium-scale LS 20-10. This work was initiated within the Compala consortium in collaboration with Oxford Lasers, to construct the next generation of CVL MOPA system based on two medium-scale devices. The primary issue involved stretching of the optical pulse of the master oscillator in view of improving the beam quality of the MOPA output, whilst sustaining the output power of the oscillator at an acceptable level as it is designed to contribute to the total output power of the MOPA system. To this purpose, various modifications to the electronic driving circuit were investigated. A successful method involving a double-pulse magnetic compression circuit will be presented.

3.2 'GUZZ & GOLDIE' MOPA SYSTEM

I INTRODUCTION During the characterisation and optimisation of the small-scale master oscillator 'Guzz', the primary objective was to establish a pulse duration which was sufficiently long to seed the full $35 - 40$ ns gain pulse from the PA with only high beam quality output. With roundtrip times of around $7 - 8$ ns, and given that the first burst of ASE (2-pass output) was to be discarded, the total pulse duration of the Guzz was aimed to be $45 - 50$ ns to accommodate 6 roundtrips. Earlier studies performed by Brown & Coutts (1996) on a mini-MOPA system using a small-scale oscillator indicated that the required power levels to reach saturation of the amplifier were of order 0.1 W, and as such obtaining high power output was not the main design issue. Furthermore, by employing a double-pass MOPA arrangement as first reported by Coutts et al. (1998), the output requirements for the small-scale oscillator are further relaxed.

II SMALL-SCALE MASTER-OSCILLATOR ('GUZZ') The small-scale Master Oscillator 'Guzz' was designed and constructed in house, following recent advances made by Brown & Coutts (1994) in constructing MOPA systems based around on small-scale oscillators. The design is sketched in figure 3.1. The main body of the laser consist of a water-cooled jacket which contains the silica envelope (700 mm length, Ø105.5 mm), supported on each end together by the end-flanges and collars which also provide a vacuum tight side-seal. The inner part of the end-flanges are machined with anti-reflection baffles to reduce the amount of infrared radiation from the plasma reaching the windows. The electrodes are made of standard grade copper and machined to have smooth curving ends, ensuring that no sharp corners

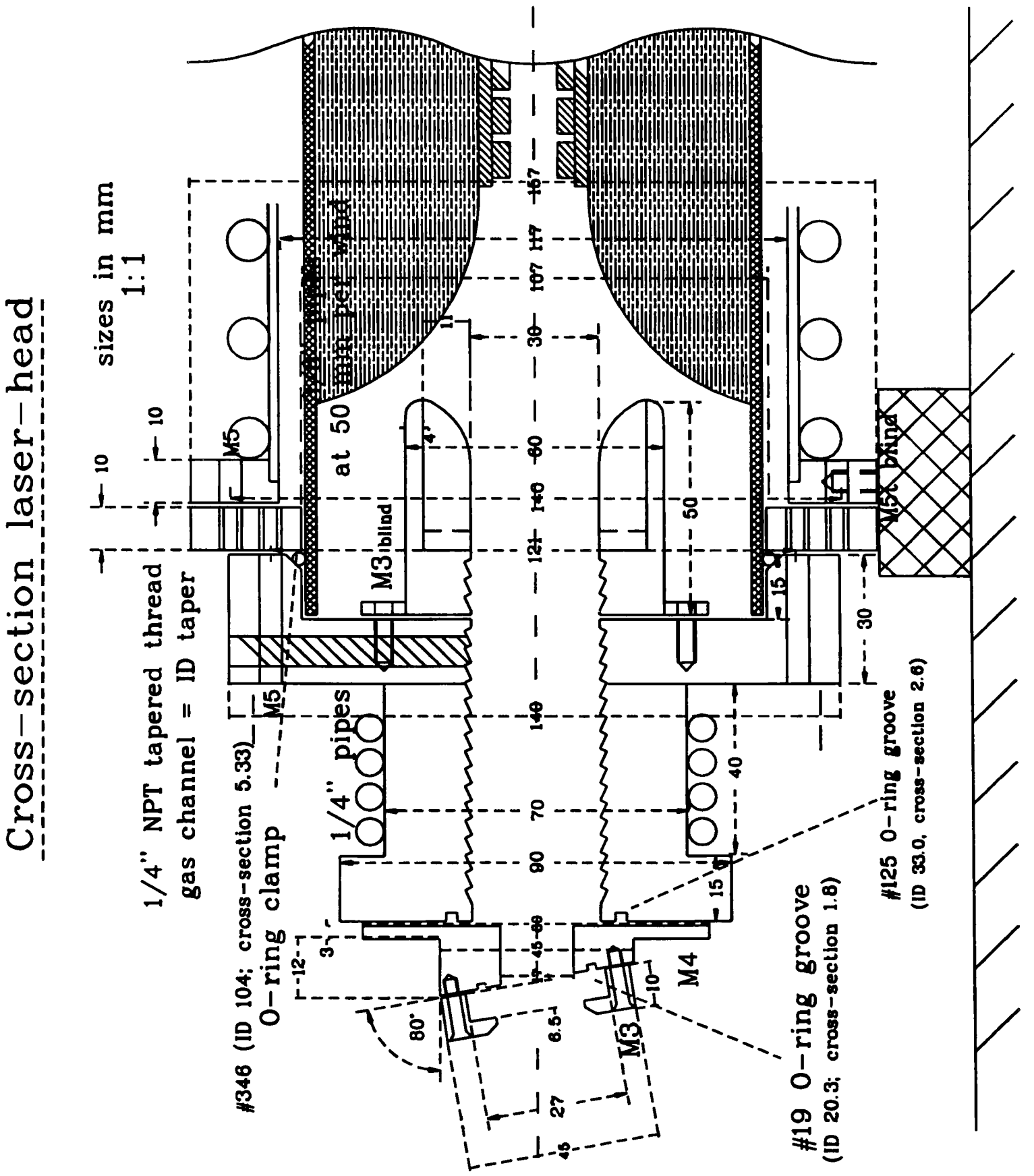


FIGURE 3.1: Cross-section of the in-house built small-bore master oscillator, showing the end–windows, the side-sealed end-flanges, the main silica envelope and the fluted plasma tube design.

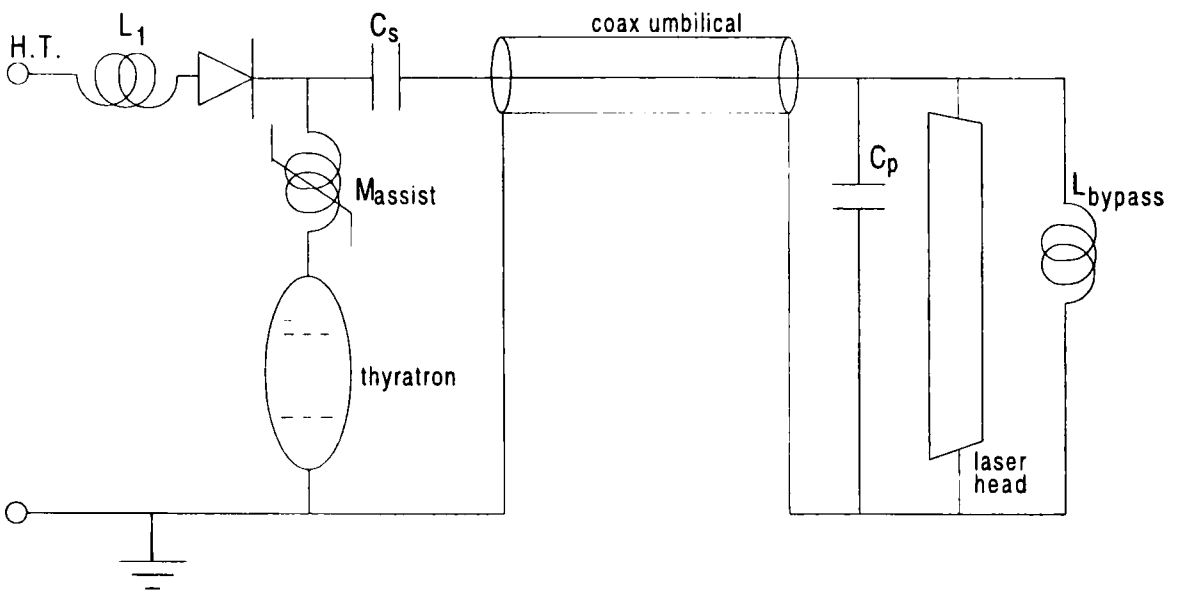


FIGURE 3.2: Charge-transfer circuit used for the small-scale oscillator with $L_1 \approx 0.5$ H; storage capacitor $c_s = 5$ nF; peaking capacitor $c_p = 2$ nF; An EEV CX1535 thyratron was used to drive the circuit, and to decrease the switching time of the thyratron a magnetic assist was incorporated which was made of teflon coated copper wire wrapped around a toroidal ferrrite core.

are present which may cause spurious anchoring of the discharge. Around the perimeter ~ 50 regularly spaced slots are cut, each around 1 mm wide, to provide a hollow-cathode effect to enhance the homogeneity of the plasma discharge (Chang et al. 1997). Upon inspection after approximately 100 hours of operation, the electrodes showed homogeneous distribution of the discharge where all the slots were slightly widened by thermal effects or sputtering. The window-mounts can be moved independently relative to the end-flanges for ease of alignment of the optical axis relative to the plasma tube. Infrasil windows (CVI Corporation) are used to reduce thermal lensing due to absorption of infrared radiation, and are mounted at 10° to prevent parasitic lasing.

The plasma tube is contained in high-grade alumina fibre insulation, consisting of wrapped alumina fibre-sheets (Ash 1400) and solid alumina brick (Rath, maximum hold-off temperature $\sim 1800\,^\circ$ C), all of which are enclosed in the primary silica tube. Owing to the small bore diameter, the plasma tube is designed to contain regularly spaced ceramic 'flutes' (2 cm length, Ø17.7 mm OD / 12.5 mm ID) placed in a larger enveloping primary plasma tube (50 cm long, 20.0 mm ID / 26.0 mm OD). In this arrangement the copper reservoirs are recessed, as otherwise a significant portion of the optical aperture would be obstructed by the copper shadow. This design was also used in the construction of a medium-scale fluted tube, as depicted in figure 3.8. Construction of the fluted tube involved wrapping three tightly wound layers of the alumina fibre sheets around the flute, and carefully placing the flutes in the main plasma tube one at a time using a plunger. In the first arrangement a total of 9 flutes were placed at intervals of 2 cm, leaving 80 mm on either end of the plasma tube to function as cool end-zones where the copper vapour can condense. Due to the relatively low power output (less than 1 W) ascribed to the small total gain length, 12 flutes were placed in the Mark II design leaving only 20 mm at each end of the plasma tube. To accommodate cooling-down regions, the primary plasma tube is extended pieces of 44 mm

PRF (kHz)	V_{in} (kV)	I_{in} (A)	p_{Ne} (mbar)	P_{out} (W)	τ_p @ base (ns)
Mark I					
6.2	5.4	0.27	25	1.6	50
6.2	5.4	0.27	40	1.0	50
10	4.5	0.35	25	1.9	40
Mark II					
7	5.3	0.30	40	2.0	55
10	4.2	0.34	35	2.2	50
10	4.7	0.39	20	3.0	43
Molly					
6.2	5	0.3	45	3.3-3.6	60
10	4	0.4	45	3.3	50

TABLE III: Characterisation of the small-scale MO 'Guzz', operated at various levels of neon buffer gas pressure and electrical input power with $c_s = 5$ nF and $c_p = 2$ nF for the Mark I and Mark II tube design. Data for a similar small-scale MO 'Molly' are included for comparison, where $c_s = 5$ nF and $c_p = 1.75$ nF with an active gain medium length of 70 cm.

long thin ('egg-shell') ceramic tubes (same diameter as the plasma tube). While this reduces the spacing between the end of the plasma tube and the electrodes down to 10 mm on either side, the electrodes did not overheat and Guzz was found to operate happily now giving over 2 W.

A standard three-phase transformer (maximum rating 3.0 kVA) served as a high voltage power supply for the laser head, which was driven by a thyratron switched (EEV CX1535) charge-transfer circuit (see figure 3.2). A magnetic assist M_{assist} was used to hold-off the volts on the thyratron anode. A static fill of nominally pure neon (>99.99%) was used as a buffer gas, which was replaced daily during the run-up sequence. Since the Goldie PA was normally run at 10 kHz, Guzz was also run at 10 kHz with typical operating conditions of $4.3 - 4.4$ kV from the DC power supply with an average supply current of 0.35 A (1.5 kW) with 50 mbar of neon buffer gas pressure. For the ballistic pendulum experiments (see chapter 4), the MOPA was run at 7 kHz where it gave 3.5 mJ pulse energy.

To find (near-)optimum operating conditions, Guzz was operated under different condition, varying the electrical input power, buffer gas pressure, and capacitance C_s and C_p of the charge-transfer circuit. Also, the effect of changing the PRF on the pulse duration was investigated to allow comparison with a similar small-scale master oscillator ('Molly') which was normally operated at 6.2 kHz (Coutts & Brown 1995*a*). The operating characteristics of the small-scale oscillators are listed in table III. Clearly, the overall performance of the Mark II tube in terms of pulse duration and total output power is better compared to the Mark I design. The enhanced performance is ascribed to the extended gain length of the Mark II tube, and compares favourably with Molly, whose gain length was 70 cm.

Time-traces of the optical output of Guzz are shown in figure 3.3, showing the significant enhancement of the Mark II tube. The far-field intensity profile is plotted in figure 3.4, using the same scale as figures 2.7 and 2.8. Operating the Mark II at higher input powers does result in higher power output, but also considerably shorter pulse, as indicated in table III. Generally operation of Guzz was sensitive

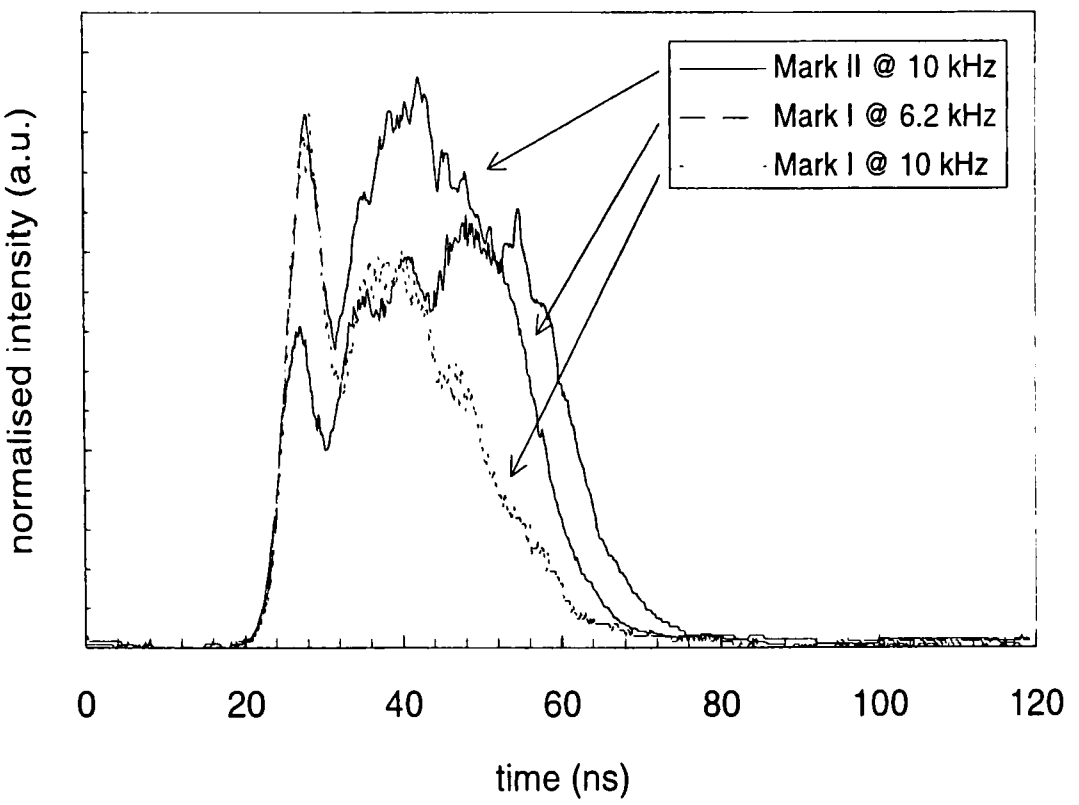


FIGURE 3.3: Optical pulse shapes from the small-scale oscillator Guzz.

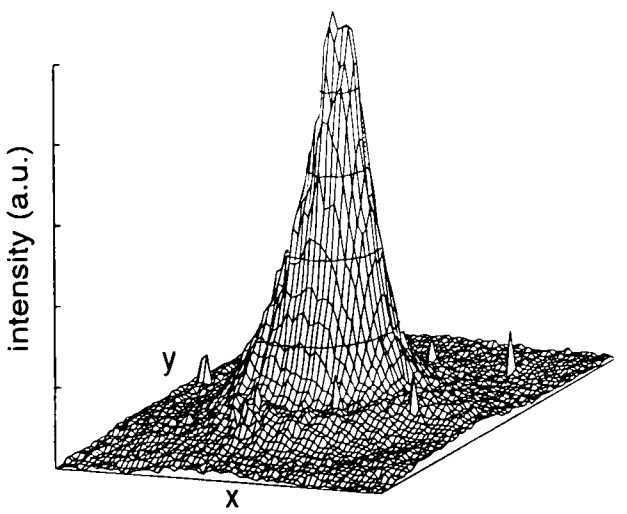


FIGURE 3.4: Measured far-field intensity distribution for the small-scale oscillator Guzz. Full extend of the plotted xy-plane corresponds to 0.1 mrad.

to the input voltage V_{in} (and associated current I_{in}), where marginal increases of 0.1 kV could result in significant changes in output power and pulse duration τ_p. Given output powers in excess of 2 W with the Mark II design, fine adjustment of V_{in} was done in view of optimising τ_p, critical for efficient MOPA operation. Only marginal differences in the τ_p was observed by changing C_s, C_p, and for all results reported here values for $C_s = 5$ nF and $C_p = 2$ nF were used (see also discussion in the following section). It was further observed that the pulse duration was sensitive to the amount of copper resident in the gain volume. For all small-bore tubes, lifetimes of copper fills were found to be of order $100 - 150$ hours, after which significant decrease of the output power and pulse duration occurs. Under normal operation, Guzz was refilled every 100 hours.

III CHARACTERISTICS 'GUZZ & GOLDIE' MOPA SYSTEM The critical issue in the construction of CVL MOPA systems regards the relative timing of the master-oscillator output to the power-amplifier gain pulse. While the small-scale oscillator Guzz provided ample output power and sufficiently long seeding pulses, it was found that the use of a conventional single-pass MOPA configuration was slightly unstable in terms of sustaining maximum power output over many hours of operation. Effects which result in a decrease in the pulse duration of Guzz, as discussed above, will generally result in a proportional decrease (up to several watts) in the high beam-quality output of the MOPA system as a whole. To alleviate these problem a double-pass MOPA arrangement was used (Coutts et al. 1998), as depicted in figure 3.5. The unpolarised master oscillator output was sent through a polarising beam splitter held in a rotation mount, a $7 - 10$ mm aperture, and then focused with a 500 mm achromatic lens through a 1 mm diameter central hole in the 45°, double-pass amplifier coupling mirror. After a single transit through the amplifier, a 2 m radius of curvature concave high reflector at the rear of the amplifier produced a 25 mm diameter collimated beam which is returned for a second pass through the amplifier, this time efficiently extracting power from the whole gain volume. The double-pass output was extracted by reflection of the 45° coupling mirror, and sent through a second, fixed, polarising beam splitter cube. By rotation of the first polarising beam splitter, full control over the MOPA power was obtained without any variation in any other beam parameter.

The alignment procedure was as follows. First, the centre-hole mirror was centrally positioned relative to the optical axis defined by the plasma tube of the PA. Then, by beam-walking the output of the master oscillator using the output coupler of the oscillator and the first turning mirror, the oscillator beam was ensured to be colinear with the centre-hole and the PA. The lens ($f = 500$ mm) was put in place with the focus nominally at the centre-hole mirror. To protect the substrate of the centre-hole mirror during the alignment procedure a sacrificial metal pinhole was mounted of the back-face, fixed using a magnetic strip to allow for adjustment. Finally, the HR of the PA was positioned and aligned relative to the centre-hole mirror. By looking at the collimation of the MOPA output beam, the focusing lens was adjusted to move towards the amplifier if the beam was slightly converging, or away from the PA when diverging. The iris was used for final adjustments to match the oscillator beam diameter to the imaging conditions defined by the geometric conditions of the double-pass amplifier, hence reducing diffraction losses.

By employing a double-pass MOPA arrangement, the constraint on the oscillator to saturate the amplifier gain medium was relaxed. Furthermore, considering the transit time of $4 - 5$ ns over a single-pass in the amplifier, the output of the MOPA was less sensitive to decreases in the pulse duration of the

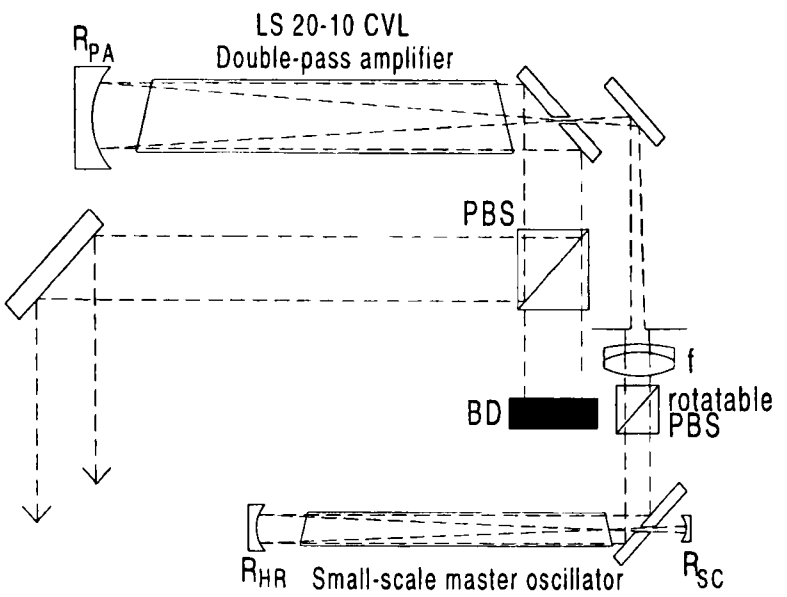


FIGURE 3.5: The double-pass MOPA arrangement, with $R_{HR} = 2.0$ m; $R_{SC} = 25$ mm; $R_{PA} = 3.6$ m; $f = 500$ mm; BD = beam-dump; PBS = polarising beam-splitter.

oscillator seed. Note, however, that the double-pass MOPA systems still operates as a travelling-wave amplifier, in contrast to an ICO/ISO arrangement (Chang 1995). In view of micromachining applications, parasitic lasing due to spurious feedback into amplifier medium may be an issue when employing double-pass MOPA systems. However, for all experiments reported here the presence of a high reflector in double-pass MOPA set-up was found not to cause any problems, where throughout beam-paths of a few metres were used.

Looking at the performance of the double-pass MOPA setup, the long term power fluctuations were eliminated. Sustained maximum power extraction up to 30 W was established, to be compared with 23 W maximum output power from Goldie when fitted with a plane-plane resonator (table I). However, significant shot-to-shot variations in the pulse energy were still observed in the output from the double-pass MOPA. This was found to be caused by timing jitter in the absolute and relative triggering of the two lasers. A number of possible causes were identified. First, the single-phase DC voltage supply of Guzz was found to have a 50 Hz modulation up to ten percent of the peak DC voltage. This modulation resulted in a measured relative jitter of $10 - 12$ ns peak-to-peak between the onset of the ASE output and the thyratron trigger pulse on Guzz. By incorporating a low-pass LC-filter with a capacitance $C = 2$ μF, and a water-cooled inductor with a nominal inductance $L = 0.5$ H, the timing jitter could be reduced below 5 ns.

Other possible internal sources of noise within the circuit of each individual laser, such as may exist in the resonant LC charging circuit, the magnetic pulse compression stages (discussed in more detail below), or due to fluctuations in the discharge at the electrodes, were further investigated. For Goldie, significant flickering of the discharge was observed, indeed suggesting possible fluctuations caused by the copper electrodes. Upon inspection Goldie's electrodes showed significant traces of sputtering, indicating

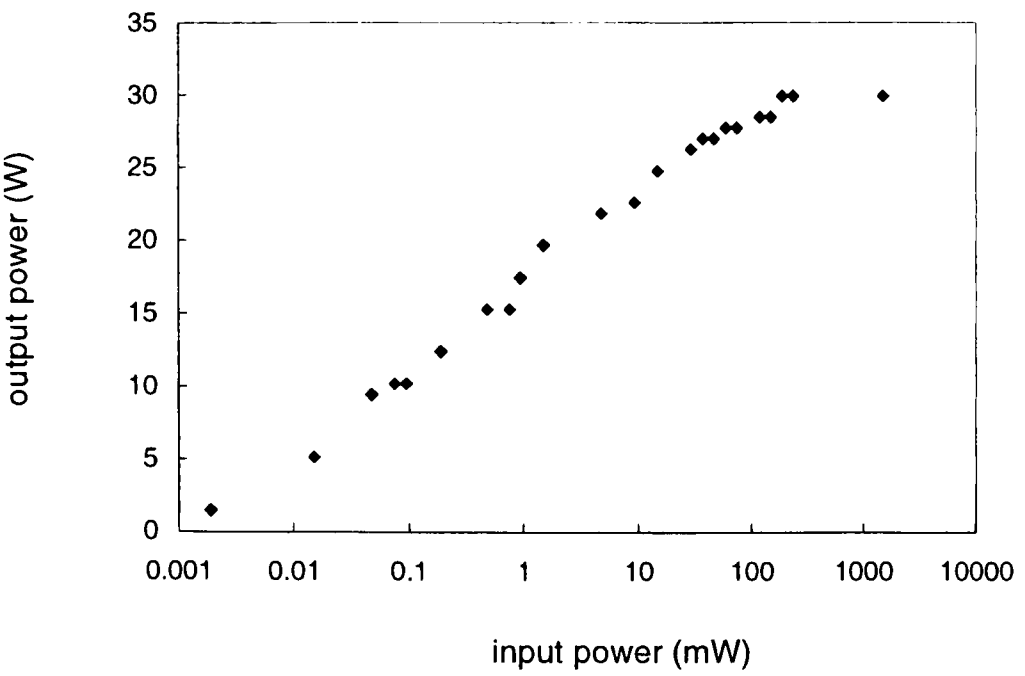


FIGURE 3.6: The total output power from the double-pass MOPA as a function of the input power from the master-oscillator.

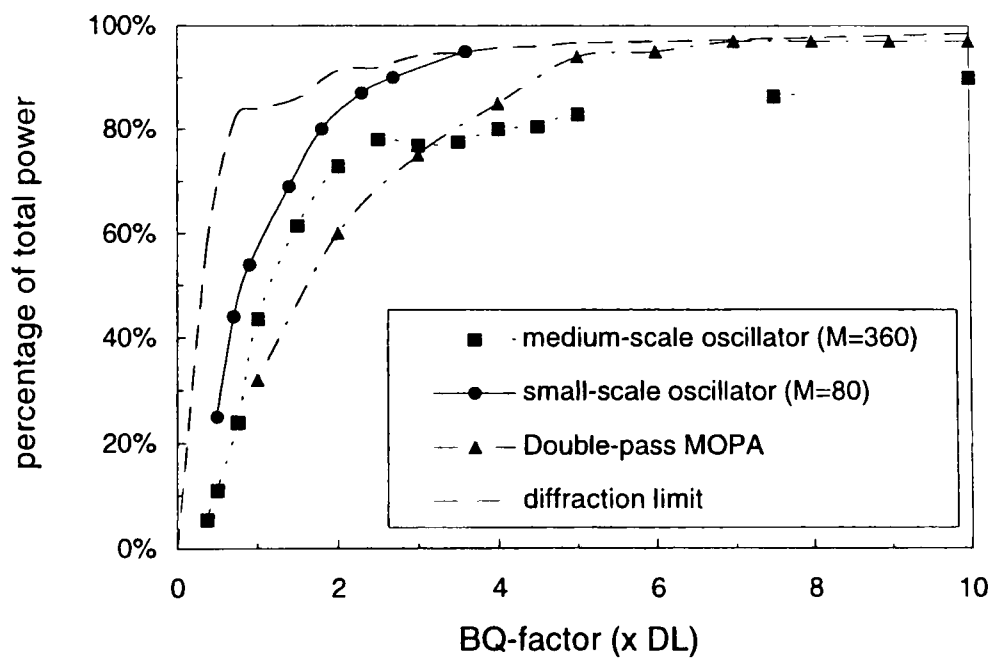


FIGURE 3.7: Power-in-the-bucket measurement for the small-bore oscillator and the double-pass MOPA system, compared to that for the LS 20-10 laser with $M = 360$ as described in chapter 2. Also shown is the calculated throughput for a diffraction limited beam.

anchoring of the discharge on specific spots. To reduce the electrode jitter, the electrodes were refurbished to have rounded corners and slots, following the design of hollow-cathode electrodes as reported by Chang et al. (1996) and Chang et al. (1997). Around the perimeter 48 slots were cut with 0.25 mm blade. In doing so, a sleeve was left on the outside (no through cut) to prevent the discharge from wandering to the outside, but rather lock in the inner part of the electrode. This modification resulted in alleviation of the electrode jitter, which was measured to be 3 ns peak-peak using the hollow-cathode electrodes, compared to initial peak-peak timing variations of order 10 ns when Goldie was triggered internally.

Besides the absolute timing fidelity of the internal high-voltage switching circuit of each laser, the electronics controlling the relative timing of the two lasers was scanned for possible noise sources. In practise, timing jitter of the MOPA should be reduced below 1 ns to ensure reliable shot-to-shot stability. The relative timing signals (high impedance TTL logic) were provided by a digital delay generator (Stanford DG535) with an absolute and relative accuracy of 1 ps. Channel A was used to drive the external trigger channel of the Goldie-amplifier, while channel B and C were relayed via the delay shutter control unit (DSCU) to trigger the Guzz-oscillator. The in-house design of the DSCU allowed switching between two different delay settings, corresponding to the "on" and "off" state of the MOPA, on shot-to-shot basis. In this way, the MOPA output could be operated at any multiple of the fundamental pulse frequency, typically $7 - 10$ kHz (Körner et al. 1996). Additionally, in burst-mode operation the pulse-train format could be tailored to deliver bunches of n-shots (at the fundamental PRF) which are repeated at lower repetition rates of $1 - 10^3$ Hz. It was found that due to the internal logic design and switching electronics, the output trigger pulses from the DSCU exhibited slow rise-times of around 0.8 μs for the 4 V TTL pulse. As the internal circuit of Goldie was designed to operate with 15 V trigger pulses, an amplifying circuit was incorporated to further reduce the timing jitter due to the DCSU. The signal booster device consisted of a 9 V battery powered matched transistor pair amplifying circuit, giving 9 V trigger pulses with reasonably sharp rise-times of < 0.1 μs.

The overall result of all the measures taken to reduce variations in the relative timing of the MOPA system resulted in improvement in the stability of the high beam-quality output power performance. The remaining jitter of 5 ns peak-peak was not found to cause any further problems. Adjusting the relative timing of the two lasers showed that the tolerance to obtain maximum power output ($28 - 30$ W) was around ± 10 ns, confirming that the residual jitter indeed was sufficiently low for reliable operation. To further characterise the MOPA performance, the total output power of Goldie was measured for over 6 decades variation in input power, controlled by attenuation of Guzz's output. The saturation and output power scaling of the double-pass MOPA is plotted in figure 3.6, showing an exponential increase in output power by increasing the input seed power from 1 μW to 0.1 W. For seed powers in excess of $0.1 - 0.2$ W, the total output power saturates at the maximum value approaching 30 W. Power-in-the-bucket measurement of the MOPA output is further shown in figure 3.7. For large apertures (> 4 times the diffraction-limited aperture), the beam-quality of the MOPA is comparable to that of the unamplified small-scale oscillator. Towards smaller apertures, the MOPA beam-quality is marginally worse compared to the stand-alone operation output of Goldie when fitted with the high magnification $M = 360$ unstable resonator. This degradation of the beam-quality during the amplification process can be assigned to effects such as thermal dither, spherical aberration of the amplifier gain medium, or spurious aberrations

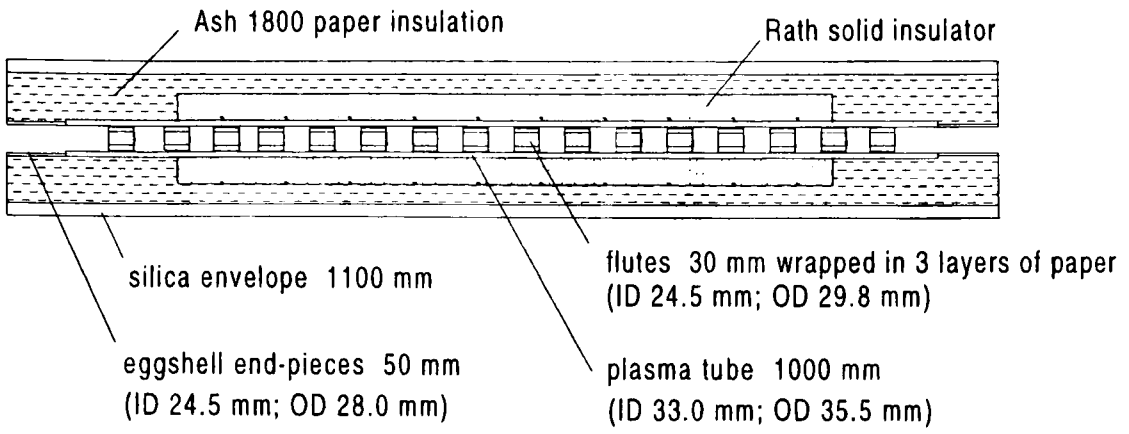


FIGURE 3.8: Design of the fluted medium-scale plasma tube.

in the optical system where the initial seed beam is magnified by a factor 2.5.

IV SUMMARY A CVL MOPA system was constructed using a small-scale master-oscillator (Guzz) and a medium-scale power-amplifier (Goldie). The $1-2$ W output available from Guzz' 10 mm bore diameter, 0.5 m long plasma tube was sufficient to fully control and saturate Goldie's 25 mm bore, 1 m long gain medium in a double-pass MOPA arrangement. Reduction of the relative shot-to-shot jitter to below 5 ns was necessary to obtain reliable and stable high beam-quality output power performance over many hours of operation. Due to the low copper-fill lifetimes, it was critical to replenish the copper content of Guzz every 100 hours. As the yellow output component of any CVL will usually decrease significantly when it is copper-starved, Goldie's yellow output could no longer be efficiently controlled when Guzz was low on copper, as was observed by the presence of highly divergent yellow ASE output from Goldie. Also, shortening of the pulse duration due to copper-starvation was further observed to be detrimental to the overall performance of the MOPA.

3.3 PULSE STRETCHING OF MEDIUM-SCALE CVL OSCILLATORS

I INTRODUCTION One of the aims of the COMPALA programme was the development of a prototype $40-50$ W CVL system suitable for industrial applications. A dual-laser MOPA arrangement based around two medium-scale devices was identified as the most viable option, and a number of enhancements have been implemented on current state-of-the-art commercial devices. First, similar to the design of the small-scale oscillator Guzz, it was found that the presence of copper reservoirs in the bottom half of the beam limited further improvements of the beam quality and total output power. Therefore, the fluted-tube design was also incorporated for the medium-scale LS 20–10 systems, of which the first prototype was designed and constructed at the Clarendon Laboratory, as shown in figure 3.8. 16 flutes (24.5 mm ID, 29.8 mm OD) were wrapped with a few layers of insulating alumina fibre sheets for secure placement inside the 1 m long primary alumina plasma tube. The centre-part of the plasma tube was insulated with solid alumina brick (Rath, 1800° C hold-off temperature), chosen to provide rigidity and prevent sagging of the tube. The whole was subsequently wrapped in insulating alumina fibre sheets (Ash 1800), up to the diameter of the silica envelope. To prevent collapse of the alumina fibre at the end, eggshell alumina end pieces where used to provide structural support.

Long-term testing of the fluted-tube design showed stable long-term operation, where a significant increase of the copper-fill lifetime up to 2600 hours was also established due to the larger volume of the primary plasma tube. To prevent obstruction of the beam path due to unwanted accumulation of solid copper deposition at the cool ends of the plasma tube, condensation zones were incorporated for controlled management of the copper vapour. To further increase the output power, a stretched 25 mm bore diameter, 1.5 m long tube was constructed, and found to yield output powers up to 35 W. Combined with the additional 10 W available from a high beam-quality medium-scale oscillator employing high magnification on-axis unstable resonators as described in chapter 2, the target for a $40 - 50$ W CVL MOPA was within reach. In the following one key aspect in the development of this system will be described, namely techniques for producing longer pulses from the medium-scale oscillator. Similar to the design issues of the Guzz-Goldie system, the main aim is to lengthen the pulse from a medium-scale oscillator by one extra roundtrip such that the ASE output can be discarded, and only the higher order roundtrips are used for seeding the amplifier. At the same time, given power requirements of the overall MOPA, the pulse-stretched output should maintain significant output powers > 5 W. Two approaches to this end will be described below.

II EFFECT OF PEAKING CAPACITOR ON PULSE DURATION In a standard charge-transfer circuit (see figure 3.2) the ratio of the value of the storage capacitors and the peaking capacitor C_s/C_p influences the speed of the excitation, where the rise-times of the voltage pulse on the laser head are decreased for smaller values of C_p relative to C_s. In view of the copper vapour kinetics (see chapter 2), to achieve efficient preferential excitation of the ^2D upper laser levels via electron collisions the need for a fast-rising discharge pulse is paramount. In contrast to this, the duration of the voltage waveform scales as $\propto \sqrt{L_{\rm pl} C_p}$ where $L_{\rm pl}$ is the inductance of the laser head as determined by its physical design and geometry and the current density profile of the discharge (Blau 1994). Therefore, in order to lengthen the excitation pulse to obtain longer gain durations requires an increase of C_p.

In practise a host of other effects further complicate this simplified representation of the CVL operation. For example, the pulse length depends on the (wall-)temperature, which is also influenced by changing the C_s, C_p as the thermal heat deposition of the medium is altered. Furthermore, the inductance $L_{\rm pl}$ is not truly constant, and where the current density profile of the discharge depends on various operating conditions (Blau 1994). Even if extended pulse durations can be established in transient operation, the associated set of operating parameters may well be beyond the stable operating regime of the laser, which ultimately depends on the interplay and balance of the rise-time of the discharge pulse, thermal heat deposition, level of thermal insulation, H_2 content, and other effects such as discussed in chapter 2.

Experiments on the effect of the peaking capacitor on the pulse duration of the laser output were, therefore, conducted as preliminary trials to estimate the overall sensitivity of the gain medium to the discharge speed. For these experiments, the medium-scale LS20-10 (Goldie) was driven by a charge-transfer circuit (figure 3.2), with $C_s = 3.5$ nF and $C_p = 1.75$ nF. No magnetic pulse compression (MPC) was used, as the aim was to produce a relatively slow discharge pulse. For these parameters and operation at total neon buffer gas pressures of $80 - 100$ mbar, the output pulse is similar to those in figure 2.6, showing a pulse duration of $45 - 50$ ns where three roundtrips contribute significantly to the overall

output power. Increasing $C_p = 2.75$ nF, no significant lengthening of the optical pulse was observed for stable operation at buffer gas pressures of 80 – 100 mbar. A transient 8-pass output was only observed temporarily by reducing the buffer gas pressure from 80 – 100 mbar to 30 mbar, but it could not be sustained under these operating conditions. For stable operation at 125 mbar the pulse duration was reduced, exhibiting just 2 & 4 pass outputs giving a total output of 5 W. Significant discharge flicker was observed, possibly due to the rise-times for this relatively large value of C_p. Reducing the peaking capacitor to $C_p = 1$ nF showed no significant changes in the pulse duration, which exhibited 3 roundtrips similar to when $C_p = 1.75$ nF. Further variations of the electrical input power (1.8 – 2.2 kW) and the neon buffer gas pressure (30 – 125 mbar) did not yield the desired effect of pulse stretching. It is therefore concluded that only limited variability of the laser pulse duration can be achieved by changing the peaking capacitor, electrical input power and neon buffer gas pressure. To affect the CVL gain kinetics requires more radical formatting of the discharge pulse, such as can be accomplished using MPC techniques.

III MAGNETIC PULSE COMPRESSION The use of saturable inductors as pulse-forming devices was introduced by Melville (1951), and applied for use of driving CVLs by Nehmadi et al. (1989). In principal, the basic design of magnetic pulse compression (MPC) involves the rapid change of a saturable inductor from a high inductance to a low inductance as the magnetic flux increases. As a result, the energy transfer is more rapid across the MPC stage, proportional to the compression factor which can be defined as the ratio between the rise time on the incoming and outgoing current pulse. The 'black art' of designing such saturable inductors involves careful consideration of the properties of the core material (type of metal, resistivity, saturated magnetic flux density, saturated inductance), and the overall design of the switch (number of conductor turns, stacking factor, bi-wiring to reduce saturated inductance). Thermal issues are particularly important for optimisation of the transfer efficiency, and long-term performance of the magnetic switch.

A typical CVL requires a power supply capable of delivering high voltage (15 – 20 kV), high peak currents (up to 1 kA) with short voltage rise times (< 100 ns) at high pulse repetition rates of tens of kilohertz. The primary advantage of MPC particularly for switching CVLs is to decrease the excitation pulse rise time, and increase the amount of energy supplied to the laser tube (Nehmadi et al. 1989). The MPC acts as a buffer between the thyratron (see figure 3.2) and the laser tube, and thus allows the thyratron to operate at a lower peak current, resulting in smaller losses and extended lifetimes. Extending this principle even further, the use of multistage MPC designs allows the use of all-solid state switching of the power supply where the dI/dt is increased proportional to the compression ratio (Deguchi et al. 1994). Typical compression ratios for two-stage MPC circuits can vary from 4.4 (decrease in rise time from 350 ns to 80 ns) for a 24 kW system (Seki & et al. 1994), to as high as 25 (2.5 μs to 100 ns) for a 17 kW device (Deguchi et al. 1994). In both cases typical efficiencies are in excess of 82 – 88% for a well tuned MPC circuit.

A typical LC-inversion MPC circuit comprises two loops, as schematically depicted in figure 3.9, where for the moment only a single MPC stage (C_1, L_1) will be considered. When the thyratron switches, effectively pulling the DC voltage V_1 existing across C_1 to ground, the charge stored in the bottom C_1 will be inverted due to the flow of the first current loop in the $L_{\text{inv}}.C_1$-circuit. This inversion of charge on the bottom C_1 can be relatively slow, as the saturated inductor L_1 is designed to switch only when all of

the charge of on the bottom C_1 has been inverted. In effect, the switching of the thyratron has changed the two capacitors C_1 from being in parallel with voltage V_1, to being in series with $2 \times V_1$ present across the equivalent capacitance $C_1' = C_1/2$. In comparison with the charge-transfer circuit (figure 3.2), the equivalent storage capacitance $C_s = 2C_1 = 4C_1'$ with constant stored energy $C_1 V_1^2$.

The change of the magnetic flux density $\Delta B\,(t)$ in the saturable switch L_1 is given by (Deguchi et al. 1994)

$$\Delta B\,(t) \simeq \frac{1}{NA} \int_0^t V_{C_1}\,(t')\,dt' \tag{3.1}$$

where N is the number of conductor turns and A is the magnetic cross-section of the saturable inductor. When $\Delta B\,(t)$ crosses the saturated magnetic flux density B_s, L_1 will rapidly change from having a high inductance to a low inductance. By appropriate design of the MPC parameters, the time at which this occurs is made to coincide with the time at which the voltage across C_1' reaches its maximum value $2V_1$ after 1/4 period of the $L_{\text{inv.}}C_1$-circuit. The second current loop in the (first) MPC stage will then start flowing, where now the speed of the voltage- and current-waveforms in the $L_1 C_1'$-circuit is increased approximately by a factor $\sqrt{2L_{\text{inv.}}/L_1}$, and is now no longer limited by the switching speed of the thyratron. The stored energy $C_1 V_1^2$ is now transferred onto the peaking capacitor C_p, and subsequently discharged through the laser head. The use of multi-stage MPC circuits allows further compression of the initial (slow) thyratron switched LC-inversion circuit, to produce even faster voltage-waveforms (Deguchi et al. 1994). From the point of view of efficient excitation of the copper gain medium, the proportional increase in the peak voltage with each MPC stage is beneficial for the overall performance of the laser, as discussed earlier.

IV DOUBLE-PULSE MPC CIRCUIT For the purpose of extending the gain pulse duration, the scheme shown in figure 3.9 is based on the principle of a double-pulse MPC circuit to deliver two discharge pulses to the laser tube with a set delay. Note that now the MPC is not only used as a compression device, but also a timing device where two parallel saturable inductors are designed to switch with a relative delay of order of tens of nanoseconds. In view of generating three to four roundtrips of high-beam quality (non-ASE) output, the underlying idea was to pre-excite the copper gain medium with a fraction of the total available input power to allow the first ASE roundtrip to develop in advance of the main (second) discharge pulse. In this fashion, the full gain duration of the main pulse can be subsequently used to produce the higher order roundtrips, high beam-quality output. The scheme bears some analogy to those reported by Nerheim (1977) and Vetter & Nerheim (1977), although their main objective for pre-excitation was to generate sufficiently high concentrations of copper vapour with a view to establishing efficient lasing from CuCl-halide lasers.

By incorporating a second MPC circuit in parallel (C_2, L_2) as shown in figure 3.9, a second discharge pulse can be delivered through the laser tube with one single switch from the thyratron. The power ratio of the two discharge pulses is roughly determined by the ratio C_1/C_2, while the relative timing is determined by the saturated inductance of L_1 and L_2. Bi-wired toroidal ferromagnetic cores were used throughout, and in practise similar switches were used such that the difference in the saturation induction is primarily determined by the number of conductor turns $N_1 : N_2$ (cf. equation (3.1)). Two settings

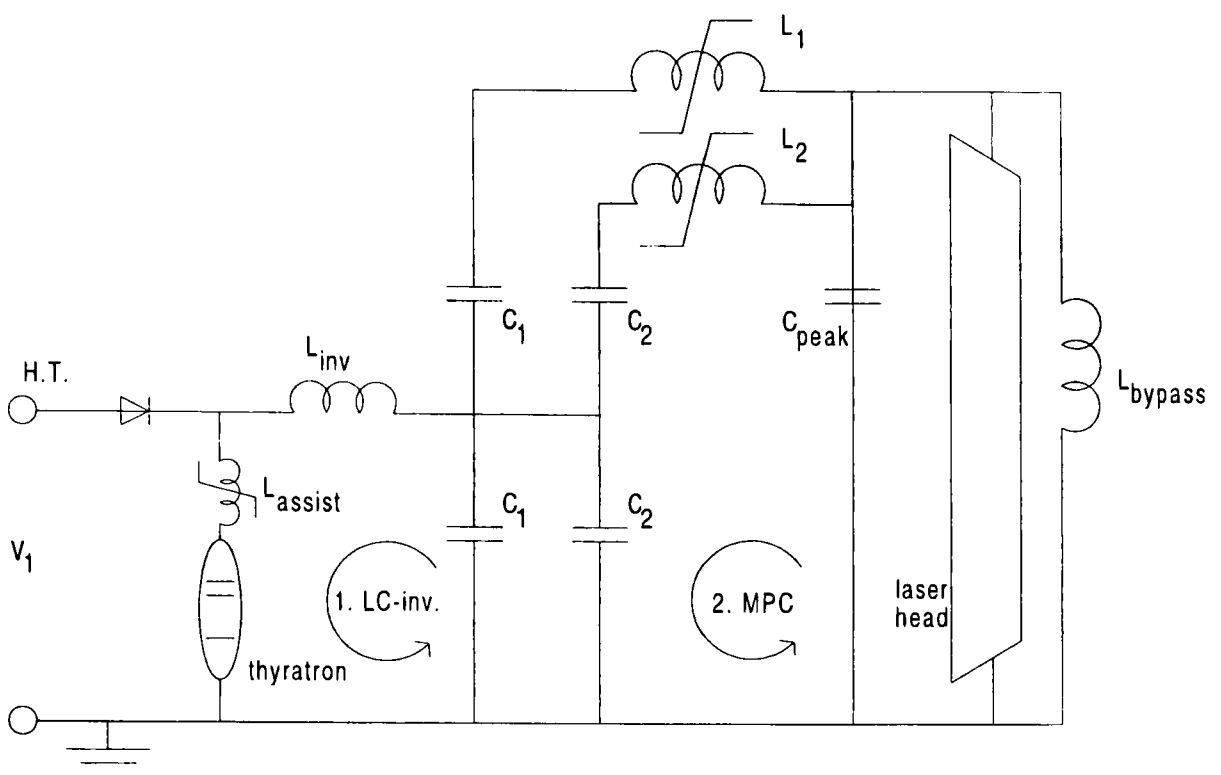


FIGURE 3.9: The double-MPC exitation circuit: $C_1 = 1.75$ nF, $C_2 = 0.25$ nF / 0.5 nF, $C_p = 0.25$ nF; number of conductor turns $N_1 : N_2 = 12 : 8$ or $12 : 5$.

of $N_1 : N_2$ were tried, involving ratios of $12 : 8$ or $12 : 5$, while C_2 was taken to be 0.25 nF or 0.5 nF, compared to $C_1 = 1.7$ nF. The peaking capacitor $C_p = 0.25$ nF was sufficiently low such that the ratio $C_s/C_p = 1.7$ is larger than unity to enhance the charge-transfer from the MPC stage to the laser head.

In comparison with the characteristics of the standard LC-inversion circuit (figure 3.10), the current and voltage traces of the double-pulse MPC circuit are shown in figure 3.11 for the best results with $C_2 = 0.5$ nF and $N_1 : N_2 = 12 : 8$. In the standard circuit the voltage on the laser head rises to a peak value of 17 kV within 50 ns, lasting for a total of around 100 ns. The associated tube current as measured at the laser head with a Pearson induction coil lasts for approximately 130 ns, with a peak value of 0.3 kA. For the double-pulse MPC circuit the voltage on the laser head only rises to 10 kV within 50 ns, but lasts significantly longer up to 200 ns where the double-humped structure associated with the two discharge pulses is nearly resolved. The tube current reaches similar peak values of 0.3 kA, but also lasts up to 200 ns, more than 50 ns longer compared to the standard circuit.

The optical output for the double-pulse MPC circuit is shown in figure 3.12 for normal steady-state operation at total neon buffer gas pressures of around 100 mbar, and electrical input powers of $2.1 - 2.2$ kW. Besides the initial ASE (2-pass) output up to four higher order roundtrips are clearly visible (even with a small decaying fifth roundtrip), for a total pulse duration of 65 ns. Depending on the choice of cavity magnification, up to 13 W high beam-quality output could be generated in the case of $M = 72$. Going to the highest magnifications of $M = 360$, however, resulted in poor control of the oscillator itself where the combination of the already low initial ASE seed signal, together with the

dye concentrations in each amplifier cell (Hnilo & Inez 1987).

Operation of copper vapour lasers (CVLs) in MOPA systems has a number of distinct advantages related to the characteristics of copper medium (Brown & Coutts 1996, Coutts & Brown 1995*b*). Firstly, for high gain devices such as the CVL, saturation of the amplifier medium is readily achieved even at relatively low oscillator input powers. This is particularly useful from the point of view of generation of high beam quality output, as has been reviewed by Brown & Coutts (1996). By employing a MOPA arrangement the design constraints set by the trade-off between using high magnification unstable resonators to establish high beam quality output at the cost of reduced efficient power extraction, can be separated (Brown & Coutts 1996). For example, small-scale oscillators with bore diameters of order 10 mm with high aspect ratios (up to 1 m long) are preferred to generate a high beam quality seed. Despite the relatively low power output, such a small-scale MO can be used to efficiently seed a medium-scale ($\emptyset$ 18 – 25 mm) or large-bore ($\emptyset \geq 25$ mm) PA with relatively long gain lengths (≥ 1 m) to generate tens of watts of average output power (Brown & Coutts 1996). Furthermore, by employing a MOPA arrangement the combined efficiency of the PA units is generally better than would be the case if each PA was operated as a stand-alone oscillator. As the only practical route to generating high beam quality output involves the use of unstable resonators with high magnifications, operation of each of separate oscillator would be relatively inefficient. In a MOPA arrangement only one unit would be operated as an oscillator, while the full output power capability of each PA is extracted to amplify the high beam quality output, often giving output powers greater than the maximum output power when the power amplifier would have been operated as an oscillator with a plane-plane resonator (Brown & Coutts 1996).

In addition, the use of MOPA arrangements allows manipulation of the overall beam quality of the system. The oscillator output can be 'cleaned-up' using a spatial filter with a constricting aperture stop (pinhole) placed at the common focus of a Cassegrian telescope. Only the transmitted oscillator signal will be subsequently amplified, where the MOPA beam quality is now primarily determined by the imaging condition of the spatial filter, similar to the principle of self-filtering unstable resonators (Pini et al. 1990). In theory, this technique can be applied to generate high-power, diffraction-limited output, provided the beam quality and output power of the oscillator output are sufficiently high such that the fraction of the initial seed signal propagated through the spatial filter is sufficient to saturate the amplifier. Practically, the use of 'hard' spatial filters is limited by complications and spurious side effects, such as parasitic lasing due to reflection of the edges of the pinhole. Also, the positioning and structural rigidity of the pinhole becomes increasingly more critical for increasingly tight spatial filters, and issues related to vibrations and turbulence disturbing the beam propagation become more pressing to maintain overall stability and reliability of the MOPA system.

Another important technique for beam-quality manipulation of MOPA systems makes use of the evolutionary character of the beam quality from CVL oscillators, as discussed earlier in chapter 2. By adjusting the relative timing between the oscillator and amplifier, the amplifier can be set to preferentially amplify the diffraction-limited components of the oscillator output (Coutts & Brown 1995*b*). This technique requires the pulse duration of the oscillator to be sufficiently long such that by discarding the ASE and high divergence components of the output, the net pulse duration of the high beam-quality output is as long as the gain duration of the amplifier. This aspect of the design of MOPA systems will be

considered in this chapter.

Besides beam-quality manipulation, the relative timing between the oscillator and amplifier also can be used for delay shutter control of the MOPA output (Körner et al. 1996). Due to the significant population densities of the metastable ^2D lower laser levels (see chapter 2) in the afterglow of the excitation pulse, the copper medium can act as an efficient absorber at the laser transitions. As such, the total output of the MOPA can be switched on and off by alternating the timing of the oscillator pulse relative to the amplifier to be either in sync or delayed by approximately 100 ns. Despite the high pulse repetition frequency (PRF) of typically 10 kHz, the pulse-train format of the MOPA output can be controlled on single-shot basis with sufficiently fast switching electronics. Operation with a wide range of PRFs varying from parametric fractions of the fundamental PRF, burst-mode operation down to sub-Hz single shot operation has been demonstrated (Körner et al. 1996).

II INJECTION-CONTROLLED OSCILLATORS An alternative approach to generate high beam-quality output from multiple CVLs involves injection-controlled oscillators (Warner 1986, Naylor et al. 1986, Naylor et al. 1988, Chang 1995). In an injection-controlled oscillator (ICO) arrangement, the power amplifier is operated as an oscillator which is seeded with the output from the master oscillator. This technique is sometimes referred to as an injection seeded oscillator (ISO), the small difference being that for the ICO the two cavities share a common mirror. The primary advantage of the ICO arrangements is that the master oscillator and injection-controlled oscillator are allowed to have different pulse lengths, since the master-oscillator seed is only required during the build-up period of the ICO. In practice the trailing part of the master-oscillator laser pulse is used for this purpose, as output from higher order roundtrips is often essentially diffraction limited. Thus, the constraint on the master oscillator to produce sufficiently long optical pulse durations relative to the gain duration of the amplifier, is relaxed.

It is important to note that in the ICO arrangement, the two resonators are not locked or mode-matched in any way (as is the case for e.g. cw systems), but that by using highly diffractive unstable resonators the master-oscillator seed is self-filtered to obtain the high beam quality output from the ICO. Due to the high diffraction losses of the ICO unstable resonator, the latter part of the ICO output is essentially operating in free-running mode and generally has different beam propagation properties from the initial master-oscillator seed. As a result, most of the output power from the master oscillator seed is lost, which constitutes a major disadvantage. Furthermore, the optimum operating condition of the ICO is critically dependant on the alignment of the two resonators. Chang (1995) observed that relatively small misalignment can lead to significant spatial and temporal fluctuations in the far-field (multiple spots, beam dither etc.).

Finally, it is known that for a large–scale ICO ($\emptyset$ = 40 mm, 2.7 m long) optimum operation conditions are very sensitive to the relative timing of the MO-ICO when using an on-axis arrangement. Since the ICO needs to sustain free-running oscillator modes like a stand-alone oscillator, radial effects of the gain medium significantly influence its performance for similar reasons as discussed in chapter 2. For large-scale devices, reliable and efficient operation can only be obtained when an off-axis injection scheme is used (Kearsley et al. 1987, Chang 1995), which is not preferred for HBQ applications requiring a symmetric far-field intensity distribution.

III OUTLINE OF EXPERIMENTS Within the framework of the Compala project, the primary objective was to generate 25 – 30 W of output from a CVL with near diffraction-limited beam quality (2 times or better), which could be used routinely for the various studies on laser ablation. To this purpose various design issues regarding the construction and optimisation of dual CVL MOPA systems were addressed. First, the construction and design of a MOPA system based around a small-scale MO will be presented. The design and characterisation of a small-scale master oscillator ('Guzz ') is presented. In combination with a medium-scale Oxford Lasers LS 20-10 device ('Goldie'), a mini-MOPA system as first reported by Brown & Coutts (1996) is constructed and characterised. The primary issue involved optimisation of Guzz to provide a sufficiently long optical pulse length to seed Goldie. To ensure maximum power extraction, best performance was obtained using a double-pass amplifier arrangement (Coutts et al. 1998) of which the operation characteristics will also be presented.

The second part of the experiment addresses the issue of generating an extended optical pulse from the medium-scale LS 20-10. This work was initiated within the Compala consortium in collaboration with Oxford Lasers, to construct the next generation of CVL MOPA system based on two medium-scale devices. The primary issue involved stretching of the optical pulse of the master oscillator in view of improving the beam quality of the MOPA output, whilst sustaining the output power of the oscillator at an acceptable level as it is designed to contribute to the total output power of the MOPA system. To this purpose, various modifications to the electronic driving circuit were investigated. A successful method involving a double-pulse magnetic compression circuit will be presented.

3.2 'GUZZ & GOLDIE' MOPA SYSTEM

I INTRODUCTION During the characterisation and optimisation of the small-scale master oscillator 'Guzz', the primary objective was to establish a pulse duration which was sufficiently long to seed the full $35 - 40$ ns gain pulse from the PA with only high beam quality output. With roundtrip times of around $7 - 8$ ns, and given that the first burst of ASE (2-pass output) was to be discarded, the total pulse duration of the Guzz was aimed to be $45 - 50$ ns to accommodate 6 roundtrips. Earlier studies performed by Brown & Coutts (1996) on a mini-MOPA system using a small-scale oscillator indicated that the required power levels to reach saturation of the amplifier were of order 0.1 W, and as such obtaining high power output was not the main design issue. Furthermore, by employing a double-pass MOPA arrangement as first reported by Coutts et al. (1998), the output requirements for the small-scale oscillator are further relaxed.

II SMALL-SCALE MASTER-OSCILLATOR ('GUZZ') The small-scale Master Oscillator 'Guzz' was designed and constructed in house, following recent advances made by Brown & Coutts (1994) in constructing MOPA systems based around on small-scale oscillators. The design is sketched in figure 3.1. The main body of the laser consist of a water-cooled jacket which contains the silica envelope (700 mm length, Ø105.5 mm), supported on each end together by the end-flanges and collars which also provide a vacuum tight side-seal. The inner part of the end-flanges are machined with anti-reflection baffles to reduce the amount of infrared radiation from the plasma reaching the windows. The electrodes are made of standard grade copper and machined to have smooth curving ends, ensuring that no sharp corners

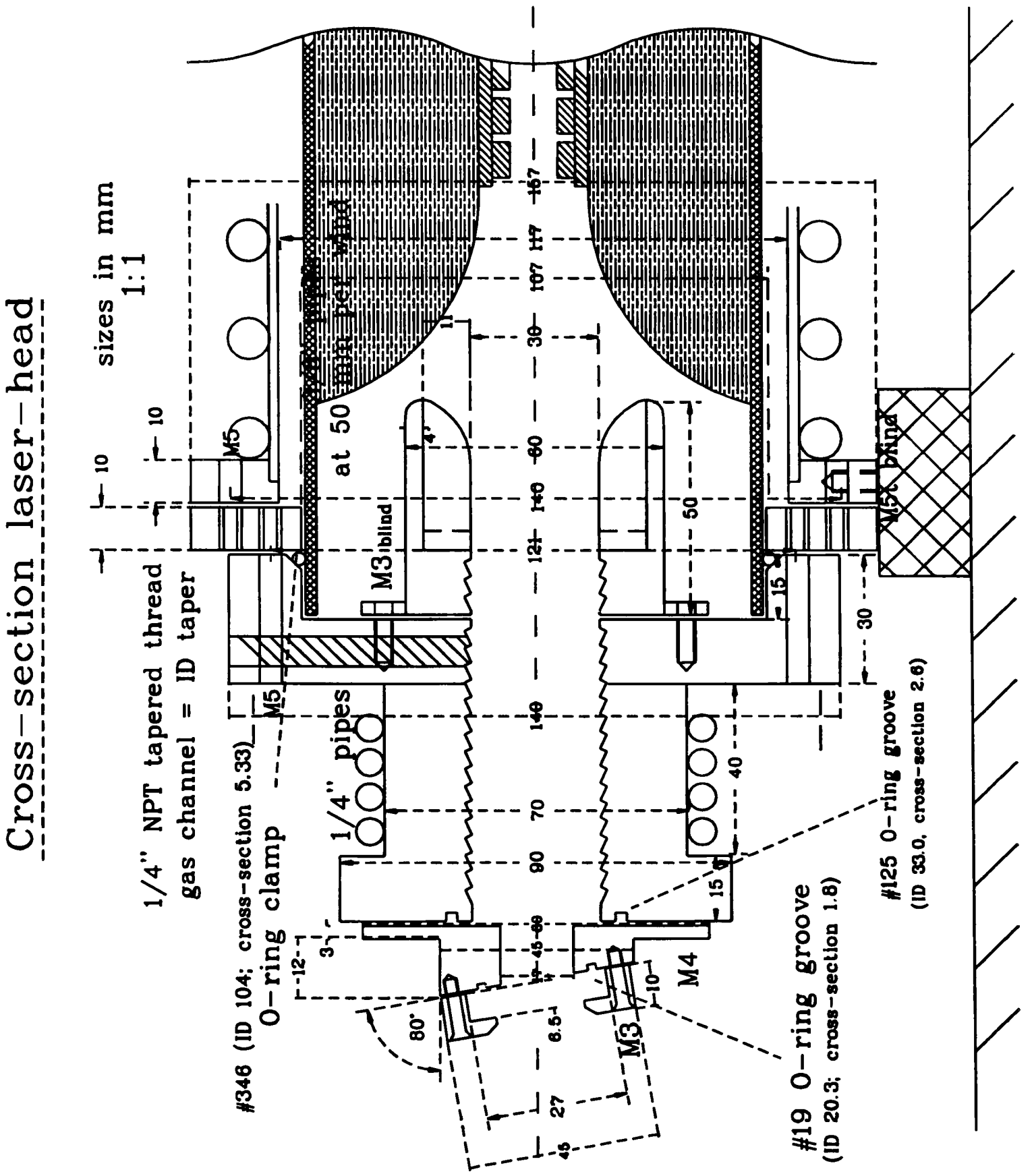


FIGURE 3.1: Cross-section of the in-house built small-bore master oscillator, showing the end–windows, the side-sealed end-flanges, the main silica envelope and the fluted plasma tube design.

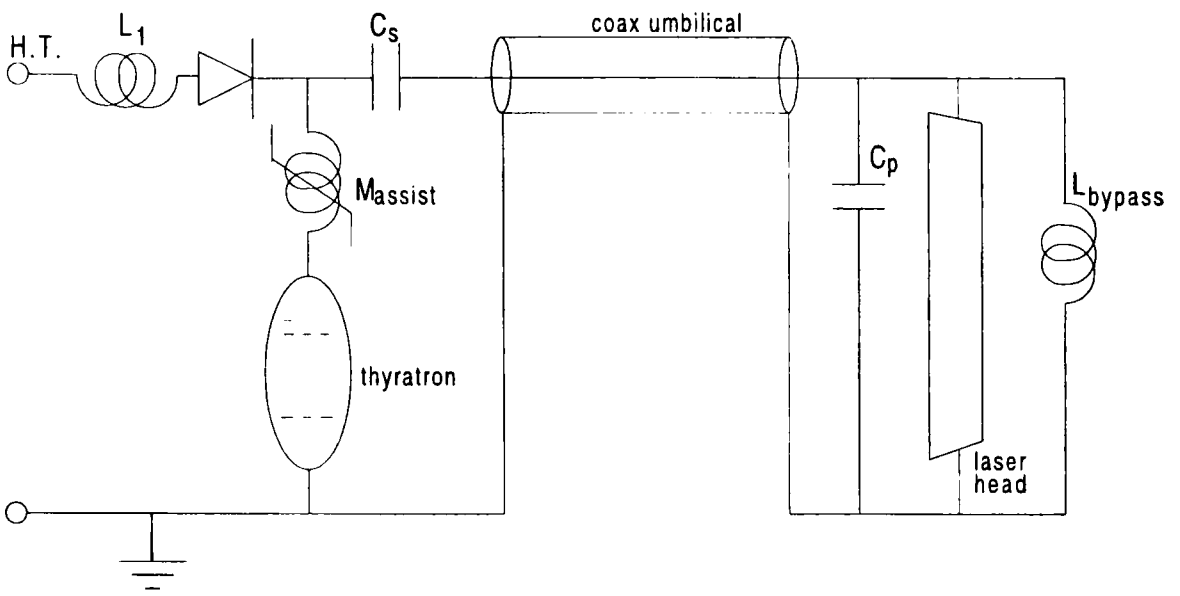


FIGURE 3.2: Charge-transfer circuit used for the small-scale oscillator with $L_1 \approx 0.5$ H; storage capacitor $c_s = 5$ nF; peaking capacitor $c_p = 2$ nF; An EEV CX1535 thyratron was used to drive the circuit, and to decrease the switching time of the thyratron a magnetic assist was incorporated which was made of teflon coated copper wire wrapped around a toroidal ferrrite core.

are present which may cause spurious anchoring of the discharge. Around the perimeter ~ 50 regularly spaced slots are cut, each around 1 mm wide, to provide a hollow-cathode effect to enhance the homogeneity of the plasma discharge (Chang et al. 1997). Upon inspection after approximately 100 hours of operation, the electrodes showed homogeneous distribution of the discharge where all the slots were slightly widened by thermal effects or sputtering. The window-mounts can be moved independently relative to the end-flanges for ease of alignment of the optical axis relative to the plasma tube. Infrasil windows (CVI Corporation) are used to reduce thermal lensing due to absorption of infrared radiation, and are mounted at 10° to prevent parasitic lasing.

The plasma tube is contained in high-grade alumina fibre insulation, consisting of wrapped alumina fibre-sheets (Ash 1400) and solid alumina brick (Rath, maximum hold-off temperature $\sim 1800\,^\circ$ C), all of which are enclosed in the primary silica tube. Owing to the small bore diameter, the plasma tube is designed to contain regularly spaced ceramic 'flutes' (2 cm length, Ø17.7 mm OD / 12.5 mm ID) placed in a larger enveloping primary plasma tube (50 cm long, 20.0 mm ID / 26.0 mm OD). In this arrangement the copper reservoirs are recessed, as otherwise a significant portion of the optical aperture would be obstructed by the copper shadow. This design was also used in the construction of a medium-scale fluted tube, as depicted in figure 3.8. Construction of the fluted tube involved wrapping three tightly wound layers of the alumina fibre sheets around the flute, and carefully placing the flutes in the main plasma tube one at a time using a plunger. In the first arrangement a total of 9 flutes were placed at intervals of 2 cm, leaving 80 mm on either end of the plasma tube to function as cool end-zones where the copper vapour can condense. Due to the relatively low power output (less than 1 W) ascribed to the small total gain length, 12 flutes were placed in the Mark II design leaving only 20 mm at each end of the plasma tube. To accommodate cooling-down regions, the primary plasma tube is extended pieces of 44 mm

PRF (kHz)	V_{in} (kV)	I_{in} (A)	p_{Ne} (mbar)	P_{out} (W)	τ_p @ base (ns)
Mark I					
6.2	5.4	0.27	25	1.6	50
6.2	5.4	0.27	40	1.0	50
10	4.5	0.35	25	1.9	40
Mark II					
7	5.3	0.30	40	2.0	55
10	4.2	0.34	35	2.2	50
10	4.7	0.39	20	3.0	43
Molly					
6.2	5	0.3	45	3.3-3.6	60
10	4	0.4	45	3.3	50

TABLE III: Characterisation of the small-scale MO 'Guzz', operated at various levels of neon buffer gas pressure and electrical input power with $c_s = 5$ nF and $c_p = 2$ nF for the Mark I and Mark II tube design. Data for a similar small-scale MO 'Molly' are included for comparison, where $c_s = 5$ nF and $c_p = 1.75$ nF with an active gain medium length of 70 cm.

long thin ('egg-shell') ceramic tubes (same diameter as the plasma tube). While this reduces the spacing between the end of the plasma tube and the electrodes down to 10 mm on either side, the electrodes did not overheat and Guzz was found to operate happily now giving over 2 W.

A standard three-phase transformer (maximum rating 3.0 kVA) served as a high voltage power supply for the laser head, which was driven by a thyratron switched (EEV CX1535) charge-transfer circuit (see figure 3.2). A magnetic assist M_{assist} was used to hold-off the volts on the thyratron anode. A static fill of nominally pure neon (>99.99%) was used as a buffer gas, which was replaced daily during the run-up sequence. Since the Goldie PA was normally run at 10 kHz, Guzz was also run at 10 kHz with typical operating conditions of $4.3 - 4.4$ kV from the DC power supply with an average supply current of 0.35 A (1.5 kW) with 50 mbar of neon buffer gas pressure. For the ballistic pendulum experiments (see chapter 4), the MOPA was run at 7 kHz where it gave 3.5 mJ pulse energy.

To find (near-)optimum operating conditions, Guzz was operated under different condition, varying the electrical input power, buffer gas pressure, and capacitance C_s and C_p of the charge-transfer circuit. Also, the effect of changing the PRF on the pulse duration was investigated to allow comparison with a similar small-scale master oscillator ('Molly') which was normally operated at 6.2 kHz (Coutts & Brown 1995*a*). The operating characteristics of the small-scale oscillators are listed in table III. Clearly, the overall performance of the Mark II tube in terms of pulse duration and total output power is better compared to the Mark I design. The enhanced performance is ascribed to the extended gain length of the Mark II tube, and compares favourably with Molly, whose gain length was 70 cm.

Time-traces of the optical output of Guzz are shown in figure 3.3, showing the significant enhancement of the Mark II tube. The far-field intensity profile is plotted in figure 3.4, using the same scale as figures 2.7 and 2.8. Operating the Mark II at higher input powers does result in higher power output, but also considerably shorter pulse, as indicated in table III. Generally operation of Guzz was sensitive

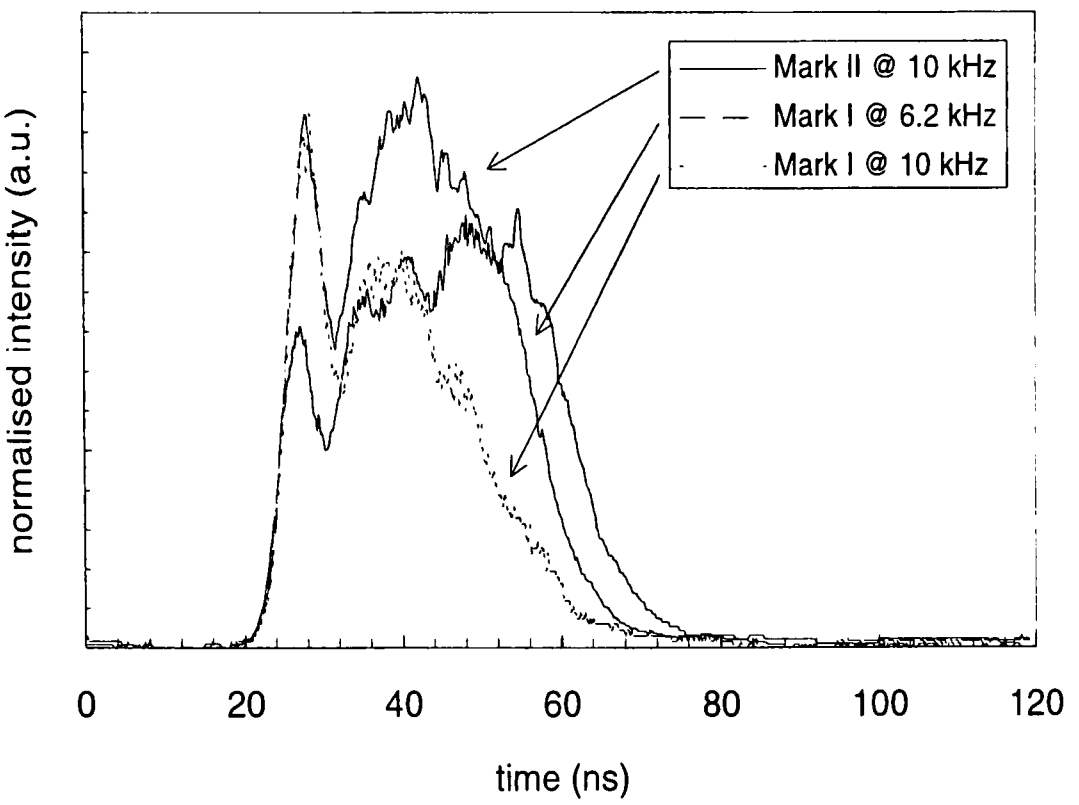


FIGURE 3.3: Optical pulse shapes from the small-scale oscillator Guzz.

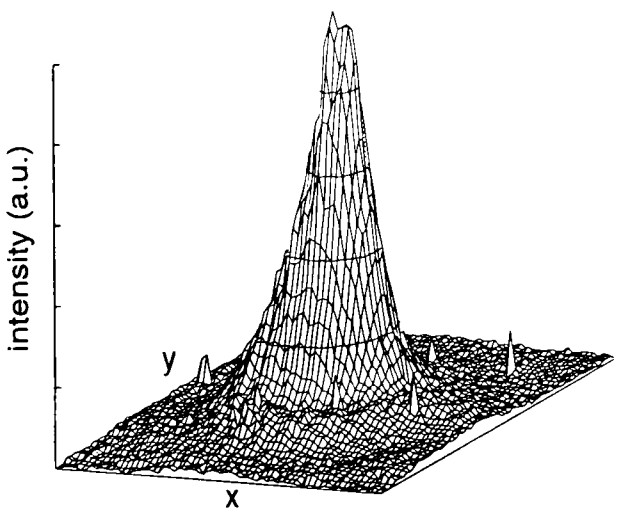


FIGURE 3.4: Measured far-field intensity distribution for the small-scale oscillator Guzz. Full extend of the plotted xy-plane corresponds to 0.1 mrad.

to the input voltage V_{in} (and associated current I_{in}), where marginal increases of 0.1 kV could result in significant changes in output power and pulse duration τ_p. Given output powers in excess of 2 W with the Mark II design, fine adjustment of V_{in} was done in view of optimising τ_p, critical for efficient MOPA operation. Only marginal differences in the τ_p was observed by changing C_s, C_p, and for all results reported here values for $C_s = 5$ nF and $C_p = 2$ nF were used (see also discussion in the following section). It was further observed that the pulse duration was sensitive to the amount of copper resident in the gain volume. For all small-bore tubes, lifetimes of copper fills were found to be of order $100 - 150$ hours, after which significant decrease of the output power and pulse duration occurs. Under normal operation, Guzz was refilled every 100 hours.

III CHARACTERISTICS 'GUZZ & GOLDIE' MOPA SYSTEM The critical issue in the construction of CVL MOPA systems regards the relative timing of the master-oscillator output to the power-amplifier gain pulse. While the small-scale oscillator Guzz provided ample output power and sufficiently long seeding pulses, it was found that the use of a conventional single-pass MOPA configuration was slightly unstable in terms of sustaining maximum power output over many hours of operation. Effects which result in a decrease in the pulse duration of Guzz, as discussed above, will generally result in a proportional decrease (up to several watts) in the high beam-quality output of the MOPA system as a whole. To alleviate these problem a double-pass MOPA arrangement was used (Coutts et al. 1998), as depicted in figure 3.5. The unpolarised master oscillator output was sent through a polarising beam splitter held in a rotation mount, a $7 - 10$ mm aperture, and then focused with a 500 mm achromatic lens through a 1 mm diameter central hole in the 45°, double-pass amplifier coupling mirror. After a single transit through the amplifier, a 2 m radius of curvature concave high reflector at the rear of the amplifier produced a 25 mm diameter collimated beam which is returned for a second pass through the amplifier, this time efficiently extracting power from the whole gain volume. The double-pass output was extracted by reflection of the 45° coupling mirror, and sent through a second, fixed, polarising beam splitter cube. By rotation of the first polarising beam splitter, full control over the MOPA power was obtained without any variation in any other beam parameter.

The alignment procedure was as follows. First, the centre-hole mirror was centrally positioned relative to the optical axis defined by the plasma tube of the PA. Then, by beam-walking the output of the master oscillator using the output coupler of the oscillator and the first turning mirror, the oscillator beam was ensured to be colinear with the centre-hole and the PA. The lens ($f = 500$ mm) was put in place with the focus nominally at the centre-hole mirror. To protect the substrate of the centre-hole mirror during the alignment procedure a sacrificial metal pinhole was mounted of the back-face, fixed using a magnetic strip to allow for adjustment. Finally, the HR of the PA was positioned and aligned relative to the centre-hole mirror. By looking at the collimation of the MOPA output beam, the focusing lens was adjusted to move towards the amplifier if the beam was slightly converging, or away from the PA when diverging. The iris was used for final adjustments to match the oscillator beam diameter to the imaging conditions defined by the geometric conditions of the double-pass amplifier, hence reducing diffraction losses.

By employing a double-pass MOPA arrangement, the constraint on the oscillator to saturate the amplifier gain medium was relaxed. Furthermore, considering the transit time of $4 - 5$ ns over a single-pass in the amplifier, the output of the MOPA was less sensitive to decreases in the pulse duration of the

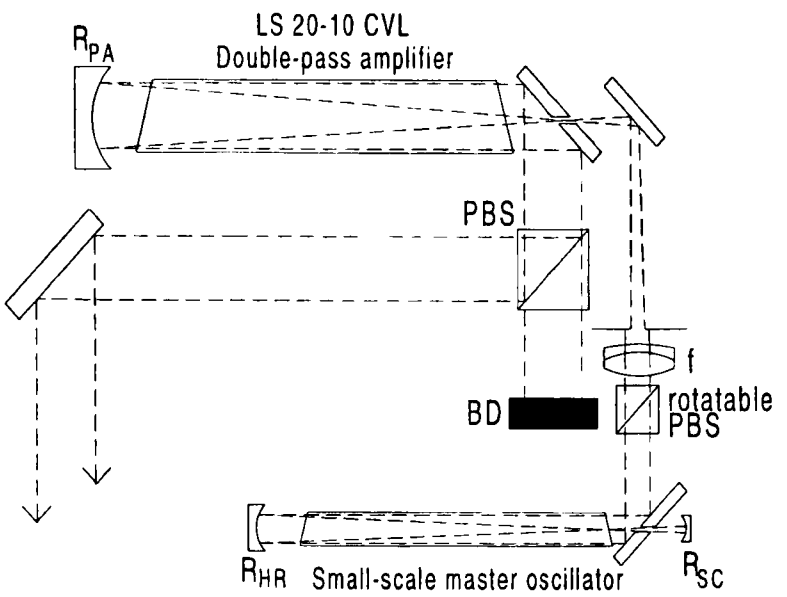


FIGURE 3.5: The double-pass MOPA arrangement, with $R_{HR} = 2.0$ m; $R_{SC} = 25$ mm; $R_{PA} = 3.6$ m; $f = 500$ mm; BD = beam-dump; PBS = polarising beam-splitter.

oscillator seed. Note, however, that the double-pass MOPA systems still operates as a travelling-wave amplifier, in contrast to an ICO/ISO arrangement (Chang 1995). In view of micromachining applications, parasitic lasing due to spurious feedback into amplifier medium may be an issue when employing double-pass MOPA systems. However, for all experiments reported here the presence of a high reflector in double-pass MOPA set-up was found not to cause any problems, where throughout beam-paths of a few metres were used.

Looking at the performance of the double-pass MOPA setup, the long term power fluctuations were eliminated. Sustained maximum power extraction up to 30 W was established, to be compared with 23 W maximum output power from Goldie when fitted with a plane-plane resonator (table I). However, significant shot-to-shot variations in the pulse energy were still observed in the output from the double-pass MOPA. This was found to be caused by timing jitter in the absolute and relative triggering of the two lasers. A number of possible causes were identified. First, the single-phase DC voltage supply of Guzz was found to have a 50 Hz modulation up to ten percent of the peak DC voltage. This modulation resulted in a measured relative jitter of $10 - 12$ ns peak-to-peak between the onset of the ASE output and the thyratron trigger pulse on Guzz. By incorporating a low-pass LC-filter with a capacitance $C = 2$ μF, and a water-cooled inductor with a nominal inductance $L = 0.5$ H, the timing jitter could be reduced below 5 ns.

Other possible internal sources of noise within the circuit of each individual laser, such as may exist in the resonant LC charging circuit, the magnetic pulse compression stages (discussed in more detail below), or due to fluctuations in the discharge at the electrodes, were further investigated. For Goldie, significant flickering of the discharge was observed, indeed suggesting possible fluctuations caused by the copper electrodes. Upon inspection Goldie's electrodes showed significant traces of sputtering, indicating

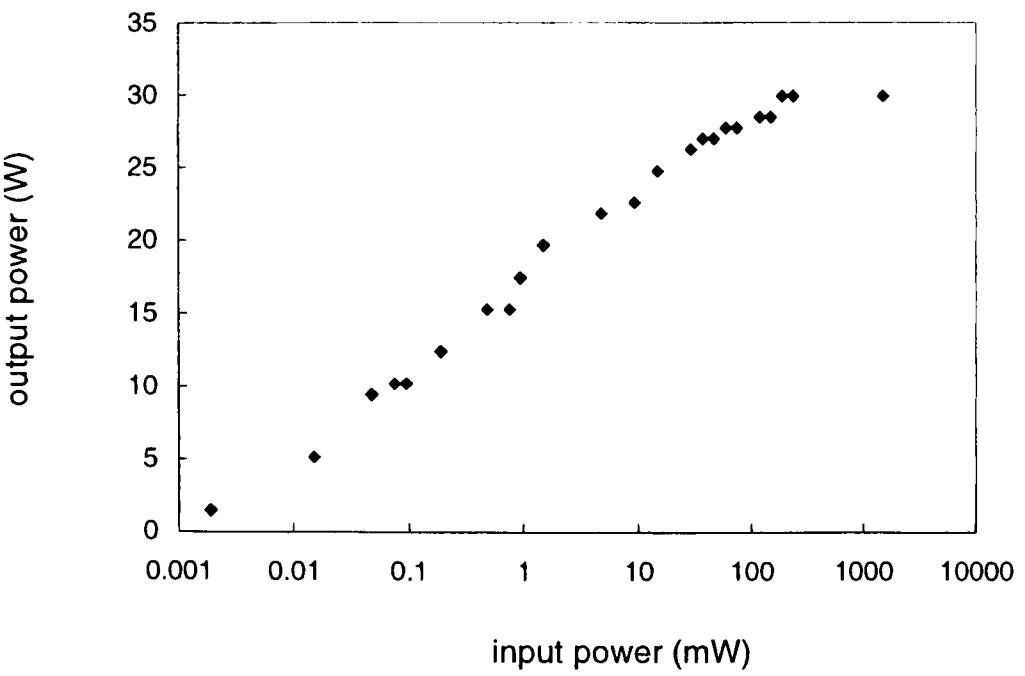


FIGURE 3.6: The total output power from the double-pass MOPA as a function of the input power from the master-oscillator.

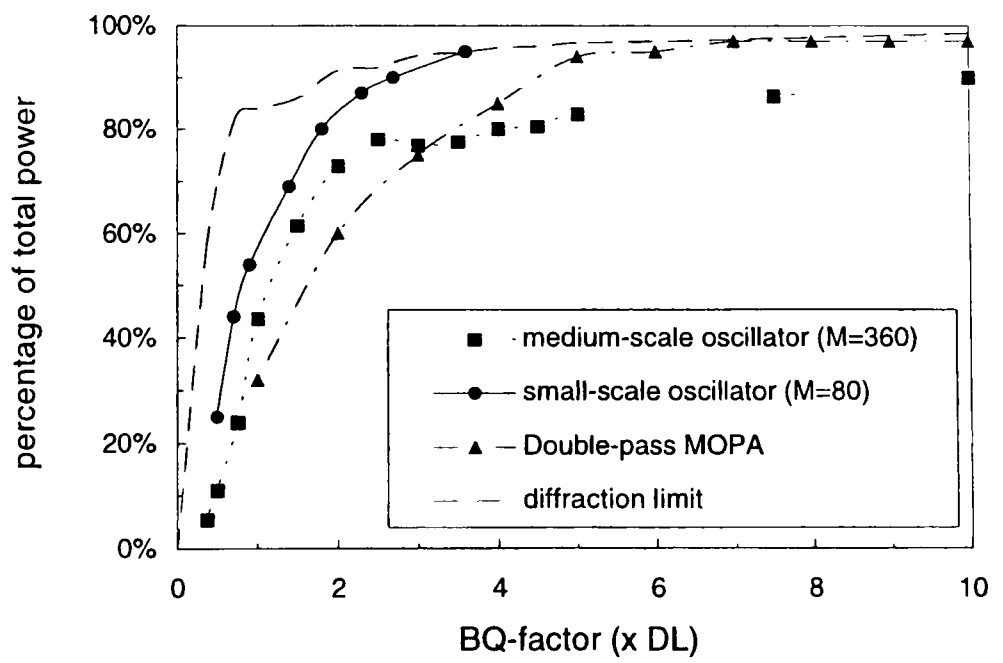


FIGURE 3.7: Power-in-the-bucket measurement for the small-bore oscillator and the double-pass MOPA system, compared to that for the LS 20-10 laser with $M = 360$ as described in chapter 2. Also shown is the calculated throughput for a diffraction limited beam.

anchoring of the discharge on specific spots. To reduce the electrode jitter, the electrodes were refurbished to have rounded corners and slots, following the design of hollow-cathode electrodes as reported by Chang et al. (1996) and Chang et al. (1997). Around the perimeter 48 slots were cut with 0.25 mm blade. In doing so, a sleeve was left on the outside (no through cut) to prevent the discharge from wandering to the outside, but rather lock in the inner part of the electrode. This modification resulted in alleviation of the electrode jitter, which was measured to be 3 ns peak-peak using the hollow-cathode electrodes, compared to initial peak-peak timing variations of order 10 ns when Goldie was triggered internally.

Besides the absolute timing fidelity of the internal high-voltage switching circuit of each laser, the electronics controlling the relative timing of the two lasers was scanned for possible noise sources. In practise, timing jitter of the MOPA should be reduced below 1 ns to ensure reliable shot-to-shot stability. The relative timing signals (high impedance TTL logic) were provided by a digital delay generator (Stanford DG535) with an absolute and relative accuracy of 1 ps. Channel A was used to drive the external trigger channel of the Goldie-amplifier, while channel B and C were relayed via the delay shutter control unit (DSCU) to trigger the Guzz-oscillator. The in-house design of the DSCU allowed switching between two different delay settings, corresponding to the "on" and "off" state of the MOPA, on shot-to-shot basis. In this way, the MOPA output could be operated at any multiple of the fundamental pulse frequency, typically $7 - 10$ kHz (Körner et al. 1996). Additionally, in burst-mode operation the pulse-train format could be tailored to deliver bunches of n-shots (at the fundamental PRF) which are repeated at lower repetition rates of $1 - 10^3$ Hz. It was found that due to the internal logic design and switching electronics, the output trigger pulses from the DSCU exhibited slow rise-times of around 0.8 μs for the 4 V TTL pulse. As the internal circuit of Goldie was designed to operate with 15 V trigger pulses, an amplifying circuit was incorporated to further reduce the timing jitter due to the DCSU. The signal booster device consisted of a 9 V battery powered matched transistor pair amplifying circuit, giving 9 V trigger pulses with reasonably sharp rise-times of < 0.1 μs.

The overall result of all the measures taken to reduce variations in the relative timing of the MOPA system resulted in improvement in the stability of the high beam-quality output power performance. The remaining jitter of 5 ns peak-peak was not found to cause any further problems. Adjusting the relative timing of the two lasers showed that the tolerance to obtain maximum power output ($28 - 30$ W) was around ± 10 ns, confirming that the residual jitter indeed was sufficiently low for reliable operation. To further characterise the MOPA performance, the total output power of Goldie was measured for over 6 decades variation in input power, controlled by attenuation of Guzz's output. The saturation and output power scaling of the double-pass MOPA is plotted in figure 3.6, showing an exponential increase in output power by increasing the input seed power from 1 μW to 0.1 W. For seed powers in excess of $0.1 - 0.2$ W, the total output power saturates at the maximum value approaching 30 W. Power-in-the-bucket measurement of the MOPA output is further shown in figure 3.7. For large apertures (> 4 times the diffraction-limited aperture), the beam-quality of the MOPA is comparable to that of the unamplified small-scale oscillator. Towards smaller apertures, the MOPA beam-quality is marginally worse compared to the stand-alone operation output of Goldie when fitted with the high magnification $M = 360$ unstable resonator. This degradation of the beam-quality during the amplification process can be assigned to effects such as thermal dither, spherical aberration of the amplifier gain medium, or spurious aberrations

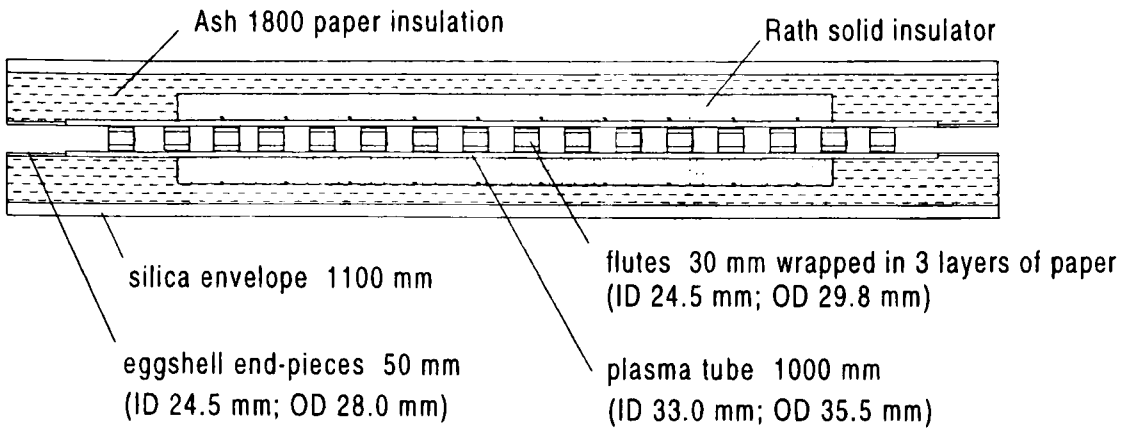


FIGURE 3.8: Design of the fluted medium-scale plasma tube.

in the optical system where the initial seed beam is magnified by a factor 2.5.

IV SUMMARY A CVL MOPA system was constructed using a small-scale master-oscillator (Guzz) and a medium-scale power-amplifier (Goldie). The $1-2$ W output available from Guzz' 10 mm bore diameter, 0.5 m long plasma tube was sufficient to fully control and saturate Goldie's 25 mm bore, 1 m long gain medium in a double-pass MOPA arrangement. Reduction of the relative shot-to-shot jitter to below 5 ns was necessary to obtain reliable and stable high beam-quality output power performance over many hours of operation. Due to the low copper-fill lifetimes, it was critical to replenish the copper content of Guzz every 100 hours. As the yellow output component of any CVL will usually decrease significantly when it is copper-starved, Goldie's yellow output could no longer be efficiently controlled when Guzz was low on copper, as was observed by the presence of highly divergent yellow ASE output from Goldie. Also, shortening of the pulse duration due to copper-starvation was further observed to be detrimental to the overall performance of the MOPA.

3.3 PULSE STRETCHING OF MEDIUM-SCALE CVL OSCILLATORS

I INTRODUCTION One of the aims of the COMPALA programme was the development of a prototype $40-50$ W CVL system suitable for industrial applications. A dual-laser MOPA arrangement based around two medium-scale devices was identified as the most viable option, and a number of enhancements have been implemented on current state-of-the-art commercial devices. First, similar to the design of the small-scale oscillator Guzz, it was found that the presence of copper reservoirs in the bottom half of the beam limited further improvements of the beam quality and total output power. Therefore, the fluted-tube design was also incorporated for the medium-scale LS 20–10 systems, of which the first prototype was designed and constructed at the Clarendon Laboratory, as shown in figure 3.8. 16 flutes (24.5 mm ID, 29.8 mm OD) were wrapped with a few layers of insulating alumina fibre sheets for secure placement inside the 1 m long primary alumina plasma tube. The centre-part of the plasma tube was insulated with solid alumina brick (Rath, 1800° C hold-off temperature), chosen to provide rigidity and prevent sagging of the tube. The whole was subsequently wrapped in insulating alumina fibre sheets (Ash 1800), up to the diameter of the silica envelope. To prevent collapse of the alumina fibre at the end, eggshell alumina end pieces where used to provide structural support.

Long-term testing of the fluted-tube design showed stable long-term operation, where a significant increase of the copper-fill lifetime up to 2600 hours was also established due to the larger volume of the primary plasma tube. To prevent obstruction of the beam path due to unwanted accumulation of solid copper deposition at the cool ends of the plasma tube, condensation zones were incorporated for controlled management of the copper vapour. To further increase the output power, a stretched 25 mm bore diameter, 1.5 m long tube was constructed, and found to yield output powers up to 35 W. Combined with the additional 10 W available from a high beam-quality medium-scale oscillator employing high magnification on-axis unstable resonators as described in chapter 2, the target for a $40 - 50$ W CVL MOPA was within reach. In the following one key aspect in the development of this system will be described, namely techniques for producing longer pulses from the medium-scale oscillator. Similar to the design issues of the Guzz-Goldie system, the main aim is to lengthen the pulse from a medium-scale oscillator by one extra roundtrip such that the ASE output can be discarded, and only the higher order roundtrips are used for seeding the amplifier. At the same time, given power requirements of the overall MOPA, the pulse-stretched output should maintain significant output powers > 5 W. Two approaches to this end will be described below.

II EFFECT OF PEAKING CAPACITOR ON PULSE DURATION In a standard charge-transfer circuit (see figure 3.2) the ratio of the value of the storage capacitors and the peaking capacitor C_s/C_p influences the speed of the excitation, where the rise-times of the voltage pulse on the laser head are decreased for smaller values of C_p relative to C_s. In view of the copper vapour kinetics (see chapter 2), to achieve efficient preferential excitation of the ^2D upper laser levels via electron collisions the need for a fast-rising discharge pulse is paramount. In contrast to this, the duration of the voltage waveform scales as $\propto \sqrt{L_{\rm pl} C_p}$ where $L_{\rm pl}$ is the inductance of the laser head as determined by its physical design and geometry and the current density profile of the discharge (Blau 1994). Therefore, in order to lengthen the excitation pulse to obtain longer gain durations requires an increase of C_p.

In practise a host of other effects further complicate this simplified representation of the CVL operation. For example, the pulse length depends on the (wall-)temperature, which is also influenced by changing the C_s, C_p as the thermal heat deposition of the medium is altered. Furthermore, the inductance $L_{\rm pl}$ is not truly constant, and where the current density profile of the discharge depends on various operating conditions (Blau 1994). Even if extended pulse durations can be established in transient operation, the associated set of operating parameters may well be beyond the stable operating regime of the laser, which ultimately depends on the interplay and balance of the rise-time of the discharge pulse, thermal heat deposition, level of thermal insulation, H_2 content, and other effects such as discussed in chapter 2.

Experiments on the effect of the peaking capacitor on the pulse duration of the laser output were, therefore, conducted as preliminary trials to estimate the overall sensitivity of the gain medium to the discharge speed. For these experiments, the medium-scale LS20-10 (Goldie) was driven by a charge-transfer circuit (figure 3.2), with $C_s = 3.5$ nF and $C_p = 1.75$ nF. No magnetic pulse compression (MPC) was used, as the aim was to produce a relatively slow discharge pulse. For these parameters and operation at total neon buffer gas pressures of $80 - 100$ mbar, the output pulse is similar to those in figure 2.6, showing a pulse duration of $45 - 50$ ns where three roundtrips contribute significantly to the overall

output power. Increasing $C_p = 2.75$ nF, no significant lengthening of the optical pulse was observed for stable operation at buffer gas pressures of 80 – 100 mbar. A transient 8-pass output was only observed temporarily by reducing the buffer gas pressure from 80 – 100 mbar to 30 mbar, but it could not be sustained under these operating conditions. For stable operation at 125 mbar the pulse duration was reduced, exhibiting just 2 & 4 pass outputs giving a total output of 5 W. Significant discharge flicker was observed, possibly due to the rise-times for this relatively large value of C_p. Reducing the peaking capacitor to $C_p = 1$ nF showed no significant changes in the pulse duration, which exhibited 3 roundtrips similar to when $C_p = 1.75$ nF. Further variations of the electrical input power (1.8 – 2.2 kW) and the neon buffer gas pressure (30 – 125 mbar) did not yield the desired effect of pulse stretching. It is therefore concluded that only limited variability of the laser pulse duration can be achieved by changing the peaking capacitor, electrical input power and neon buffer gas pressure. To affect the CVL gain kinetics requires more radical formatting of the discharge pulse, such as can be accomplished using MPC techniques.

III MAGNETIC PULSE COMPRESSION The use of saturable inductors as pulse-forming devices was introduced by Melville (1951), and applied for use of driving CVLs by Nehmadi et al. (1989). In principal, the basic design of magnetic pulse compression (MPC) involves the rapid change of a saturable inductor from a high inductance to a low inductance as the magnetic flux increases. As a result, the energy transfer is more rapid across the MPC stage, proportional to the compression factor which can be defined as the ratio between the rise time on the incoming and outgoing current pulse. The 'black art' of designing such saturable inductors involves careful consideration of the properties of the core material (type of metal, resistivity, saturated magnetic flux density, saturated inductance), and the overall design of the switch (number of conductor turns, stacking factor, bi-wiring to reduce saturated inductance). Thermal issues are particularly important for optimisation of the transfer efficiency, and long-term performance of the magnetic switch.

A typical CVL requires a power supply capable of delivering high voltage (15 – 20 kV), high peak currents (up to 1 kA) with short voltage rise times (< 100 ns) at high pulse repetition rates of tens of kilohertz. The primary advantage of MPC particularly for switching CVLs is to decrease the excitation pulse rise time, and increase the amount of energy supplied to the laser tube (Nehmadi et al. 1989). The MPC acts as a buffer between the thyratron (see figure 3.2) and the laser tube, and thus allows the thyratron to operate at a lower peak current, resulting in smaller losses and extended lifetimes. Extending this principle even further, the use of multistage MPC designs allows the use of all-solid state switching of the power supply where the dI/dt is increased proportional to the compression ratio (Deguchi et al. 1994). Typical compression ratios for two-stage MPC circuits can vary from 4.4 (decrease in rise time from 350 ns to 80 ns) for a 24 kW system (Seki & et al. 1994), to as high as 25 (2.5 μs to 100 ns) for a 17 kW device (Deguchi et al. 1994). In both cases typical efficiencies are in excess of 82 – 88% for a well tuned MPC circuit.

A typical LC-inversion MPC circuit comprises two loops, as schematically depicted in figure 3.9, where for the moment only a single MPC stage (C_1, L_1) will be considered. When the thyratron switches, effectively pulling the DC voltage V_1 existing across C_1 to ground, the charge stored in the bottom C_1 will be inverted due to the flow of the first current loop in the $L_{\text{inv}}.C_1$-circuit. This inversion of charge on the bottom C_1 can be relatively slow, as the saturated inductor L_1 is designed to switch only when all of

the charge of on the bottom C_1 has been inverted. In effect, the switching of the thyratron has changed the two capacitors C_1 from being in parallel with voltage V_1, to being in series with $2 \times V_1$ present across the equivalent capacitance $C_1' = C_1/2$. In comparison with the charge-transfer circuit (figure 3.2), the equivalent storage capacitance $C_s = 2C_1 = 4C_1'$ with constant stored energy $C_1 V_1^2$.

The change of the magnetic flux density $\Delta B\,(t)$ in the saturable switch L_1 is given by (Deguchi et al. 1994)

$$\Delta B\,(t) \simeq \frac{1}{NA} \int_0^t V_{C_1}\,(t')\,dt' \tag{3.1}$$

where N is the number of conductor turns and A is the magnetic cross-section of the saturable inductor. When $\Delta B\,(t)$ crosses the saturated magnetic flux density B_s, L_1 will rapidly change from having a high inductance to a low inductance. By appropriate design of the MPC parameters, the time at which this occurs is made to coincide with the time at which the voltage across C_1' reaches its maximum value $2V_1$ after 1/4 period of the $L_{\text{inv.}}C_1$-circuit. The second current loop in the (first) MPC stage will then start flowing, where now the speed of the voltage- and current-waveforms in the $L_1 C_1'$-circuit is increased approximately by a factor $\sqrt{2L_{\text{inv.}}/L_1}$, and is now no longer limited by the switching speed of the thyratron. The stored energy $C_1 V_1^2$ is now transferred onto the peaking capacitor C_p, and subsequently discharged through the laser head. The use of multi-stage MPC circuits allows further compression of the initial (slow) thyratron switched LC-inversion circuit, to produce even faster voltage-waveforms (Deguchi et al. 1994). From the point of view of efficient excitation of the copper gain medium, the proportional increase in the peak voltage with each MPC stage is beneficial for the overall performance of the laser, as discussed earlier.

IV DOUBLE-PULSE MPC CIRCUIT For the purpose of extending the gain pulse duration, the scheme shown in figure 3.9 is based on the principle of a double-pulse MPC circuit to deliver two discharge pulses to the laser tube with a set delay. Note that now the MPC is not only used as a compression device, but also a timing device where two parallel saturable inductors are designed to switch with a relative delay of order of tens of nanoseconds. In view of generating three to four roundtrips of high-beam quality (non-ASE) output, the underlying idea was to pre-excite the copper gain medium with a fraction of the total available input power to allow the first ASE roundtrip to develop in advance of the main (second) discharge pulse. In this fashion, the full gain duration of the main pulse can be subsequently used to produce the higher order roundtrips, high beam-quality output. The scheme bears some analogy to those reported by Nerheim (1977) and Vetter & Nerheim (1977), although their main objective for pre-excitation was to generate sufficiently high concentrations of copper vapour with a view to establishing efficient lasing from CuCl-halide lasers.

By incorporating a second MPC circuit in parallel (C_2, L_2) as shown in figure 3.9, a second discharge pulse can be delivered through the laser tube with one single switch from the thyratron. The power ratio of the two discharge pulses is roughly determined by the ratio C_1/C_2, while the relative timing is determined by the saturated inductance of L_1 and L_2. Bi-wired toroidal ferromagnetic cores were used throughout, and in practise similar switches were used such that the difference in the saturation induction is primarily determined by the number of conductor turns $N_1 : N_2$ (cf. equation (3.1)). Two settings

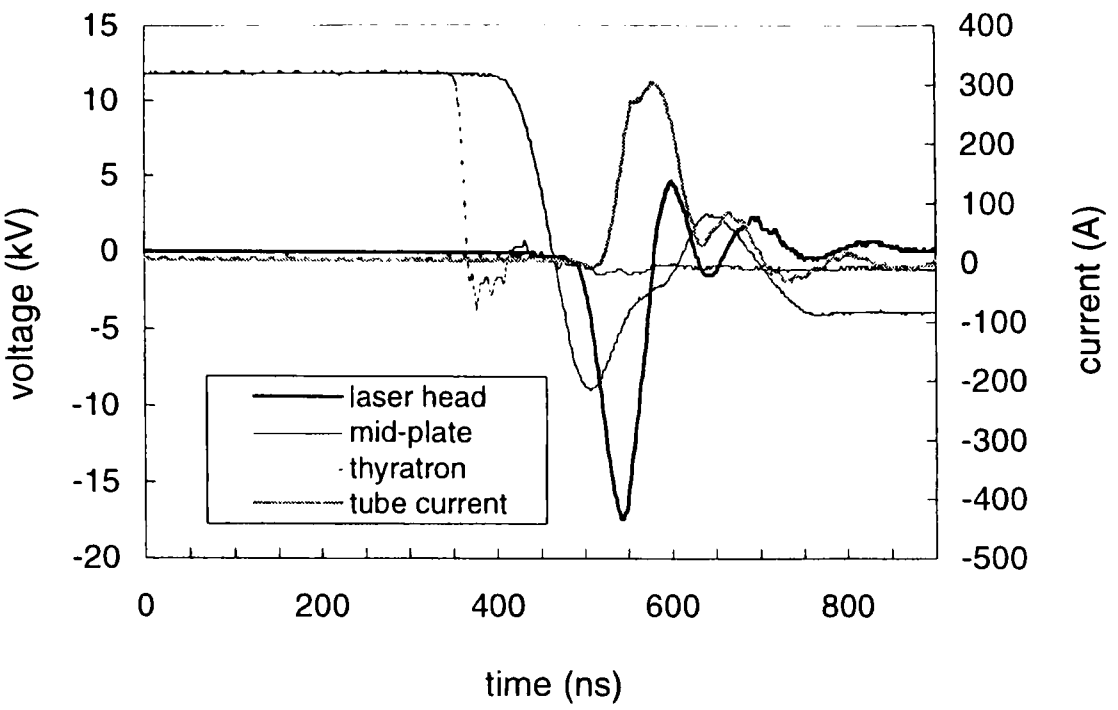


FIGURE 3.10: Standard electrical current and voltage of the LC-inversion exitation circuit.

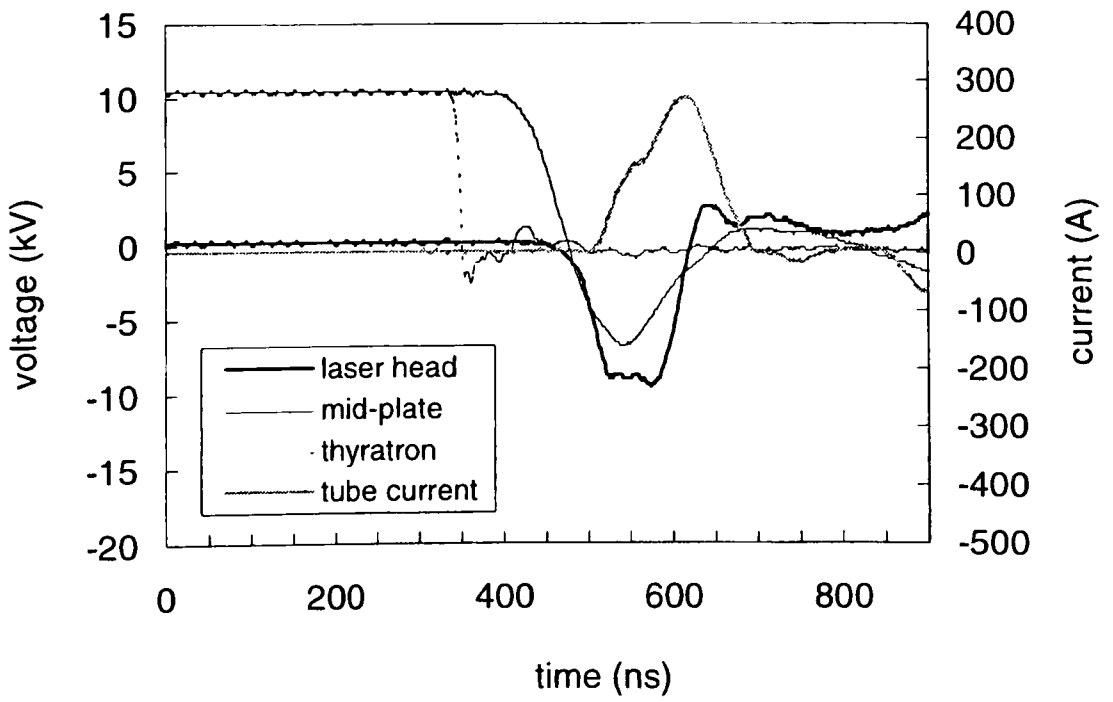


FIGURE 3.11: Electrical current and voltage of the double-MPC exitation circuit.

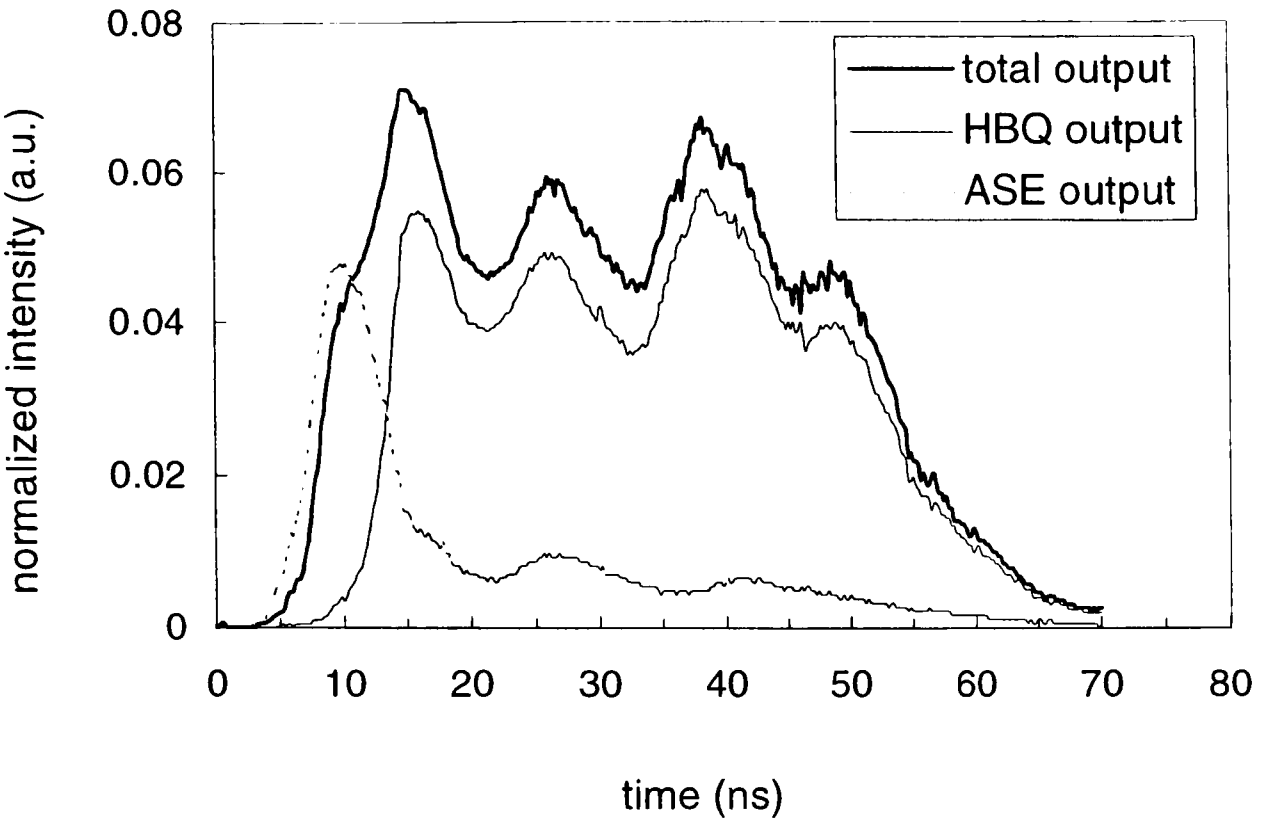


FIGURE 3.12: The optical output obtained with the double-MPC excitation circuit, showing the total, ASE and HBQ components.

low effective reflectivity, resulted in low output powers < 5 W, and extension of highly divergent ASE output for the full pulse duration of 65 ns. Regarding the trade-off between using high M cavities such that the higher order roundtrips are essentially diffraction limited, and obtaining highest useable output power of the oscillator, near-optimum conditions were found for $M = 144$ which delivered 7 W of high beam-quality output power.

To further illustrate the capability of the double-pulse MPC circuit, the voltage waveform of the laser head, and the optical output as obtained for $N_1 : N_2 = 12 : 5$ are shown in figure 3.13 for two different values of the capacitor $C_2 = 0.5$ nF and 0.25 nF. Due to the larger $N_1 : N_2$ ratio, the peak of the two voltage pulses are now separated by 60 ns, and no longer produce a single, extended excitation pulse compared to the result shown in figure 3.11. As expected, the peak voltage for the pre-pulse is largest (7.5 kV) for the larger $C_2 = 0.5$ nF, while for the smaller $C_2 = 0.25$ nF the peak voltage of the pre-pulse is only 5 kV. This difference in the laser head voltage waveform translates in significant difference in the optical output (figure 3.13 **b**), where only for $C_2 = 0.25$ nF significant power output is observed in the second roundtrip, giving 8 W total power of which 5 W high beam-quality output. In comparison, these figures for $C_2 = 0.5$ nF are 6 W, and 4 W respectively. Given the large separation of the two excitation pulses, it is likely that the pre-pulse does not contribute to the formation of optical output at all. As such, the absence of the second roundtrip for $C_2 = 0.5$ nF is tentatively ascribed to the depletion of the ground-state copper density due to the larger pre-pulse. In the case of $C_2 = 0.25$ nF less pre-excitation has occurred prior to the main (second) excitation pulse, and as such a pronounced second roundtrip can still be produced. These observations clearly illustrate that, besides the design of the MPC excitation circuit itself, the dynamics of the copper gain medium are equally important determining the optimal

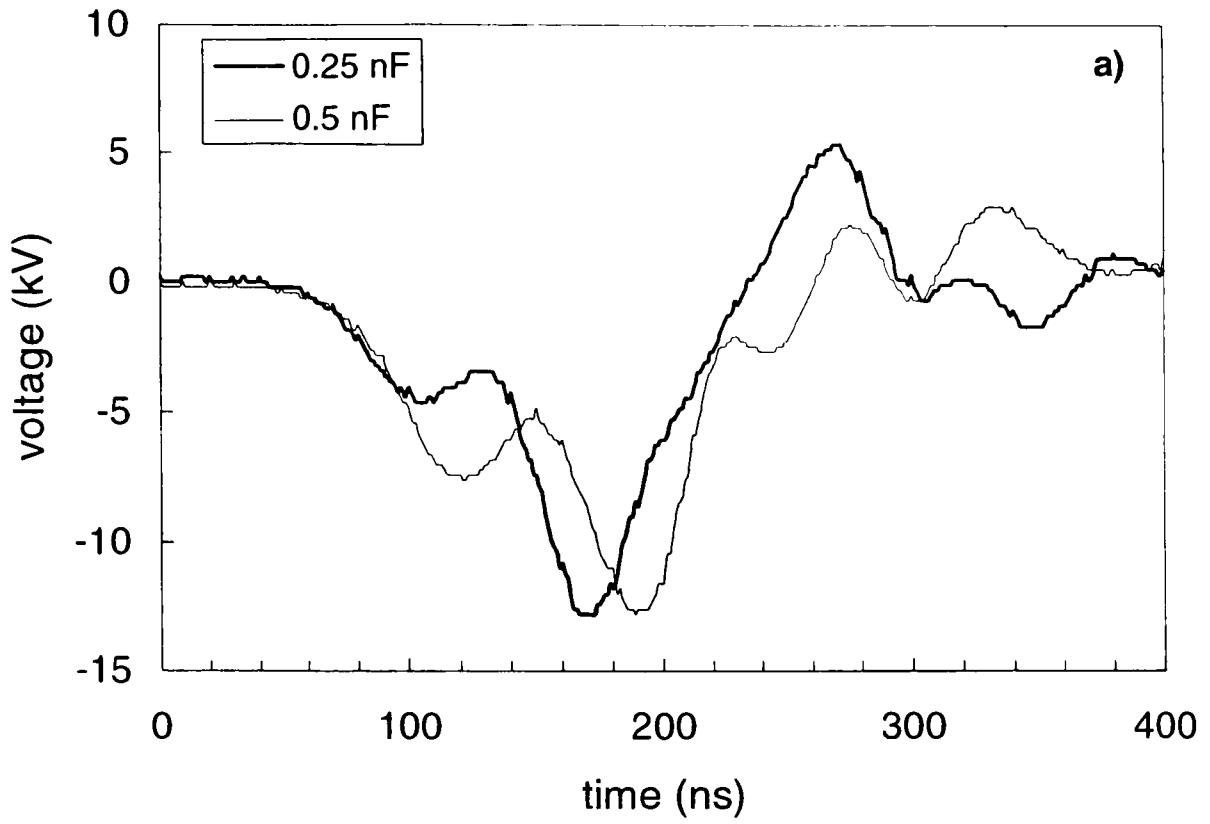


FIGURE 3.13: Laser-head voltage **(a)** and optical output **(b)** of the double-pulse MPC excitation circuit for two different values of the capacitor C_2, with the ratio of conductor turns $L_1 : L_2 = 12 : 5$; capacitor $C_1 = 1.7$ nF; peaking capacitor $C_p = 0.25$ nF

excitation waveform to extend the pulse gain duration.

3.4 Conclusion

In summary, this chapter has detailed the construction and reliable operation of a CVL MOPA system comprising a small-scale (12.5 mm bore diameter, 0.5 m long gain medium) master-oscillator, and a medium-scale (25 mm, 1 m long gain medium) power-amplifier. Seed powers of $1-2$ W from the small oscillator are sufficient to fully saturate the amplifier medium, and $25-30$ W of high beam-quality (approximately three times diffraction limited) output can be generated reliably. Issues regarding the absolute and relative timing of the two lasers which influence the overall stability and long-term operation of the MOPA system have been addressed. The use of a double-pass power-amplifier arrangement has been shown to further stabilise the overall performance of the MOPA system. A fluted tube design has been successfully employed in both the small-scale oscillator, and a medium-scale device.

An important design issue regarding the optimisation of the performance of CVL MOPA systems based on medium-scale devices, has been resolved by demonstration of pulse stretching of a medium-scale oscillator by employing a novel double-pulse MPC excitation scheme. The pulse duration for such a device has been extended by 50%, from 45 ns to 65 ns, whilst maintaining reasonable high beam-quality output power levels of around 7 W with an unstable on-axis resonator $M = 144$. The extended pulse duration allows for efficient seeding of medium- and large-scale power-amplifiers, where the first two roundtrips of high divergent (ASE) output can be discarded. Further tests of such pulse-stretched medium-scale master-oscillators have already been demonstrated the capability for efficient generation of $45-50$ W of high beam-quality output from a CVL MOPA system comprising two similar medium-scale devices.

Chapter 4
Shock-Wave Formation During Pulsed Laser Ablation

In spite of the equations being approximate, they can be beautiful
PAUL DIRAC

The effect of the background gas properties on the formation of shock-waves is characterised by measurement of momentum transfer during laser ablation of solid metal targets using a ballistic pendulum. Experiments are performed for background gas pressures P_1 in the range of $10^{-2} - 10^3$ mbar, using various gases (He, Ne, Ar, Kr, Xe, N_2, CO_2, SF_6) with different molecular weight M_1 and ratio of heat capacities γ. The results allow verification of Sedov-Taylor-von Neumann (STN) shock-wave theory, and assessment of modified STN theories which accounts for the effect of the source mass. A qualitative picture of the complete temporal evolution of the shock-wave will presented within the context of other reports and applications of laser ablation in the fluence regime $1 - 10^3$ J/cm^3 using pulsed nanosecond lasers. The contribution of Graham Quelch regarding the design of the pendulum is gratefully acknowledged.

4.1 Shock-Wave Theory

I Introduction The physical phenomenon of spherical shock-waves generated by a point release of energy has been widely studied in the past to describe the dynamics of nuclear explosions. The evolution of a strong shock in a continuous fluid has been described by Sedov (1993), Taylor (1949) and von Neumann (1944)(henceforth refered to as STN)[1] within the framework of dimensional analysis and self-similar flow. Within this Sedov-Taylor-von Neumann (STN) theory, complete analytical solutions for the (idealised) problem of a strong explosion in a continuous fluid can be derived provided that i) the mass of the energy source is small compared to the mass contained within the shocked volume; ii) the temporal and spatial extent of the energy release is small relative to any other physical dimension of the problem; iii) the mean-free path in background gas which needs to sustain shock wave is small in order to sustain a thin shock-front; iv) the initial static background pressure is negligible with respect to the (peak) overpressure generated in the shock. In practice, the STN theory provides accurate solutions to strong-shock waves with high Mach numbers M, where $M = \dot{R}(t)/c_0$ is defined as the ratio of the

[1] The problem of strong explosions received much interest during the Second World War, during which time the Russian Sedov was the first to derive the full analytical solutions. His American contemporary von Neumann addresed the problem as part of the Manhattan project. However, together with the efforts of the Brit Taylor, the Allied physicist were only able to derive numerical solutions only, later published in the public domain (Neumann & Richtmeyer 1950, Brode 1955, Goldstine & Neumann 1955).

propagation velocity $\dot{R}(t)$ over the sound velocity in the medium c_0, at distances sufficiently far away from the origin for the point-source approximation to be valid.

Recently, STN theory has received renewed attention to describe laser generated shock-waves observed in many applications involving laser ablation of solid targets, including inertial confinement fusion (Lindl 1995), mitigation of space-debris (Phipps & Reilly 1996, ?), pulsed laser deposition (Gupta et al. 1991, Geohegan 1994), and laser materials processing (Dyer & Sidhu 1988). However, the aforementioned approximations do not generally hold in the case of laser generated shock-waves, and deviations from the STN theory have long since been observed (Bobin et al. 1968). Particularly, departures from STN theory have been observed during the initial stages of the evolution of the shock-waves (Dyer & Sidhu 1988, Gupta et al. 1991, Geohegan 1992), where the mass of the 'piston' formed by the ejected ablated material can not be neglected. As such, the piston which drives the shock-wave initially undergoes a free-flow expansion. Furthermore, it is not evident *ab initio* whether the assumption of an instantaneous point-release of energy is valid at all, since the absolute dimensions of laser generated shock-waves are orders of magnitude smaller than those of 'macroscopic' explosions. To address this issue, the focal spotsize and the laser pulse duration need to be compared with the characteristic length and time-scales of the shock-wave evolution. Also, for laser ablation in rarefied atmospheres, for example in the field of pulsed laser deposition (Geohegan 1994) at typical background pressures of order $10^{-6} - 10^{-4}$ mbar, the mean free path of the background gas becomes of the order of the typical length scale of the shock-wave. In this case the fluid flow can no longer be described in terms of (macroscopic) continuum fluid dynamics, but requires (in principle) full solutions of the Boltzmann equation to account for the microscopic features of rarefied gasdynamics. Formation of Knudsen layers (Rothenberg & Kelly 1984, Kelly & Rothenberg 1985, Kelly & Dreyfus 1988) at the target surface complicate the flow significantly, often requiring numerical analysis to derive the flow characteristics (Garrelie et al. 1998).

The main aim of the work presented in this chapter is to address a number of these issues regarding the formation of shock-waves during laser ablation within a wider context of other reports (Dyer & Sidhu 1988, Gupta et al. 1991, Gilgenbach & Ventzek 1991, Geohegan 1992, Ho et al. 1995, Callies et al. 1996, Aden et al. 1997, Jeong et al. 1998). A description of the evolution of laser generated shock-waves as presented by Leonard & Hammerling (1980) will provide a useful framework for assessing these issues. In this picture, the laser generated shock-wave is taken to evolve through three regimes, schematically depicted in figure 4.1. First, during the initial phases of material removal the ablated target material is envisaged to flow freely as one solid 'piston' into the background gas. During this free-flow 'vacuum' phase, the piston propagates relatively unhindered, engulfing more of the background gas which is swept at the contact-front. At the point where the mass of the piston has become negligible compared to the mass engulfed by the contact-front a (strong) shock-wave develops at the shock-front. The shock-front detaches from the contact-front (Cheng & Kirsch 1969), propagating at velocities following STN theory. In the region between the shock- and contact-surface, the thermodynamic properties of the adiabatically shocked background gas (reduced pressure and density, and increase pressure) are described by STN theory. In the final third phase, the shock decays into an acoustic wave (Sedov 1993, Dyer et al. 1990) at the characteristic radius $R_0 \propto (E_0/P_1)^{1/3}$, where E_0 is the (effective) laser pulse energy and P_1 the initial background gas pressure.

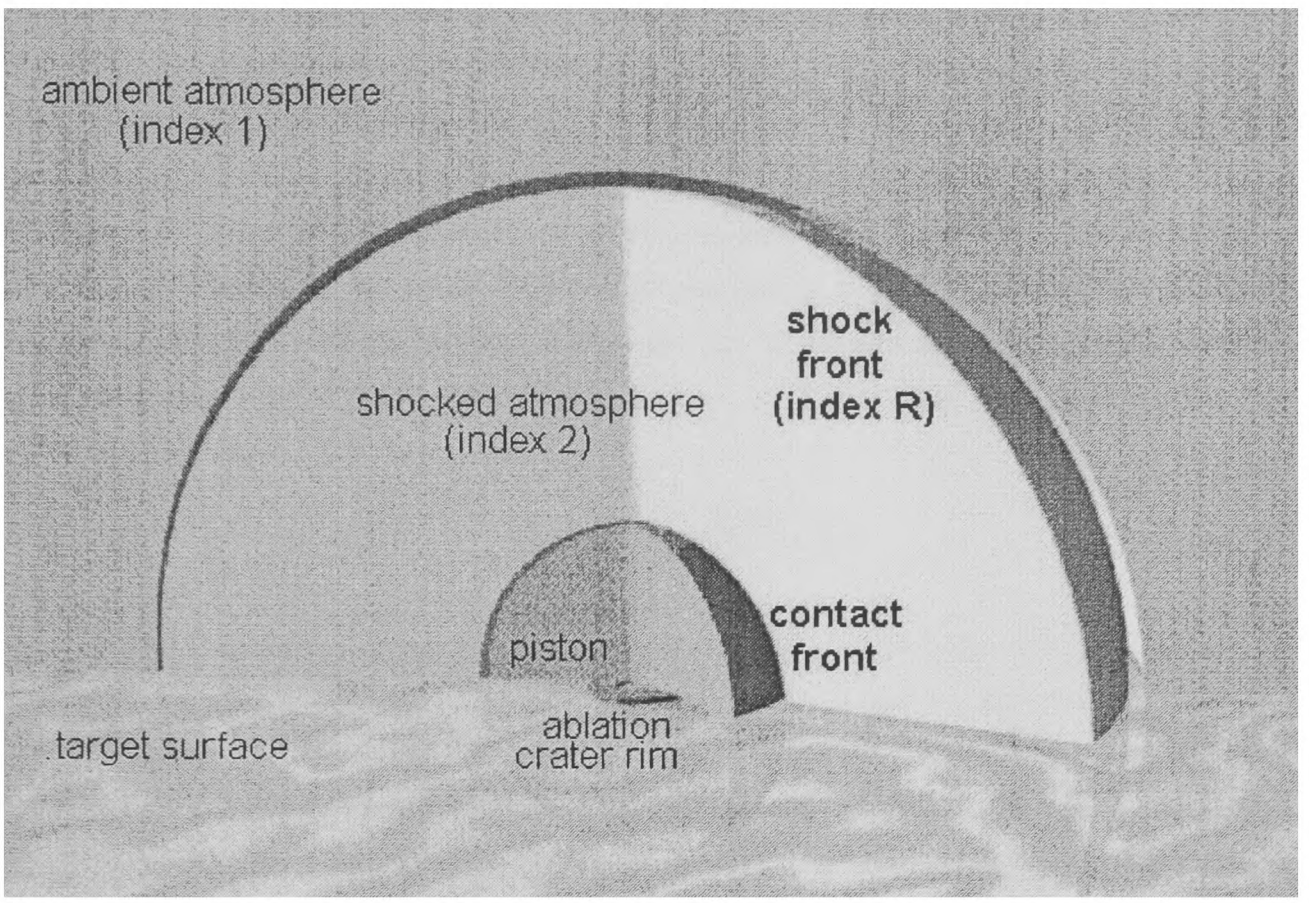


FIGURE 4.1: Schematic depiction of a spherical shock-wave generated during pulsed laser ablation.

It will be shown that by using a ballistic pendulum to measure the momentum transfer during the ablation process, a constant 'vacuum' contribution can associated with the recoil generated during the free-flow phase, and a gas dependent term which exhibit distinct scaling laws with respect to the properties of the background gas. In the ballistic pendulum experiments, therefore, two main features of the shock-wave will be studied. First, the transition from the free-flow regime to the formation of a strong STN shock will be investigated. This allows assessment of the validity of modified STN (mSTN) theories which have most recently been reformulated specifically for laser generated shock-waves (Freiwald & Axford 1975, Freiwald 1972, Hutchens 1995) to account for the source-mass effect. Secondly, the recoil imparted by the strong shock is measured as a function of the laser pulse energy E_0, and the molecular weight M_1 and ratio of heat capacities γ, to verify the scaling laws predicted by STN theory. Limitations of the (m)STN theory are also discussed. The findings of these studies provide insight into the kinetics and gross structure of shock-wave formation of interest, for example, in the development of laser ablation microprobes for stable geochemical isotope analysis (chapter 5).

In this section first an overview of STN theory will be given, followed by an introduction of the modified STN theory. Subsequently, an overview of the temporal history of laser generated shock-waves will be given to provide a useful frame of reference. A small excursion will be made to describe the background of so-called laser supported detonation waves, a different class of laser generated shock-waves, which is relevant to discussing the present work in the light of other reports. Finally, this section is concluded with the calculation of the recoil pressure integral which describes the principle of the ballistic pendulum measurements.

II SEDOV-TAYLOR-VON NEUMANN THEORY Consider a point-release of energy E_0 on the surface of a infinite half-plane solid target in an ambient atmosphere with initial pressure P_1, density ρ_1 and ratio of heat capacities γ, where index 1 denotes the physical quantities in the ambient (still) atmosphere. In this idealised arrangement the gas flow is determined by only two dimensional parameters, namely E_0 and ρ_1, since in the strong shock approximation ($M \gg 1$) the initial background pressure is negligible compared to the peak shock-pressures at the shock-front. By employing dimensional analysis (Sedov 1993) self-similar solutions can be derived which describe the motion of the shock-wave to within a constant factor. The dimensionless parameter λ is introduced as

$$\lambda = \frac{r}{\left(E_0/\rho_1\right)^{1/(\nu+2)} t^{2/(\nu+2)}} \tag{4.1}$$

where $\nu = 1, 2, 3$ denotes the three one-dimensional geometric symmetries to be considered, respectively planar, cylindrical and spherical, and r, t denote one-dimensional space and time respectively. Since λ is dimensionless it can only depend on the dimensionless parameters of the problem γ and ν, and thus (4.1) fixes the fluid trajectory r, t to within a dimensionless, constant factor. The functional form of position and velocity of the shock-front, denoted by $R(t)$ and $\dot{R}(t)$ respectively, can then be derived (Sedov 1993)

$$\begin{aligned} R(t) &= \xi(\gamma,\nu)\left(\frac{E_0}{\rho_1}\right)^{1/(\nu+2)} t^{2/(\nu+2)} \\ \dot{R}(t) &= \tfrac{2}{\nu+2}\xi(\gamma,\nu)\left(\frac{E_0}{\rho_1}\right)^{1/(\nu+2)} t^{-\nu/(\nu+2)} \\ &= \tfrac{2}{\nu+2}\xi(\gamma,\nu)^{(\nu+2)/2}\left(\frac{E_0}{\rho_1}\right)^{1/2} R^{-\nu/2} \end{aligned} \tag{4.2}$$

where $\xi(\gamma,\nu)$ is a constant factor dependent only on the dimensionless parameters γ and ν, the functional form of which can be obtained by solving the full equations of motion.

Note that the concept of self-similarity applies to two distinctly different types of problems (Zel'dovich & Raizer 1966, chapter XII). In the first type, like the problem of a strong point-explosion considered, the parameters of the problem allow definition of a self-similarity variable like in (4.1), in which case power laws are determined from dimensional analysis or conservation laws. The main advantage of this approach is that solutions for the fluid motion can be determined to within a constant factor without actually solving the full set of equations of motion. More generally, however, self-similar solutions may exist but can not constructed in this fashion, constituting a second class of self-similar problems where solutions can only be obtained by solving the full equations of motion. In this case, the self-similar motion finds its origin in the asymptotic limit of an initially non-self-similar flow. The usefulness of self-similarity lies in this powerful concept that many physical processes always tend to a characteristic self-similar limit. For example, classical diffusion phenomena often approach a Gaussian distribution. This concept will be useful in the discussion of the temporal history of the shock-wave.

Returning to the problem of a strong explosion, the velocity, density and pressure at the shock-front is now derived by applying the continuity equations across the shock-front relating the velocity, density

and pressure distribution of the still air (index 1) v_1, ρ_1, P_1 respectively, to the value in the shocked atmosphere immediately behind the shock (index R) v_R, ρ_R, P_R. Within the strong-shock approximation of STN theory, the velocity of sound in the still air v_0 is taken to be much smaller than the (supersonic) propagation velocity of the shock-front $\dot{R}$, i.e. the shock-front propagates with high Mach number M. This approximation is equivalent to the assumption made earlier where the initial background gas pressure P_1 was neglected relative to the (peak) shock-pressures ($P_1 \ll P_R$). In this limit, the continuity equations are simplified to give (Sedov 1993)

$$\begin{aligned} v_R &= \frac{2}{\gamma+1}\dot{R}, \\ \rho_R &= \frac{\gamma+1}{\gamma-1}\rho_1, \\ P_R &= \frac{2}{\gamma+1}\rho_1\dot{R}^2. \end{aligned} \tag{4.3}$$

By expanding the v_R, ρ_R, P_R in powers of $v_0/\dot{R}$, Sedov (1993) has shown that these approximate shock conditions are accurate to within 5% for $v_0/\dot{R} < 0.1$, or $M > 10$. Note that the *particle* velocity of the fluid at the shock-front v_R should not be confused with the propagation velocity of the shock-front $\dot{R}$.

Thus, inserting the self-similar solutions of $R(t)$ into the jump conditions the full fluid motion of the shock-wave is determined by the solutions

$$\begin{aligned} v_R(t) &= \frac{4\xi(\gamma,\nu)}{(\nu+2)(\gamma+1)}\left(\frac{E_0}{\rho_1}\right)^{1/(\nu+2)} t^{-\nu/(\nu+2)} \\ &= \frac{4\xi(\gamma,\nu)^{(\nu+2)/2}}{(\nu+2)(\gamma+1)}\left(\frac{E_0}{\rho_1}\right)^{1/2} R^{-\nu/2} \\ \rho_R(t) &= \frac{\gamma+1}{\gamma-1}\rho_1 \\ P_R(t) &= \frac{8\xi(\gamma,\nu)^2}{(\nu+2)^2(\gamma+1)}\rho_1\left(\frac{E_0}{\rho_1}\right)^{2/(\nu+2)} t^{-2\nu/(\nu+2)} \\ &= \frac{8\xi(\gamma,\nu)^{\nu+2}}{(\nu+2)^2(\gamma+1)}E_0 R^{-\nu} \end{aligned} \tag{4.4}$$

together with the equation of state for an ideal gas

$$T_2 = \frac{M_1 P_2}{\rho_2 k_B} \tag{4.5}$$

In the final step towards full solutions of the problem of a strong point explosion, the equations of motions are re-written in terms of the dimensionless parameter λ. The full velocity, density and pressure and distributions behind the shock-front (denoted by index 2), denoted respectively $v_{2,}\rho_2$ and P_2, are factorised in a spatial and temporal part

$$r_2 = \lambda R(t) \tag{4.6}$$

$$\begin{aligned} v_2 &= f(\lambda)\, v_R(t) \\ \rho_2 &= g(\lambda)\, \rho_R(t) \\ P_2 &= h(\lambda)\, P_R(t) \end{aligned}$$

For a fixed instant, the spatial distribution is determined by the dimensionless functions $f(\lambda), g(\lambda)$ and $h(\lambda)$ in terms of λ. From equation (4.1) and (4.2), λ can be identified as the spatial coordinate normalised with respect to the shock-front position R, i.e. $\lambda \in [0,1]$. The temporal evolution is determined by the particle velocity, density and pressure *at the shock-front*, denoted v_R, ρ_R and P_R. Note that for a fixed instant t' the parameter λ is just the spatial coordinate normalised with respect to R, as can be verified from equation (4.1) amd (4.2). The fact that the motion of the fluid can be factorised in this fashion forms a key element of the theory of self-similar motion.

The functional forms of the dimensionless functions $f(\lambda), g(\lambda)$ and $h(\lambda)$ can be obtained by integration of the equations of motion, and although terse, the derivation is straightforward. Numerical solutions are presented by (Sedov 1993) and analytical solutions can be found in e.g. Landau & Lifshitz (1987) or Ryu & Vishniac (1987). For the present work, the explicit analytical forms of $f(\lambda), g(\lambda)$ and $h(\lambda)$ in spherical geometry will be used, which are given below following the notation of Ryu & Vishniac (1987)

$$f(\lambda) = \lambda V, \tag{4.7}$$

$$g(\lambda) = \lambda^{-5\eta_3/\eta_2} V^{-2\eta_3/\eta_s} \left[\frac{5(\gamma+1)-2(3\gamma-1)V}{7-\gamma}\right]^{-\eta_1\eta_3/\eta_2+\eta_4} \left(\frac{\gamma+1-2V}{\gamma-1}\right)^{\eta_5}, \tag{4.8}$$

$$h(\lambda) = V^{-2\eta_3/\eta_2+2/\eta_2+2} \left[\frac{5(\gamma+1)-2(3\gamma-1)V}{7-\gamma}\right]^{-\eta_1\eta_3/\eta_2+\eta_4+\eta_1/\eta_2} \left(\frac{\gamma+1-2V}{\gamma-1}\right)^{\eta_5+1}, \tag{4.9}$$

where

$$V^2 \left[\frac{5(\gamma+1)-2(3\gamma-1)V}{7-\gamma}\right]^{\eta_1} \left(\frac{2\gamma V-\gamma-1}{\gamma-1}\right)^{\eta_2} = \lambda^{-5}, \tag{4.10}$$

with

$$\begin{aligned} \eta_1 &= \frac{13\gamma^2-7\gamma+12}{(3\gamma-1)(2\gamma+1)}, \\ \eta_2 &= -5\frac{\gamma-1}{2\gamma+1}, \\ \eta_3 &= \frac{3}{2\gamma+1}, \\ \eta_4 &= \frac{13\gamma^2-7\gamma+12}{(2\gamma-1)(3\gamma-1)(2\gamma+1)}, \\ \eta_5 &= -\frac{2}{2-\gamma}. \end{aligned} \tag{4.11}$$

The equations $(4.7-4.11)$ provide the full analytical solutions to the problem of a strong explosion, and can be numerically evaluated to, for example, calculate the functional form of $\xi(\gamma,\nu)$ (section 4.1.VI).

III MODIFIED STN THEORY Beyond the framework of STN theory, an extended theory has been proposed. In what shall be referred to as the modified STN (mSTN) theory, the structure of a strong blast wave is described to originate from an expanding inner contact surface, also more generally referred to the piston problem (Slemrod 1996). Most recently the mSTN theory has been reformulated by Freiwald (1972), Freiwald & Axford (1975) and Hutchens (1995) specifically for laser generated shock-waves for respectively planar, spherical and cylindrical geometry, but its origin dates back from earlier theoretical work in the field of fluid mechanics (Cheng & Kirsch 1969, and references therein). Following Freiwald (1972), the main feature of mSTN theory is to consider the redistribution of the initial pulse energy E_0 over the source mass energy (index s) and the ambient gas (index g) as a function of time

$$E_0 = E_s(t) + E_g(t). \tag{4.12}$$

Both terms of equation (4.12) contain a kinetic energy term $\frac{1}{2}\rho v^2$ and an internal energy term ρu, which upon integration over the total volume should be conserved

$$E_0 = \int dV \left[\left(\tfrac{1}{2}v_s^2 + u_s\right)\rho_s + \left(\tfrac{1}{2}v_g^2 + u_g\right)\rho_g\right], \tag{4.13}$$

Here the limits of the integral are determined by appropriate estimates of the physical extent of the piston source-mass (the contact-front) and the shock-wave (the shock-front). For one dimensional planar, cylindrical or spherical geometry ($\nu = 1, 2, 3$) the energy integral can be cast into the form (Freiwald 1972)

$$E_0 = \left[C_1 + C_2 R^\nu\right]\dot{R}^2 \tag{4.14}$$

The two terms in the square brackets in equation (4.14) have the dimension of mass, and are respectively associated with the kinetic energy contained of the piston-mass (proportional to the mass density of the solid target ρ_s), and the kinetic energy of engulfed background gas with mass $C_2 R^\nu$ (proportional to the mass density of the background gas ρ_1). The value for C_1, C_2 are listed in table IV for the different geometries. The dimension R_s defines an effective volume containing the piston mass $M_s \simeq \rho_s R_s^\nu$. Rewriting (4.14) an expression for the shock-front velocity $\dot{R}$ can be obtained

$$\dot{R} = \sqrt{\frac{E_0}{C_1 + C_2 R^\nu}} \tag{4.15}$$

and subsequently the pressure at the shock-front P_R (and density ρ_R) can be obtained from the continuity shock conditions (4.3). To solve the dynamics of the problem (4.15) is re-arranged by separating variables and substituting $\dot{R} = dR/dt$ to give

$$\sqrt{E_0}\,t = \int_0^R dx\,\sqrt{C_1 + C_2 x^\nu} \tag{4.16}$$

	$\nu = 1$	$\nu = 2$	$\nu = 3$
C_1	$\frac{\rho_s A L}{2(\gamma+1)^2}$	$\frac{2\pi\rho_s R_s^2}{(\gamma+1)^2}$	$\frac{8\pi\rho_s R_s^3}{3(\gamma+1)^2}$
C_2	$\frac{(5\gamma-3)\rho_1 A}{(\gamma^2-1)(\gamma+1)}$	$\frac{2\pi(3\gamma-1)\rho_1}{(\gamma^2-1)(\gamma+1)}$	$\frac{8\pi}{3}\frac{(3\gamma-1)\rho_1}{(\gamma^2-1)(\gamma+1)}$

TABLE IV: Constants in the modified STN theory. Note that in the planar case A is the area (of the shock tube) and L is the initial thickness of the detonation charge

which can be solved numerically to obtain the functional form of $R(t)$.

Considering the denominator of (4.15) the mSTN theory indeed provides a physical description of two distinct regimes. In the case $C_1 \gg C_2 R^\nu$, the piston-mass is much larger than the mass of the shocked background gas. Therefore, the piston propagates at (near) constant velocities $\dot{R}$, and most of the energy E_0 is predominantly contained in the kinetic energy of the piston-mass. For sufficiently large R the limit $C_2 R^\nu \gg C_1$ applies, where now the mass of the shocked background gas is much larger than the piston-mass, and most of the energy has been transferred to the kinetic energy of the shocked gas. In this limit the STN result $\dot{R} \propto R^{-\nu/2}$ is reproduced conform (4.4). Thus, the transition radius R^* defined as

$$R^* = \left(\frac{C_1}{C_2}\right)^{1/\nu} \tag{4.17}$$

marks the transition from free-flow to the formation of a strong STN shock, with an associated time $t^* \propto R^*/c_0$. Note that the source mass radius R_s only enters the equations to represent the total source mass $M_s \propto \rho_s R_s^\nu$, and that in practise M_s may be determined without specific knowledge about the value of R_s. The validity of the mSTN theory will be further discussed in section 4.3.

IV TEMPORAL HISTORY OF LASER GENERATED SHOCK-WAVES Having outlined the essential elements of shock-wave theory, now consider the evolution of laser generated shock-waves (Leonard & Hammerling 1980) in terms of the temporal history of the shock-front position $R(t)$, the shock-front velocity $\dot{R}(t)$ and pressure $P_R(t)$, which is shown in figure 4.2 for the present experimental arrangement. To allow scaling to any particular experiment, the physical quantities will be described in dimensionless parameters by normalisation with respect to R_0, t_0, c_0 and P_1. The underlying principle for such a parameterisation lies in the fact that any adiabatic disturbance propagating in a continuous fluid ultimately decays at a given characteristic time- and length-scale. In the case of strong shocks, the approximation that the background gas pressure is negligible compared to the shock pressure, $P_R \gg P_1$ becomes increasingly less accurate at later stages of the evolution. For Mach numbers $M \leq 3$, the strong shock approximation is no longer valid resulting in significant departures from Sedov's analytical solutions (4.4) and requiring a more laborious mathematical treatment (Bach & Lee 1970). Ultimately, the shock decays into an acoustic wave for larger times and distance (Sedov 1993). The characteristic dimensions at which the acoustic transition occurs can be roughly identified to occur at R_0

$$R_0 = \left(\frac{E_0}{P_1}\right)^{1/\nu} \tag{4.18}$$

which can be argued intuitively by considering that the volumetric adiabatic expansion should follow R^ν.

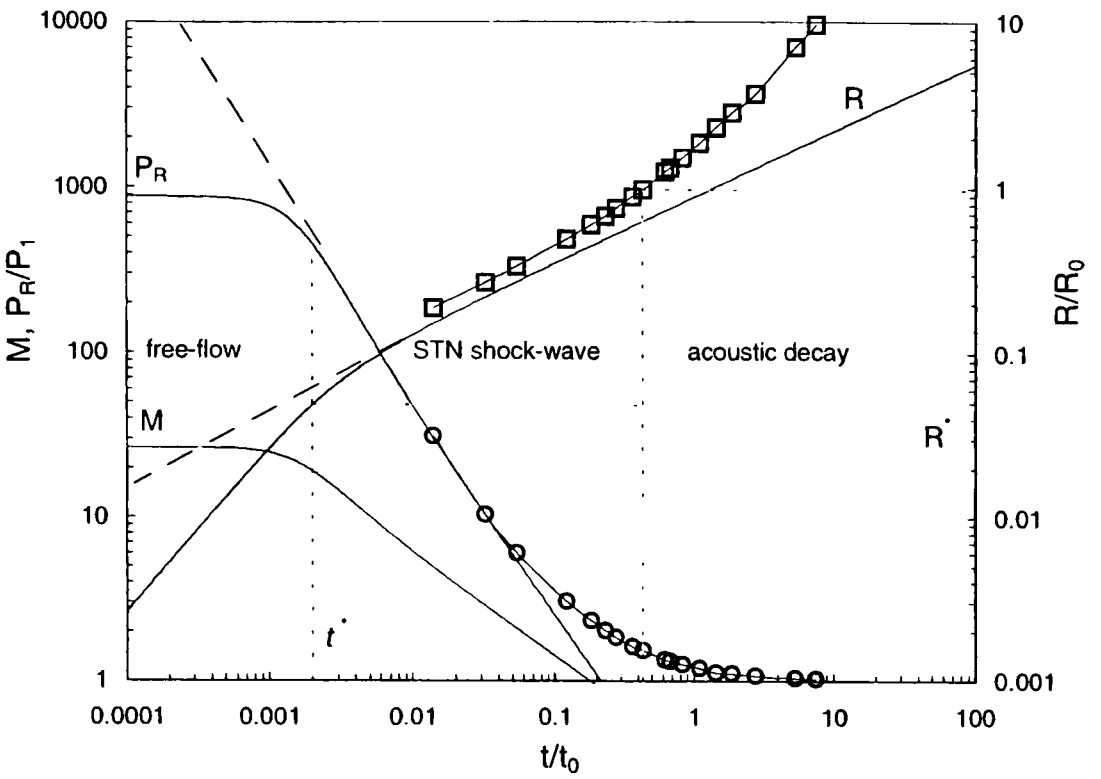


FIGURE 4.2: The temporal history of a spherical shock-wave, showing the normalised shock-front pressure P_R/P_1, Mach number M and normalised shock-fron radium R/R_0 as a function of normalised time t/t_0. Parameters for the source are from experiment with $E_0 = 3.5$ mJ, $R_s \simeq 25$ μm for an aluminium target. The pressure (o) and the shock-front position (□) in the acoustic phase are reproduced from Sedov 1993, page 308.

The corresponding time t_0 can be obtained from (4.4), and is of order $t_0 \simeq R_0/c_0$. Thus, normalised parameters are defined as $R/R_0, t/t_0, P_R/P_1$ and $M = \dot{R}/c_0$. Intuitively, the onset of the acoustic decay phase is obtained in the limit where the dimensionless parameters for the shock-front radius, velocity and pressure approach unity, shown in figure 4.2 for the pressure (o) and the shock-front position (□) reproduced from Sedov (1993).

The evolution of a spherical shock-wave, shown in figure 4.2 by the solid curves, was calculated using mSTN theory. Anticipating the pendulum experiments, the calculations are performed for an aluminium target in an argon atmosphere with $E_0 = 3.5$ mJ, $R_s = 25$ μm. Reading the graph from left to right, it is shown that during the free-flow phase the shock-front pressure and velocity are constant, as indeed obtained from considering free expansion into vacuum (Keller 1948, Greenspan & Butler 1962, Molmud 1960). During this free-flow vacuum phase the maximum pressure at the shock front $P_R/P_1 \simeq 10^3$ with corresponding $M \simeq 30$ for this particular configuration. At the transition R^*, t^* the evolution approaches the STN self-similar limit yielding the characteristic $R \propto t^{2/5}$ law. From equation (4.3) $P_R \propto \dot{R}^2$, which is illustrated in figure 4.2 by the slope of $P_R\,(t)$ being twice the slope of $M\,(t)$. Finally, in the third phase the shock-wave decays into an acoustic wave as described earlier.

Returning to the concept of self-similarity it should be pointed out that, in order to decrease the transition point (R^*, t^*), the strength of the shock (signified by M) should be increased. In practise, this involves increasing the ratio between the pulse energy and source-mass since from equation (4.15) follows that the maximum value for $M \propto \sqrt{E_0/M_s}$. This illustrates the principle of similarity mentioned earlier: the motion during the free-flow phase is not self-similar, but at later times it will asymptotically

approach the self-similar limit. Decreasing t^* effectively means that the point-source approximation is more accurate, when for example the pulse energy E_0 is increased for the same source mass M_s. In short, ablation of a large piston mass results in low M numbers, thus making the corrections described by mSTN more significant. This point is further studied in the experiments described in chapter 7, where the recoil momentum is measured in vacuum for different metal targets.

V LASER SUPPORTED DETONATION WAVES Before turning to the application of the (modified) STN theory as outlined above to describe the ballistic pendulum experiments, first a small digression is made to introduce the concept of detonation waves as this will prove relevant to the present experiments. The physical nature of a detonation wave relies on the presence of a propagating combustion process which drives the shock-wave. In comparison, the STN theory describes the formation of a shock-wave originating from a driving piston (thus often referred to as the piston problem, or blast-wave). In a combustion process, the driving energy source consists of a particular (chemical) exothermic reaction which is propagated as the burning gas heats the surrounding (combustible) medium. For ordinary slow combustion processes, the propagation is dominated by heat diffusion. Another possible mechanism for ignition involves propagation of shock-waves into the medium, which upon passing ignites the combustion, thus propagating the combustion at the shock velocity which is much faster than ordinary combustion. This process is referred to as detonation.

In the case of shock-wave formation during laser ablation, laser supported detonation (LSD) has been observed by Pirri et al. (1972) and later the subject of various reports (Pirri 1973, Nielsen 1975, Shui et al. 1978). These reports involve laser ablation with CO_2 lasers, where significant plasma coupling is present due to inverse Brehmsstrahlung absorption at the long 10.6 μm wavelength. In LSD, the 'combustion' process is supported by the laser beam, resulting in an observed cylindrical plume which propagates downstream along the beam-path. In comparison, STN-like shock-waves are always observed to be perpendicular to the target surface. Inherent to the nature of the detonation process, the propagation of LSD waves can not be expressed in terms of self-similar motion as it depends on the geometry of the set-up. Note that, strictly speaking, LSD is not a true combustion process since the observed heating and ionisation of the background gas is an endothermic process.

Despite the physical difference between LSD waves and STN shock-waves, Pirri (1973) has shown that the kinetic characteristics of are nearly identical, obeying similar scaling-laws in terms of the laser pulse energy E_0, and the background gas properties. Regarding shock-wave formation during laser ablation, some debate remains as to which of the two mechanisms is the most dominant (Callies et al. 1996, Chang & Warner 1996, Banishev et al. 1996, Turcu et al. 1997), depending on, for example, the pressure and type of background gas, the incident optical power density and the laser wavelength. In this context, various studies relating to the plasma coupling efficiency are relevant. For example, Buscher et al. (1965) have measured the threshold for optical breakdown for pulsed lasers at various wavelengths for various gases. The observations made by Buscher et al. (1965) showed that for visible lasers plasma coupling is least efficient for a given optical power density, since in the infrared inverse Brehmsstrahlung becomes significant, while towards the UV the highly energetic photons can cause ionisation. Only for intensities in excess of 10^{12} W/cm^2 does multiphoton ionisation become significant in the visible (Agostini et al. 1970). More detailed investigations have shown that optical breakdown depends on the background gas pressure

(Alcock et al. 1972, Turcu et al. 1997, Banishev et al. 1996), and a non-trivial interplay of laser pulse energy and pulse duration (Weyl et al. 1982, Weyl & Rosen 1985). A more general correlation relating the laser-induced breakdown thresholds has also based on the number density and refractive index has been presented by Bettis (1992).

Another relevant mechanism in this context is laser induced thermionic emission, which has long since been observed for metal targets (Lichtman & Ready 1963, Honig & Woolston 1963, Honig 1963, Giori et al. 1963, Cobb & Murray 1965). In this process, the heated target material emits electrons (and/or ions for sufficiently high temperatures) in an evaporative process obeying the so-called Richardson equation which contains an exponential Arrhenius-like rate constant related to the free work function and the temperature of the substrate. Thermionic emission has been observed to reduce the breakdown threshold of the background gas (Kumar & Thareja 1992*a*), even in the absence of significant ablative material removal, thus facilitating plasma coupling due to the presence of free electrons (Borets-Pervak & Vorob'ev 1991). Interestingly, this has been studied for application to plasma switches (Kumar & Thareja 1992*b*). These, and other plasma spectroscopic processes will also be discussed in more detail in chapter 6.

VI THE RECOIL PRESSURE INTEGRAL Following on from the review of shock-wave theory, the relevant results are now applied to derive expressions for the integrated recoil impulse as measured by the ballistic pendulum. To this purpose, an analytical expression is derived for the shock-wave recoil as a function of the background gas properties, and the laser pulse energy. Subsequently, numerical calculations will be presented to clarify the pendulum experiments.

The underlying physical interpretation assumes that the motion of the pendulum is due to the pressure differential across the front and back-face of the pendulum, integrated over time and area, i.e. the recoil pressure integral given by

$$p_{tot} = \int dA \int dt \, [P_2(r,t) - P_1] \tag{4.19}$$

where $P_2(r,t)$ is the pressure at the target surface due to the blast-wave. From self-similar theory the pressure distribution in the shocked atmosphere can be factorised

$$P_2(\lambda,t) = h(\lambda) \, P_R(t) \tag{4.20}$$

in terms of the dimensionless parameter $\lambda \equiv r/R$. Thus, the double integral over P_2 can be separated and yields explicitly for spherical geometry

$$\begin{aligned} \int dA \int dt \, P_2(r,t) &= \int_0^1 d\lambda \, 2\pi\lambda \, h(\lambda) \cdot \int_0^{t_0} dt \, P_R(t) \, R^2(t) \\ &\equiv b(\gamma) \int dt \, P_R(t) \, R^2(t) \end{aligned} \tag{4.21}$$

where the spatial integral is identified as a constant form-factor $b(\gamma)$ dependent only on γ. The second

model	$\xi(\gamma,3)$	ref.
STN	$\left[\frac{75}{16\pi}\frac{(\gamma-1)(\gamma+1)^2}{(3\gamma-1)}\right]^{1/5}$ (Chernyi solution)	(Zel'dovich & Raizer 1966)
mSTN	$\left(\frac{5}{2}\right)^{2/5}\left(\frac{3}{4\pi}\right)^{1/5}\left(\frac{\gamma+1}{2}\right)^{2/5}$	(Freiwald & Axford 1975)
LSD	$6\left(\frac{\gamma+1}{2\gamma}\right)^{3\gamma/(\gamma-1)}\frac{(\gamma^2-1)}{(\gamma+1)^{3/2}}$	(Pirri 1973)

TABLE V: The gamma-factor as derived in various reports. The Chernyi solution given for STN theory will be used in the present work. In the case of the laser supported detonation theory as presented by Pirri, the listed factor is the constant relating the recoil impulse to the pulse energy

term on the right-hand side of (4.21) simply yields $\pi P_1 \int dt\, R^2(t)$, resulting in

$$p_{tot} = \int dt\, \left[b(\gamma)\, P_R(t) - \pi P_1\right] R^2(t) \tag{4.22}$$

In order to derive the functional dependency of the recoil integral on the parameters E_0, γ, ρ_1 and P_1, equation (4.22) is evaluated analytically using the solutions (4.4) describing the shock-wave motion. Choice of the upper limit for the temporal integral $t_{\max}$ is taken to be when $P_R = P_1$, since for larger times the solutions (4.4) are no longer valid as $P_R < P_1$. This interpretation is identical to the physical picture that beyond the acoustic transition point R_0, t_0 the recoil pressure does not have a significant contribution to the integrated recoil impulse. Thus, using equation (4.4) one can show that

$$(t_{\max})^{\nu/(\nu+2)} = \xi(\gamma,\nu)\sqrt{\frac{8\rho_1}{(\nu+2)^2(\gamma+1)}}\left(\frac{E}{\rho_1}\right)^{1/(\nu+2)} P_1^{-1/2} \tag{4.23}$$

further noting that the associated $R_{\max} \simeq 0.1 R_0$. Anticipating the experimental results, the time-integrated recoil pressure due to the shock-wave p_{sw} is calculated explicitly using STN theory (equation (4.4)) in the case a spherical shock-wave

$$\begin{aligned} p_{sw} &= \xi(\gamma)^5 (\gamma+1)^{-3/2} \frac{16\sqrt{2}}{75}\left[b(\gamma) - \frac{\pi}{3}\right]\sqrt{\frac{M_1}{k_B T_1}} E_0 \\ &\equiv \xi'(\gamma)\sqrt{\frac{M_1}{k_B T_1}} E_0 \end{aligned} \tag{4.24}$$

The main result of equation (4.24) indicates that the integrated shock-wave recoil pressure is proportional to $p_{sw} \propto E_0/c_0$. This scaling-law is generally true, independent of the geometry of the explosion. In retrospect this result is also intelligible from dimensional analysis. From (4.24) it is also evident that in order to derive the functional dependence of heat capacities γ, the functional form of $\xi(\gamma)$ is required (in this case for $\nu = 3$). As pointed earlier, the self-similar solutions derived in section 4.1.III only provide analytical expression to within a constant factor, which is often set $\xi \equiv 1$. To obtain $\xi(\gamma)$ the full set of differential equations need to be solved. This is not straight-forward, and involves a number of ap-

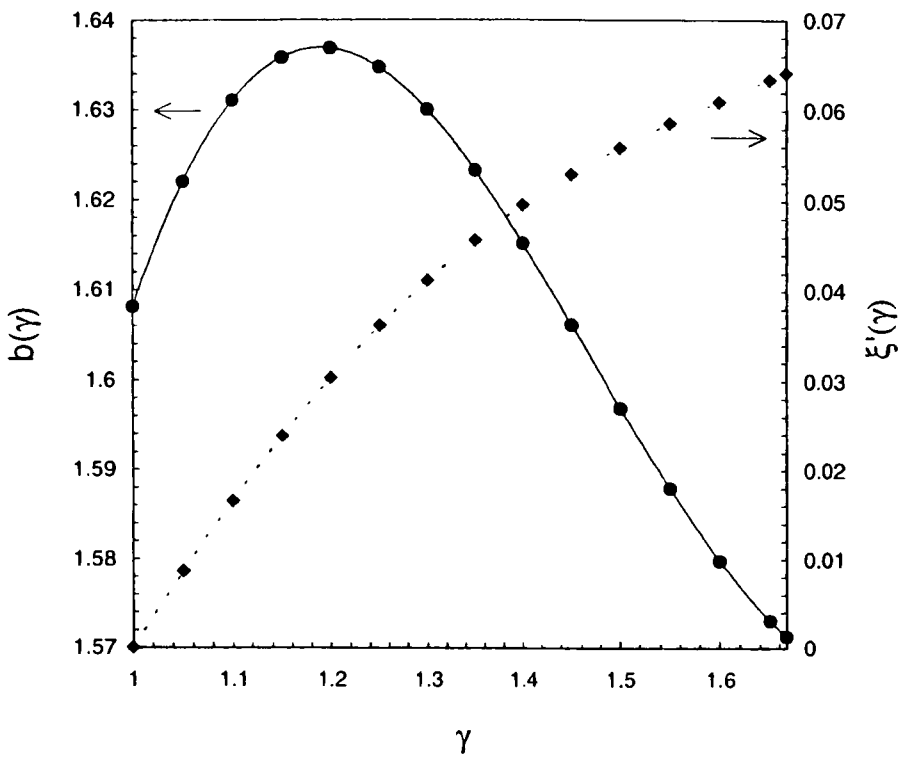


FIGURE 4.3: The integrated form-factor $b(\gamma)$ and constant $\xi'(\gamma)$. The solid line shows a third-order polynomial fit $b(\gamma) = 0.76\gamma^3 - 3.37\gamma^2 + 4.79\gamma - 0.57$.

proximations. In fact, various reports on the exact form of $\xi(\gamma, \nu)$ are inconsistent. In table V they are listed for the case $\nu = 3$, i.e. in spherical geometry

The physical picture associated with γ relates to the degree with which the background gas can absorb energy into internal degrees of motion (rotational and vibrational excitations, and ultimately electronic excitations and ionisation for sufficiently high temperatures). This reduces the amount of kinetic energy carried in the blast-wave, leading to a reduction in the integrated pressure to yield the recoil momentum. It is therefore concluded, that for $\gamma \to 1$, the shock-wave recoil momentum p_{sw} should tend to zero. This will be verified with experiment. Clearly, the value for $\xi(\gamma, 3)$ reported by Freiwald & Axford (1975) (table V) is inconsistent with this, and will be shown to disagree with experiment. Instead, the Chernyi solution from Zel'dovich & Raizer (1966) will be used (see table V), and shown to be accurate as verified against experiment. Explicitly, (4.24) is rewritten as

$$p_{sw} = \sqrt{2}\left[\frac{b(\gamma)}{\pi} - \frac{1}{3}\right]\sqrt{\gamma+1}\,\frac{\gamma-1}{3\gamma-1}\sqrt{\frac{M_1}{k_B T_1}}E_0 \tag{4.25}$$

It is interesting to note that LSD theory discussed earlier (Pirri 1973) also yields the correct physical limit, namely that if $\gamma \to 1$ then $p_{sw} \to 0$. Thus, regardless of the physical mechanism of energy release into the medium, either due to a a driving piston or a detonation, the kinetics of the problem obey the same energy-momentum relationships.

Having derived (4.25) explicitly, equations (4.7 – 4.11) are now evaluated numerically to obtain

$b(\gamma)$. Using MatchCad 6.0, values for V are solved sequentially for $\lambda \in [0,1]$ on a mesh of $n = 200$ using equation (4.10). The numerical algorithms for finding the roots are based on the Newton-Raphson method, and hence are sensitive to the starting value of the variable. Considering equation (4.10) the singularity in the limit $\lambda \to 0$

$$\lim_{\lambda \to 0} V \to \frac{\gamma + 1}{2\gamma} \tag{4.26}$$

renders difficulties if starting values of $V < (\gamma + 1)/2\gamma$ are assigned, since then the numerical algorithm will not converge. Hence, the limit $\lambda \to 0$ is approached from the top, starting at $\lambda = 1$, and the calculated value of V is used as the starting value for the next iteration. The forms of the dimensionless functions $f(\lambda), g(\lambda)$ and $h(\lambda)$ have been presented by Ryu & Vishniac (1987), and will be considered in more detail in chapter 5. To obtain values for $b(\gamma)$, the solutions for $h(\gamma)$ are integrated numerically, as shown in figure 4.3. For later use, the numerical results are fitted to a third-order polynomial to yield an approximate value for $b(\gamma)$. Also shown in figure 4.3 are the calculated values for $\xi'(\gamma)$. Further discussion of these numerical results will be given later in the light of the experimental results.

4.2 THE BALLISTIC PENDULUM EXPERIMENT

I MEASUREMENT OF MOMENTUM TRANSFER DURING LASER ABLATION Soon after the invention of the ruby laser in 1960 by Maiman numerous laboratories started investigating the effects of high power laser radiation on solid materials, particularly metals. By the mid-sixties already a significant amount of pioneering work had been done, excellently reviewed by DeMichelis (1970). Specifically, the studies of momentum transfer by 'giant' laser pulses using ballistic pendula were reported (Neuman 1964, Gregg & Thomas 1966). Neuman (1964) measured the relative target momenta upon laser ablation in vacuum generated with single 0.3 J pulses (50 ns) for various materials including copper, aluminium, brass, lead and glazed porcelain. By defocusing the focal spot Neuman (1964) observed that for fluences above 0.4 J/cm^2 the momentum transfer was constant, while below this threshold it scaled with the root of the energy density. Similarly, Gregg & Thomas (1966) measured momentum coupling constant in vacuum for Be, C, Al, Zn, Ag, and W with power densities in the range of $10^8 - 10^{10}$ W/cm^2 (7.5 ns). For all materials investigated an certain optimum power density was determined which resulted in the largest amount of momentum transfer per joule of laser energy. Above this optimum the coupling constant was fitted to $\propto I^{-n}$ where n was experimentally determined to be of order $0.25 - 0.35$.

Towards the 1970s the development of high power CO_2 lasers, and later the Nd:glass laser, led to considerable interest in momentum transfer experiments at intensities up to 10^{14} W/cm^2. The main incentive of this work originates in applications of internal confinement fusion (Lindl 1995), and in table table VI the key reports in this field are listed for experiments performed under ambient atmospheric conditions. The main results of these experiments confirmed the LSD theory, where significant plasma coupling dominates the momentum transfer process, due to the relatively long wavelengths combined with the high power densities. Phipps et al. (1988) have produced a review of various of these reports and have shown that above the optimum peak-coupling intensity the momentum transfer can be determined to within a factor of two by $I\lambda\sqrt{\tau}$. Note that most of these report have not investigated the effect of the background gas properties on the recoil impulse. Only Metz (1973) has reported on the difference between ablation in vacuum vs. air, but did not provide a description in terms of LSD theory.

reported system	target	pendulum	observations
[1]: CO_2 (1 kJ) 1 μs – 1 ms $10^7 - 10^8$ W/cm^2	carbon Al W	current/magnetic coils 10^{-3} Ns	LSD material independent
[2]: Nd-glass 60 ps–2 ns $10^6 - 10^{14}$ W/cm^2	Al Ti	torsion / ballistic second pendulum to detect debris 10^{-6} Ns	LSD resonant plasma absorption for 60 ps
[3]: Nd-glass 4 ns $10^{11} - 10^{14}$ W/cm^2	polystyrene (CH)	ballistic multiple pendula to detect debris 7 mV per 10^{-5} Ns	measured ratio of plasma recoil vs. debris recoil

TABLE VI: Experimental reports of momentum transfer experiments during laser ablation at ambient atmospheric conditions, taken from references listed in table VII.

ref.	reported by
[1]	Hettche et al. (1973) Lowder et al. (1973) Metz (1973) Lowder & Pettinghill (1974) Metz et al. (1975)
[2]	Hettche et al. (1976) Arad et al. (1979) Arad et al. (1980) Combis et al. (1991)
[3]	Grun et al. (1981) Grun & Ripin (1982)

TABLE VII: References of pendulum experiments

Besides the ballistic pendulum, techniques based on detection of the compression wave *inside* the solid target have been developed to provide absolute, time-resolved pressure measurements, including coherent Raman spectroscopy (Tas et al. 1997), detection of surface plasmons (Schilling et al. 1996, Yavaş et al. 1997), interferometric techniques (Metz et al. 1975, Hettche et al. 1976), and piezoelectric transducers (Dyer & Srinivasan 1986, Dyer et al. 1992*b*, Dyer et al. 1992*a*, Olmes et al. 1997). These studies are of particular interest for applications involving shock processing, or testing of materials for fatigue and stresses (Fournier et al. 1991, Peyre & Fabbro 1995). However, due to the large hydrodynamical impedance of the solid interface, the pressures generated by the shock-waves are not propagated into the bulk, rendering these techniques unsuitable to provide information on the evolution of the plasma plume. Indeed, various reports have indicated there is no marked difference between air and vacuum (Hettche et al. 1976, Dyer et al. 1992*b*).

Alternatively, imaging techniques can be employed to directly monitor the evolution of the shock-wave. In classic shock-tube experiments the use of shadowgraphy and Schlieren-imaging has long since been employed (Duff & Blackwell 1966, Dresner 1970, Glenn & Crowley 1971). For shock-waves generated with sufficiently powerful lasers (pulse energies in excess 1 J), the physical dimensions of the shock are sufficiently large to allow for direct imaging (Geohegan 1994), where various techniques have been employed including shadowgraphy and Schlieren imaging (Ventzek et al. 1992*a*, Ventzek et al. 1990, Callies et al. 1996, Siano et al. 1996, Aden et al. 1997), gated intensified-CCD imaging (Geohegan & Puretzky 1995, Zerkle & Sappey 1996), resonance absorption spectroscopy (Gilgenbach & Ventzek 1991, Ventzek et al. 1992*a*), and interferometry (Schittenhelm et al. 1997). While these techniques can provide detailed studies of the system, they can be quite laborious and complex. Part of the main achievements of the present work is to show that the use of a ballistic pendulum can provide quantitative data. Though the analysis is not straight-forward, it allows for unambiguous interpretation despite the fact that it only measures spatial and time-integrated quantities.

II THE BALLISTIC PENDULUM The schematic design of the ballistic pendulum is shown in figure 4.4, while photographs of the actual device are shown in figure 4.5 and figure 4.6. The pendulum consists of a vertical, rectangular aluminium body suspended on two point contacts in the horizontal plane. The point contacts are formed by a thin stainless steel razor blade, which is rested on two glass 'gutters' to provide ease of alignment within the curved inner surface. To reduce the damping on the metal-glass contact, the ends of the glass rods were heated to melting temperature to make protrusion which ensured a low-friction point contact was made.

The sensitivity of the pendulum was maximised by balancing the centre of mass near the pivot point, resulting in periods $T \simeq 1$ s, and by maximizing the distance to the point of impact $L \simeq 25$ mm, whilst keeping the total mass ($\simeq 3$ g) and moment of inertia I ($\simeq 5 \cdot 10^{-7}$ kg m^2) to a minimum. To detect small deflection angles an optical lever was used, consisting of a red HeNe beam reflected of a microscope cover-slip which was glued on the top of the pendulum. With a 6 m path length X, and a minimal deflection $\Delta x = 1$ mm which could be detected by appropriate imaging of the HeNe beam, small deflection angles $\Theta = \Delta x/2X$ down to 0.1 mrad could be detected. Calibration of the pendulum was performed by measuring T and calculating the moment of inertia I from the simple geometric design. Thus, the total recoil momentum p_{tot} was measured using

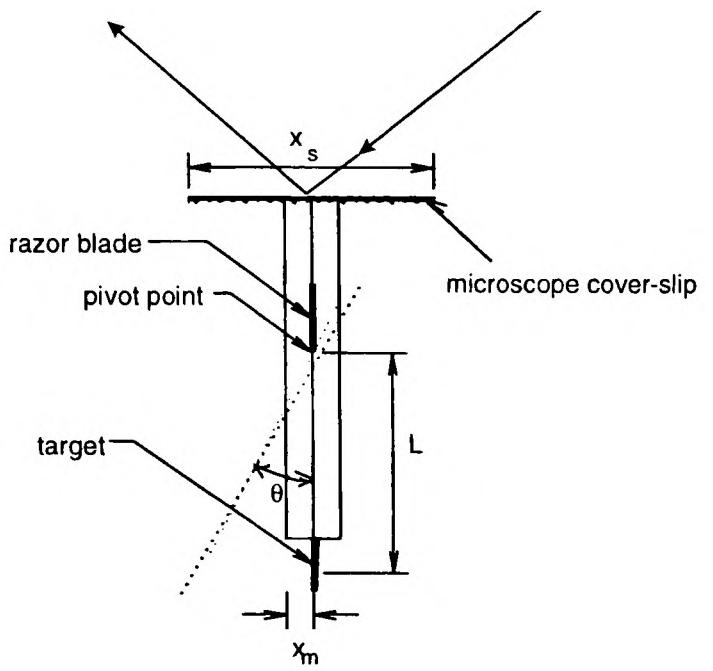


FIGURE 4.4: Schematic design of the ballistic pendulum, showing the main rectangular body, the razor-blade providing the pivot point, and the microscope cover slip for reflection of the optical lever.

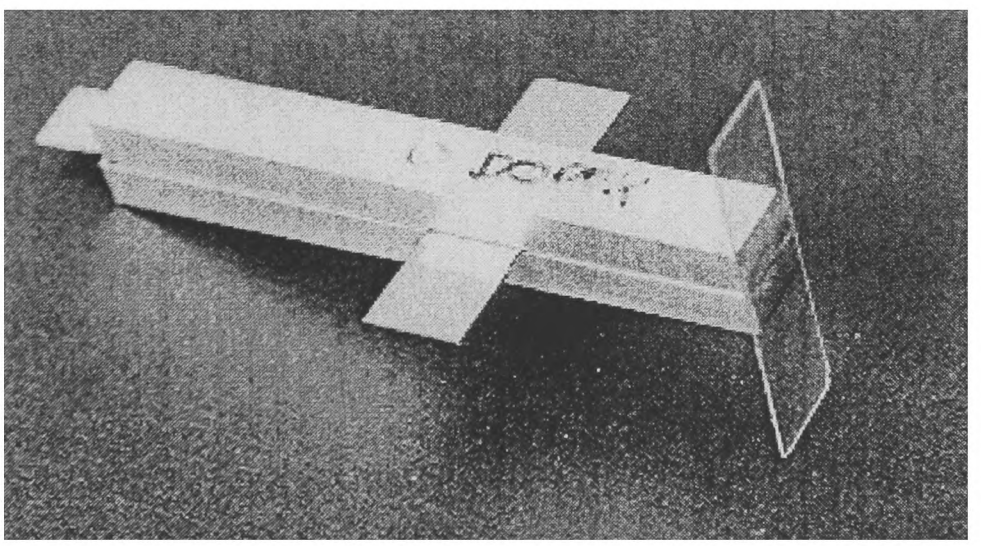


FIGURE 4.5: The aluminium pendulum 'Dopey', showing the main retangular body, the top microscope cover slip, and the central screw which clamps the steel razor blade and target at the bottom. In later designs a circular microscope cover slip was used for greater stability.

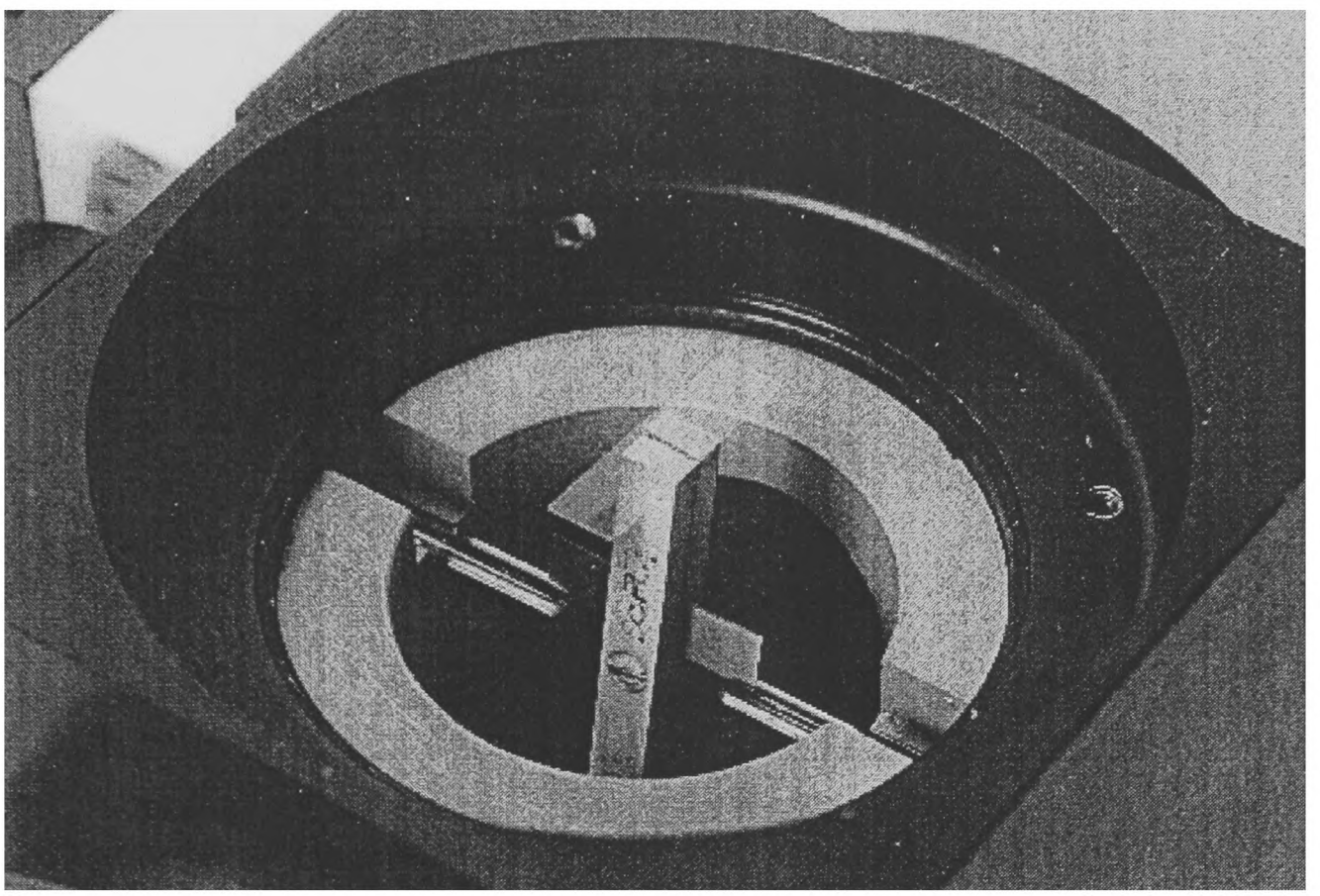


FIGURE 4.6: The pendulum suspended on the glass gutters inside the vacuum chamber.

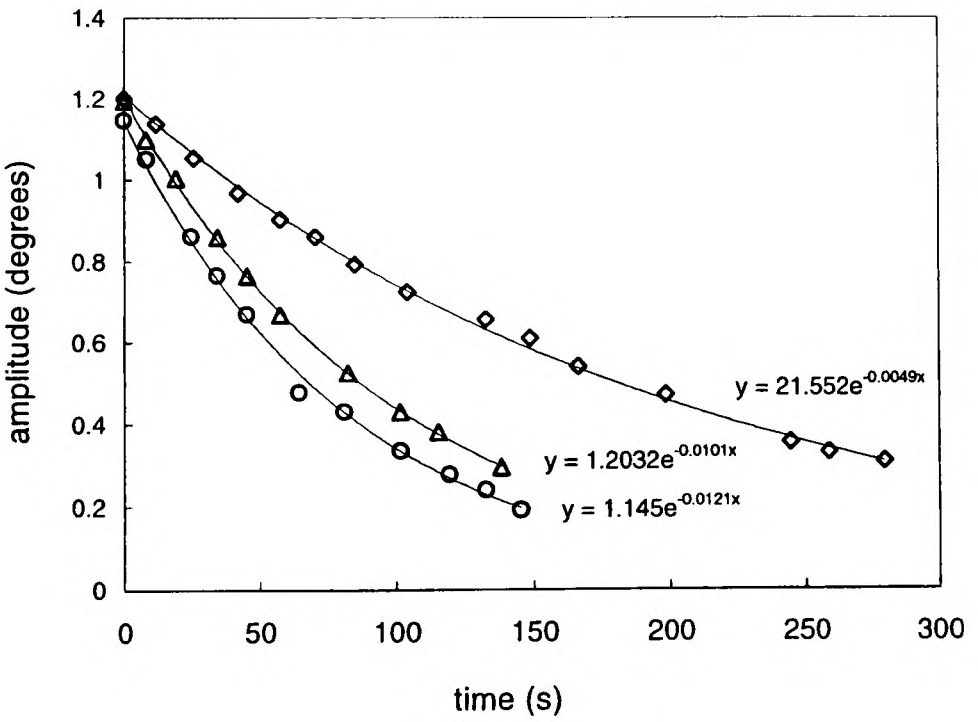


FIGURE 4.7: Damping of the ballistic pendulum motion. In air ($\diamond$) at atmospheric pressure, $T = 1.60$, $Q = 400$; CO_2 ($\triangle$)at 800 mbar, $T = 1.37$, $Q = 227$; Ar ($\circ$) at 800 mbar $T = 1.37$, $Q = 189$.

parameter	value		error	
I	$5 \cdot 10^{-7}$	$\mathrm{kg\,m^2}$	$\delta I/I$	3%
T	1.5	s	$\delta T/T$	1.5%
L	25	mm	δL	0.1 mm
Θ	$1-5$	mrad	$\delta\Theta$	0.08 mrad

TABLE VIII: Parameters of the ballistic pendulum.

$$p_{tot} = 2\pi \frac{I}{TL} \Theta_{\mathrm{max}} \tag{4.27}$$

with a sensitivity down to $0.5{\cdot}10^{-8}$ Ns.

The full details on the specifics of the dynamics of a compound pendulum are included in Appendix A, where it is shown only correction due to damping caused by air drag may constitute a significant correction in terms of the systematics of the ballistic pendulum. To verify the fidelity of the pendulum, damping was measured for various gases at (near) atmospheric pressures as shown in figure 4.7. It is observed that damping is more severe for heavier gases, in this case resulting in the largest damping constant of order $\simeq 10^{-2}$ s for argon. However, for all gases at all pressures considered here the corresponding Q-factors of always of order $\simeq 200$, which is sufficiently high to render corrections to the pendulum frequency insignificant. Furthermore, corrections due to damping to the measured maximum deflection as measured directly after the first quarter oscillation is also insignificantly small.

The accuracy in the measured recoil momenta are dominated by the experimental errors. The accuracy of the system is determined by considering the errors in the calibration of the pendulum and measurement of the deflection angle

$$\delta p^2 = \left(\frac{\partial p}{\partial I}\right)^2 \delta I^2 + \left(\frac{\partial p}{\partial T}\right)^2 \delta T^2 + \left(\frac{\partial p}{\partial L}\right)^2 \delta L^2 + \left(\frac{\partial p}{\partial \Theta_{\mathrm{max}}}\right)^2 \delta \Theta_{\mathrm{max}}^2 \quad . \tag{4.28}$$

Using (4.27) the relative accuracy is given by

$$\left(\frac{\delta p}{p}\right)^2 = \left(\frac{\delta I}{I}\right)^2 + \left(\frac{\delta T}{T}\right)^2 + \left(\frac{\delta L}{L}\right)^2 + \left(\frac{\delta \Theta_{\mathrm{max}}}{\Theta_{\mathrm{max}}}\right)^2 . \tag{4.29}$$

In addition, practical considerations such as damping of unwanted vibrations, friction at the pivot point and air drag need to be estimated to give a total estimate of the absolute precision with which the total transferred impulse p_{tot} can be determined. For example, due to the ferromagnetic stainless steel razor blade the pendulum motion was susceptible to perturbations due to magnetic fields. In the presence of magnetic clamping mounts, the equilibrium position was observed to change by few tens of milliradians. However, provided that any external magnetic field was conservative and static the pendulum motion was observed to be symmetric at all times, thus rendering corrections due to e.g. the Earth's magnetic field insignificant. An advantage of the use of ferromagnetic elements was that the pendulum motion could be stopped manually by applying an asynchronous oscillating magnetic field, which proved useful

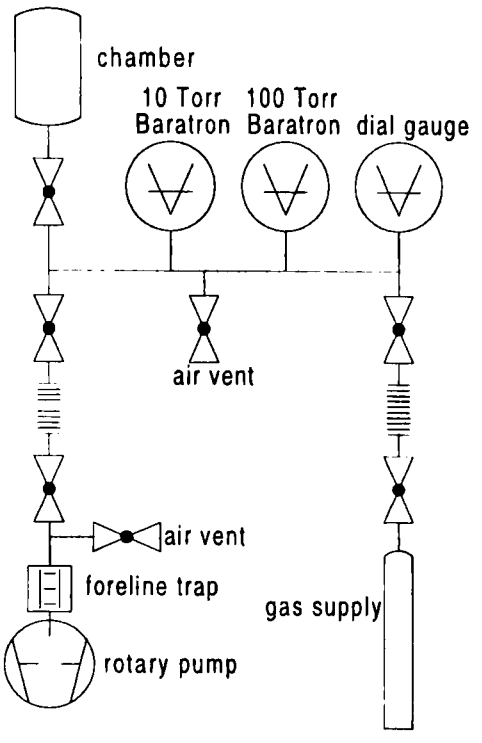


FIGURE 4.8: The vacuum system used in the ballistic pendulum experiments, showing the two Baratron gauges (10 Torr and 100 Torr full-scale) and the dial gauge (atmospheric pressures) used for the pressure reading.

for practical purposes (waving a magnetic magic wand).

In table VIII typical values and the corresponding experimental errors are listed. For small deflections (corresponding to Δx up to $\sim$ 10 mm) the inaccuracy is dominated by the absolute error in the measurement of Θ, with $\Delta p = \pm 0.5 \cdot 10^{-8}$ Ns. For larger deflections, the error is primarily due to the $\delta I/I$, thus giving a relative accuracy of 3% or equivalent absolute errors of $\Delta p = \pm 1.0 \cdot 10^{-8}$ Ns. In comparison, the thermal limit associated with energy fluctuations of order $k_B T$ corresponds to $\Theta \simeq 10^{-7}$ rad, $\Delta p \simeq 10^{-11}$ Ns. The detection limit of the pendulum of order 10^{-8} Ns is approximately equivalent to a mass of one microgram (a grain of salt) falling over one metre in Earth's gravitational field.

III EXPERIMENTAL SETUP The gas handling system used in the experiments is shown in figure 4.8. The main body of the vacuum system was connected directly to the main vacuum chamber using aluminium pipelines with standard Edwards NW flanges, keeping the total volume of the system to a minimum. An 2 litre rotary vane pump (Edwards E2M2) fitted with a foreline trap (Edwards FL20K) was used to obtain high vacuum down to $2 \cdot 10^{-2}$ mbar, with a leak rate of less than 10^{-2} mbar/min. for the total volume of the system. Measurement of the pressure in the vacuum chamber was done using three different pressure gauges to span 5 orders of magnitude from $10^{-2} - 10^{3}$ mbar. Two capacitance manometers (MKS 10 and 100 Torr full-scale Baratron® 222AES-A-B-100) was used to measure the pressure in the range $10^{-2} - 100$ mbar. A capsule dial gauge (Edwards CG3) was used to span the $10^{2} - 10^{3}$ mbar range. Both the Baratron and capsule dial gauge provide direct pressure measurement, and are independent of the gas type.

To ensure consistent pressure reading over the 5 decades a mercury manometer providing accurate absolute pressure reference in the range $1 - 10^3$ mbar with 1 mbar accuracy was used to calibrate the capsule dial gauge and the upper range of the Baratron. Also, in the $1 - 10$ mbar range the two Baratron® manometers were calibrated against each other. The calibration curves are shown in figure 4.9. The response of the dial gauge is clearly linear, with a small off-set of order 20 mbar. The response curve of the Baratron is typical of capacitance manometers (O'Hanlon 1989), showing an increasingly less accurate reading at pressures less than 0.1% over the range $10^{-2} - 10^3$ mbar.

When the measured recoil momentum was first observed to be dependent on the pressure of the background gas, various preliminary experiments were performed to eliminate possible spurious effect. By defocusing the laser beam below the ablation threshold, no deflection could be measured, thus ruling out momentum transfer due to the radiometer effect or radiation pressure. Also, by placing the pendulum in a larger enclosure or removing the windows of the vacuum chamber, no change in the deflection was observed under atmospheric conditions. Thus, motion of the pendulum due to (reflected) acoustic waves could be neglected. Furthermore, at the typical pulse energies $E_0 \simeq 3$ mJ, ignition of LSD shock-waves is insignificant. Chang & Warner (1996) has shown that for CVLs, the threshold is typically of order $E_0 \simeq 40$ mJ. This was verified by observing the plume to always be perpendicular to the target surface, even when the beam was declined away from normal incidence.

For all the experiments presented in this chapter, pure aluminium foil (99.5%, 200 μm thick) was used as the target material throughout. A single doublet-achromat focusing lens with focal length $f = 250$ mm was used throughout, where use of shorter focal length lenses was deemed impractical due to the short depth of field, and inaccurate due to the higher sensitivity to aberrations (astigmatism) around the focal point. Use of larger focal length resulted in significant decrease of the maximum signal, thus reducing the dynamic range of the apparatus. Upon inspection with an optical microscope, the morphology of the single-shot ablation craters were found to be independent of the background gas conditions, and was reproduced at all times (figure 4.10). The source-mass radius R_s was measured to be 25 μm, which will be shown below to be sufficiently small to consider the shock-wave in spherical geometry. The piston-mass was approximately determined $M_s \simeq \rho_s R_s^3$ with ρ_s the solid density of aluminium $\left(2.7\ \mathrm{g/cm^3}\right)$. Study of the vacuum recoil impulse for different target will be presented in chapter 7.

IV RESULTS In figure 4.11 the measured total recoil momentum p_{tot} is plotted for background gas pressures P_1 in the range of $10^{-2} - 10^3$ mbar for He, Ne, Ar and Xe. At low pressures (< 0.1 mbar), p_{tot} asymptotically approaches a minimum value, denoted p_0. Increasing P_1 in the range $(0.1 - 100$ mbar) causes p_{tot} to increase monotonically. Eventually, the maximum value for p_{tot} is approached asymptotically for sufficiently high pressures (> 10 mbar). From these observations, the total recoil momentum p_{tot} is interpreted to consist of two components (Ho et al. 1995)

$$p_{tot} = p_0 + p_{sw} \quad , \tag{4.30}$$

where p_0 is the (dynamic) pressure caused by ejection of target material, while p_{sw} is the (static) overpressure generated by the shock-wave persisting for time-scales much longer than the ablation process. To underline this interpretation, the product $P_R(t)\, R^2(t)$ from (4.22) is identified as the force on the

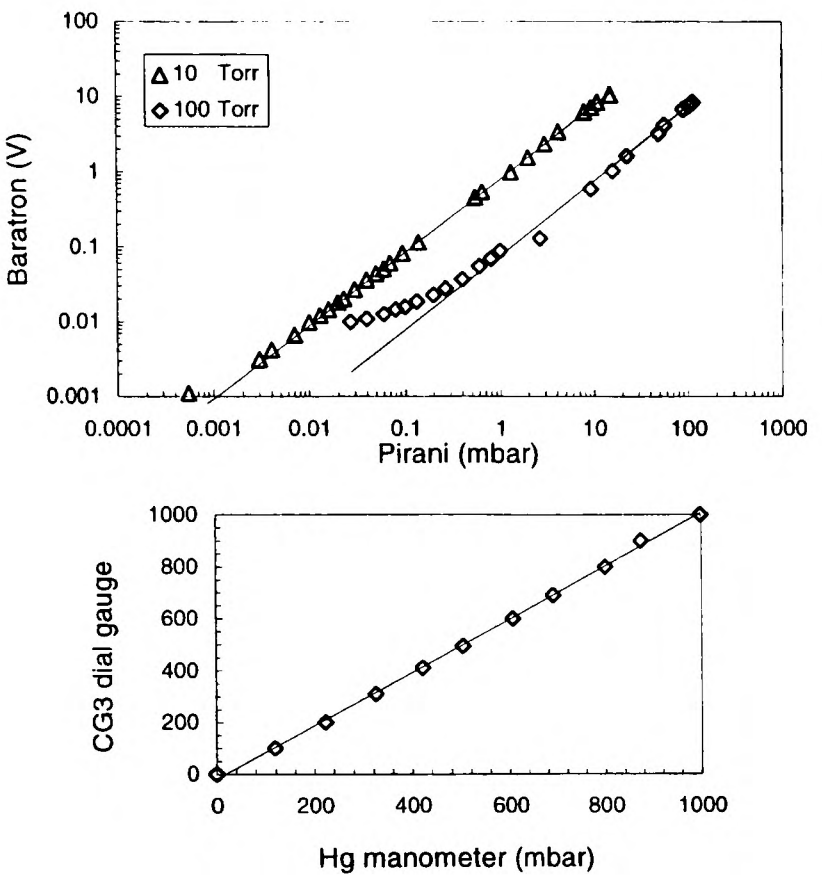


FIGURE 4.9: Callibration plots of the two Baratron pressure gauges and the dial gauge.

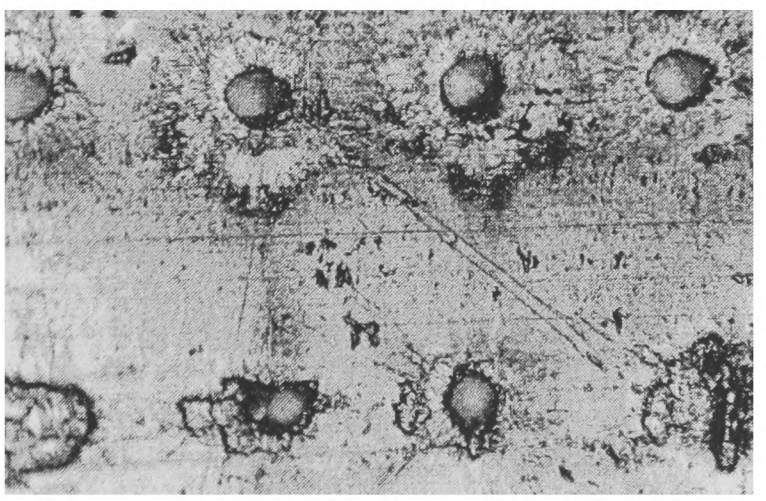


FIGURE 4.10: The single-shot ablation craters produced in the aluminium foil targets. The top row shows the well-defined craters, which are reproduced from shot-to-shot, with a diameter of 50 μm. The bottow row shows a focal scan in order to determine the focal position. Astigmatism of the laser beam is clearly visible, resulting in elongated ablation marks.

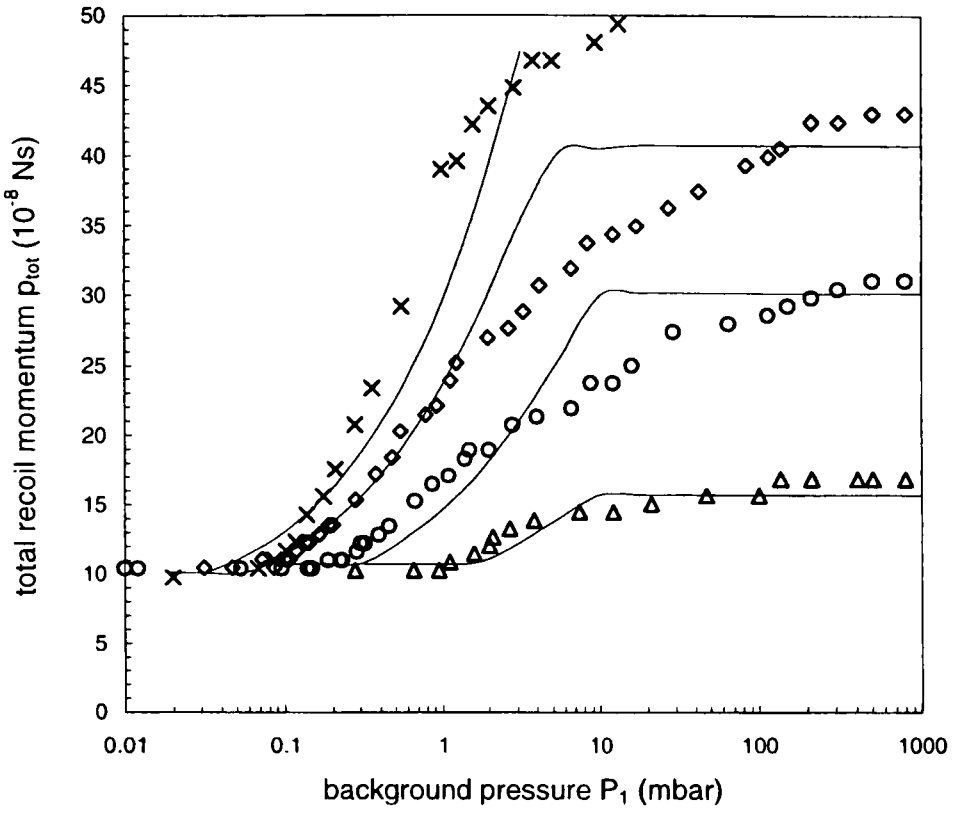


FIGURE 4.11: Measured total recoil momentum as a function of pressure for helium (△), neon (○), argon (◇), and xenon (×). The solid lines show results from numerical calculations using mSTN theory (aluminium target, 25 μm spot radius, $E_0 = 3.5$ mJ), with corresponding estimates for the piston mass $M_s \simeq 10$ ng..

pendulum.

Illustrated in figure 4.12, $P_R(t)\,R^2(t)$ is plotted as function of time for the current experiments. For STN theory, the force and shock-front velocity tend to infinity as $t \to 0$, showing the limitations of the point-source approximation. The mSTN resolves this problem by allowing the piston-mass to be finite, undergoing free-flow expansion with constant velocity up to the transition point (R^*, t^*) (4.17). Furthermore, figure 4.12 shows that the force during the STN phase is the dominant contribution to the total recoil impulse, represented by the area under the curve. Ultimately, the onset of the acoustic decay phase at $R_0 = 15$ mm, $t_0 \simeq 5$ μs marks the end of the momentum transfer as the integrand in (4.19) approaches zero.

From this picture, the piston-recoil p_0 is identified with the integrated recoil pressure of equation (4.19) from $(0,0)$ up (R^*, t^*), in the absence of (or prior to) shock-wave formation. Using known solutions regarding free expansion of dense cloud vapours into vacuum (Keller 1948) (see the discussion below), values of $p_0 \simeq 5 \cdot 10^{-8}$ Ns are calculated using mSTN theory, which can also be obtained by considering $p_0 \simeq M_s \dot{R}(0)$. This validates the interpretation that p_0 is the piston-mass recoil in the absence of (or prior to) momentum transfer due to shock-wave formation. Furthermore, the calculated values of p_0 are in agreement with experiment within a factor of two, where the measured value $p_0 \simeq 10^{-7}$ Ns. The discrepancy is ascribed to secondary emission of molten material (Grun & Ripin 1982), not accounted for within mSTN. For softer metals like indium, it has indeed been verified that secondary emission results

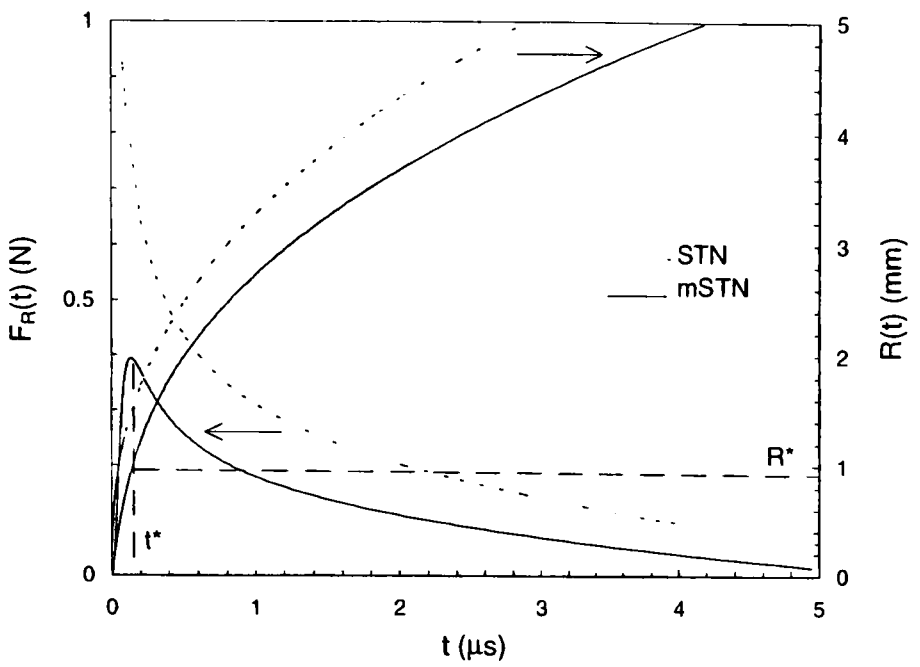


FIGURE 4.12: The force acting on the pendulum $F(t) = P_R(t) R^2(t)$ plotted as a function of time using STN (dashed line) and mSTN (solid line) theory. In this particular case, $R_0 = 15$ mm and $t_0 = 4.5$ μs (aluminium target, 25 μm spot radius, $E_0 = 3.5$ mJ, 10 mbar argon).

in a significant increase of p_0, which will be discussed in more detail in chapter 7.

Turning to the shock-wave recoil p_{sw} contribution to p_{tot}, first consider the observed pressure dependence of figure 4.11. As the maximum extent of the shock-wave R_0 decreases with increasing pressure (4.18), by increasing the pressure more of the shock-wave is confined within the extent of target, leading to a increasing contribution of p_{sw} to p_{tot}. At low pressures, the maximum spatial extent of the shock-wave R_0 (17 mm at 10^{-2} mbar) is larger than the physical dimensions of the pendulum target $d \simeq 5$ mm, and thus the upper limit of (4.19) is determined by d. For sufficiently high pressures R_0 (3 mm at 10^3 mbar) $< d$, and all of the shock-wave recoil is integrated. This geometric effect was confirmed experimentally by measuring the recoil momentum as a function of the distance of the ablation point to the edge of the target, shown in figure 4.13 for 10 mbar xenon atmosphere. Near the edge, the recoil impulse was approximately half the maximum value. Increasing the distance from the edge causes p_{tot} to increase monotonically, where for distances ≥ 4 mm the maximum recoil was approached asymptotically. This geometric effect was simulated using mSTN to account for the observed pressure dependence of figure 4.11 (solid lines), showing reasonable agreement with experiment.

Having set-out the physical interpretation of figure 4.11, the shock-wave recoil p_{sw} was measured at near-atmospheric pressures (where p_{sw} dominates the total recoil impulse p_{tot}) for different E_0, M_1 and γ in view of confirming (4.25). Varying the pulse energy, a linear dependence $p_{sw} \propto E_0$ is observed for measurements in 500 mbar krypton (figure 4.14). Also, the piston-mass recoil p_0 is found to be linearly dependent on E_0. Changing the molecular weight of the background gas, figure 4.15 shows that the

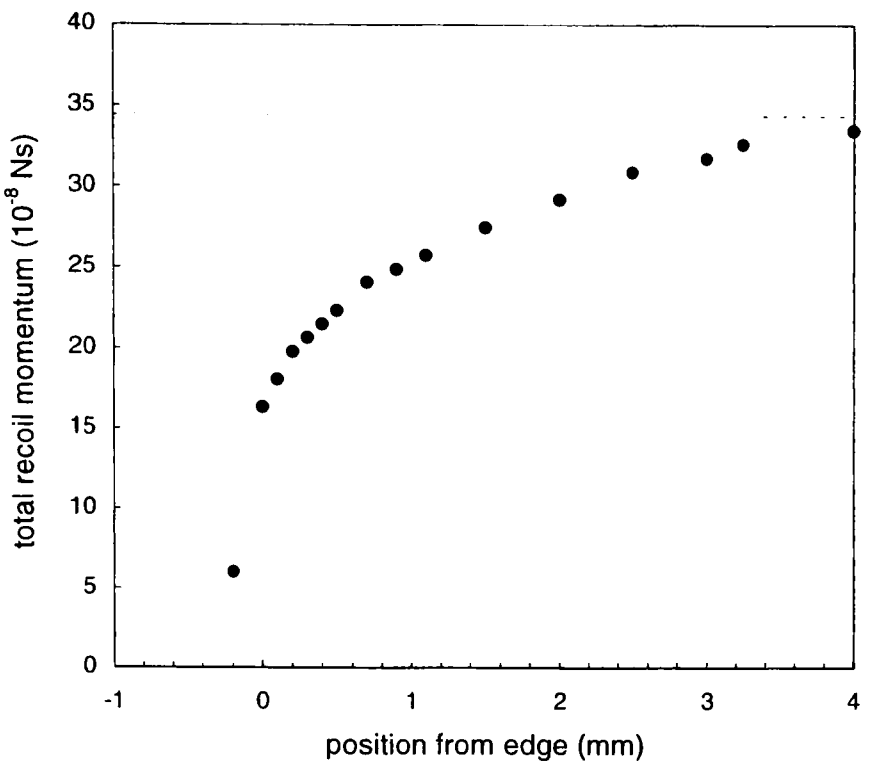


FIGURE 4.13: Measured total recoil momentum as a function of the relative position to the target edge ($E_0 = 3.0$ mJ, 10 mbar xenon).

maximum values of p_{sw} as measured for five noble gases follow $(M_1)^{0.5}$.

Most interestingly, the current experimental arrangement allows for direct measurement of the effect of γ on the shock-wave formation. In figure 4.16 the values of p_{sw} as measured for N_2, CO_2 and SF_6 are plotted relative to the value of p_{sw} for monoatomic gases of similar weight (Ne, Ar, and Xe respectively). By correcting $p_{sw} \propto (M_{poly}/M_{mono})^{0.5}$ the effect of M_1 and γ were separated, using $(M_{N_2}/M_{Ne})^{0.5} = 1.18$; $(M_{CO_2}/M_{Ar})^{0.5} = 1.05$; $(M_{SF_6}/M_{Xe})^{0.5} = 1.05$. An effective value for γ was obtained from standard thermochemical reference data, where the error bars in figure 4.16 reflect the changes within the $300 - 6000$ K temperature range, obtained from thermochemical data tables (Chase et al. 1985). Also shown is the predicted scaling law as discussed earlier (solid line), given by the Chernyi solution listed in table V. Due to the increase of internal degrees of freedom with decreasing γ, the kinetic energy contained in the shock-wave decreases resulting in decreasing p_{sw} decreases as $\gamma \rightarrow 1$. This will be discussed in more detail below.

4.3 DISCUSSION

I SHOCK-WAVE FORMATION & EVOLUTION In the experiments described above it has been shown that the measured recoil impulse is accurately described within the mSTN theory. The piston-mass momentum p_0 is identified as the integrated recoil pressure during the free-flow phase. The measured dependence of the shock-wave recoil p_{sw} on P_1, E_0, M_1 and γ is also accurately described by the self-similar solutions. These findings are in line with the interpretation that the temporal evolution of laser generated shock-waves consist of three regimes, as sketched earlier in figure 4.2. The two components

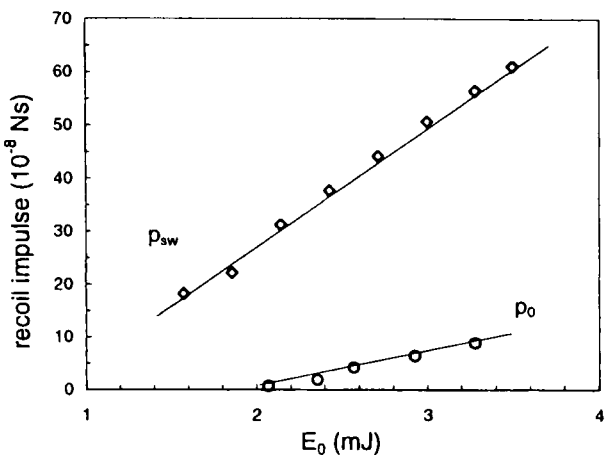


FIGURE 4.14: Measured vacuum recoil momentum p_0 (o) and STN shock recoil momentum p_{sw} ($\diamond$) as a function of E_0 (500 mbar krypton),

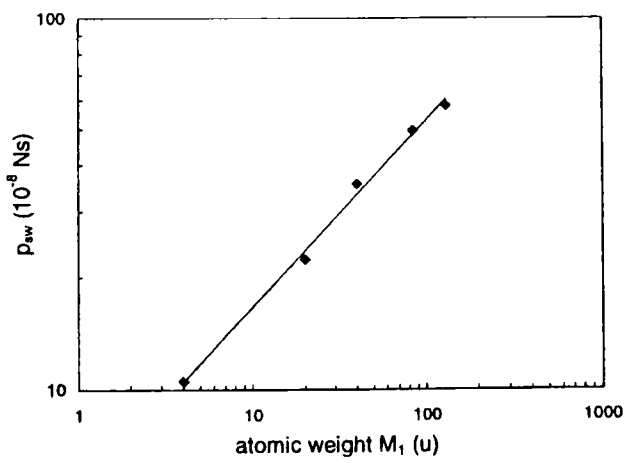


FIGURE 4.15: Measured shock-wave recoil p_{sw} at near-atmospheric pressures plotted against atomic weight for He, Ne, Ar, Kr and Xe. The solid line is a least-squares fit giving $p_{sw} \propto (M_1)^{0.5}$ ($E_0 = 3.5$ mJ).

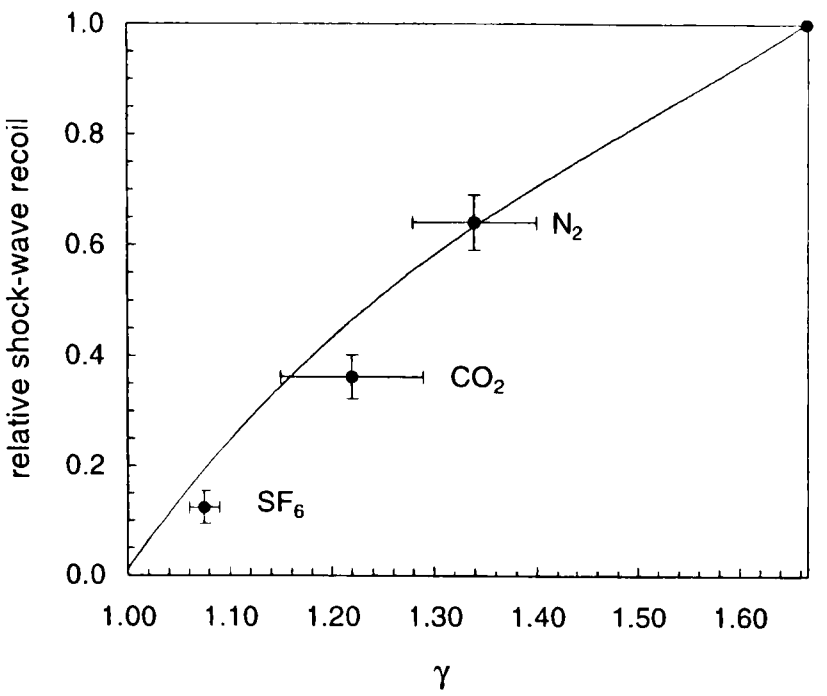


FIGURE 4.16: Measured relative shock recoil momentum p_{sw} at near-atmospheric pressures for different polyatomic gases with respect to monoatomic gases with similar atomic weight ($E_0 = 3.5$ mJ). The vertical error-bars represent the experimental accuracy, while the horizontal error-bars are obtained from estimated effective value for γ based on thermochemical data.

of the total recoil impulse are identified, as shown in figure 4.12, to originate from the initial free-flow phase (p_0), and the strong-shock phase (p_{sw}), while the final acoustic decay phase is argued not to have a significant contribution to the recoil impulse.

These observations validate the mSTN theory, and provide a useful picture of the shock-wave evolution during laser ablation. Addressing the issue of shock-wave formation, these findings lead to the conclusion that a strong, STN-like shock can only be sustained for $R \in [R^*, R_0], t \in [t^*, t_0]$. Explicitly for the experiments described here, the characteristic spatial dimensions and time-scales for the shock-wave in argon at $P_1 = 10^3$ mbar are : $R \in [0.2\text{ mm}, 3\text{ mm}], t \in [25\text{ ns}, 10\ \mu\text{s}]$; and for $P_1 = 10^{-2}$ mbar: $R \in [9\text{ mm}, 14\text{ cm}], t \in [1\ \mu\text{s}, 0.5\text{ ms}]$. Using the $R, t \propto P_1^{-1/3}$ scaling from equations (4.17) and (4.18), similar values can be obtained for the other experimental conditions. Comparing these time- and length-scales with, for example, the time and length-scales of the laser source, respectively. 40 ns and 25 μm, one finds that the conditions $\tau_L < t^*$ and $R_s < R^*$ holds in almost all cases, thus validating the point-source approximation. Only at near-atmospheric pressures does t^* become of order of the laser pulse duration τ_L. (Callies et al. 1996) have considered this limit, by allowing τ_L to have a finite width, and subsequently perform numerical integration of the equations of motion of the shock-wave. These calculations by Callies et al. (1996) showed this modification constitutes a small, but experimentally verified, correction to the shock-front position $R(t)$ during the first 100 ns of the shock-wave evolution. In view of the pendulum experiments, however, this correction is insignificant since the major contribution to p_{tot} occurs on timescales of microseconds (see figure 4.12).

More generally, the condition

$$R^* < R_0 \tag{4.31}$$

determines whether for a given system a strong shock will be formed. This condition not only depends on the background gas conditions but also on the amount of material M_s removed for a given E_0. As shown in Appendix B, (4.31) can be rewritten as

$$E_0 > M_s c_0^2. \tag{4.32}$$

The condition (4.32) states that a shock-wave can only develop when the available (effective) pulse energy is sufficiently larger than the kinetic energy of the piston-mass. In this case, the piston will be expelled at super-sonic velocities into the background gas, where the a shock-wave will develop to take up the (excess) energy. Such an interpretation reflects that the asymptotic limit of self-similar motion will approached more quickly for a strong, high M number shock-wave in which cases the initial assumptions of STN theory become more accurate. In other experiments which will be discussed in chapter 7, it was observed that by defocusing the laser beam, increasing the spotsize radius from 25 μm to 100 μm, the piston-mass recoil p_0 increases up to a factor of two. However, the shock-wave recoil p_{sw} was found to decrease. This confirms that for constant pulse energy, the strongest shock is formed for the smallest source-mass M_s. Estimating the kinetic energy contained in shock using $p_{sw} \simeq E/c_0$, with typically $p_{sw} \simeq 40 \cdot 10^{-8}$ Ns, $c_0 \simeq 300$ m/s, one finds that the shock-wave contains about 1.2 mJ, thus dissipating about $30 - 40\%$ of the total pulse energy $E_0 \simeq 3.5$ mJ. In term of the energy balance of the ablation process, and is in agreement with e.g. the calculations and experiments reported by Aden et al. (1997).

The interpretation of the ballistic pendulum experiments in terms of mSTN theory are also in line with reported photographic studies (Gupta et al. 1991, Geohegan 1992). Gupta et al. (1991) and Geohegan (1992) have verified the piston-mass propagates at constant velocity, observed in the linear form of the shock-front position $R(t)$ measured at low pressures $(10^{-5} - 10^{-6}$ mbar$)$. While Geohegan (1992) proposes a heuristic drag-model, the reported results are more appropriately described within mSTN theory. Dyer & Sidhu (1988) has performed spectroscopic and photographic studies, observing a marked difference in the evolution of the luminous sheet associated with the position of the shock-front. For $P_1 = 15$ mbar, a strong STN-like shock is readily formed. Reducing the pressure to $P_1 = 5$ mbar, agreement with STN theory becomes poorer, but the presence of a luminous sheet indicated a shock-wave was still formed. At the lowest pressure $P_1 = 0.5$ mbar, no luminous front was observed until larger distances $R > 7.5$ mm, which is of order of R^* as shown in calculations above. From this Dyer & Sidhu (1988) concluded that in the low pressure regime, the initial piston expansion follows a free-flow regime, only to develop in a (weak) shock at sufficiently large time- and lengthscales for which departures from (m)STN theory has been discussed by Bach & Lee (1970).

II BEYOND MSTN: SHOCK WAVE STRUCTURE IN GASES Stepping beyond the macroscopic, kinetic considerations considered above to describe the shock-wave evolution, a more detailed discussion regarding the microscopic properties of the background gas is required to describe the internal structure of the shock-wave. First, recall the results shown in figure 4.16, where the effect of internal degrees of freedom on the

shock-wave strength has been quantified. Closer inspection of these experimental results, however, raises the question that despite the good agreement with the predicted effect of γ given in section 4.1.VI, it is not evident *a priori* that an (average) effective γ can be defined for these shocks given that the state of the background gas undergoes significant changes. The good experimental agreement shown in figure 4.16 is ascribed to the fact that particularly for ablation with copper vapour lasers, and generally for laser with low pulse energies of few millijoules, secondary effects due to electronic excitation or radiation transport do not play an important role. For example, for ablation of polystyrene foil with $E_0 = 200$ J, the value of γ for xenon has been measured to decrease to (1.06 ± 0.02) due to photoionisation (Grun et al. 1991, Manka et al. 1996). At such low values of γ, the structure of the shock-wave becomes unstable, no longer exhibiting a sharp shock-front but becoming turbulent due to growth of linear perturbations during the adiabatic expansion (Ryu & Vishniac 1987).

For experiments described here, spectroscopic studies have been performed on the aluminium plasmas generated during laser ablation in air (which is the main subject of chapter 6) showing no significant emission from N_2, N_2^+ or atomic nitrogen. Thus, electronic excitation, dissociation or ionisation of the background gas caused either by the shock heating at the shock front, or due to emission of energetic photons from the plasma core, are not important. Typically, electronic transitions require energies of several electronvolts, while it has been established that the maximum temperature in the shocked atmosphere is only a fraction of that.

Yet, it remains somewhat surprising that even in the absence of electronic excitation and dissociation, the measured values of γ related to the shock wave strength as described by the Chernyi solution (see table V) are within 5% agreement with the values for an ideal gas. For ideal gases, the well know relation

$$\gamma = \left(1 + \frac{2}{f}\right) \tag{4.33}$$

relates the ratio of heat capacities to the maximum number of (accessible) internal degrees of freedom f. The fact that the ideal gas approximation yields accurate results is related to the adiabatic nature of the shock-wave expansion where the pressure and temperature increase simultaneously.. In Appendix C it is shown rigorously that for a van der Waals gas, the change in the specific heat capacities as a function of temperature and pressure is negligible compared to the initial value at P_1, T_1 provided the ratio (P_2/T_2^2) remains small. This condition is fulfilled for any adiabatic process for which $TP^{-(\gamma-1)/\gamma}$ is constant.

Thus, it is concluded that the good agreement of the measured effect of γ with theory is due to the low pulse energy of the CVL. As such, the present findings should also apply to e.g. ablation using femtosecond lasers where the total pulse energy is typically 0.1 mJ. In the case for ablation with $E_0 > 1$ J, using for example (fundamental) Nd:YAG lasers and excimers, a host of secondary processes may become relevant. For these systems, the structure of the shock-wave may be altered significantly. For example, the thickness of the shock-front can no longer be assumed to be 'thin' since it is directly determined by the longest relaxation process involved, i.e. $\Delta R \sim v_R \tau_{relaxation}$ (Zel'dovich & Raizer 1966, chapter VII, section 6). Wu & Fu (1970) showed that ionisation has a significant effect on the decay speed of the shock-wave. Griffith et al. (1956) measured various vibrational relaxation times for polyatomic molecules, showing that for shocks with $M \geq 2$ the internal states of the gas may not even reach thermal

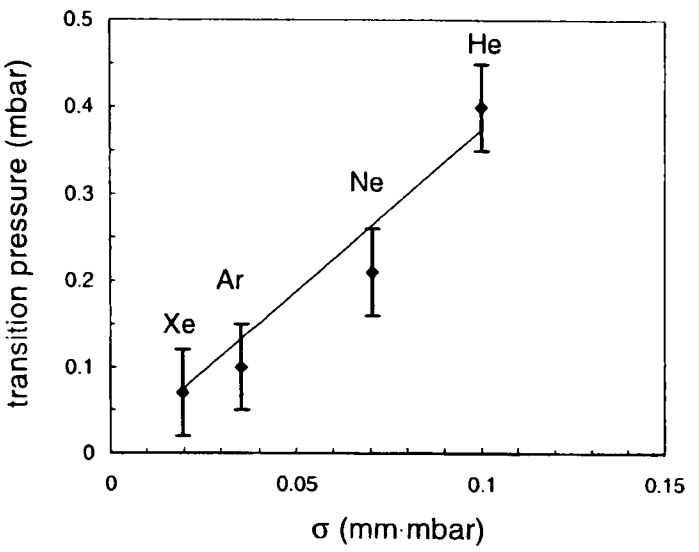


FIGURE 4.17: Experimentally determined transition pressure plotted against $\sigma = \lambda/P$ for five noble gases. The inverse of the slope yields a value for an effective mean free path $\lambda = (0.3 \pm 0.1)$ mm at the transition.

equilibrium. With typical relaxation times of order 1 μs as measured by Griffith et al. (1956), one finds that for $M \simeq 5, \Delta R \simeq 2$ mm, illustrating that the thin-shell approximation becomes invalid considering that for laser produced shocks $R_0 \simeq 10$ mm. Callies et al. (1996) have observed the presence of an ionisation front which is distinctly different from the shock-front, and trails behind the shock front. The thickness of the ionisation front is considerably larger (factor of 5) compared to the shock-front thickness.

Another issue related to the present discussion pertains to the fundamental principle that for increasingly smaller length-scales the gas can no longer be considered as a macroscopic continuum. To illustrate this point, consider figure 4.17, where the low pressure turning point of figure 4.11 is plotted for the four noble gases as a function of $\sigma = \lambda/P_1$, where σ describes the proportionality constant for the mean free path λ as a function of pressure. The inverse of the slope yields $\lambda = (0.3 \pm 0.1)$ mm, defining the transition pressure at which p_{sw} starts to contribute to p_{tot}. This value of λ is associated with the condition that the mean free path of the (shocked) gas should be sufficiently small to sustain a 'thin' shocked layer, without which no shock-wave can be formed. The shock-front thickness ΔR can be approximated to be of order of λ in the shocked-layer (Landau & Lifshitz 1987, section 93). Since $P_R \simeq M^2 P_1$, it is estimated $\Delta R \simeq \lambda_1/M^2$ where λ_1 is the mean free path in the still atmosphere. Given $R_0 \simeq 10$ mm, it is found that when the pressure has decreased below typically 1 mbar, the assumption that the background gas can be described as a continuous fluid becomes increasingly more inaccurate.

All these consideration underline the principle that macroscopic self-similar theory can not be scaled indefinitely to apply to systems where the absolute dimensions of the explosions approach the microscopic

length-scale of the fluid. For example, continuum fluid dynamics can not be applied to account for subtle dynamic effects observed in rarefied atmospheres at low pressures ($P_1 < 1$ mbar) encountered in PLD applications (Sibold & Urbassek 1991, Urbassek & Sibold 1993, Chen et al. 1995, Gonzalo et al. 1995, Wood et al. 1997, Gonzalo et al. 1998). In this case, theories of expansion of dense vapour clouds in atmospheres need to be applied (Keller 1948, Molmud 1960, Greenspan & Butler 1962) which in principle require full solution of the Boltzmann equation (Mott-Smith 1951). The formation of Knudsen layers and unsteady adiabatic expansion has been proposed as a mechanism for the observed forward peaked velocity distributions observed for low fluence ablation (?, Kelly 1990). Often numerical methods and Monte Carlo simulations provide the only practical route to describe these rarefied gas flows (Kools 1993, Itina et al. 1997, Itina et al. 1998). Most recent developments reported by Wood et al. (1997) use the concept of a multiple scattering model to decompose the different components in the plume corresponding to the number of collisions with the background gas. The first order reaches the detector without scattering, the second order undergoes one scattering event, and so on. Such an empirical approach has proven fruitful in reproducing experimental data of time-resolved particle flux measurements, indicating that the importance of molecular processes when operating in the regime of rarefied gasdynamics.

4.4 Conclusion

The modified Sedov-Taylor-von Neumann theory has been shown to provide an accurate description for the formation of shock-waves during laser ablation of aluminium with copper vapour lasers. Measurement of momentum transfer with a ballistic pendulum have shown that the vacuum recoil impulse p_0 can be identified with the recoil due to the piston-mass during the free–flow phase of the shock-wave. Agreement within a factor of two of the calculated value of p_0 with experiment has been established. The influence of the background gas properties on the shock-wave recoil p_{sw} has been measured, and the observed variation of p_{sw} with pressure P_1, molecular weight M_1, and ratio of heat capacities γ are found to be in very good agreement with theory. As such, the mSTN theory can be applied to describe the gross structure of shock-waves formed during laser ablation of materials, provided i) there is no significant coupling between the incident optical field, and the surrounding gas; and ii) the shock-pressure and -temperature are sufficiently low for excitation, dissociation, or ionisation of the background gas to be negligible. For example, shock-waves generated during laser ablation with femtosecond pulsed Ti:Sapphire lasers, or nanosecond pulsed Nd:YAG lasers with low pulse energies ≤ 10 mJ, should be well–described within the regime discussed here. Also, the use of a ballistic pendulum has been demonstrated to provide a simple, yet versatile tool to measure the kinetics of the shock-wave formation process under different background gas conditions. Because the mSTN theory provides full analytical solutions to the shock-wave problem, the theory can be applied to map the (gross) distribution of density, pressure and density of the shocked background gas. These parameters are of critical importance in applications when reactions of the ablated material with the background gas need to be established (Dyer et al. 1990), such as in the development of laser ablation fluorination microprobes for stable isotope important which is the subject of chapter 5.

Beyond the mSTN, however, it should be noted that any description within the framework of continuum fluid dynamics will remain inadequate to describe subtle effects, such as have been observed in laser ablation plasmas in rarefied atmospheres of pulsed laser deposition applications. In this regime, where

continuum fluid dynamics cease to be valid, one has to resort to more complicated rarefied gasdynamical theories, which often involve numerical approaches to solve the Boltzmann equation. Perhaps the findings of the work presented in this chapter are characteristic of the 'spirit' of dimensional analysis, as once formulated by one of its main proponents, Leonid Sedov (1993):

> 'Sometimes at the initial stage of investigation of certain complicated phenomena, dimensional and similarity theory is the only possible theoretical method. However, the possibilities of this method should not be overestimated. The results, which can be obtained with the aid of dimensional theory, are limited and, in many cases, trivial. At the same time, the widespread opinion that dimensional theory does not provide important results at all is completely untrue'

Chapter 5
In-Situ Oxygen Isotope Analysis: Laser Fluorination Microprobes

We must know. We will know.
David Hilbert

The (modified) Sedov-Taylor-von Neumann theory is applied to characterise the shock-wave dynamics relevant to the development of laser fluorination techniques for in-situ oxygen isotope analysis using a UV-CVL microprobe. The fluorination of the liberated metal-oxides is assessed in terms of the thermodynamic evolution of the shocked background gas, which sustains the collisional driven fluorination process. Transport phenomena and geometric effects in the plasma plume are discussed in view of reduction of sampling sizes of laser fluorination microprobes for geochemical applications. The work presented here forms part of a collaboration with E.D. Young at the Department of Earth Sciences, University of Oxford.

5.1 Introduction

I Stable isotope geochemistry The field of stable isotope geochemistry[1] involves the study of the relative isotope fractionation occuring the Nature. In the range of atomic numbers from $Z = 1$ (H) to $Z = 83$ (Bi), only 21 elements are pure elements in the sense that they have only one stable isotope. All other elements are mixtures of at least two stable isotopes for which differences in chemical and physical properties arise from variations in their atomic mass. It is well known that the electronic structure of any element essentially determines its chemical behaviour, causing isotopes to have very similar chemical behaviour. However, this similarity is not complete, and differences exist primarily due to the difference in atomic mass. Due to the relatively large mass difference, isotope effects are therefore most pronounced amongst the lightest elements.

The origin of these small perturbations to the physical chemistry of isotopes lies in their quantum mechanical structure. Chemical isotope effects are primarily caused by changes in the vibrational motion of the elements; rotational and translational motions having little effect on isotope separations. For example, the vibrational zero-point energy of a diatomic molecule, will be lower for the heavy isotope compared to the lighter isotope. Thus the bonds formed by the light isotope are weaker, resulting in a small increase in its reactivity compared to the heavy isotope.

The partitioning of isotopes between two substances or phases of the same substance with different

[1] The short introduction given in the following sections is based entirely on the excellent monograph by Hoefs (1996).

isotope ratios is called 'isotope fractionation'. The main phenomena producing isotope fractionations are i) isotope exchange reactions; and ii) kinetic isotope effects. Isotope exchange reactions are a special case of general chemical equilibrium, where the equilibrium constant is dependent on the ratios of the partition function of the different isotopic species contained in the difference in the vibrational spectra. The difference in the zero-point energy dominates the fractionation process, and is dependent on temperature. Additional effect arising from perturbations such as configuration mixing and the anharmonic atomic potential may also have a small effect on the fractionation process. An important example of isotope exchange reactions are evaporation-condensation processes, where the differences in vapour pressures of isotopic compounds lead to significant isotope fractionations.

The second main group of fractionation phenomena comprises kinetic isotope effects, which are associated with incomplete and unidirectional processes such as evaporation, dissociation reactions, biologically mediated reactions, and diffusion, the latter being particularly significant for geological purposes. Quantitatively, many observed deviations from simple equilibrium processes can be interpreted as consequences of the various isotopic components having different rates of reaction. Isotope measurements taken during unidirectional chemical reactions always show a preferential enrichment of the lighter isotope in the reaction products.

Finally, other factors such as chemical composition, crystal structure and non-mass-dependent isotope effects affect the fractionation of stable isotopes. In these cases, the exact structure of the chemical compound is altered for different isotopes, causing preferential bonding of a particular isotope in, for example, minerals. Non-mass-dependent effect in oxygen isotopes have only recently been explained in terms of the symmetry arguments of molecular dynamics, for example, during the production of ozone using an electrical discharge (Heidenreich & Thiemens 1983, Heidenreich & Thiemens 1985). For a long time non-mass-dependent processes were thought only to occur for nuclear processes, but as shown by Heidenreich & Thiemens (1985) anomalous fractionation can occur during the formation of molecules.

The foundations of stable isotope geochemistry (Hoefs 1996) evolve around two main principles. The thermodynamic properties of isotopic substances as first discussed by Urey (1947), established the concept that the measured isotope exchange equilibrium in (geological) samples is directly related to the chemical equilibrium of the rock. The fact that the fractionation factors are dependent on the temperature forms the key element in isotope geothermometry. The second main technique in isotope geochemistry involves the development of the ratio mass spectrometer (MS) (Nier et al. 1947) as an effective means for measuring isotope abundances.

Without discussing the full details of the naturally occuring variation in stable isotopes for the different elements, there are some generalities that are pertinent in the field of stable isotope geochemistry as a whole. First, detectable isotope fractination occurs only for light elements for which the relative mass difference is large. Besides oxygen, common stable isotopes studied include hydrogen, lithium, carbon, nitrogen, silicon and chlorine, up to mass number of about 40. Also, all elements that form solid, liquid and gaseous compounds which are stable over a wide temperature range are likely to have variations in their isotopic composition. It is generally true that heavy isotopes tend to accumulate in the solid phase, or in molecules where they are often present in the highest oxidation stage. Finally, isotopic variation in most biological systems can be best explained by assuming kinetic effects, where for example

during photosynthesis the lighter isotope is often enriched in the reaction product relative to the starting substances. In the following paragraph, these principles are exemplified for oxygen isotope geochemistry.

II MICROANALYSIS OF OXYGEN ISOTOPES IN NATURE Oxygen is the most abundant rock-forming element in our solar system. The terrestrial abundances of its three stable isotopes are

$$\begin{aligned} {}^{16}\mathrm{O} &: 99.763\% \\ {}^{17}\mathrm{O} &: 0.0375\% \\ {}^{18}\mathrm{O} &: 0.1995\% \end{aligned}$$

Because of its higher abundance, usually the $^{18}O/^{16}O$ ratio is analysed, which may vary in natural samples by about 10%, or equivalently 1:475 to 1:525. The most common standard used refers to the isotopic composition of Standard Mean Ocean Water (SMOW), and is expressed in terms of the 'delta' (δ) values defined as (in this case for the ratio $^{18}O/^{16}O$)

$$\delta\,{}^{18}\mathrm{O} = \frac{({}^{18}\mathrm{O}/{}^{16}\mathrm{O}) - ({}^{18}\mathrm{O}/{}^{16}\mathrm{O})_{\mathrm{SMOW}}}{({}^{18}\mathrm{O}/{}^{16}\mathrm{O})_{\mathrm{SMOW}}} \tag{5.1}$$

Owing to its prevalence in the universe, oxygen isotope geochemistry involves study of both terrestrial and extraterrestrial minerals. Also, the importance of oxygen to biological organisms makes it a significant parameter in the study of the biosphere, for example, in the interaction of the atmosphere within terrestrial living organic matter.

Conventional oxygen isotope analysis primarily involves conversion of the analyte oxygen to CO_2 over heated graphite for subsequent mass-spectrometric analysis. Extraction of oxygen from the silicates and oxides is done through flourination with F_2, BrF_5, or ClF_3 in nickel reaction vessels which are externally heated to temperatures of $450 - 650$ °C for up to 18 hours. Alternatively, decomposition by carbon reduction at $1000 - 2000$ °C may be suitable for quartz and iron oxides. The use of relatively large nickel reaction vessels is prone to give large spurious concentrations of native oxygen effusing from the apparatus to preclude analysis of small samples, restricting minimum samples sizes to be of order $5 - 30$ mg with typical precision down to $0.2\,{}^{0}/_{00}$ for certain minerals. The major drawback of these conventional techniques is the long turn-over time for sampling.

Modern trends in the field oxygen isotope geochemistry increasingly focus to develop new techniques to analyse compounds with higher accuracy and precision, at the same time reducing the sampling size to be less than a few micrograms. The present work focuses the characterisation of a laser ablation microprobe, which constitutes a key element in newly developed chemical microanalytical techniques. Below, first an outline of some of the major applications of oxygen isotope microanalysis is given. Subsequently, recent developments in mass-spectrometry and chemical microanalysis are discussed, in as much as they are relevant to the present work. Then, in the final paragraph of this introduction, an overview of the current state-of-the-art of laser ablation microprobes is given, leading to the main body of work in the subsequent section.

The early universe and formation of planetary systems Isotope variations found in extraterrestrial materials have been classified according to different processes such as chemical mass fractionation, nuclear reactions, nucleosynthesis, and/or different sources such as interplanetary dust, solar materials, asteroids and comets. A major difference between extraterrestrial and terrestrial materials is the existence of primordial isotopic heterogeneities in the early solar system. These heterogeneities are not observed on the Earth or the Moon, because they have become obliterated during high-temperature processes over geological time. In primitive meteorites, however, components that acquired their isotopic composition through interaction with constituents of solar nebula have remained unchanged.

Previously, it had been thought that all chemical processes must produce mass-dependent O-isotope fractionations. As first outlined by Bigeleisen (1965) for any mass-dependent isotope effect for two isotopes of mass m and m', and mass difference $\Delta m = m' - m$

$$\log(\text{isotope effect}) \sim \left(\frac{\Delta m}{mm'}\right) \cdot \text{force constant}$$

In the case of oxygen, the enrichment of δ^{18}O relative to δ^{16}O is expected to be approximately twice as large as the enrichment of δ^{17}O relative to δ^{16}O, which is observed for the observed 'terrestrial fractionation line' for which $\delta^{17}\text{O} = 0.52\,\delta^{18}\text{O}$ on a three-isotope correlation relative to δ^{16}O (Clayton 19993). However, selected anhydrous high-temperature minerals in carbonaceous chondrites[2], notably from the Allende meteorite, follow another trend of $\delta^{17}\text{O} = 0.94 \pm 0.02\ \delta^{18}\text{O}$. This observation is based on *bulk* measurements of the calcium-aluminium-rich refractory inclusions (CAI) (Clayton 19993), with relatively poor spatial resolution of the various different mineral types present on the meteorite. While (Clayton 19993) have been able to show a systematic relationship between O-isotopic compositions and mineral type, they concluded that simplest model to describe these observations implies that at least three different nebular isotopic reservoirs must have existed, since there are distinct differences in bulk meteoric O-isotope compositions.

The most recent development of the laser fluorination microprobe described in this chapter have allowed *localised* sampling with accuracies of order 50 μm. With this improved spatial resolution, Young & Russell (1998) have been able to show that of the isotopic composition of the *unaltered* melilite present on the Allende meteorite follow a line with a slope of exactly 1.00 on a plot of δ^{17}O against δ^{18}O, while the isotopic content for minerals which are *altered* due to mass-dependent fractionation or isotope exchange approaches the 0.94 slope as measured by Clayton (19993). Only with the improved spatial resolution have Young & Russell (1998) been able to propose a novel interpretation on the origin of primitive oxygen isotope reservoirs in the early solar nebula. Ongoing research in the field of cosmochemistry continues to address these new findings in terms of non-mass-depedent chemical isotope processes, or the existence of a two-component primordial reservoir in the early solar system.

Terrestrial minerals Studies on the isotopic composition of the upper mantle involves study of highly refractory minerals, such as olivine, zircon or magnesium-rich garnets. Laser microprobe techniques allow minerals with the highest melting temperatures to be analysed on dimensions of single grains.

[2] Chondrites constitute a class of meteorite minerals which display a structure consisting of 'bubbles' or 'spheres', the chondrules.

Investigations of grain-to-grain variation within one sample horizon (horizontal), or with depth (vertical) allow study of subtle heterogeneous isotopic compositions, such as climatic variations over geological time (Girard et al. 1997). In the study of magmatic rocks, the observed variation in isotopic composition is much greater than expected from their temperature of formation. The precision of the laser microprobe may also provide new insights into the behaviour of oxygen at magmatic temperatures (MacPherson & Mattey 1998).

Teeth from fossils and modern mammals The oxygen isotope ratio of tooth enamel has long been considered a useful record of climate, because it is well preserved in fossil records, and tooth compositions depend on variables such as rain and food source compositions, which in turn depend on local and global climate change. In addition, tooth growth over a period of a year or more provides a 'tape-recorder' of short-term seasonal variations both from fossils and for modern mammals. The sampling accuracy determines the temporal precision that can be obtained, related to the rate of tooth growth. In the case of fast growth in herbivores such as horses, millimeter sampling precision is sufficient, while for elephant teeth sample sizes of around 50 μm are required. In order to correlate the stable isotope fractionation data obtained from fossils to climatic changes (Sharp & Cerling 1998) requires understanding of the factors that influence the animal's isotopic composition (Kohn et al. 1996).

III MASS SPECTROMETRY & MICROANALYTICAL TECHNIQUES As outlined in the above, applications in stable isotope geochemistry often involve analysis of small quantities of sample material, for which purpose a host of so-called microanalytical techniques have been developed. A number of chemical analytical techniques have been been integrated and developed alongside microprobe technology, which are key to obtaining the required analytical precision and accuracy.

Firstly, the principle of non-destructive *in situ* microsampling techniques has been employed. Conventional *in situ* analysis involves use of small mechanical drills to extract material for thermal ionisation mass spectrometry (Neal et al. 1995). The major advantage of standard thermal ionisation over techniques using either inductively coupled plasmas or ions beams to ionise the analyte for mass spectrometry, is the much greater precission, and it provides the only route to measure isotope ratios to better than $0.1\,^{0}/_{00}$ (Neal et al. 1995). The principle of *in situ* analysis has been extended to include laser ablation microprobes which replace the mechanical drill.

Secondly, the conventional technique used in oxygen isotope geochemistry involved conversion of (small) amounts of O_2 to CO_2 for mass spectrometer analysis. This conversion step not only puts a lower limit on the sampling size, but also poses difficulties with isotope fractionation (Wiechert & Hoefs 1995). By analysing the O_2 gas directly in the mass spectrometer, the possibility of isotope fractionation during the conversion of O_2 to CO_2 is avoided (Rumble et al. 1997). Modern technologies in the field of oxygen isotope geochemistry focus on the use of fluorinating agents to extract O_2 from the metal-oxide minerals, as first described by Clayton & Mayeda (1963) using BrF_5, and since has undergone rapid development: from 1981 until the present day over 800 papers have reported the use of the fluorination technique for measurement of oxygen isotopes. The current trend towards achieving higher precision forms the main subject of the present work.

Finally, the development of the Oxford laser microprobe systems culminated in the construction of a combined gas chromatography mass spectrometers (GCMS). This technique allows sample sizes to be

reduced from 1 μmole (approximately 0.1 mg of silicate) down to the nanomole level (of order 1 μg of silicate) (Rumble et al. 1997, Young et al. 1998). Conventional gas-source mass spectrometers rely on viscous flow of sample gases, as it is well known that during molecular (rarefied) flow where the mean free path is large, significant fractionation can occur due to non-equilibrium velocity distributions between the light (high velocity) and heavy (low velocity) components. It is common practise in the field of mass-spectrometry to arrange the inlet system to be in the regime of viscous flow to prevent such mass discrimination. Typically, gas pressures of order 100 mbar are used (Hoefs 1996). To further reduce the sampling size, the technique of cryofocusing (Brand 1996) has been employed to pre-concentrate the oxygen analyte at the interface of the vacuum from the sampling chamber (held at pressures of typically $5 - 25$ mbar) and the helium carrier gas.

IV LASER ABLATION MICROPROBES Driven by modern trends in stable isotope geochemistry, and the development of microanalytical techniques, the development of laser ablation microprobes offers the prospect of a number of advantages over conventional stable isotope analysis (Spicuzza et al. 1998), including i) ability to analyse smaller samples; ii) abitily to study refractory materials as laser plasma can sustain sufficiently high temperatures for efficient fluorination; iii) high precision; iv) rapid turn-over; and v) rapid day-to-day calibration. Some of the characteristics of laser microprobes are similar to secondary ion mass spectrometry (SIMS) (Neal et al. 1995), where a beam of primary ions (Cs^+) is focused onto a solid sample to obtain localised analysis. However, while ion probes can obtain sub-micron spatial resolution, they generally suffer from poor analytical precision compared to oxygen extraction by fluorination and isotope ratio gas chromatography mass spectrometry (irm-GCMS) (Rumble et al. 1997, Young et al. 1998). Due to matrix effects, and the secondary ionisation process itself (Hoefs 1996, Neal et al. 1995), signification fractionation of 15-60 $^0/_{00}$ occurs, which can only be corrected to yield precisions of typically $\pm 1 - 2^0/_{00}$. The use of laser ablation microprobes on the other hand, not only allows for reduction of sample sizes, and high spatial resolution (typically tens of microns, depending on the beam quality of the laser beam), but potentially allows for high analytical precision. By appropriate choice of the laser parameters, the sampling of the target via laser ablation can essentially be optimised to provide stoichiometric, material independent sampling. Nevertheless, for applications which do not require high precision, ion-probes may prove a useful alternative to laser fluorination. Fortier et al. (1995) have presented isotope fractionation measurements of magnetite and water at 350°C, using both a laser fluorination and ion microprobe apparatus. Values measured with laser fluorination of -8.47 ± 0.23, and the ion probe -8.60 ± 0.65 were found to be in good agreement, showing the advantage of the use of laser microprobes when higher precision is required (Fortier et al. 1995).

To date the development of laser microprobes has consisted of two approaches. Historically, infrared lasers like CO_2 (Spicuzza et al. 1998, Sharp & Cerling 1998, Rumble & Hoering 1994) and fundamental Nd:YAG lasers (Elsenheimer & Valley 1992, Mattey & MacPherson 1993) were first employed to provide a (quasi-)cw heating source. Typical average powers of order $20 - 60$ W were used, focused down to spotsizes with diameters $50 - 500$ μm. During the long exposure, the molten analyte is allowed to react with the fluorinating background gas, while the laser power is adjusted to remain below the threhold for evaporative ablation ('sputtering') (Mattey & MacPherson 1993). Typically the fluorinating atmosphere consisted of 100 mbar BrF_5 (Spicuzza et al. 1998, Elsenheimer & Valley 1992) or $100 - 500$ mbar of

ClF_3 (Mattey & MacPherson 1993). Interestingly, the use of F_2 has long been unfavoured due to the scarce supply of pure fluorine for GCMS application. The fact that F_2 is a hazardous gas, and the presence any hydrogen impurities to form HF which is severly corrosive to most materials, make the use of F_2 impractical. Furthermore, commercially available fluorine is contaminated with $1-2\%$ of O_2 and N_2, which would interfere with the required accuracy of the GCMS system. Only since the development of solid-state fluorine generators (Asprey 1976), which have been developed alongside KrF excimer technology, has F_2 become of practical importance to this application.

The main limitation when using infrared cw lasers has been the fractionation in the (resolidified) crater rims of the mineral sample. Corrections have to be made for fractionation at the beam edges, where during the volatilisation process the sample has only been partially reacted. Morphological X-ray studies of the crater rims have shown that significant fractionation occurs in the annular regions extending up to several hundred microns radially beyond the rim (Elsenheimer & Valley 1992, Sharp 1992, Rumble & Hoering 1994). One possible solution to this problem requires the use of prepared, small samples which are fluorinated entirely.

A more elegant solution, however, comprises the second category of laser ablation microprobes which have only recently been developed (Wiechert & Hoefs 1995, Rumble et al. 1997, Young et al. 1998), where the extraction of analyte is performed via explosive, evaporative ablation with nanosecond pulsed lasers in the UV, primarily using excimers, and only recently using the frequency doubled UV-CVL output as described here (Young et al. 1998). The short wavelength of the incident radiation is required to establish efficient coupling to the wide-bandgap materials, while the vapourised analyte is allowed to react with the fluorinating background gas in the plasma formed during the explosive ablation process. Furthermore, Rumble et al. (1997) found that crater rim fractionation is not a significant source of error for analysis with UV lasers.

Besides the two main concept of quasi-cw heating and evaporative ablation, there are a couple of other schemes which presently are being developed. The use of relatively low power Ar^+-ion lasers ($7-8$ W, $20\,kW/cm^2$ on target) for analysis of sulphur isotopes relies on combustion of the sulphide minerals (Kelley & Fallick 1990). While the combustion proces provides an easy route to material extraction, it suffers from significant fractionation of around $0-8\ ^0/_{00}$. As the fractionation is mineral specific and reproducible, it can be accounted for to result in best obtainble precision of $0.25\ ^0/_{00}$ (Kelley & Fallick 1990). Future developments beyond current laser microprobe technology incorporates an inductively coupled plasma device (ICP) to overcome unwanted fractionation during extraction of material via laser ablation (Hirata & Nesbitt 1995, Alexander et al. 1998, Eggins et al. 1998, Figg et al. 1998). Particularly for isotope geochemistry of heavy elements such as lead and uranium, differences in the volatility of the atomic species results in significant fractionation. By employing an independent plasma, the formation of molecular species which are a major cause of fractionation, is counteracted (Gray 1985, Arrowsmith 1987). The use of ICPs may prove to be the next generation in the development of laser ablation microprobes, where in the case of oxygen isotope analysis the fluorination process can be controlled with the ICP, independently from the material extraction stage during the laser ablation process. Comparison of different laser sources for ICP-MS made by Geertsen et al. (1994) showed superior performance of UV over infrared lasers in many analytical aspects (reproducibility, matrix effects, quantification, spatial resolution, and sensitivity),

where the use of the shorter UV wavelength reduces undesired plasma coupling, and enhances the laser ablation process of the target matrix.

5.2 SHOCK-WAVE FORMATION & FLUORINATION

I INTRODUCTION In the following, the theory of shock-wave formation as described in chapter 4 is applied to characterise the fluorination process in plasma plume typical of laser ablation microprobes. The incentive for such an analysis was driven by the work of E.D. Young at the Department of Earth Sciences, University of Oxford, on the development of a UV-CVL isotope ratio monitoring gas-chromatography mass-spectrometer (irm-GCMS) system (Young et al. 1998). All of the experimental work described below were performed by E.D. Young. One of the issues which arose during the development of the irm-GCMS system was related to the effects of shock-wave dynamics on the fluorination process, where initially the use of BrF_5 as the fluorinating agent did not always yield reliable and reproducible isotopic sampling. Furthermore, increasing fractionation with increasing sampling size was observed when using BrF_5. On the other hand, use of F_2 resulted in a major improvement in the overall performance of the system.

The main aim of the present analysis, therefore, is to provide an semi-qualitative comparison between F_2 and BrF_5, using (m)STN theory to quantify the thermodynamics of the fluorination process in the plasma plume. In addition, possible mechanisms for spurious fractionantion will be addressed in the subsequent discussion, where various relevant studies from the field of pulsed laser deposition (PLD) will be applied to characterise the fluorination process. Also, a comparison will be made between the Oxford UV-CVL system and the system reported by Rumble et al. (1997) based on excimer laser technology. Before turning to the main body of the exposition, a brief outline of UV ablation of wide-bandgap materials is given.

II UV ABLATION OF WIDE-BANDGAP MATERIALS The physical mechanism of UV ablation of wide-bandgap materials has been widely studied, initially primarily related to the phenomenon of optical damage in solid-state laser engineering (Koechner 1996) but now increasingly focused on applications of UV laser ablation (Duley 1996). One can distinguish between intrinsic and extrinsic processes to generate conduction electrons which mediate the coupling of radiation to the lattice. Intrinsic processes include linear absorption, colour-centre formation and a variety of nonlinear processes such as self-focusing, multiphoton absorption and electron avalanche breakdown. However, for UV ablation at peak power densities of $10^8 - 10^9$ W/cm^2, most of these intrinsic processes are not likely to dominate the optical coupling process. For example, the bandgap in silicates (SiO_2), garnets ($Y_3Al_5O_{12}$) and metal-oxides (FeO, MgO) are typically of order $8 - 12$ eV, well above the typical photon energies of 5 eV (KrF at 248 nm, frequency doubled CVL at 255 nm) up to 6.4 eV (ArF at nm) available from UV laser sources. Also, nonlinear processes will only become relevant for intensities in excess of 10^{15} W/cm^2. Experimentally, the lack of fluence-dependent absorption indicates that linear single-photon processes dominate during ablation with nanosecond pulsed laser (Lowndes et al. 1993).

In the case of geological minerals, extrinsic processes originating from impurities and lattice defects are most likely the dominant pathway for optical aborption. The presence of preexisting ionic impurities

(Fe^{3+}) and charged or neutral oxygen vacancies have associated transitions ranging from 4 to 6 eV, readily accesible by UV photons. In addition, formation of intrinsic colour-centres and exciton induced vacancies (Itoh et al. 1994) can potentially increase the number of defects, ultimately approaching an emperical threshold defect density beyond which single-photon extrinsic ablation is sufficient for ablation. Indeed, experimentally the existence of an incubation period has been observed for ablation of wide-bandgap materials (Ihlemann et al. 1992, Lowndes et al. 1993, Ihlemann et al. 1995, Uger & Kautek 1996), similar to long term colour centre formation in optical materials (Bäuerle 1996, section 13.4.2). However, the exact dynamics for formation of intrinsic defects remains unclear, and the dynamical properties of excitons in wide-bandgap materials continues to be investigated with femtosecond pump-probe experiments (Itoh et al. 1994).

Some trial experiments have been conducted to compare ablation of metal-oxides with the green and UV outputs from the CVL. These experiments comfirmed that material extraction for analytical purposes is best done in the UV. While the available output powers in the visible are an order of magnitude higher (typically 10 W compared to fractions of one watt), efficient vaporisation could not be established for ablation of garnets with the green output. Instead, if any material removal was established at all, this occured via ejection of solid clusters (spallation, fracture), particularly for granular materials, which do not readily fluorinate to yield reliable analysis. Therefore, the UV-CVL output was used in all subsequent experiments. Regarding the ablation process itself, it would be interesting to see whether short-pulse (sub-)picosecond laser sources capable of delivering peak power densities which are sufficiently high for multiphoton excitation to sustain efficient vaporisation for fluorination, or whether this would result in unwanted ejection of macroparticulates (Ihlemann et al. 1992, Ihlemann et al. 1995, Stuart et al. 1995, Stuart et al. 1996, Uger & Kautek 1996).

III THE FLUORINATION PROCESS Fluorination reactions have long since been employed for isotopic analysis (Clayton & Mayeda 1963), first using BrF_5 but later also F_2 and ClF_3. Due to the long 'cooking' times in the reaction vessels, the characeristics of the fluorination agents are quite similar, although it is known that there are differences in terms of the kinetic pathways by which oxygen is liberated from the sample material. Choice of agent was often determined from the point of view of availability, purity, stability, hazard etc. In the case of fluorination in laser generated plasmas, however, the differences in the chemical and kinetic properties of the fluorination agent can be expected to become much more critical. Due to the highly transient nature of the shock-wave where the temperature and density of the shocked gas rapidly evolve on timescales of order 1 μs, the fluorination process can only be sustained for a limited period, and is confined to a certain reaction volume typically of order of the shock-front radius. Clearly the fast fluorination process in such plasmas is different from the long, continuous reaction in nickel vessels.

The main aim of the present discussion is to explore the kinetic differences of the fluorination process arising from the differences in the shock-wave evolution as determined by the properties of the fluorinating background gas, i.e. the initial pressure P_1, the molecular weight M_1, and the ratio of heat capacities γ (following the same notation of chapter 4). Considering the physical picture sketched in figure 4.1, and the temporal evolution of the laser generated shock-wave of figure 4.2, the key issue is to identify where most of the fluorination takes place. Given the absolute timescales of the three phases, i.e. the free-

flow, shock and acoustic phase, it is unlikely that during the short (timescales smaller than 1 μs) initial free-flow phase any fluorination will occur. Instead, it seems reasonable to assume that fluorination will predominantly occur at the contact front, where large amounts of the analyte material comes in contact with the shock–heated fluorinating agent, and where temperatures are sufficiently high to activate the reaction. To what extent this collisionally driven process occurs during the strong shock phase (when the plasma is most dense and hot) or during the subsequent acoustic decay phase (long reaction times) is not evident *a prioiri*. These issues will be addressed in the following, using a simplified collisional model in conjunction with the (m)STN shock-wave theory as described in chapter 4.

Consider the following simplified model, where the fluorination process is assumed to be driven by collisions between the metal-oxide (MO) and the fluorinating agent (F). The reaction rate R is then given by (Atkins 1994)

$$R = k_2 n_{MO_x} n_F \tag{5.2}$$

with k_2 the second-order rate constant, and $n_i = \rho_i / M_i$ is the number density. Assuming an Arrhenius-type reaction rate for molecular collisions, the rate constant k_2 is given by (Atkins 1994)

$$\begin{aligned} k_2 &= \sigma \sqrt{\frac{8 k_B T}{\pi \mu}} \exp\left(-\Delta E_a / k_B T\right) \\ &= A \exp\left(-\Delta E_a / k_B T\right) \end{aligned} \tag{5.3}$$

where ΔE_a is the activation energy for the reaction of interest, μ the reduced mass

$$\frac{1}{\mu} = \frac{1}{M_{MO}} + \frac{1}{M_F} \tag{5.4}$$

and σ is the effective collisional cross-section

$$\sigma = \pi \bar{d}^2 \tag{5.5}$$

determined by the average of the diameters $\bar{d}$ of the two different molecules

$$\bar{d} = \frac{1}{2} \left(d_{MO} + d_F\right) \tag{5.6}$$

By employing the solutions for the thermodynamic properties of the shocked background gas (chapter 4) in terms of the particle velocity v_2, the density ρ_2 and pressure P_2, equations (5.2)-(5.3) are evaluated at different times and positions in the shocked volume in order to arrive at a first order estimate on how the structure and evolution of the shock-wave influences the fluorination reaction. Using the ideal gas law $T_2 = \left(M_2 / k_B\right) \left(P_2 / \rho_2\right)$ yields

$$R \propto \rho_2 \sqrt{T_2} = \sqrt{\frac{M_1}{k_B} \rho_2 P_2} \tag{5.7}$$

		$\mathbf{F_2}$	$\mathbf{BrF_5}$
M_1	[amu]	38.00	174.90
γ		1.4	1.07
d_1	(Å)	2.3 / 3.4	5.5
μ_{SiO}	[amu]	20.41	35.21
A'	[Å^2/amu]	0.2	0.1
ΔE_a	[eV]	0.04 (460 K)	

TABLE IX: Molecular properties of the two fluorination reagents F_2 and BrF_5

and thus (5.2) can be expressed as

$$\begin{aligned} R &= \sigma n_s \sqrt{\frac{8}{\pi \mu M_1}} \sqrt{P_2 \rho_2} \exp\left(-\Delta E_a / k_B T_2\right) \\ &= A' n_s \sqrt{P_2 \rho_2} \exp\left(-\Delta E_a / k_B T_2\right) \end{aligned} \tag{5.8}$$

Equation (5.8) shows explicitly how the reaction rate R depends on ρ_2, P_2, T_2, which can be compared vis-à-vis the molecular properties of the reaction itself, i.e. the pre-exponential A' and the activation energy ΔE_a. This result forms the basis of the present analysis. In the following paragraphs a number of calculations will be presented on how eq. (5.8) can lead to significant differences in the fluorination process, using the (m)STN theory as discussed in chapter 4 . Two fluorination agents, F_2 and BrF_5, will be considered. In the subsequent discussion various issues related to optimisation of the laser fluorination process will be addressed, together with an explicit comparison between the Oxford UV-CVL system and the arrangement reported by Rumble et al. (1997) using excimer laser technology.

IV CALCULATIONS Consider the molecular properties of F_2 and BrF_5 as listed in table IX, obtained from the standard literature (Chase et al. 1985). Chemical data for F_2 and BrF_5 are obtained from the Gmelin database (Meyer 1990, Meyer 1991). The molecular weight M_1 and the ratio of heat capacities are required for the calculations using the Sedov-Taylor-von Neumann theory, as discussed previously in chapter 4. In order to calculate the pre-exponential A', an approximate value for the molecular diameter is also given. The listed values for d_1 are based classical approximations using either the van der Waals b-coefficient (see also Appendix C) or cross-sections derived from viscosity measurements (Meyer 1990, Meyer 1991). Alternatively, an effective diameter based on calculation of the Lennard-Jones potential for the particular molecule can be used(Reid et al. 1987). An approximation for the activation energy ΔE_a is obtained from comparison of different fluorination reactions of metal-oxides. Typically, for example, for fluorination with F_2 of CuO, $\Delta E_a = 0.04$ eV, and for TiO_2, $\Delta E_a = 0.06$ eV, and similar activation energies apply for fluorination with BrF_5. Clearly the chemical reactivity also depends on the exact thermodynamic conditions (pressure, density), rendering the value listed here only to be gross estimates. To evaluate the difference in A' for F_2 and BrF_5, the fluorination of an SiO molecule is taken as a characteristic example. Thus, taking the reduced mass μ and effective average collisional cross-section σ into account, one finds that A' is only a factor of two larger for F_2 compared to and BrF_5. As will be shown below, this small difference in the pre-exponential factor A' between the different fluorination

laser	sampling per shot	reagent	$R^* \sim \left(\frac{M_s}{\rho_1}\right)^{1/3}$	$R_0 \sim \left(\frac{E_0}{P_1}\right)^{1/3}$
UV-CVL (255 nm)	20x20x0.02 μm	5 mbar F_2	20 μm	6 mm
0.1 mJ	0.03 ng	24 mbar BrF_5	10 μm	3 mm
KrF (248 nm)	800x600x0.05 μm	40 mbar F_2	1.5 mm	25 mm
60 mJ	0.1 μg	40 mbar BrF_5	1.3 mm	25 mm

TABLE X: Main process parameters for the excimer and UV-CVL oxygen microprobe experiments. The analyte masses are based on almandine targets (4.1 g/cc) and inferred from the multishot averages of the oxygen yields or based on the morphology of the ablation crater

agents is negligible compared to the variation in the product $\sqrt{\rho_2 P_2}$.

In table X the characteristics of the UV-CVL system are listed, giving laser pulse energy, the average material extraction per shot, and the properties of the two fluorination agents, to be used to the calculations below. For later comparison, the details from the excimer system reported by Rumble et al. (1997) are also listed. For the present analysis it is assumed that the amount of extracted material $\left(M_s \simeq \rho_s R_s^3\right)$ is independent of the background gas, as discussed earlier in chapter 4. Although no direct measurements of momentum transfer have been performed on the UV ablation system, it is assumed to a first approximation that a large fraction ($> 50\%$) of the incident pulse energy $E_0 = 0.1$ mJ drives the shock-wave, similar to the measured values for ablation of aluminium as described in chapter 4. This assumption seems reasonable since the strong-shock conditon $E_0 > M_s c_0^2$ is satisfied $\left(0.1 \text{ mJ} > 0.03 \text{ ng} \cdot (300 \text{ m/s})^2\right)$.

Applying mSTN theory yields the following results for the calculated thermodynamic characteristics of the shock-wave in the fluorinating gas. Shown in figure 5.1 is the evolution of the shock-front $R(t)$, alongside the product $\sqrt{\rho_R P_R}$ as a measure for the collisional rate. Typically, the maximum shock-front radius R_0 (also given in table X) is around a few millimeters both for F_2 and BrF_5, which both also exhibit similar expansion timescales. The product $\sqrt{\rho_R P_R}$ is also similar for F_2 and BrF_5, showing only a small difference during the free-flow phase due to the difference in density. The shock-front temperature T_R is plotted in figure 5.2 as a function of the shock-front position R. Due to the lower value of γ, the peak temperatures in BrF_5 is calculated to be lower at all times relative to F_2, due to the excitation of internal rotational and vibrational modes as described in chapter 4.

The temperature distribution and normalised collision rate of the shocked gas behind the shock front is plotted in figure 5.3, showing the normalised value of the product $\sqrt{\rho_2 P_2}$ and temperature T_2 relative to $\sqrt{\rho_R P_R}$ and T_R respectively, against the dimensionless parameter $\lambda \equiv r/R$. Due to the difference in γ for the two gases, the self-similar form-factors are significantly different. Rarefaction behind the shock-front is larger for BrF_5, showing that for $\lambda < 0.5$ no significant collisional rates can be expected. On the other hand, the product $\sqrt{\rho_2 P_2}$ for F_2 extends up to $\lambda = 0.2$, indicating that rarefaction is less severe, leaving more of the fluorinating background gas within the shocked volume.

5.3 DISCUSSION

I EFFECT OF THE BACKGROUND GAS PROPERTIES ON FLUORINATION Considering the main results from the calculations, the first main observation regards the degree of rarefaction behind the shock-front, which is significantly different for gases with different γ. Following the physical picture given in

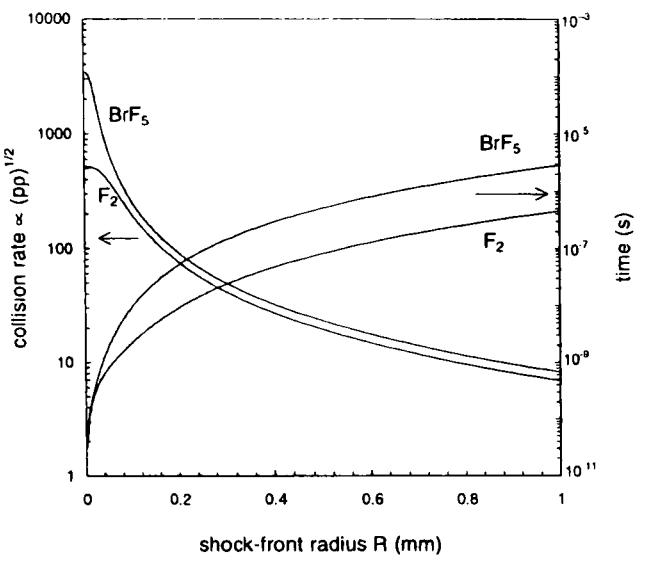


FIGURE 5.1: The collisional rate $R \propto \sqrt{\rho_R P_R}$ (R has dimensions $\mathrm{m^{-3}s^{-1}}$) plotted against shock-front radius $R(t)$ for the F_2 and BrF_5 system.

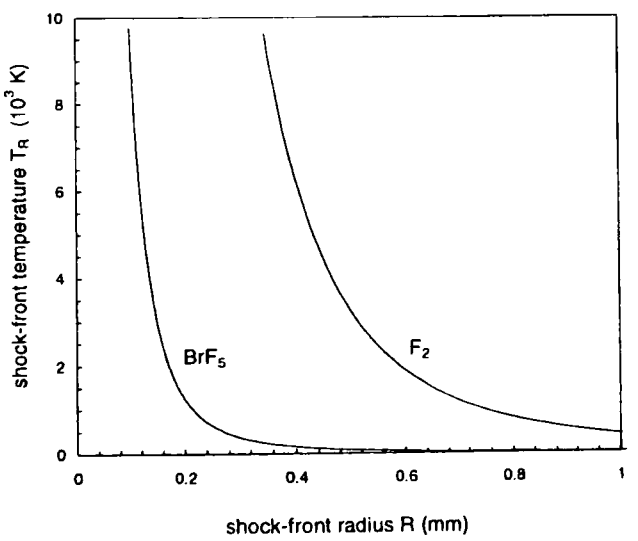


FIGURE 5.2: The shock-front temperature T_R plotted against the shock-front radius for F_2 and BrF_5.

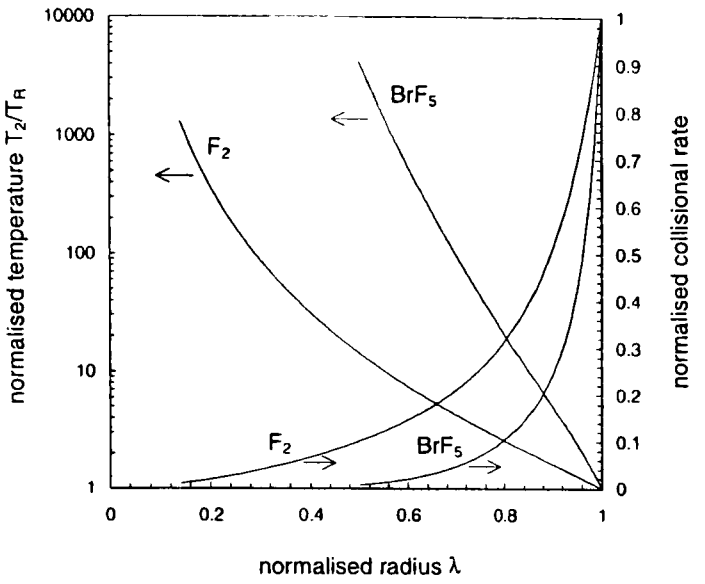


FIGURE 5.3: The normalised temperature T_2 and collisional rate $\propto \sqrt{\rho_2 P_2}$ plotted against the (self-similar) normalised shock-front radius $\lambda \equiv r/R$, where the values of T_2, $\sqrt{\rho_R P_R}$ at the shock-front are set to unity, for F_2 and BrF_5.

chapter 4, the analyte metal-oxide vapour is assumed to be primarily contained within the contact-front radius R^*, with corresponding analyte densities $n_{MO} \propto \left(M_s/R^{*3}\right)$. Thus, the fluorination process is likely to occur at the contact surface, where significant amount of analyte material is mixed with the shocked (high temperature) fluorinating agent. If, due to the inherent structure of the shock-wave, no significant reaction rates can be sustained at the contact-front, this can be expected to result in a poor fluorination process. As illustrated in figure 5.3, the product $\sqrt{\rho_2 P_2}$ decays more rapidly for BrF_5 than for F_2 with increasing distance away from the shock-front. Given that at the shock-front $\sqrt{\rho_R P_R}$ is of the same magnitude for both gases (figure 5.1), it is concluded that the use of F_2 is favoured over BrF_5 to achieve efficient fluorination based on the comparison of distribution of $\sqrt{\rho_2 P_2}$ inside the shock-front .

Secondly, consider the exponential $1/T_2$ dependence of the fluorination rate equation (5.8). As shown in figure 5.2 there is a significant difference in the maximum shock-front temperature, with T_R being up to an order of magnitude higher for F_2 than BrF_5. From the temperature distribution in the shocked-gas T_2 shown in figure 5.3, on the other hand, the ratio T_2/T_R is calculated to be a factor ten or more higher for BrF_5, thus diminishing the absolute difference in temperature for the two gases. Physically, this difference in temperature is associated with the excitation and subsequent relaxation of internal rotational and vibrational modes of the background gas. This causes the maximum temperature at the shock-front to be higher for F_2, which has fewer internal modes than BrF_5. A corollary of this, is that the ratio T_2/T_R is higher for BrF_5 where during the relaxation behind the shock-front the internal energy is converted back to kinetic energy. Within the (m)STN model this relaxation is assumed to occur on timescales much shorter than the typical timescales of the propagation of the shock-front. Realistically, however, vibrational relaxation times may be sufficiently long (Griffith et al. 1956), leading to significant changes in the shock-wave structure as discussed in chapter 4.

All these consideration lead to the conclusion that with the present analysis no definite statement can be made regarding the effect of the temperature on the rate of the fluorination process for the two different gases. However, given that the the magnitude of the activation energy ΔE_a (table IX) for the fluorination reaction is much smaller than the shock-wave temperature at all times, the temperature dependence is not expected to have a dominant effect in terms of the reaction rate. On the other hand, other effects which are (strongly) temperature dependent may well influence the fluorination process. For example, the different fluorination pathways for F_2 and BrF_5 may lead to re-formation of metal-oxides (Young et al. 1998). In the case of F_2, the two reactions

$$\begin{aligned} F_2^o + Mg^o + 2O^o &\rightleftharpoons MgF_2^o + O_2 \\ 2F^o + Mg^o + 2O^o &\rightleftharpoons MgF_2^o + O_2 \end{aligned}$$

proceed from right to left for temperatures above approximately 5000 K, which is of little relavance outside the shock-wave itself. For BrF_5, on the other hand, the reaction

$$BrF_5 + MgO^+ \rightleftharpoons MgF_2^+ + \frac{1}{2}O_2^+ + BrF_3^+$$

proceeds from right to left below approximately 3000 K, and thus may contribute to re-oxidation of metal-oxides during the after-glow of the plasma.

II FRACTIONATION DUE TO KINETIC & TRANSPORT EFFECTS In order to assess whether kinetic effects may lead to fractionation due to differences in the fluorination rates of the different isotopes, consider the ratio of the reaction rates for two different isotopes O and $'$O

$$\frac{R^{'O}}{R^O} = \frac{A'_O}{A'_O} \exp\left(\frac{\Delta E_O - \Delta E_{'O}}{k_B T_2}\right) \tag{5.9}$$

As shown earlier, the difference in the pre-exponential factor is neglible for F_2 and BrF_5, and similarly it is evident that the difference for different isotope is smaller still. Thus, the remaining kinetic factor which may cause fractionation is contained in the difference in zero-point energies. The magnitude of isotope effect associated with the mass-difference can be estimated by considering the energy difference for the vibrational motion of the diatomic oxygen molecule. The ratio of energies ϕ can be estimated using a classic harmonic potential (Herzberg 1950)

$$\phi = \frac{E_{\mu_1}}{E_{\mu_2}} \simeq \sqrt{\frac{M_{\mu_2}}{M_{\mu_1}}} \tag{5.10}$$

where μ_i is the reduced mass of the diatomic molecule. Thus, taking SiO as an example, we estimate the

relative activation energy for the two possible isotopic combinations with respect to $Si^{16}O$

$$\begin{aligned} Si^{17}O &: 0.9811 \\ Si^{18}O &: 0.9640 \end{aligned}$$

Further, using the approximate value for the activation energy ΔE_a for the fluorination process as given in table IX, compared with the typical temperatures in the plasma T_2 of order of few thousand degrees, an estimate for fractionation due to the difference in the reaction rate using (5.9) is given by

$$\begin{aligned} \frac{R'^{O}}{R^{O}} &= \exp\left(-\frac{\Delta E_a\,(1-\phi)}{k_B T_2}\right) \\ &\simeq 0.992 \qquad (\Delta E_a = 460\ \mathrm{K};\ \mathrm{T}_2 = 2000\ \mathrm{K}) \end{aligned} \tag{5.11}$$

Equation (5.11) shows that for sufficiently high temperatures the difference in the reaction rate due to the difference in the zero-point energy between the isotopes is negligible. Based on classical collisional theory (transitional state theory) the ratio of these constants to first order do not change with temperature, pressure or density since they are related to the inherent properties of the isotopes (collisional cross-section). As such, it is concluded that within the model of collisionally activated fluorination, the predominant effect determining the relative performance of F_2 and BrF_5 is contained in the factor $\sqrt{\rho_2 P_2}$, and is primarily influenced by the difference in shock-wave structure and formation for the different reagents.

Transport effects constitute another class of mechanisms which may lead to spurious fractionation during the fluorination process. Similar mechanisms which may cause fractionation when using non-viscous flows in mass-spectrometers, the relative volatily and kinetic energies of the various molecular species are known to exhibit non-equilibrium distributions. From the field of pulsed laser deposition (PLD) (Geohegan 1994) it is now known that in laser generated plasmas phenomena such as plume splitting and the existence of 'slow' and 'fast' plume components are related to the molecular weight of the different species (Sibold & Urbassek 1991, Urbassek & Sibold 1993, Chen et al. 1995, Wood et al. 1997). A crucial element in the quality control of thin-films produced by PLD is the requirement for good stoichiometric ablation of the substrate. However, often lighter, more volatile species are lost during the transport process (Gonzalo et al. 1995, Gonzalo et al. 1998). For example, Gonzalo et al. (1995) found that the use of an argon or O_2 background gas during PLD growth of BiSrCaCuO films always resulted in an enrichment of the heavier bismuth, relative to the lighter species (strontium, calcium and copper). Subsequent analysis of the plume dynamics by Gonzalo et al. (1998) showed that the stoichiometry is influenced by the background gas pressure, related to the plume length and mean free path effects as discussed in chapter 4.

Transport effects may affect the fluorination process in the following way. Wood et al. (1997) have shown that for ablation of silicon (Si) in helium and argon, more pronounced 'plume splitting' into a 'fast' and 'slow' component was observed for the heavier argon. The observation of 'fast' and 'slow' plume components which are separated on timescales of order 10 μs, longer than the typical shock–

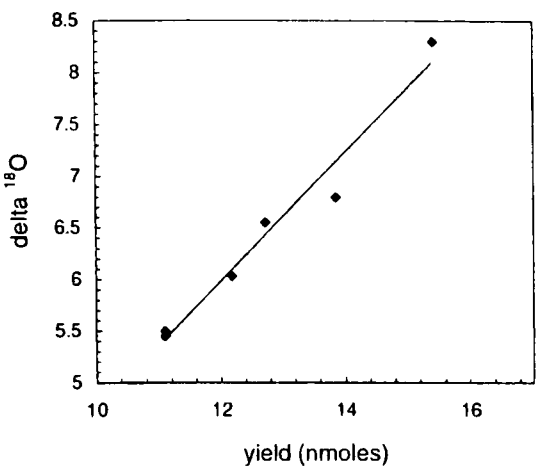


FIGURE 5.4: Measured $\delta\,^{18}O$ ratio using BrF_5 as a function of the total absolute yield (strength of the signal), indicating the presence of fractionation with increasing sampling size. The standard used should yield $\delta\,^{18}O = 6.1 \pm 0.3\ ^{0}/_{00}$. Data are courtesy of E.D. Young.

wave duration of 1 μs, does not seem to favour homogeneous fluorination of metal-oxides as the 'fast' component often consists of volatile lighter elements, while the slow component constitute the heavier species(Sibold & Urbassek 1991, Urbassek & Sibold 1993). Thus, relative differences in the transit time through the fluorinating background plasma is correlated to the mass of the analyte material, which is likely to cause fractionation. Since the degree of plume splitting is related to the relative molecular weight of the background gas with respect to the analyte material, the lighter F_2 seems to be the fluorinating agent of choice. Wood et al. (1997) underline that transfer of kinetic energy between the analyte and background gas molecules forms the key process to equilibrate the velocity distribution. Given that most of the kinetic energy is carried by the analyte, energy transfer is more favourable for lighter background gases.

Indication that transport effects are indeed important is illustrated in figure 5.4, where the fractionation of $\delta\,^{18}O$ is plotted as a function of the yield (signal strength) which is related to the amount of material removed. In this case, the differences in the sampled amount of material per measurement arise due to stochastic variations caused by (small) differences in the laser output power, surface finish of the sampled area etc. The data from figure 5.4 shows that for an increase in material extraction, the isotopic analysis becomes increasingly 'heavy', deviating from the expected standard of $\delta\ ^{18}O = 6.1 \pm 0.3\ ^{0}/_{00}$. This observation could be interpreted that with increasing sampling size, the need to establish fast fluorination becomes more stringent. An increase in the amount of material extracted should, to first order, not change the thermodynamics of the background gas, thus leaving reaction rates unchanged. However, an absolute increase in the amount of analyte material may well require longer reaction times, during which transport effects may cause fractionation due to preferential 'escape' of lighter isotopes, which remain unfluorinated in the form of metal-oxides and hence are not detected.

III COMPARISON OF EXCIMER & UV-CVL LASER MICROPROBES Having discussed the characteristics of the two different fluorinating agents, the performance of the Oxford UV-CVL system is now compared to the system as described by Rumble et al. (1997). The details of each system are given in table X. In terms of the chemical microanalyis and interfacing to the GCMS the two systems are near enough identical, both employing cryofocusing techniques for direct *in situ* analysis of O_2 gas, also using similar pressures for the F_2 or BrF_5 fluorinating agent. However, while both systems operate at similar fluences of $12-15$ J/cm^2, there is a significant difference in the geometry of the ablation process. While the excimer samples relatively large areas of 600×800 μm using single pulses with $E_0 = 55-70$ mJ to sample 0.1 μg in one single shot, the UV-CVL uses smaller spotsizes of $20-30$ μm diameter at $E_0 = 0.1$ mJ which is raster-scanned using the 4 kHz pulse repetition frequency of the UV-CVL to yield similar values of the average material extraction per measurement. Assuming that to first order the ablation depth per pulse is similar for the two systems, as this is primarily a fluence dependent effect, the amount of material removed per shot is up to a factor 10^3 larger for the excimer. In the above, it has been assumed that the fluorination occurs on shot-to-shot basis where no significant secondary activation of material removed in previous shots occurs. Therefore, the difference in the amount of sampled material for the two systems constitutes a significant difference in the thermodynamics of the fluorination process in the plasma.

First examining the excimer system, Rumble et al. (1997) reports that *in situ* analysis using BrF_5 are less precise, and consistently results in $\delta\,^{18}O$ measurements which are $0.3-1.0\ ^0/_{00}$ higher relative to analysis obtained using F_2. The F_2 results are validated by interlaboratory comparison of the UWG-2 garnet standard for oxygen isotope ratios (Valley et al. 1995). Rumble et al. (1997) also observed the $\delta\,^{18}O$ values to be dependent on BrF_5 pressure, showing an decrease by $1.0\ ^0/_{00}$ for an increase in pressure of 10 Torr. Most accurate results were obtained for 30 Torr of BrF_5. In the case of F_2, however, no pressure effect was observed on $\delta\,^{18}O$ values in the range 15 to 150 Torr. In addition, Rumble et al. (1997) notes that absorption at the 248 nm laser wavelength is larger for BrF_5, resulting in an effective increase in laser fluence of 20% on target when using F_2. The combination of these observations led to the conclusion that F_2 is the prefered fluorination agent.

In comparison with the Oxford system, the observed performance of BrF_5 reported by Rumble et al. (1997) are in line with the proposed mechanism for isotope fractionation due to plume splitting, exemplified in figure 5.4. The dependence of $\delta\,^{18}O$ values with BrF_5 pressure has not been verified on the Oxford system, but overall the interlaboratory comparison has established F_2 as the reagent of choice. Furthermore, reports by Wiechert & Hoefs (1995) confirmed that use of other fluorinating agents such as ClF_3 have failed to match the performance obtained with F_2, while for a 650 mJ KrF system using $10-20$ mbar of F_2 the findings of Rumble et al. (1997) and the Oxford UV-CVL system were confirmed.

Pushing beyond current technology, efforts continue with the goal of achieving ablation crater sizes of 50 μm or less with an accuracy and precision of $0.2\ ^0/_{00}$. In order to explore the physical limitations to reducing the sample size, scale effects relating to hydrodynamics will become important. Modelling of plume instabilities (Yabe et al. 1991) have shown that the stability of the shock-wave is dependent on the dimensionality, i.e. the transition between a planar geometry for large spotsizes towards a smaller, more point-like spherical geometry. Also, Callies et al. (1996) observed that the transition from the

initial planar geometry to the formation of a spherical shock-wave is accompanied with a radial flow along the target surface due to stagnation flow of the evaporated material. The material contained in this radial flow may not readily fluorinate, possibly causing fractionation. In short, for constant fluence the fluorination process may differ greatly depending on the sampling geometry, and at present it remains to be verified which combination of laser parameters and background gas conditions are best suited.

In practice, the use of low pulse energies (< 1 mJ)at high pulse repetition frequencies ($4 - 10$ kHz) seems favourable over high pulse energies (> 50 mJ) at low pulse repetition frequencies ($1 - 20$ Hz) as in the latter case most of the output energy per pulse will need to be attenuated to maintain the fluence in the $10 - 20$ J/cm^2 regime, which has been proven to yield best analytical results. Furthermore, to allow chemical microanalysis of smaller quantities of the analyte generally requires reduction of the reagent pressure. Since the plume length scales as $\propto P_1^{-1/3}$, problems arising due to deposition of analyte material on the chamber windows facing the sample may occur. This underlines the need for careful consideration of the laser parameters with relation to the background gas condition and the formation of shock-waves.

Potentially the use of inductively coupled plasmas (ICP) may allow for separate optimisation of the material extraction process and the ensuing fluorination. However, incorporation of an ICP between the vacuum (ablation) chamber and the GCMS may pose significant technological difficulties, particularly when aimed towards reducing the sampling sizes. The use of secondary gases (argon being the most common) to sustain the discharge may well affect the fluorination process and lead to fractionation via other pathways than those discussed here. Another possible route to generate a secondary plasma to enhance the fluorination process involves use of dual (or multiple) laser pulses (Mukherjee et al. 1998), whereby a second (longer wavelength) laser pulses serves to ignite the plasma generated by the first ablation pulse. Indeed, when operating at high pulse repetition frequency (> 1 kHz) evidence of significant shot-to-shot interaction has been observed in metallic plasmas (see chapter 7), which may be employed to this purpose.

5.4 Conclusion

The present chapter has shown that, by employing the Sedov-Taylor-von Neumann shock-wave theorry in conjunction with a classical Arrhenius-type collisional model for chemical activation, a semi-quantitative characterisation can be made of chemical reactions in laser generated shock-waves. The present work has focused on the fluorination process of geological materials such as silicates, garnets and metal-oxides, using F_2 and BrF_5. In the analysis is was argued that in the pressure range of $1 - 200$ mbar the dominant parameter determining the reaction rates is the product $\sqrt{\rho_2 P_2}$ which effectively determines the collisional rate of the background reagent with the extracted analyte material in the shocked atmosphere. Additional transport phenomena and geometric effects have been discussed, drawing from recent developments in the field of pulsed laser deposition. On balance, all these considerations favour the use of F_2 over BrF_5 due to the following two main effects. First, the shock-wave structure in F_2 has a higher collisional frequency at the contact-front, where fluorination is likely to occur predominantly. And secondly, the lower molecular mass of F_2 enhances kinetic energy transfer from the analyte, which in turn leads to homogenising the plume velocity distributions and thus decreases the probabilty fractionation due to loss of lighter isotopes.

Chapter 6
Continuum Radiation From Cool, Dense Metallic Plasmas

Ex chao lux
GENESIS

The atomic emission spectra from metallic laser ablation plasmas is studied. Estimates for the electron temperature and density for plasmas generated during copper vapour laser ablation of metals are made based on experimentally measured spectra. Characteristics of the observed continuum emission at the plasma core during the early phase of the ablation process are compared with recently developed computer codes to predict spectra from neutral and near neutral species from cool, dense plasmas. The relative contribution of opacity versus collisional Stark line broadening is assessed in view of validation of different spectrophysical plasma models for plasma diagnostic purposes. The contribution of R. Hinch, R. Bates and C. Gardner in assisting with the practical work is gratefully acknowledged, as is also the work of D.J. Heading in applying his code to the experiments described.

6.1 Introduction

I Spectroscopy and plasma diagnostics Spectroscopic techniques have long since been employed as a diagnostic tool for studying plasmas (Bates 1962, Huddlestone & Leonard 1965, Griem 1974, Hutchinson 1987, Thorne 1988, Griem 1997). Besides the interest in the physics community to obtain understanding of plasmas generated during the laser ablation process, the need for versatile diagnostics is also relevant for other practical purposes such as process characterisation or on-line process control tools. In the past decade the number of reports on spectroscopic study of laser generated plasmas in the regime of optical power densities of $10^8 - 10^{11}$ J/cm^2 has increased significantly, spanning a wide range of applications. To list a few, these include welding applications with CO/CO_2 lasers (Boulmer-Leborgne et al. 1992, Schellhorn & Eichhorn 1996) or fundamental Nd:YAG (Lacroix et al. 1997), laser-induced breakdown spectroscopy (LIBS) for quantitative analysis of alloys (Leisz et al. 1989, Sdorra et al. 1989, André et al. 1994, Thiem et al. 1994, Német & Kozma 1995, Német & Kozma 1996, Pichahchy et al. 1997) or environmental samples (Barbinin et al. 1997); study of velocity distributions for pulsed laser deposition of superconducting ceramic materials such as YBCO (Dyer et al. 1988, Geohegan & Mashburn 1989, Fried & Reck 1991, Engst et al. 1994, Geohegan 1994, Morrow et al. 1994), diamond-like carbon (Harilal et al. 1997*a*, Harilal et al. 1997*c*, Harilal et al. 1997*b*, Harilal et al. 1998, Neogi et al. 1998), or metals ni-

trides (TiN) (Hermann et al. 1995); and micromachining of various materials including polymers (Ventzek et al. 1992*a*), metal-oxides (Dreyfus et al. 1986, Dreyfus 1991) and metals (Knudtson et al. 1987, Gilgenbach & Ventzek 1991, Wang et al. 1991, Tambay et al. 1992, Autin et al. 1993).

Due to the rapid expansion of the laser ablation plasma plumes, large density and temperature gradients will exist along the axis of the incoming beam often aligned at normal incidence to the target. Generally, different plasma regimes can be identified, and depending on the specific issues to be addressed via spectroscopic analysis, different diagnostic techniques will be employed. For example, for purposes of LIBS often the recombination radiation emitted in the later relaxation stages of the plume is of interest, as these well defined spectral lines provide the most reliable probe for quantitative analysis via measurement of isolated (resonance) lines of neutral species (André et al. 1994, Engst et al. 1994). The spectra of these recombination plasmas consist of isolated, relatively narrow ($\Delta\lambda < 1$ nm) spectral features as observed at delay times typically $\gtrsim 1 - 2$ μs, and distances of around $2 - 7$ mm away from the target associated with the sonic expansion velocities of the plume over such timescales (Német & Kozma 1995, Német & Kozma 1996). Equally, for applications involving chemical reactions of the ablated material with the ambient background gas to form compounds such as metal-nitrides, the process of cluster and dimer formation during the recombination phase (or also termed recondensation phase) is critical (Marine et al. 1994). By employing laser-induced fluorescence spectroscopy of the vibrational (and rotational) molecular spectra insight into the chemistry and molecular dynamics can be obtained (Dreyfus et al. 1986, Dreyfus 1991, Wang et al. 1991, Matsuo et al. 1997, Geohegan 1994).

II THE EARLY CONTINUUM PHASE

Zooming in to earlier times before the recombination stage, looking at the core of the plasma near the target surface, the presence of broadband radiation 'background' has been observed during the early phase at times < 1 μs in many systems (Knudtson et al. 1987, Fried & Reck 1991, Autin et al. 1993, Engst et al. 1994, Német & Kozma 1995). The atomic emission spectra during what henceforth shall be referred to as the 'continuum' stage, is characterised by very broad spectral features ($\Delta\lambda \gtrsim 10$ nm) which sometimes merge into a blackbody-like continuum, where the concept of individual line shape or line intensity breaks down due to significant overlap of the wings of neighbouring transitions. By using streak-cameras or multichannel optical analysers (OMAs) for parallel scanning of a range of wavelengths (typically $40 - 100$ nm), this continuum has been observed to evolve into the line spectra of the recombination stage, where with increasing time over the expansion of the plasma, the line widths of the individual transitions decrease to ultimately produce the sharp spectral lines (Fried & Reck 1991, Engst et al. 1994). Thus, due to this 'collapse' of the spectral line widths, the ratio of the peak intensity at line centre versus background continuum increases over the evolution of the plasma. This general characteristic particularly holds true for bound-bound transitions, where the total intensity integrated over the whole (broadened) line corresponds to the (constant) oscillator strength (Heading et al. 1997*b*). While issues pertaining to the resolution and imaging conditions of the spectroscopic apparatus need also to be considered (Thorne 1988), the common use of delay times > 1 μs when performing spectroscopic diagnostics on laser ablation plasmas is primarily driven by the need to enhance the ratio of line versus continuum intensities (André et al. 1994).

In contrast to standard plasma spectroscopic methods, which focus on the characterisation of individual spectral lines shapes such as those observed during the recombination stage, diagnosis of the densities

and temperatures from broadband emission becomes increasingly difficult and inaccurate as lines broaden and merge in wavelength space. It is the plasma spectroscopy of this regime, as associated with the emission from the plasma core during the early phase of the evolution of the ablation plume, that will be considered here.

III OUTLINE The main aims of the work presented in the following chapter are twofold. Firstly, from an experimental viewpoint, estimates of the parameters of plasma generated during copper vapour laser ablation of metals are made based on measured spectroscopic data. Identification of neutral and ion transitions are made using photographic plates obtained from time-integrated measurements with a 1 m prism spectrometer. Further time-resolved measurements on the evolution of different spectral lines provide data on the time-scales over which the CVL ablation plasma develops. The results are discussed in relation to the large number of reported experiments, to obtain (first order) estimates of the electron temperature T_e and density n_e and an overall qualitative comparison of these plasmas to other laser ablation systems which operate in similar regime, but with significant differences in for example, the laser pulse energy, and incident wavelength.

Secondly, spectral simulations using the code developed by Heading et al. (1997*a*) and Heading et al. (1997*b*) (henceforth referred to as *CROMWELL*) based on the modified semi-empirical method (MSEM) will be compared with experimental results. To assess the validity and applicability of the MSEM towards describing the broadband emission during the continuum stage, and particularly Heading et al. (1995*b*) approach towards fast computation of such spectra, a discussion of line-broadening mechanisms in plasmas is presented. While an extensive review of classical plasma theory would be well beyond the scope of the present work, and only some elementary concepts are introduced in Appendix D, arguments based on first principles and order of magnitude estimates will provide guidelines as to if, when and where *CROMWELL* is likely to be reasonable and practical towards diagnostics of laser ablation plasmas. Of particular importance in this discussion, is experimental evidence on the importance of self-absorption and opacity broadening in laser ablation plasmas (Autin et al. 1993, Hermann et al. 1998), an effect which is currently not accounted for within *CROMWELL*. In conclusion, implications of these findings are applied to address the practical and academic significance of such spectroscopic plasma diagnostic techniques, compared to other tools and methods which may be employed to develop on-line process control algorithms.

6.2 TIME-INTEGRATED OPTICAL SPECTROSCOPY

I EXPERIMENTAL SETUP As a first step towards spectroscopic study of the laser ablation plasma, studies have been performed on plasmas produced by CVL ablation in air of the following three common, commercial grade metal foils of approximately 0.1 mm thickness:

metal alloy	**composition**
aluminium	Al (> 95%), Mg
copper	Cu (> 95%), Fe (423 ppm), Cr (140 ppm), Cl (115 ppm)
stainless steel	Fe (> 75%), Cr (> 15%), Ni (> 5%)

The composition of the aluminium and stainless steel samples are nominal values for these type of alloys. During the spectral identification it was established that lines from magnesium were present in the aluminium plasma. While investigating the copper spectra, the question arose whether impurities were present in the sample due to unidentified spectral lines. The composition of the copper sample was therefore examined using a scanning proton microprobe (NAPL department, courtesy of Dr. Geoff Grime).

The metal foils of were mounted on either a rotating cylinder or a scanning XY-CNC table to ensure a clean piece of material is continuously exposed during the data acquisition and prevent drilling of the sample. While in practise different CVL systems were used, the characteristics of the lasers were comparable and similar to that of the LS 20-10 described earlier. Both the green and yellow output was used, and focused onto the target using medium to long focal length achromatic lenses (160 – 750 mm) to give power densities of order $10^8 - 10^9$ W/cm^2. All experiments were performed under ambient atmospheric conditions. The plasma plume was imaged onto the slit of a spectrometer using a singlet silica lens, whereby the line of sight was quasi-longitudinal to the incoming laser beam. The choice for such spatial integration of the plume was partly driven by maximising the absolute light yield. Time-integrated spectra were measured using a 1 m prism spectrometer which allowed recording of the spectral region between 200 and 500 nm (UV to green) onto a photographic film approximately 10 cm long. Typical exposure times are around one minute with a slit width of 12 μm. No spectra in the red part of the visible and infrared were recorded, as most characteristic lines of atomic species occur at shorter wavelengths. A Hg - Cd - Zn lamp was used for calibration. The spectral lines were measured using a travelling microscope, and the calibration spectra were fitted to a sixth order polynomial to give a resolution of 0.3 – 0.5 nm over the measured spectral region. Identification of spectral lines was performed using the standard literature (Bashkin & Jr. 1975, Harrison 1969, Lide 1995, Moore 1971).

II SPECTRAL IDENTIFICATION Typical recorded spectra are shown in figure 6.1, figure 6.2 and figure 6.3, respectively for the aluminium, copper and stainless steel sample. Calibration of the spectrometer was performed for each negative separately, using the middle recorded spectrum from the Hg-Zn-Cd lamp. The two lines from the CVL are clearly visible in the bottom half of the spectrum, saturating the image around the 578 and 511 nm lines. The time-integrated (spontaneous) atomic emission spectra were identified by first looking for the resonance lines of each atomic and (singly) ionised species, i.e. those transitions which terminate on the ground-state. In some occasions these transitions are outside the accurately measurable wavelength range, in which case an identification of the next lowest lying transition is sought. Definite spectral assignments are listed below for the aluminium (table XI) and copper (table XII) samples. While spectra of stainless steel were recorded, these have not been investigated, also due to the abundance of lines on the film resulting in poor resolveability (see figure 6.3).

For ablation of the aluminium sample, neutral (Al I) and singly ionised (Al II) aluminium species were identified in the plasma plume (table XI). In Al I most transitions to the $^2P_{1/2}$ ground state were seen, including main transition from the 4s ^{2}S and 3d ^{2}D level (figure 6.4). Transitions involving states with two excited electrons were also observed from the 3s3p4s ^{4}P level to the 3s3p^2 ^{4}P level (λ = 305.0 nm, 306.6 nm). In Al II no transitions to the ground state can be seen as these lie in the VUV region. The characteristic 281.6 nm line from the 4s ^{1}S - 3p ^{1}P transition was observed, and also a series of lines

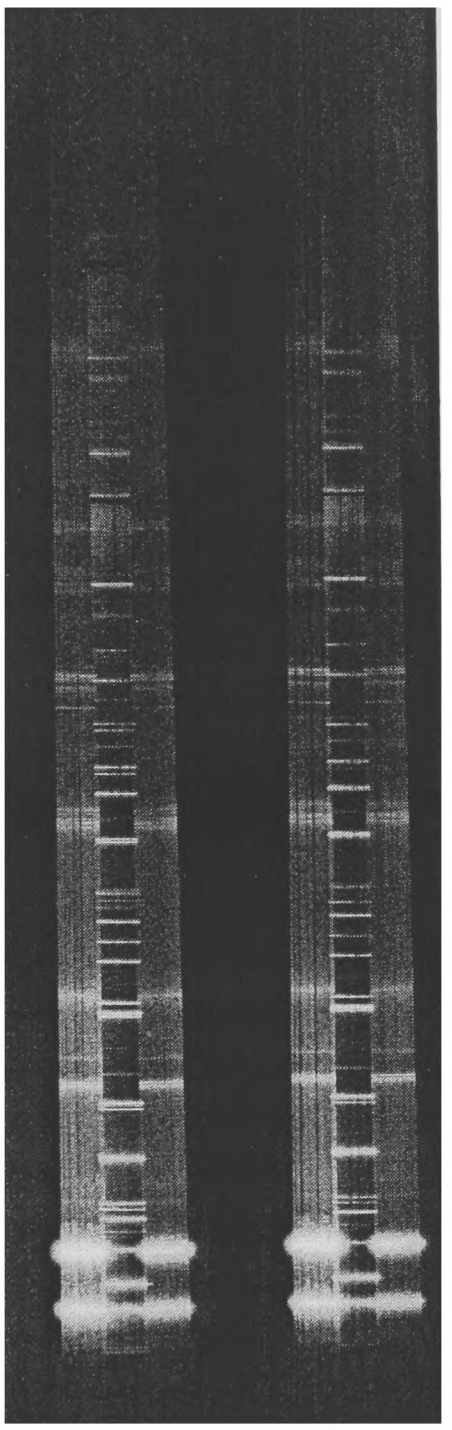


FIGURE 6.1: Two negatives of spectra recorded for aluminium. The central part of each negative shows the callibration from the Hg-Cd-Zn lamp.

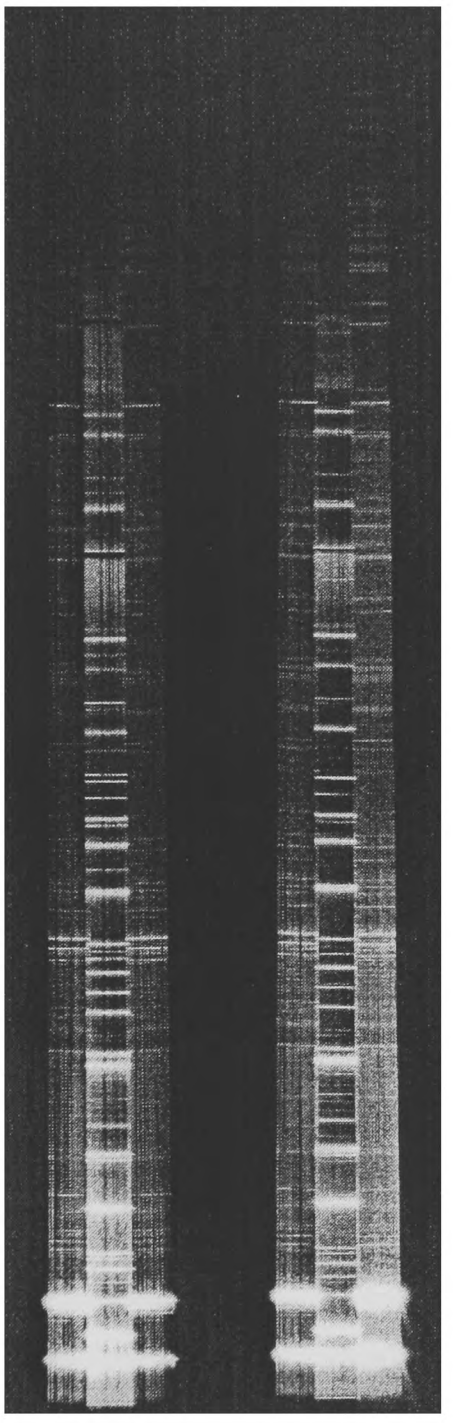


FIGURE 6.2: Two negatives of spectra recorded for copper.

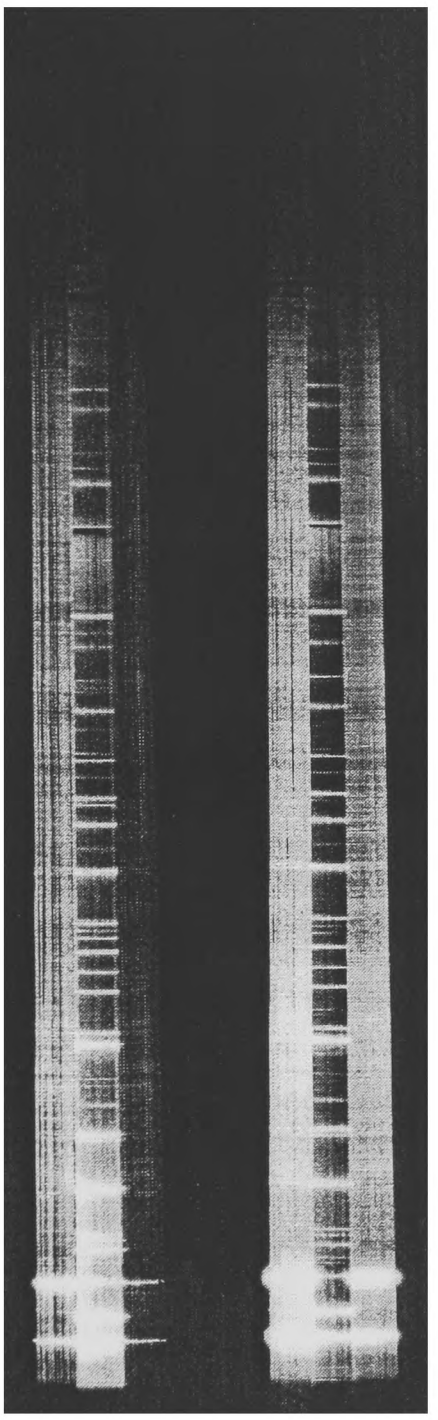


FIGURE 6.3: Two negatives of spectra recorded for stainless steel.

wavelength (nm)	transition	wavelength (nm)	transition
Al I	to $3s^2 3p\ ^2P$ ground-state	Al II	
396.2 / 394.4	$3s^2 4s\ ^2S$	281.6	$3s4s\ ^1S \rightarrow 3p\ ^1P$
309.3 / 308.2	$3s^2 3d\ ^2D$	402.7	$3s6p\ ^1P \rightarrow 3d\ ^1D$
266.0 / 265.2	$3s^2 5s\ ^2S$	299.7	$3s13p\ ^1P \rightarrow 3d\ ^1D$
257.5 / 256.8	$3s^2 4d\ ^2D$	252.0	$3s16p\ ^1P \rightarrow 3d\ ^1D$
237.3 / 236.7	$3s^2 5d\ ^2D$	253.2 / 251.3	$3s14f\ ^1F \rightarrow 3d\ ^1D$
226.9 / 226.3	$3s^2 6d\ ^2D$	358.7 / 358.6	$3s4f\ ^3F \rightarrow 3d\ ^3D$
		263.8	$3s5f\ ^3F \rightarrow 3d\ ^3D$

TABLE XI: Identified resonance transitions to the ground state in neutral aluminium (Al I), and transitions in the singlet and triplet system of singly ionised aluminium (Al II).

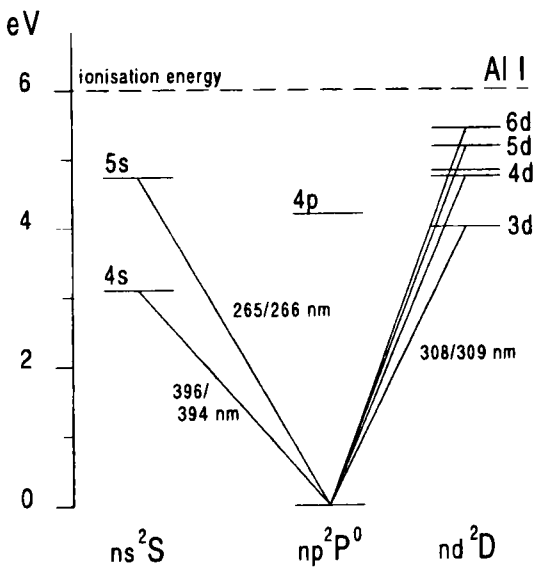


FIGURE 6.4: Partial Grotrian diagram of neutral aluminium, showing the observed main transitions.

wavelength (nm)	transition	wavelength (nm	transition
Cu I	to $3d^{10}4s\ ^2S_{1/2}$ ground state	Cu II	
324.8	$3d^{10}4p\ ^2P_{3/2}$	240.0	$3d^94p\ ^3P \rightarrow 4s\ ^1D$
327.4	$3d^{10}4p\ ^2P_{1/2}$	237.1	$3d^94p\ ^3F \rightarrow 4s\ ^1D$
244.3	$3d^94s4p\ ^4P_{3/2}$		
244.2	$3d^94s4p\ ^4P_{1/2}$		
217.9	$3d^94s4p\ ^2P_{3/2}$		
	to $3d^94s^2\ ^2D_{5/2}$ metastable	450.1	$3d^84s^2\ ^3P \rightarrow 3d^9\,4p\ ^3P$
345.9	$3d^94s4p\ ^4P_{3/2}$	368.8	$3d^84s^2\ ^1G \rightarrow 3d^94p\ ^3F$
333.8	$3d^94s4p\ ^4F_{7/2}$	250.7	$3d^95s\ ^3D \rightarrow 4p\ ^3F$
296.2	$3d^94s4p\ ^2F_{7/2}$	242.4	$3d^95s\ ^3D \rightarrow 4p\ ^3P$
288.4	$3d^94s4p\ ^2P_{3/2}$	287.9	$3d^95s\ ^3D \rightarrow 4p\ ^1P$
	to $3d^94s^2\ ^2D_{3/2}$ metastable		
353.1	$3d^94s4p\ ^4F_{5/2}$	274.6	$3d^95s\ ^3D \rightarrow 4p\ ^1F$
361.0	$3d^94s4p\ ^4P_{1/2}$	271.9	$3d^95s\ ^1D \rightarrow 4p\ ^1P$
328.1	$3d^94s4p\ ^2F_{5/2}$	270.2	$3d^95s\ ^1D \rightarrow 4p\ ^1D$
276.7	$3d^{10}5p\ ^2P_{3/2}$	260.1	$3d^95s\ ^1D \rightarrow 4p\ ^1F$

TABLE XII: Identified transitions in Cu I and Cu II.

to the 3s3d ^{1}D term, and to the 3s3d ^{3}D term (figure 6.5).

For ablation of the copper sample, the majority of the lowest lying optical transitions in Cu I and Cu II were identified (table XII). The main resonance transitions from the $3d^{10}4p\ ^2D$ and $3d^94s4p\ ^4P$ level to the $3d^{10}4s\ ^2S$ ground state of Cu I were observed, alongside transitions to the two metastable states. The resonance lines of Cu II could not be observed as they lie just outside the measurable wavelength range, but a large number of higher lying transitions were identified.

In both the aluminium and copper plasma, additional lines from other elements were observed, identified as impurities or alloy metals. Within the aluminium plasma, additional lines originating from magnesium were identified. Transitions to the lowest singlet and triplet ground state of Mg I were seen, and also transitions to the two lowest levels of Mg II, as listed in table XIII. Practically all lines recorded from the aluminium plasma could be identified as coming from aluminium or magnesium species. In the case of the copper plasma, however, a number of bright lines were observed which remained unidentified are listed in table XIV which are tentatively assigned as transitions originating from doubly ionised Cu III. Other relatively strong lines, possibly from iron impurities, are also listed. However, given that no doubly ionised species were identified in the aluminium plasma, and the relatively low concentration of 423 ppm of iron in the copper sample, the spectral identification of these lines remains inconclusive.

III DISCUSSION From the photographic plates of the time-integrated atomic emission spectra, some qualitative statements regarding the nature of the plasma can be made. First, no significant emission from neutral or ionised background gas species were observed. Particularly, the absence of the well-known N_2 bands (Herzberg 1950) at 337.1 nm ($\Delta\nu = 0$), 357.7 nm ($\Delta\nu = -1$), 380.5 nm ($\Delta\nu = -2$), and 315.9 nm ($\Delta\nu = 1$) leads to the conclusion that no significant power deposition occurs into the background gas, either via direct coupling of the laser radiation, or via shock-heating as discussed earlier in chapter 4.

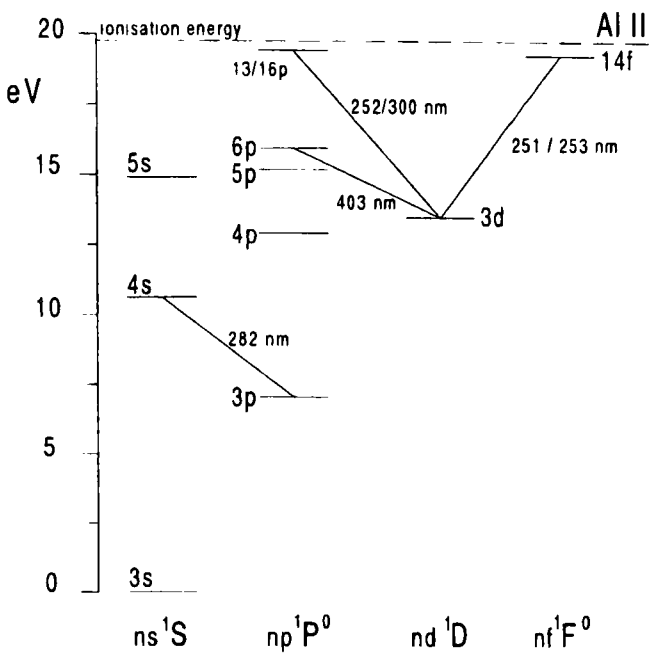


FIGURE 6.5: Partial Grotrian diagram the singlet system of singly ionised aluminium (Al II).

wavelength (nm)	**transition**	**wavelength (nm)**	**transition**
Mg I		Mg II	
285.2	$3s3p\ ^1P \rightarrow 3s^2\ ^1S$	280.3	$3p\ ^2P \rightarrow 3s\ ^2S$
294.2	$3s6s\ ^3S \rightarrow 3p\ ^3P$	279.6	$3p\ ^2P \rightarrow 3s\ ^2S$
293.8	$3s6s\ ^3S \rightarrow 3p\ ^3P$	279.8 - 279.1 (multiplet)	$3d\ ^2D \rightarrow 3p\ ^2P$

TABLE XIII: Identified transitions of Mg I and Mg II in the aluminium plasma.

wavelength (nm)		
Cu III	Iron	unknown
380.9 – 380.4	396.8 (Fe I 396.9)	362.6 – 362.2
250.8	314.8 – 314.2 (Fe II 314.2)	345.6
248.6 – 248.2	247.3 (Fe II 247.3)	344.0
237.4		326.1
236.8 – 236.2		317.6 - 317.1
		242.8
		235.3 – 235.1

TABLE XIV: Bright spectral lines in copper plasma, some tentatively assigned to Cu III and iron species.

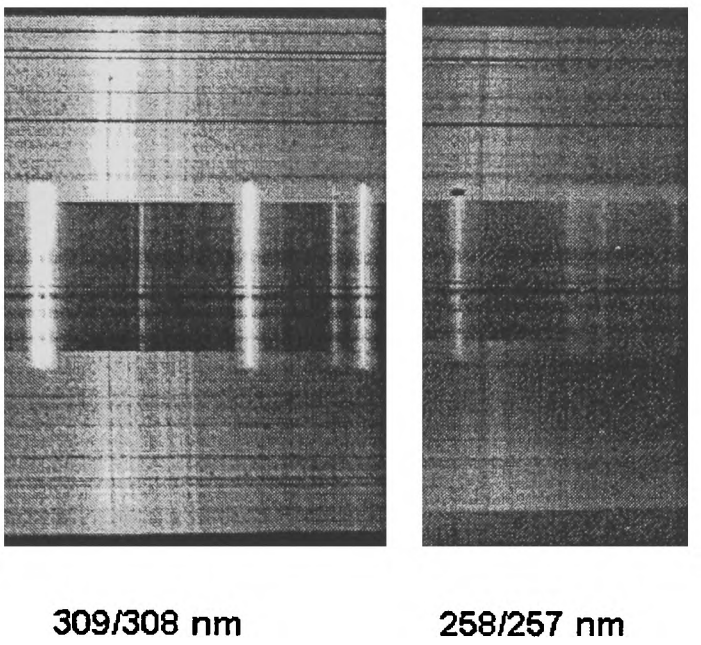


FIGURE 6.6: Observed self-reversal of spectral lines in neutral aluminium.

Secondly, the presence of self-reversed lines in the spectrum of neutral aluminium (figure 6.6) suggests that opacity effects are important in these plasmas. In figure 6.6, an enhanced enlargement of the 309/308 nm, and 258/257 nm aluminium lines clearly show a sharp absorption shadow at line centre against the bright background of the broadened line. Reversal of the 396/294 nm resonance transitions, however, is not observed although this would be expected by considering the partial Grotrian diagram of neutral aluminium (figure 6.4). The absence of self-reversal on the 396/294 nm lines can be ascribed to the relatively low dispersion of the prism spectrometer at longer wavelengths which make it impossible to resolve possible sharp self-reversal shadows. Furthermore, given the high brightness of the 396/294 nm lines, saturation of the photographic film may further obscure observation of self-reversal shadows of these transitions.

Also, the observation that only neutral and ionised species re observed in the emission spectrum already provides a starting point for (order of magnitude) estimates of the electron density n_e and electron temperature T_e. The resonance lines and lower lying transitions of the neutral species are the most characteristic bright features, followed by the lowest lying transition in the singly ionised species which could be seen within the UV-visible wavelength range. While in the case of copper there remains some ambiguity whether Cu III have been identified, for the aluminium plasma no Al III lines have been observed at all times. None of the characteristic transitions of Al III at 361.2/360.1 nm, 371.3/370.2 nm 415.0 nm, or 452.9/451.3 nm (Knudtson et al. 1987, Heading et al. 1995*b*) were observed, which leads to the conclusion that the for the brightest part of the plume, the ionisation fractions are dominated by neutral and singly ionised species. Note that owing to the experimental setup, this statement refers to the total time- and spatially integrated light yield from the plasma, and is therefore likely to be most relevant for the phase where the absolute light yield of the plasma is highest.

To obtain a rough order of magnitude estimate of n_e and T_e, the relative population densities are calculated under the assumption of LTE using the Saha equation (see Appendix D) in the case of the aluminium plasma (figure 6.7). Here the literature values have been used for the ionisation potential for Al I, Al II and Al III of 5.99, 18.83 and 28.45 eV, respectively. To ensure self-consistency, the starting

value of the electron density n_e (fixed for each computation), is compared to the calculated n_e obtained from the ionisation fractions

$$n_e = n_{\text{Al II}} + 2n_{\text{Al III}} + \ldots \tag{6.1}$$

Further, the calculated total density of aluminium species (neutrals and ions) n_{Al}

$$n_{\text{Al}} = n_{\text{Al I}} \left(1 + \frac{n_{\text{Al II}}}{n_{\text{Al I}}} + \frac{n_{\text{Al III}}}{n_{\text{Al II}}} \frac{n_{\text{Al II}}}{n_{\text{Al I}}} + \ldots \right) \tag{6.2}$$

should be consistent with the calculated relative electron densities, and remain below the upper limit set by the solid density of the aluminium target $\simeq 10^{22}$. For electron temperatures $T_e > 3 - 5 \cdot 10^3$ K this resulted in consistent values for n_e, n_{Al} for the three cases considered here. Furthermore, McWirther's condition for the minimum value for n_e to sustain collisional equilibrium (Appendix (D.14)) is also met for all cases considered here. Note that any contribution to n_e due to thermionic emission from the solid target surface is neglected, which may not necessarily be a valid assumption (Cobb & Murray 1965, Kumar & Thareja 1992*a*).

From figure 6.7 it is concluded that, for the observed (integrated) atomic emission spectra to be dominated by neutral and singly ionised species, the electron temperature T_e is limited to be below $\lesssim 2 \cdot 10^4$ K for the larger duration of the plasma evolution. Given the strong dependence of the ionisation fractions on T_e (see Appendix (D.11)), this provides an estimates of $T_e \simeq 5 - 10 \cdot 10^3$ K. However, given the relatively weak inverse scaling law of the ionisation fraction on n_e, the regime of electron density can still vary by three order of magnitude. For lower electron densities $\left(n_e = 10^{17}\ \text{cm}^{-3}\right)$ the excitation to higher ionised stages occurs at slightly lower temperatures, while for higher $n_e = 10^{19}\ \text{cm}^{-3}$ the plasma will consist of Al I and Al II over a larger range of T_e.

These initial estimates for n_e, T_e indicate that plasmas generated during CVL ablation are significantly cooler than those produced by other lasers often used in materials processing (Knudtson et al. 1987, Boulmer-Leborgne et al. 1992, Tambay et al. 1992). The production of such a cool plasma can be ascribed to the combination of the shorter visible wavelength (compared to infrared lasers), the relatively short pulse duration (of few tens of nanoseconds, compared to hundred of nanoseconds), and the low pulse energies (few millijoules, compared to $10 - 100$ mJ). This is clearly illustrated by comparing the present experiments with work reported by Boulmer-Leborgne et al. (1992) on the spectroscopy of CO_2-laser ablation plasmas ($\lambda = 10.6\ \mu$m, $\tau_p \simeq 5\ \mu$s, $E_0 \simeq 50$ mJ). For CO_2-laser ablation, Boulmer-Leborgne et al. (1992) observed inverse Brehmsstrahlung absorption to be the dominant mechanism of power deposition, related to the phenomenon of laser supported detonation discussed earlier in section 4.1.V. In this regime a highly ionised plasma containing triply ionised target species (in this case Ti^{3+}), and singly ionised background gas species (He^+, Ar^+) due to the effect of plasma shielding, whereby machining is achieved due to 'plasma etching' (Boulmer-Leborgne et al. 1992). Also, further comparison with aluminium plasmas produced with single 2 J pulses (50 ns pulse duration) from a flashlamp pumped Rhodamine 6G dye laser for which significant Al III emission has been observed (Knudtson et al. 1987), also show that the CVL plasma is significantly cooler for which only singly ionised aluminium species have been observed here. Similarly, when using Nd:YAG pulses up to 1 J (8 ns), significant emission from Al III has been observed (Tambay et al. 1992). The fact that Tambay et al. (1992) report incident opti-

cal intensities of $3 \cdot 10^{10}$ W/cm^2, similar to CVL experiments reported here, leads to the conclusion that for laser with similar pulse durations (tens of nanoseconds), and similar wavelength (visible to near infrared), the ionisation fractions (and thus electron temperature T_e) of the ablation plasma are primarily determined by the laser pulse fluence. The second order effects of wavelength, and also intensity, are relatively weak, as has been demonstrated by Tambay et al. (1992) who measured the electron temperature T_e for the four different wavelengths accessible with a Nd:YAG laser. Tambay et al. (1992) measured $\lambda^{-0.3}$ wavelength dependence for T_e at constant intensity, while for 1.06 μm radiation T_e scales with laser intensity as $I^{0.3}$.

The plasmas produced with the CVL are more similar to those produced with laser pulse energies of 15 mJ (15 ns) from a Q-switched Nd:YAG laser operating at the fundamental wavelength (Német & Kozma 1995, Német & Kozma 1996). Experiments performed on elemental metals such as copper (Német & Kozma 1995) and gold (Német & Kozma 1996) have shown that for this system also only neutral and singly ionised species are observed in the atomic emission spectra. In the case of the Nd:YAG additional lines originating from oxygen and nitrogen species (both neutral and ionic) are also observed, where likely the longer infrared wavelength results in larger power deposition in the plasma plume. Regarding the observation of magnesium species in the aluminium alloy, experiments reported by André et al. (1994) using 150 mJ (28 ns) pulses from a XeCl laser show similar results in terms of the clear presence of magnesium lines in the aluminium plasma.

In summary, the results from the time-integrated spectroscopic measurements have provided an order of magnitude estimate of the electron density n_e and electron temperature T_e of the plasma. The observation of self-reversal of neutral aluminium resonance lines indicates that the ground-state population densities of Al I are sufficiently high for opacity effects to become important. In the ensuing section, the time-resolved evolution of individual transitions will be studied with the aim to characterise the continuum emission during the early phase of the plasma. To this purpose, the plume will be observed side-on, in order to obtain information on the characteristics of the plasma core (near the target surface) where the emission is highest.

6.3 Time-resolved optical spectroscopy

I Setup During initial trials it became apparent that the presence of backscattered laser radiation obscured reliable measurement of the atomic emission fluorescence for the duration of the laser pulse. To reduce the backscatter and enhance the signal-to-noise ratio, a double-monochromator arrangement was employed by aligning two F/4 SPEX Minimate 0.22 m Czerny-Turner monochromators in series (shown in figure 6.8, each with a 1200 lines/mm grating. The overall resolution of the double-monochromator was 1 nm using 0.25 mm slits, and calibration was performed using a Hg-Zn-Cd lamp. The real and nominal wavelengths were fitted to a second order polynomial to give an overall accuracy of 1 nm. By careful placement of beam-path covers most of the backscattered laser radiation was eliminated beyond the detection limit. The output was measured using a photomultiplier tube (9 dynodes RCA 1P28), which was coupled to a standard dynode chain incorporating storage capacitors on the final three dynode stage to give reasonably fast response times of 2 ns for sufficiently high peak currents. A high voltage (1.2 kV) supply was used to provide the high gain ($\simeq 10^6$), which was adjusted to prevent the peak signal

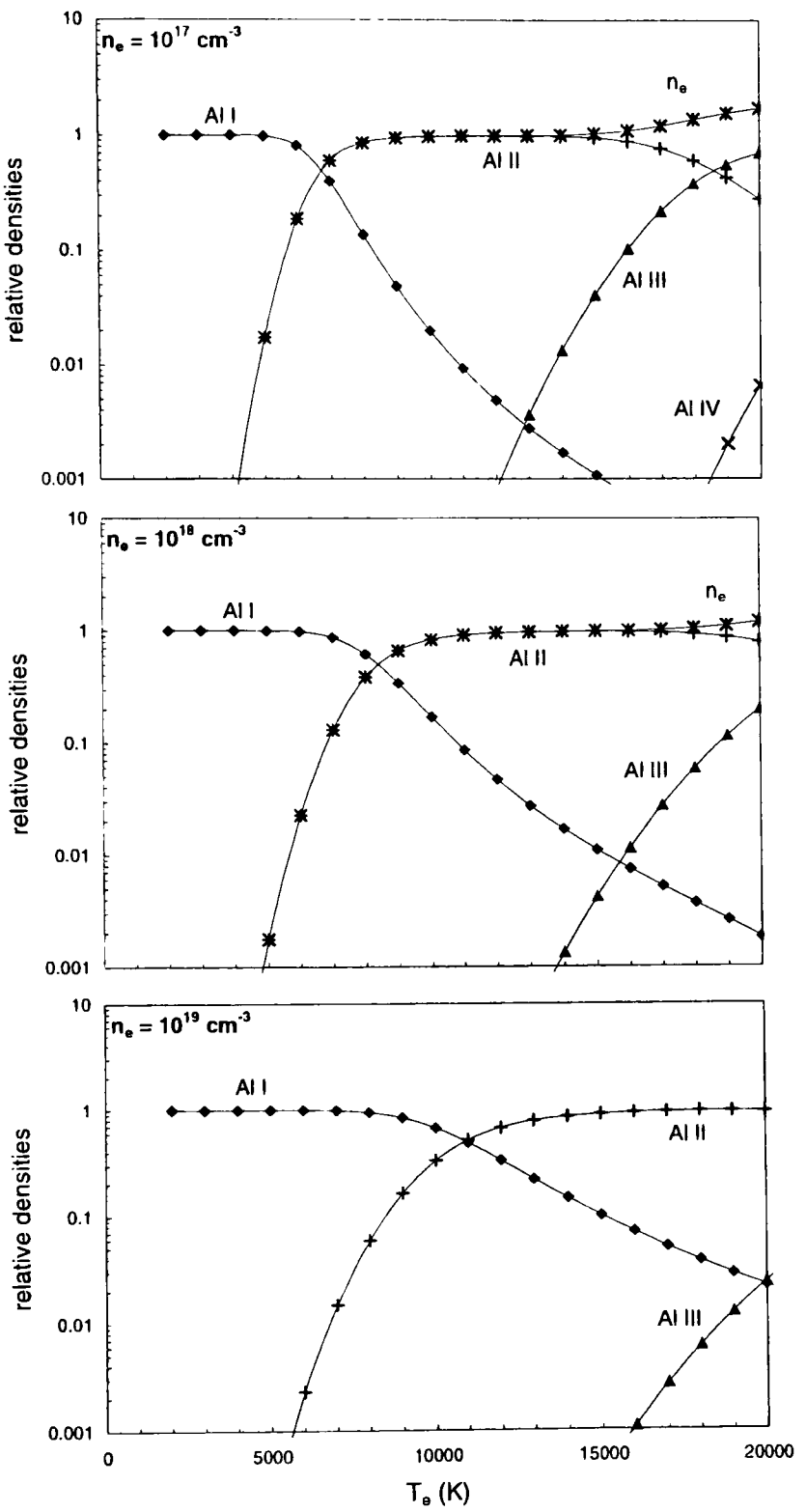


FIGURE 6.7: The relative densities of neutral and ionic species for an aluminium plasma calculated using the Saha equation for three electron densities n_e **a)** 10^{17}; **b)** 10^{18} and c) 10^{19} cm^{-3}.

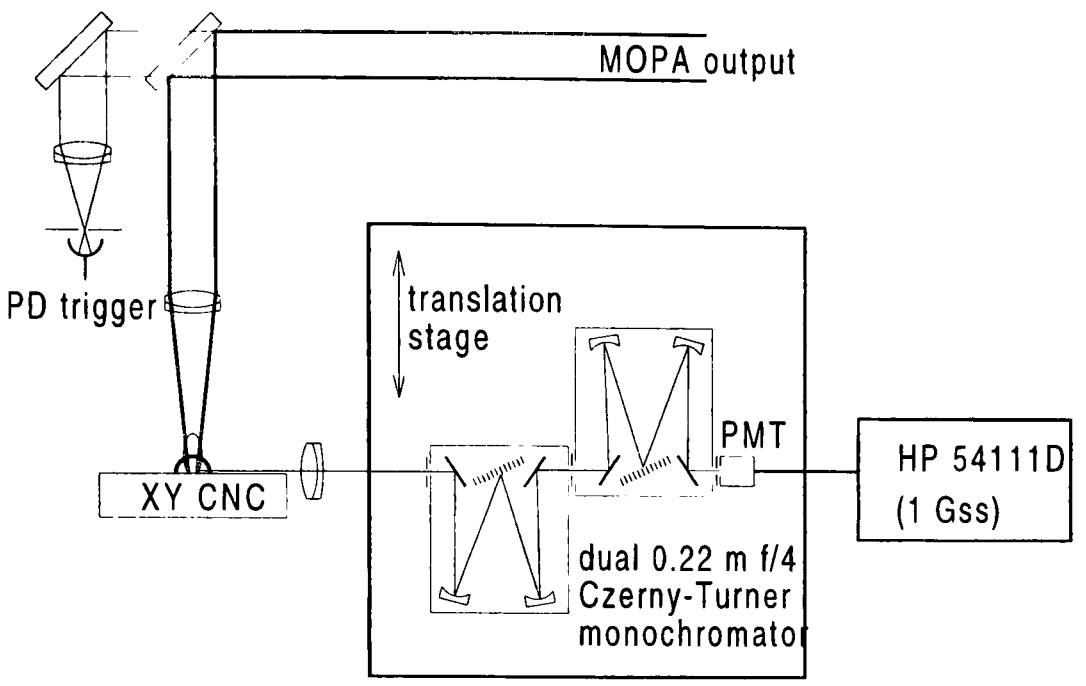


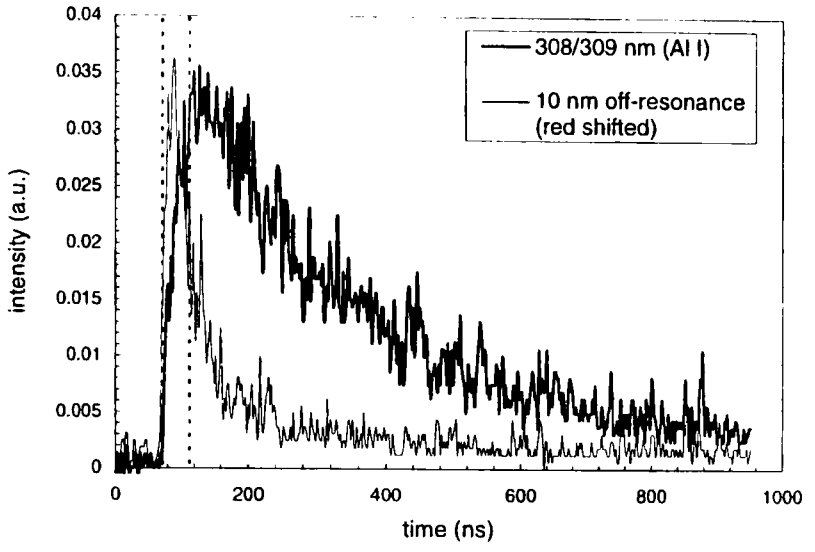
FIGURE 6.8: Experimental arrangement for the recording of the time-resolved spectra, showing the dual monochromator arrangement.

current from saturating by changing the resistance of a parallel impedance load on the photomultiplier output to the scope. Measures were taken to prevent pick-up of electrical noise being amplified by the photomultiplier, and reduction of the dark current was achieved by leaving the high voltage supply on continuously and keeping the dynodes unexposed to ambient light. UV imaging optics were used throughout to allow detection in the $200 - 600$ nm wavelength range. The spatial imaging resolution was of order 0.5 mm, and most of the spectra were recorded directly at the target surface.

The time-traces of various spectral lines, identified earlier from the photographic plates, were recorded with a digital storage oscilloscope (Hewlett-Packard 54111D, 1MΩ coupled) for single-shot, with no additional averaging or normalisation. Various optical band-pass filters were used to enhance the signal-to-noise ratio further, particularly when observing in the UV region. The optical pulse from the CVL was used as a reference trigger to allow comparison of relative timing of the different spectral lines. As discussed earlier in chapter 3, the peak-to-peak jitter of the MOPA CVL system was minimised to allow reliable temporal measurements. The MOPA was used in single-shot mode (PRF > 1 Hz) to rule out possible shot-to-shot plasma interactions. The target was mounted on the XY-CNC travelling stage which was run cyclically to ensure a virgin target surface was exposed for each shot.

II RESULTS

The recorded time-evolution of the two main resonance transitions of Al I are plotted in figure 6.9, showing the 396.2/394.4 nm and 309.3/308.2 nm lines from the 4s ^{2}S and 3d ^{2}D levels to the ground-state, respectively. The signals at line centre are compared to the signal measured 10 nm off-resonance.



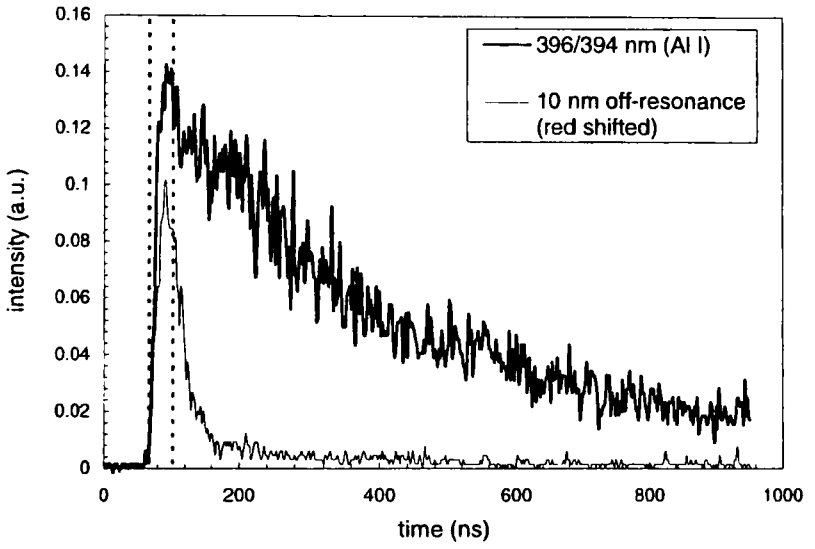
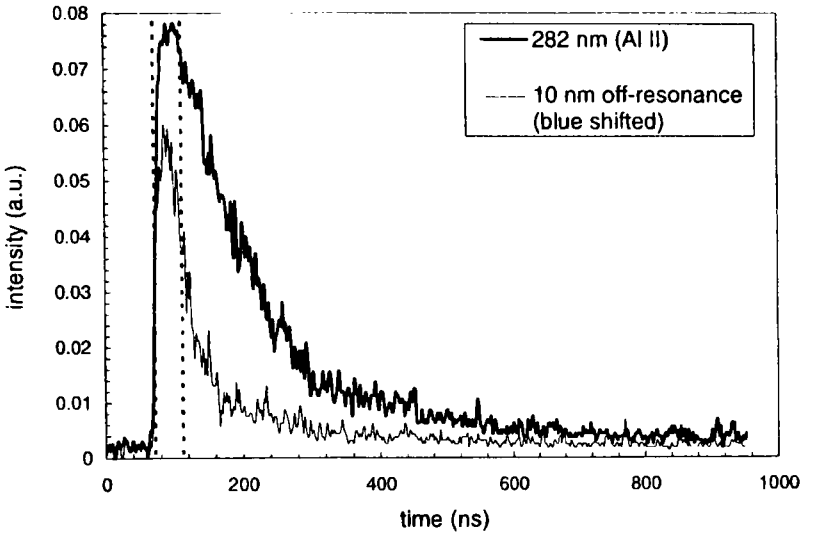


FIGURE 6.9: Temporal evolution of neutral aluminium (Al I) spectral lines, showing the 308/309 nm transition, and the 394/396 nm resonance line as recorded at the target surface.



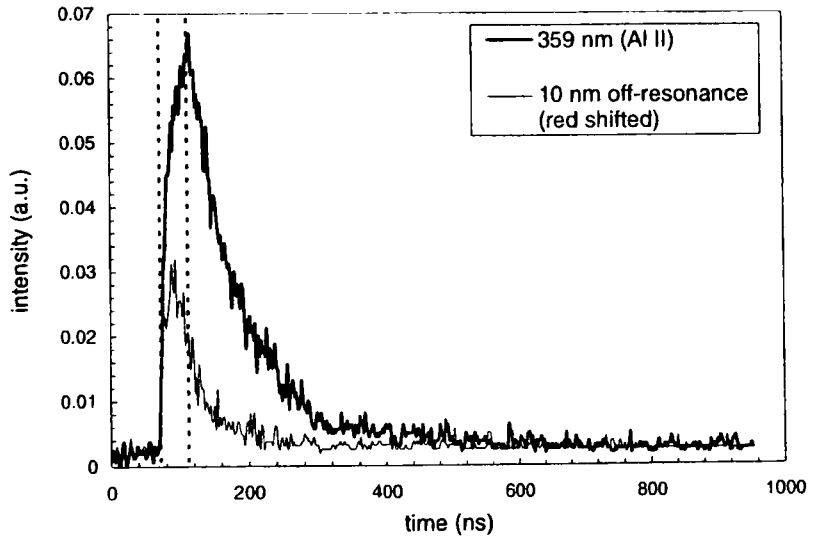


FIGURE 6.10: Temporal evolution of two singly ionised aluminium (Al II) spectral lines as recorded at the target surface.

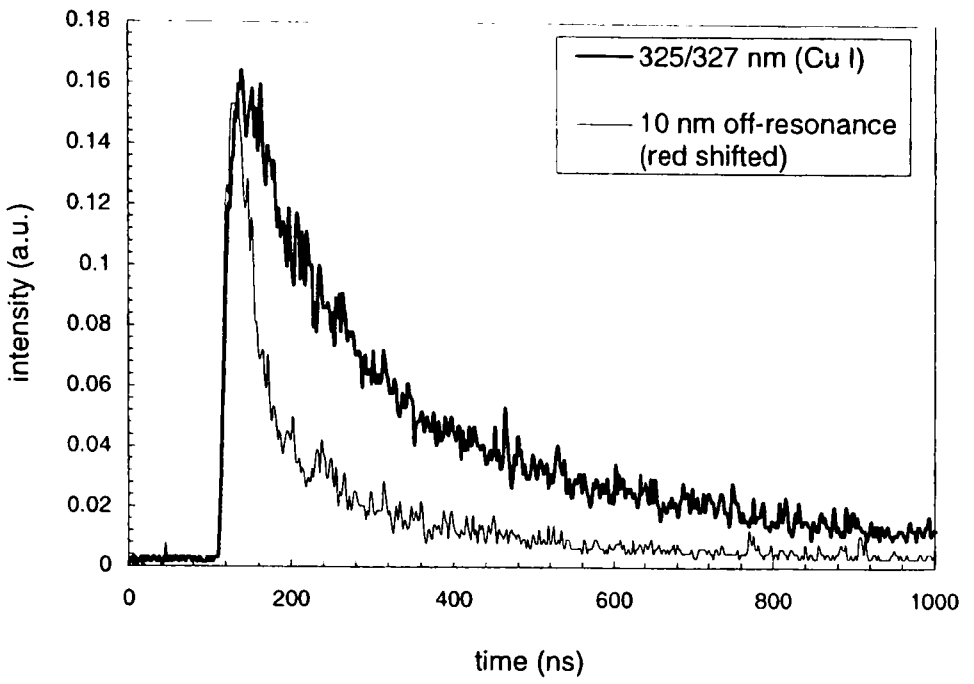


FIGURE 6.11: Temporal evolution of the main resonance line of neutral copper (Cu I) as recorded at the target surface.

Similarly, for Al II the lowest lying observed transitions, from 4s ^{1}S to 3p ^{1}P ($\lambda = 282$ nm) in the singlet system, and 3s4f ^{3}F $\rightarrow$ 3d ^{3}D ($\lambda = 358.7/358.6$ nm) in the triplet system, are shown in figure 6.10. For comparison to the aluminium plasma, the decay of the main copper resonance line is shown in figure 6.11.

From these measurements, a rough description of the temporal behaviour of the plasma core emission can be given as follows. During the first 100 ns, the presence of a broadband continuum is confirmed, where the peak intensity at 10 nm off-resonance is comparable to the peak intensity at line centre. This continuum signal is found to last approximately twice the laser pulse duration, where within the resolution of the current experimental arrangement no significant variations in the characteristic decay times are observed for the continua adjacent to different neutral and ion transitions. Between $100 - 300$ ns fast decay of emission from ions to $< 95\%$ peak value is observed. During this stage the emission from neutrals persist, only to decay over longer time-scales $0.3 - 1$ μs. Most of the atomic emission at the target surface has ceased for delay times > 1 μs after the laser pulse.

In view of verifying whether emission from higher ionised species can be observed at the plasma core, the double monochromator was tuned to various strong transitions in Al III or Cu III. In practise, the wavelength scan was performed by manually tuning the two monochromators across the visible wavelength range in steps of few nanometers. The continuum emission provided a practical feedback signal, and even when far off any main transition, the continuum signal could be maximised to ensure that the two monochromators were tuned to the same wavelength. These wavelength scanning experiments all yielded a null result, where no significant increases in the peak intensity of the continuum radiation could be observed at the line centres of spectral lines from either Al III or Cu III species. Interestingly, it was observed that the absolute intensity of the continuum emission was reached a maximum in the $350 - 400$ nm wavelength range. This finally leads to the conclusion that any emission originating from higher ionised species can only occur during the first 100 ns stage, during which it is obscured by the presence of the bright continuum.

III DISCUSSION The time-resolved experiments further corroborate the initial estimates based on the time-integrated spectra, confirming the predominance of neutral and singly ionised species in the CVL ablation plasmas. Decay of ionic species has been observed on timescales of few hundreds of nanoseconds, while the resonance lines from neutral species persist up to 1 μs. Again, the time-resolved measurements show that the aluminium plasma produced during CVL ablation is significantly cooler than those produced by lasers with higher pulse energies (> 10 mJ) with similar pulse duration (tens of nanoseconds) and wavelength (visible). For an aluminium plasma produced with a 2 J dye laser, Knudtson et al. (1987) measured significant emission from Al II lines for delays as long as 1 ms, and fits of relative emissivities from these lines yields the value for $T_e = 8.13 \pm 0.27 \cdot 10^3$ K. For the present experiments, the emission from ionised aluminium species has decayed well within 1 μs.

Turning to the observed continuum emission during the early phase of the plasma, the present results are in agreement with other reports which have also observed the presence of a broadband continuum (Autin et al. 1993). Extensive experiments performed by Autin et al. (1993) using a 3 mJ, 10 ns nitrogen laser ($\lambda = 337.1$ nm) have yielded very similar time-traces of individual spectral lines measured at line-centre and adjacent detuned continua using a photomultiplier. In case of ablation of copper samples, Autin et al. (1993) observed only Cu I and Cu II species in the plasma plume, which decay over hundreds of nanoseconds similar to experiments reported here. Further, Autin et al. (1993) measured the self-reversal of the Cu I 324.75 nm resonance line, and characterised the effect of the background gas (pressure and composition) on the line-shift and temporal decay of individual spectral lines. By increasing the background gas pressure in the range 0.4 mbar to 1 atm, line-shifts of fraction of 0.12 nm were observed. Decay of the Cu I 521.81 nm line was found occur within 0.5 μs, while in 1 atm of argon this figure was increased fivefold to 2.5 μs. Also, relating to the confinement of the plasma core, loosely identified as the piston-mass of chapter 4, Autin et al. (1993) found that self-reversal was only observed for N_2 or air background gas, but not in rare gases such as helium and neon. Furthermore, while no emission from N_2 or other species present in air was observed (similar to the present results), excitation or argon lines was observed. Autin et al. (1993) concluded that self-absorption (opacity broadening) is the dominant line-broadening mechanism in the dense plasma core, resulting in the observed continuum within the first 0.1 μs.

Regarding broadening and self-reversal due to opacity effects, a number of other reports have confirmed the presence of a blackbody-like continuum in plasmas produced by laser ablation (Fried & Reck 1991, Engst et al. 1994, Geohegan 1994). Using a scanning monochromator coupled to a photomultiplier detector, Engst et al. (1994) have observed a blackbody-like continuum at 50 ns after the laser pulse, peaking around 400 nm, during ablation of bulk BiSrCaCuO with a $35 - 40$ mJ XeCl laser (30 ns). The spectral lines of the Ca^+ and Sr^+ appear as (self-reversed) absorption lines, indicative of the presence of density gradients along the line of sight, and confirming the opacity effects observed of Autin et al. (1993). Similar experiments with a 193 nm ArF laser (150 mJ, 22 ns, 1 J/cm^2) on CuO and BaO_2 by Fried & Reck (1991) have also shown the presence of a blackbody-like continuum, which peaks in the $450 - 500$ nm wavelength range. In this case, however, the spectrum features broad but well-defined lines sitting on top of the blackbody continuum due to the integration time (1 μs) of the gated diode array detector (Fried & Reck 1991). Similarly, Geohegan (1994) have observed opacity broad-

ening and self-reversal of the 455.4 nm Ba^+ resonance line ($6p\,^2P_{3/2} \rightarrow 6s\,^2P_{1/2}$), measured at 1 mm from the YBCO pellet irradiated with 3.0 J/cm^2 (248 nm KrF) in vacuum (10^{-6} Torr) at a delay time $\Delta t = 140 - 200$ ns. In the PLD plasma considered by Geohegan (1994), the densities are sufficiently low such that resonance broadening of strongly allowed electric dipole transitions (such as resonance lines are) is observed. Resonance broadening arises due to dipole-dipole interactions of identical atoms (often in the ground state), in this case giving line widths of 0.3 Å for the 553.5 nm resonance line of barium for ground-state population densities of 1.5 10^{17} cm^{-3}.

Concluding the experimental discussion, the primary question which remains to be answered pertains the relative importance of opacity broadening versus collisional Stark broadening to describe the continuum emission (and subsequent broad line spectra). The observation of self-reversed transitions in neutral aluminium, and other substantiating experimental evidence reported in literature, indicate that indeed opacity broadening is an important (if not dominant) process for the continuum phase, which has been phenomenologically identified to exist for the duration of $0 - 100$ ns. Anticipating the outcome of the ensuing discussion, the broad ($\Delta\lambda \simeq 10$ nm) line spectra in the subsequent $0.1 - 0.3$ μs will be referred to as the Stark phase, and will be argued to be dominated by collisional broadening.

6.4 MODELLING OF COOL, DENSE PLASMAS

I STRONGLY COUPLED PLASMAS Standard line-broadening theory (Griem 1974, Griem 1997) is explicitly valid for only limited range of plasma electron densities n_e and temperatures T_e. The principal result of this theory is that electron-radiator collisions induce Lorentzian spectral profiles with line widths and shifts proportional to $n_e/\sqrt{T_e}$. To arrive at this general result, however, it has been assumed that there is no statistical correlation in the spatial positions of the free, perturbing electrons. As the electron density increases, and the temperature increases, the electron-electron correlations increases proportionally with the plasma parameter g

$$g \equiv \frac{1}{N_D} = \frac{3}{4\pi}\frac{1}{n_e \rho_D^3} \propto \sqrt{\frac{n_e}{T_e}} \tag{6.3}$$

where N_D is the number of particles in the Debye sphere, and ρ_D is the Debye radius (Appendix (D.8)). Thus, in the strong coupling limit ($g \rightarrow 1$) significant deviations from classical line-broadening theory may be expected (Hutcherson & DeSilva 1997), such as may occur in dense, cool plasmas[3].

Further complications which arise when describing the physics of dense plasmas regards the implicit assumption made within the impact approximation of classical plasma theory, which requires that the interaction time of the electron with the radiator is short. As the frequency width of the radiated spectral line ($\propto n_e$) approaches the inverse of the electron-radiation interaction time (proportional to $n_e^{1/3}$), the impact approximation itself becomes questionable for strongly coupled plasmas (Hutcherson & DeSilva 1997). In addition, predicting the ionisation balance becomes increasingly tenuous as it is difficult to calculate the degree of ionisation potential depression (IPD) for these plasmas (Heading et al. 1995*b*). At low electron densities, IPD is irrelevant since the population of excited states is negligible. However,

[3] Within the wider scope of physical plasmas, 'cool' refers to electron temperatures T_e of few electronvolts, at relatively high electron densities of $10^{18} - 10^{20}$ cm^{-3}

at increasingly higher densities calculation of the IPD is required in order to give a finite limit to the partition functions which appear in the Saha equation (Appendix (D.11)). In this case, the ratio of the ion potential (as calculated within the IPD model) to the kinetic energy of the electrons is given by the coupling parameter Γ

$$\Gamma = \frac{(Z^* e)^2}{4\pi\epsilon_0 \rho_i k_B T} \tag{6.4}$$

where Z^* is the effective ion charge, and ρ_i is the average ion sphere, will approach unity into the regime of strongly coupled plasmas (Heading et al. 1995*b*).

Recent advances in the experimental generation of dense, cool plasmas using plasma jet capillary discharges (Hutcherson & DeSilva 1997), or by confining the expansion of laser ablation plasmas of thin films (Bennet et al. 1994, Heading et al. 1995*a*) have provided means to verify existing models of strongly coupled plasmas. Perhaps somewhat surprisingly, detailed line-broadening measurements of an aluminium plasma $\left(n_e \simeq 10^{18}\ \mathrm{cm}^{-3}, T_e \simeq 1\ \mathrm{eV}\right)$ have explicitly demonstrated that the standard Stark broadening theory is insensitive to the small-g and impact approximation assumptions (Hutcherson & DeSilva 1997), and that no significant deviations were observed for these plasmas. Studies by Heading et al. (1995*b*) on confined aluminium plasmas have shown that proper inclusion of IPD does result in some modification of the relative intensities of the spectral line emission from different ionisation species at densities of $n_e \simeq 10^{19}\ \mathrm{cm}^{-3}$ and temperatures $T_e \simeq 2 - 4$ eV. However, no major difference between (near) strongly coupled and weakly coupled lines were observed because strong coupling effects do not greatly influence the spectral line shapes.. Even up to relatively high values of $\Gamma \leq 0.2$ the Saha equation for ionisation balance has been shown to be still approximately valid.

II THE MODIFIED SEMI-EMPIRICAL METHOD Besides these intricacies of the physics of strongly coupled plasmas, in view of the current discussion there are two additional issues which are of importance. First, the role of opacity broadening needs to be considered, as this effect is also often not accounted for in standard line-broadening models. Secondly, from a practical point view, the question arises whether complete continuum spectra can be calculated within reasonable computing times using existing processing technology. The philosophy behind the approach taken by Heading et al. (1997*b*) is primarily aimed to address the latter issue. Using the so-called modified semi-empirical method (MSEM), Heading et al. (1997*b*) have developed a practical and fast code (*CROMWELL*) which allows computation of the full visible-UV within $1 - 2\%$ accuracy intended for rough diagnostics of dense plasmas. The *CROMWELL* code combines semi-empirical methods for line shape calculation together with recently available databases of large quantities of atomic data for (light) elements such as the Opacity Project (Seaton 1995). While semi-*classical* approaches provide more accurate calculations of individual line shapes, they do so at the cost of an increase in computing time by over two orders of magnitude (Heading et al. 1997*b*). Considering that in order to compute continuum spectra, *all* atomic transitions and line shapes need to be calculated, any semi-classical model will quickly approach the limit of existing computational speeds.

The *CROMWELL* code assumes an optically thin, but dense plasma which is accurately described

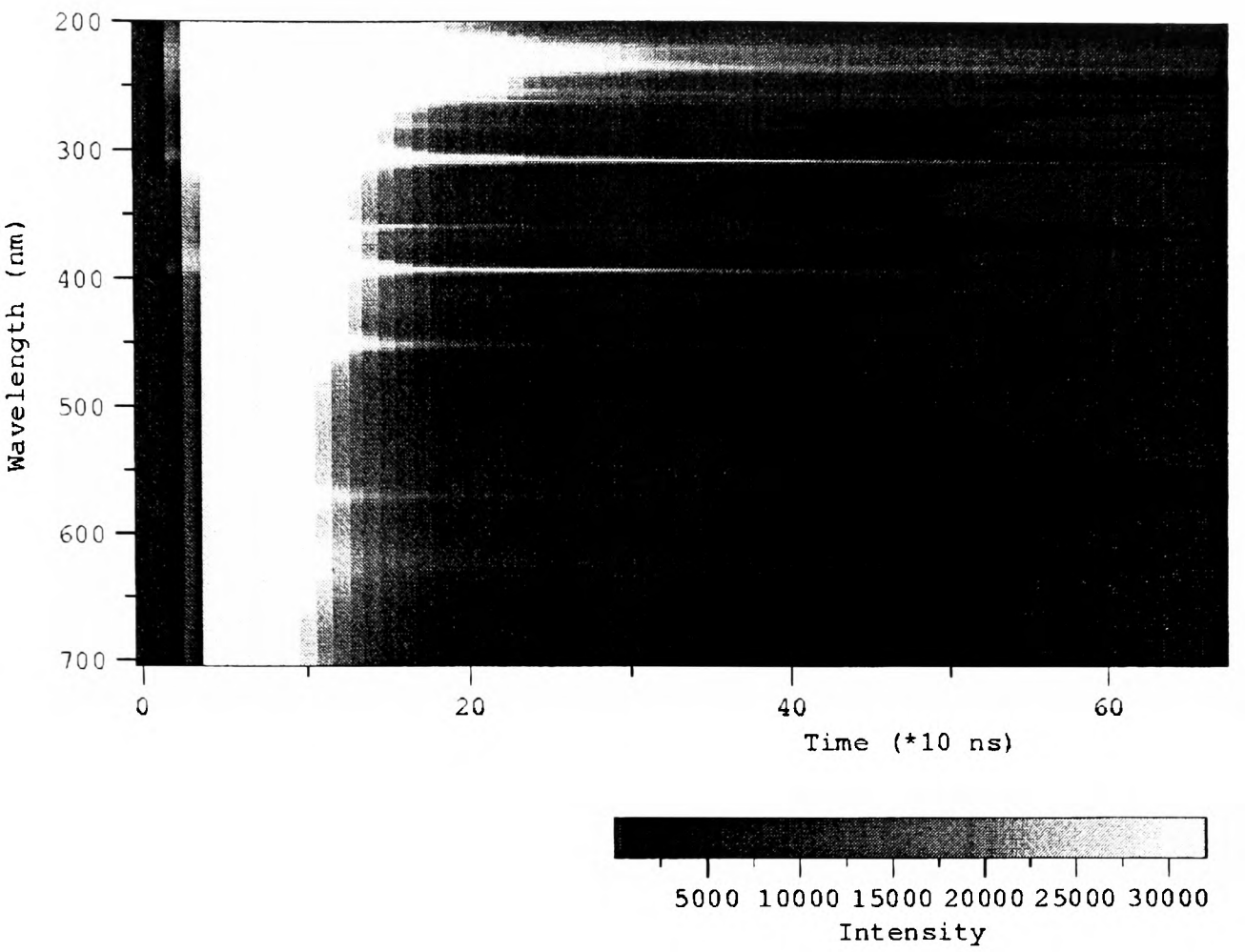


FIGURE 6.12: Result of aluminium spectrum computed with CROMWELL for $E_0 = 3$ mJ, $\tau_p = 40$ ns, and 25 μm focal spot radius.

within the impact approximation where the width w for an isolated ion line is given by

$$w = n_e \left(v \left[\sum_{i'} \sigma_{i'i} + \sum_{f'} \sigma_{f'f} \right] \right)_{\text{av}} + w_{\text{el}} \tag{6.5}$$

where v is the average electron velocity, and $\sigma_{j'j}$ is the inelastic cross section for collisional transitions to states j' from j levels (i initial, f final) of the optical transition. w_{el} is the line width induced by elastic collisions. The approach of the MSEM is to calculate the collisional Stark broadening of each line by performing the summation (6.5) over all states. Within the dipole approximation, and using Bethe's relation for the inelastic cross section, $\sigma_{j'j}$ can be expressed in terms of the square of the coordinate operator matrix elements, summed and averaged over all magnetic sub-states..

CROMWELL further uses the Debye model to obtain the IPD for the calculation of the ionisation balance, necessary to truncate the summation over states in the partition function and also to remove transitions from the calculations which have become bound-free (Heading et al. 1997*b*). The most important ingredient in this procedure is the input of atomic data, i.e. energy levels, transitions wavelengths, angular momenta, and effective quantum numbers, of all species considered. As such, the accuracy and practical value of *CROMWELL* greatly depends on the availability of such data (Heading et al. 1997*b*).

To illustrate the capacity of *CROMWELL*, figure 6.12 shows the computed time-resolved spectrum of an aluminium plasma produced by a CVL laser. Typical laser parameters used (3 mJ pulse energy,

40 ns pulse duration, 25 μm focal spot radius) reflect the actual physical experiments. To compute the temporal evolution of the UV-visible spectrum, *CROMWELL* is used as a post-processor on the output generated by the *MEDUSA* code, which calculates of n_e, T_e as a function of time and space within an 1D Langrangian hydrodynamic model (Heading et al. 1997*a*). The qualitative agreement of figure 6.12 with experimental spectroscopic data is striking, clearly showing the initial merging of broad lines to form a continuum. With time, the line widths decrease as the plasma expands, ultimately producing the characteristic sharp line features typical of the recombination stage. The simulation was run for vacuum background conditions, and the plotted data represent the total integrated emission of the plume (and not just the emission viewed side on originating from the plasma core). While the computed values for the continuum phase duration (100 ns), and duration of emission at line centre for resonance transitions in neutral aluminium (up to 1 μs for the 396/394 nm and 309/308 nm lines), this agreement may be accidental since the expansion of the ablation plume in vacuum compared to the expansion under ambient conditions are significantly different (see chapter 4).

III Opacity broadening Despite the demonstrated power of *CROMWELL* for fast computation of broadband emission spectra in dense plasmas, it does not account for opacity broadening mechanisms. As argued in the experimental sections, broadening due to self-absorption is likely to be an important process in the regime of $n_e \simeq 10^{18} - 10^{20}$ cm^{-3}, where the ion and neutral densities ($n_{\mathrm{Al\,II}}, n_{\mathrm{Al\,I}}$) are expected to be equally high, in line with the observed low values for the effective ion charge Z^*. As outlined in Appendix D, opacity broadening depends on the oscillator strength of the transition, and scales linearly with density of the ground state population n_1 of the transition considered. The aim is, therefore, to estimate the relative contribution of opacity broadening versus collisional Stark broadening.

To obtain an estimate for the opacity line broadening, the description in terms of a 'curve of growth' as outlined by Thorne (1988) is used. Due to the fact that opacity broadened lines do not exhibit a well-defined line profile, the equivalent width of such lines is described in terms of an equivalent width W, for which the area determined by its product with the peak intensity at line centre $I(0) \cdot W$ is equal to the integrated line profile. The curve of growth for a given spectral line describes the behaviour of this equivalent width W as the number of absorbing atoms in the line of sight is increased. Between the limits of an optically thin transition, and the optically thick blackbody limit, three regimes can be distinguished. Starting from an optically thin medium, by increasing the density of atoms occupying the lower level of the transition n_1, the equivalent width W_λ (here given in metres for comparison with $\Delta\lambda$) is given by (Thorne 1988)

$$W_\lambda = \frac{e^2}{4\epsilon_0 m_e c^2} n_1 \lambda_{12}^2 f_{12} l \tag{6.6}$$

where f_{12} is the oscillator strength of the transition, and e, ϵ_0, m_e and c the usual definition of fundamental physical constants. When the centre of the line is no longer optically thin, W increases less rapidly than $n_1 f_{12} l$, and the subsequent behaviour is strongly dependent on the spectral line shape, i.e. pure Gaussian, pure Lorentzian or a generic Voigt profile. No simple analytical expression can be derived for this regime. Then, by increasing $n_1 f_{12} l$ further into the third regime, the Lorentzian wings will start to rise causing W to increase as (Thorne 1988)

transition (nm)	f_{12}	$\Delta\lambda_{\rm Stark}$ [nm]	W_λ [nm]
Al I			
395.57	0.115	0.41	1.2
308.92	0.175	0.47	1.2
257.28	0.043	1.06	0.7
Al II			
281.62	0.152	0.14	0.6
365.30	0.091	4.02	3.0

TABLE XV: Calculated line widths due to Stark broadening and opacity broadening for transitions of interest in Al I and Al II, for $n_e = 10^{19}\text{cm}^{-3}$, $T_e = 10^4$ K. Data are taken from Heading et al. (1995b).

$$W_\lambda = \left(\frac{e^2}{2\epsilon_0 m_e c^2}\Delta\lambda_L\right)^{1/2}\left(n_1\lambda_{12}^2 f_{12} l\right)^{1/2} \tag{6.7}$$

where $\Delta\lambda_L$ is the Lorentzian line-width of the transition.

Given the much larger collisional Stark broadening over thermal Doppler broadening in laser ablation plasmas, for the present discussion a pure Lorentzian line shape will be assumed. Experimental observations further indicate that in the plasmas considered here the equivalent width W_λ approaches the optically thick limit, and thus equation (6.7) which will used here to evaluate the relative contribution of opacity broadening versus collisional Stark broadening. Estimates for the Stark width $\Delta\lambda_{\rm Stark}$ are obtained by extrapolating the relationship

$$\Delta\lambda_{\rm Stark} = \alpha\frac{n_e}{\sqrt{T_e}} \tag{6.8}$$

using tabulated semi-classical values of the Stark coefficient α (Heading et al. 1995*b*). In table XV the Stark widths are listed for aluminium transitions of interest, where the values are calculated for $n_e = 10^{19}$ cm^{-3}, $T_e = 10^4$ K. To arrive at a conservative estimate for the equivalent width W_λ, the physical size of the plasma is taken to be $l \simeq 0.1$ mm, and $n_1 \simeq 10^{-17}$ cm^{-3} is taken to be two orders of magnitude lower than n_e. The results from these calculations are listed in table XV.

From table XV it can be concluded that even for a conservative estimate, opacity broadening is considerable and results in equivalent widths W_λ which are up to a factor $2-3$ larger than the collisional Stark width. Comparing the ratio $W_\lambda/\Delta\lambda_{\rm Stark}$, (6.7) can be rewritten as

$$\frac{W_\lambda}{\Delta\lambda_{\rm Stark}} = \left(\frac{e^2}{2\epsilon_0 m_e c^2}\frac{1}{\Delta\lambda_{\rm Stark}}\right)^{1/2}\left(n_1\lambda_{12}^2 f_{12} l\right)^{1/2} \tag{6.9}$$

Equation (6.9) shows that for resonance transitions, which generally have high oscillator strengths $(0.1-1)$, high ground-state densities n_1, and relatively small collisional Stark widths $\Delta\lambda_{\rm Stark}$, opacity effects are significant. In comparison, transitions with higher lying upper levels generally experience larger Stark broadening due to the relatively large collisional cross-section of these states. In this case,

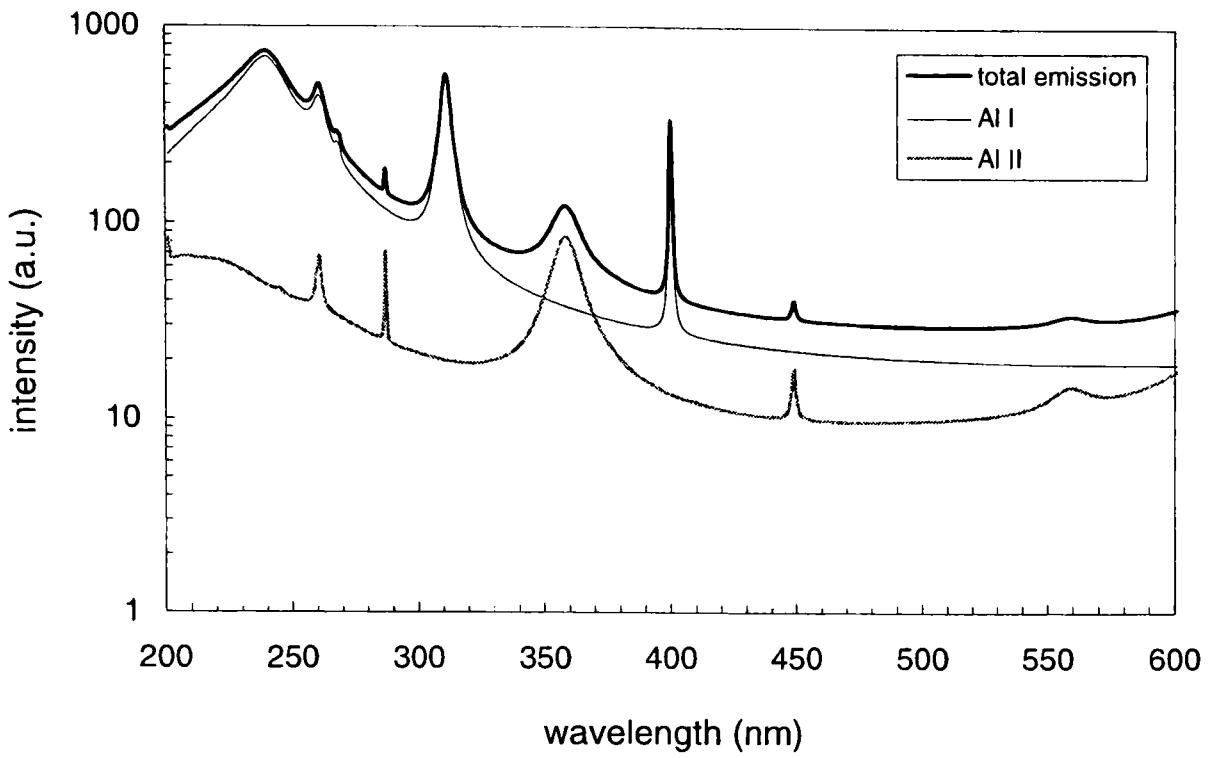


FIGURE 6.13: UV-visible spectrum of aluminium as calculated using *CROMWELL* for $n_e = 10^{19}$ cm^{-3}, $T_e = 18 \;\; 10^3$ K, showing the individual contributions of the Al I and Al II ionisation stages.

the Stark widths dominate the opacity broadened equivalent line widths. For transitions which do *not* terminate on the ground-state (or long-lived metastable states), the relatively low population densities of the lower level n_1 will further decrease the ratio $W_\lambda/\Delta\lambda_{\text{Stark}}$. Note however, that even for high lying transitions in a titanium plasma, Hermann et al. (1998) observed significant opacity broadening at modest electron densities of order 10^{17} cm^{-3}, and comparable value for n_1.

To further emphasise the importance opacity broadening, figure 6.13 shows an aluminium spectrum calculated with *CROMWELL* $\left(n_e = 10^{19}\text{ cm}^{-3}, T_e = 18 \cdot 10^3\text{ K}\right)$. Note the logarithmic scale on the y-axis. Looking at the individual contributions of the two ionisation stages, the two main transitions of Al I (395.57 nm and 308.92 nm) are clearly visible as broad lines. The large number of transitions in the 250 nm region originating from the closely spaced 4d, 5d and 6d orbitals have merged into a very broad continuum, with wings extending far into the visible region. The 281.6 nm transition in Al II is computed to be relatively narrow, while the strong 365.30 nm shows as a dominant feature with $\Delta\lambda_{\text{Stark}} > 10$ nm. The discrepancy of the Stark width as estimated in table XV for the 365.30 nm line based semi-classical atomic data, compared with the width calculated by *CROMWELL* with MSEM, illustrates the limitation of this method due to inaccuracy of the data from the Opacity database. More importantly, however, is that the overall shape of the continuum as calculated by *CROMWELL* does not resemble the shape of a true blackbody-like continuum such as has been observed by Engst et al. (1994) and Fried & Reck (1991). If a continuum was to be produced due to Stark broadening alone, the characteristic shape of the continuum could still be identified as arising from the wings of severely broadened transitions which have large collisional cross-sections as illustrated in figure 6.13. An opacity broadened continuum, on the other hand, exhibits a characteristic Planckian distribution, often accompanied with self-reversal at the line

centre of strong resonance transitions, as has been observed here. Although presently no measurements have been performed to confirm that the observed continuum emission originating from the plasma core during the first hundred nanoseconds indeed does resemble a blackbody-like spectral distribution, it is clear that the relative effect of opacity broadening is at least of the same order of magnitude (if not dominant) compared to collisional Stark broadening for the plasmas considered here.

6.5 CONCLUSION

I SUMMARY Via atomic emission spectroscopy is has been experimentally established that the metallic plasmas generated during laser ablation with CVLs constitutes a cool plasma. Given that only significant emission was observed from neutral and singly ionised species, the electron temperature T_e is estimated to be of order $5 - 10 \cdot 10^3$ K based on the assumption of LTE and Saha ionisation equilibrium. For all experiments performed under ambient conditions, no emission from nitrogen, oxygen or other atmospheric species were observed at any time. Time-resolved monitoring of individual spectral lines show the presence of a broad-band continuum lasting 100 ns, inferred from the emission at wavelengths which were approximately 10 nm detuned from specific transitions. The temporal characteristics of the emission of the plasma core as observed directly at the target surface, show an approximate evolution of the plasma in four stages. Following the continuum stage up to 0.1 μs, fast decay of emission from ions to $< 95\%$ of the peak intensity is observed during $0.1 - 0.3$ μs after the onset of ablation. During this period the emission from neutrals persists, only to decay over longer time-scales $0.3 - 1$ μs. Most of the atomic emission at the target surface has ceased for delay times > 1 μs after the laser pulse, after which recombination radiation can be observed at larger distances $> 2 - 5$ mm from the target surface.

The ensuing discussion has focused on the origin of the observed continuum, in view of other reports on line-broadening mechanisms in dense plasmas. It is argued that opacity broadening is an important, if not dominant, mechanism during the first 100 ns when the existence of a broadband continuum has been observed. The applicability of numerical codes (*CROMWELL*) based on the modified semi-empirical method (MSEM) in this regime is limited, as self-absorption and opacity effects are not accounted for. However, due to the rapid expansion of the plasma, the relative importance of opacity broadening will decrease, rendering collisional Stark broadening dominant mechanism of the broad spectral features observed during $0.1 - 1$ μs. Furthermore, the relative contribution of the opacity broadened equivalent width W_λ and the collisional Stark width critically depends on the relative magnitude of the collisional cross-section (large for higher lying terms), and the oscillator strength of the particular transition. It has been shown that for low lying resonance transitions in neutral aluminium, the equivalent width due to opacity broadening is a factor $2 - 3$ larger than the collisional Stark width.

Considering the applicability of *CROMWELL* and other codes based on MSEM, it is concluded that for the laser ablation plasmas studied here opacity effects need to be accounted for. Otherwise, *CROMWELL* can only be used to provide an approximate characterisation of the plasma during times $0.1 - 1$ μs when opacity effects are likely to have decreased due to decrease in density as a result of the volumetric expansion of the plasma plume. To describe the plasma beyond delay times of order $> 1 - 2$ μs, the standard approach of diagnostics based on individual lines seems the method of choice, as in this limit spectral lines no longer significantly overlap. Furthermore, given the accuracies of order

1 nm of MSEM and atomic databases such as the Opacity Project, the use of well catalogued transitions for which more accurate atomic data exist (semi-classical calculations or experimental values) is more appropriate. Although one could question the validity of LTE conditions during these later recombination stages of the plasma plume (see Appendix (D.14)), work by Tambay et al. (1992) has shown that even at large distances (few millimetres) and long delay times (few microseconds) the McWirther condition is still satisfied for many spectral transition. Often in these circumstances deviations from LTE equilibrium are relatively small compared to other issues such as, for example, to what extent transport processes distort the spectroscopic analysis, due to the presence of plasma zones in existing in different LTE conditions.

II FUTURE WORK A few concluding remarks on the further development of plasma diagnostics techniques can be made. From the above, it is evident that before referring to any plasma diagnostic technique one has to clearly consider (and identify) the regime of interest. Besides the underlying theoretical considerations, a number of practical issues should be taken into account. For example, issues pertaining to the dynamic range of light detectors such as photon counters, photomultiplier tubes, streak cameras, gated diode arrays or other optical multichannel analysers, often involve compromising the specific advantages and drawbacks of these devices. During the time-resolved experiments described here it was found that high gains are required in order to monitor individual spectral lines on single-shot basis. In this case the choice for a photomultiplier detector was deemed most practical, also giving high temporal resolution. This, however, at the cost of the capability of monitoring a whole wavelength range at once. On the other hand, while streak-camera can provide 1 ns temporal resolution for multichannel analysis, the gain of these devices are lower than photomultiplier tubes, which imposes limits on the minimum sizes and absolute brightness of the plasma to be studied.

Different approaches can therefore be taken to take the present work further, aiming to obtain experimental data on the evolution of the whole visible-UV spectrum. A wavelength scanning setup using an automated monochromator with photomultiplier detectors would be suitable for multichannel analysis whilst maintaining good temporal resolution. However, this is at the cost of complexity of monitoring small portions at the spectrum over thousands of shots (Engst et al. 1994). The use of gated diode arrays or OMAs naturally provide multichannel capability, but either requires integrated data collection over tens of shots to enhance the signal-to-noise ratio, or the need for long gate periods at the expense of temporal resolution (Fried & Reck 1991). Additional issues may further play a role, where for example particularly in the case of the CVL and other laser operating in the visible, the spectroscopic apparatus should have high extinction coefficients to prevent backscattered radiation from obscuring measurements near the laser wavelengths.

As a final note, going beyond academic pursuits of plasma diagnostics, the studies presented in this chapter indicate that for any development of industrially reliable process control or in-line spectroscopic monitoring tools to be successful, first and foremost a clear formulation of the problem is required to provide initial estimates for the relevant plasma parameters. In each case, this will entail careful modelling, pre-calibration and testing of the apparatus to ensure reliable and stable generation of data for feedback control algorithms within the regime of interest. Any attempts to develop generic spectroscopic analysis tools are likely to be unpractical outside a research environment.

Chapter 7
Pulsed Laser Ablation of Metals: An Energetics Picture

Epistemology models ontology
JOHN POLKINGHORNE'S WIFE

An energetic study of pulsed laser ablation with nanosecond copper vapour lasers is presented. As an introduction a comparative study on laser ablation with femtosecond-nanosecond lasers for applications in laser materials processing is made. Controlled production of sub-micron surface relief gratings is demonstrated, and discussed in view of the relative importance of thermal diffusion versus other mechanisms relevant in the near-threshold ablation regime. The recoil impulse under vacuum ablation is measured for various metals and correlated with morphological studies of the post-ablation craters in view of mapping importance of material properties on the ablation process. D.W. Coutts conducted most of the experimental work on the production of sub-micron periodic structures. M.N. McBrien performed the measurements on momentum transfer in vacuum for different target materials as part of his M.Phys project. The contribution of Philips CFT for providing some of the SEM images is gratefully acknowledged.

7.1 Ablation With Femtosecond-Nanosecond Lasers

I Introduction Recent reports on pulsed laser ablation of metals using various laser sources have fostered the discussion regarding the energetic characteristics, in particular the fundamental limits set by thermal diffusion to produce features with critical dimensions in the (sub-)micron scale. As such, the debate regarding the relative benefits of nanosecond pulsed lasers versus femtosecond ablation continues to draw much attention (Pronko et al. 1995*a*, Luft et al. 1996, Chichkov et al. 1996, Jandeleit et al. 1998). While femtosecond lasers have been shown to have considerable advantages over their nanosecond counterparts due to their short pulse duration (Momma et al. 1996, Liu et al. 1997, Nolte et al. 1997), it still remains debateable as to which class of laser is the most suitable for a given (generic) process. For example, *volumetric* mass removal required for efficient ('explosive ablation') drilling and cutting of materials generally requires a different set of (near-)optimum process parameters compared to *surface* machining, such as milling or controlled (slow 'evaporative') removal of monolayers and surface texturing. In general, different applications require different processes.

Within the context of current laser materials processing technology the following chapter will address the energetic aspects of pulsed laser ablation of metals, particularly from the perspective of employing nanosecond pulsed copper vapour lasers (CVLs). First, as an introduction to the experiments described

below, a comparative study of ablation of metals using lasers with pulse durations varying from 1 μs down to 10 fs, is presented. Drawing on a large number of reported experiments, it is argued that a semi-quantitative classification can be made by considering the energy density per unit volume u (J/cm^3), as determined by the thermal diffusion depth D, to define different thermodynamic ablation regimes. Both experimental results from literature, as well as experiments conducted within the Compala programme, will be assessed in this fashion. Subsequently, experiments on the controlled production of (sub-)micron surface gratings on stainless steel (316) using an interference technique is demonstrated as an example of near-threshold surface machining. By maintaining a low energy deposition per unit volume u, it is demonstrated that a modulated optical field intensity can be efficiently transferred directly onto the metal surface. By operating in the threshold regime for nanosecond pulsed evaporative structuring, critical dimensions approaching the thermal diffusion length can be produced. Finally, momentum transfer measurements performed in vacuum on a host of different metals are presented. The observed dependence of the vacuum recoil momentum p_0 on the material properties of the metal targets provide insight to the importance of these parameters to determining the optimum conditions for machining of metals.

The theme common to the three sections in this chapter is aimed to draw an energetics picture of pulsed laser ablation of metals. Specifically, an attempt is made to assess to the importance of the energy deposition per unit volume u on identifying different thermodynamic regimes of the ablation process. While current understanding of laser ablation still requires major advancements to arrive at a detailed description of the complex *dynamical* aspects of the thermal transport processes and phase transitions occurring the in target material, the approach taken here will focus on a semi-quantitative comparison of different laser ablation regimes based on (quasi-static) kinetic thermodynamic arguments.

II HEAT DIFFUSION & THERMAL TRANSPORT Consider an optical pulse with duration τ_p (s) and fluence F (J/cm^2) incident on a metal target of sufficient thickness to be approximated as a semi-infinite solid. Within the classical Drude–Lorentz-Sommerfeld electron gas model for metals (Kittel 1996), it is assumed that efficient coupling of the total optical pulse energy E (J) is established via inverse Brehmsstrahlung absorption. Since the present discussion is aimed towards elucidating the kinetics and thermal mechanisms of the ablation process, physical mechanisms pertaining to wavelength-scaling and plasma formation are neglected in as much that these can be incorporated in the energy coupling constant. The basis of the present discussion is given in Appendix E, where relevant elements of thermal transport theory are reviewed.

The main case in point regards the two-temperature heat-flow model as described by Corkum et al. (1988). As shown by Corkum et al. (1988), a distinction between three different dynamical regimes can be made by comparing the laser pulse duration τ_p with the characteristic relaxation time of the free electrons and the ions contained in the lattice, respectively denoted by τ_e and τ_i. Corkum et al. (1988) derived expressions for the thermal diffusion depth D_e, D_i, respectively associated with the heat transport due to the fast electrons, and the slow lattice, in term of the thermodynamic properties of the material, i.e. the thermal conductivity k, the electron and lattice heat capacities c_e, c_i respectively, and the electron-phonon coupling constant g. These expressions are listed in table XVI. Looking at the thermodynamic properties of common metals, as listed in table XVII, it can be concluded that $\tau_e \sim 10$ ps and $\tau_i \sim 0.1$ ns, both only varying within a factor of 2-5 for these metals. A similar comparison of the

regime	characteristic time-scales and diffusion lengths	Al	Fe	Cu
	$\tau_e = (8/\pi)^{1/4}\,(1/g)\,\sqrt{c_e c_i T_{th}}$	10.4 ps	13.3 ps	13.2 ps
	$\tau_i = (8/\pi)^{1/4}\,(1/g)\,\sqrt{c_i^3/T_{th}c_e} = c_i\tau_e/T_{th}c_e$	90.9 ps	149.6 ps	141.5 ps
$\tau_p < \tau_e$	$D_e = (128/\pi)^{1/8}\,(k/g)^{1/2}\,(c_i/T_{th}c_e)^{1/4}$	0.13 μm	0.26 μm	0.18 μm
$\tau_e < \tau_p < \tau_i$	$D_e^{'} = (\tau_p/\tau_e)^{1/5}\,D_e \simeq (\tau_i/\tau_e)^{1/5}\,D_e$	0.20 μm	0.42 μm	0.29 μm
$\tau_i < \tau_p$	$D_i = \sqrt{\kappa\tau_p}$ (for $\tau_p \simeq 10$ ns)	0.98 μm	0.48 μm	1.07 μm

TABLE XVI: The characteristic time-scales and diffusion lengths from the two-temperature model as derived by Corkum et al. (1988). The electron-phonon coupling constant g and the electron heat capacity c_e are taken to be 10^{11} Wcm^{-3}K^{-1} and 0.1 Jcm^{-3}K^{-1}, respectively, for all metals. Note that the difference between the fs and ps regime only involves a small correction of at most $(\tau_i/\tau_e)^{1/5}$ which is of order 1. While Corkum et al. (1988) have taken the melting point of the metal as an emperical threshold temperature (corresponding to the onset of slight morphological changes on the surface of the target), here the threshold temperature T_{th} which defines the characteristic time-scales associated with the diffusion process, is taken to be the boiling temperature since for the present discussion the main interest argument pertains material removal in the explosive ablation regime.

materials properties of metals has been presented by Kelly & Rothenberg (1985), who conclude that such a semi-quantitative comparison of different engineering metals is justified. Note that the largest error stems from the experimental measurement of the electron-phonon coupling constant g and the heat capacity of the free electrons $c_e = c_e^{'}T_e$, which both are taken to be roughly constant for the metals considered, i.e. $g = 10^{11}$ W/cm^3·K and $c_e^{'} = 10^{-2}$ J/cm^3·K (Fujimoto et al. 1984, Corkum et al. 1988).

Along these lines, a characteristic diffusion length D can be determined (Corkum et al. 1988) for respectively the 'femtosecond', 'picosecond' and 'nanosecond' regime, as indicated in table XVI and similar to the classification made by Chichkov et al. (1996). An important result obtained by Corkum et al. (1988) is that, while in the nanosecond regime (i.e. $\tau_i < \tau_p$) the diffusion length D_i is proportional to $\sqrt{\tau_p}$, in the case $\tau_p < \tau_i$ the diffusion length D_e is independent of the pulse duration and determined only by material properties. Yet, the diffusion length in the femtosecond case is considerably larger than the optical absorption depth $1/\alpha \sim 10$ nm due to diffusion of the free electron before significant electron-phonon relaxation can occur, as pointed out by Corkum et al. (1988).

III ENERGY DEPOSITION PER UNIT VOLUME Following studies by Matthias et al. (1994) and Preuss et al. (1994), now consider the energy density per unit volume u [J/cm^3] defined as

$$u = \frac{F}{D} \quad , \tag{7.1}$$

which can be regarded as the characteristic energy deposition of the incident fluence F [J/cm^2] over the volume[4] determined by the spotsize area times the diffusion depth D. It will be argued below, that u provides a 'figure of merit' to assess different kinetic regimes which are subsequently identified with different regimes of laser ablation. At this point, however, a word of caution is required. The following argument based on energy deposition per unit volume u should be seen as a zeroth order approximation

[4] Note that for all present purposes such a cylindrical symmetry holds, given that for most lasers considered the waist at focus $w_0 > 10\ \mu\text{m} > D$.

thermodynamic property	symbol	unit	Al	Fe	Cu	SS 316
solid density	ρ	[g/cm^3]	2.7	7.9	9.0	7.9
thermal conducticity	k	[W/cm·K]	2.34	0.80	3.94	0.15
heat capacity	c_p	[J/g·K]	0.9	0.4	0.4	0.5
boiling point	T_{vap}	[K]	2792	3134	3200	
enthalpy of fusion	ΔH_{fus}	[kJ/g]	0.4	0.2	0.2	
enthalpy of vaporisation	ΔH_{vap}	[kJ/g]	10.9	6.2	4.7	
diffusion constant	$\kappa = k\rho/c_p$	[cm^2/s]	0.96	0.23	1.15	0.05
required energy density	u_{vap}	[kJ/cm^3]	36.6	60.6	54.0	
absorption depth	α^{-1}	[nm]	7		14	

TABLE XVII: List of material properties and calculated required energy density for evaporation estimated by $u_{vap} = ((T_{vap} - T_0)\, c_p + \Delta H_{fus} + \Delta H_{vap})/V_{molar}$. Data are taken from WebElements (http://www.shef.ac.uk/chemistry/web-elements/) and product information sheets of engineering stainless steels.

to describe the *static* thermal properties of the ablation process. It therefore disregards *dynamical* effects, which are important in the description of pulsed laser ablation with nanosecond-femtosecond lasers in view of the much debated effect of phase explosion or explosive boiling (Miotello & Kelly 1995, Kelly et al. 1998). The phenomenon of explosive boiling associated with the fast superheating of the (liquid) metal target, is akin to the first experiments reported by Martynyuk (1974) on the catastrophic boiling of metal wires due homogeneous nucleation when heated rapidly with current pulses lasting $10^{-6} - 10^{-4}$ s. The onset of anomalies when approaching the spinodal limit (Miotello & Kelly 1995) can also be identified as the limit where the tensile strength of the liquid falls to zero, causing chaotic motion of the melt-pool to result in the observed explosion and ejection of liquid metal (Dyer et al. 1992*b*, Dyer et al. 1992*a*). To fully describe the ablation process, therefore, requires a full dynamical treatment which also accounts for the non-stationary effects of the phase transition occurring on the comparable time-scales of the thermal diffusion and laser pulse duration (Arnold et al. 1998). For the present discussion, these dynamical effects will only be addressed in passing, while the main argument will focus on the static, kinetic aspects of the ablation process.

Consider figure 7.1, where various reported experimental results on pulsed laser ablation of metals as listed in table XVIII, are plotted against the incident laser fluence F (top x-axis) and the laser pulse duration τ_p (left y-axis). The dotted lines represent lines of equal peak power density $I = F/\tau_p$ (right y-axis), which have slope unity. Furthermore, lines of equal u are plotted (dashed lines, bottom x-axis). Following the argument of Corkum et al. (1988) as outlined above, in the regime where $\tau_p > \tau_i$ the energy density per unit volume u scales as $\sqrt{\tau_p}$. Thus, for $\tau_p \gtrsim 10$ ps, the iso-u lines follow slope two. Going to the femtosecond regime where now $\tau_p < \tau_i$, the diffusion depth D_e has been argued to remain approximately constant (Corkum et al. 1988), as shown by the vertical lines of equal u for $\tau_p \lesssim 10$ ps.

Plotting the data listed in table XVIII, a qualitative classification of the various reported experiments is now made based on i) the measured material removal rates, also given in table XVIII; and ii) the characteristic surface morphology. Starting at in the threshold regime (open circles ∘, $u \lesssim 10^4$ J/cm^3),

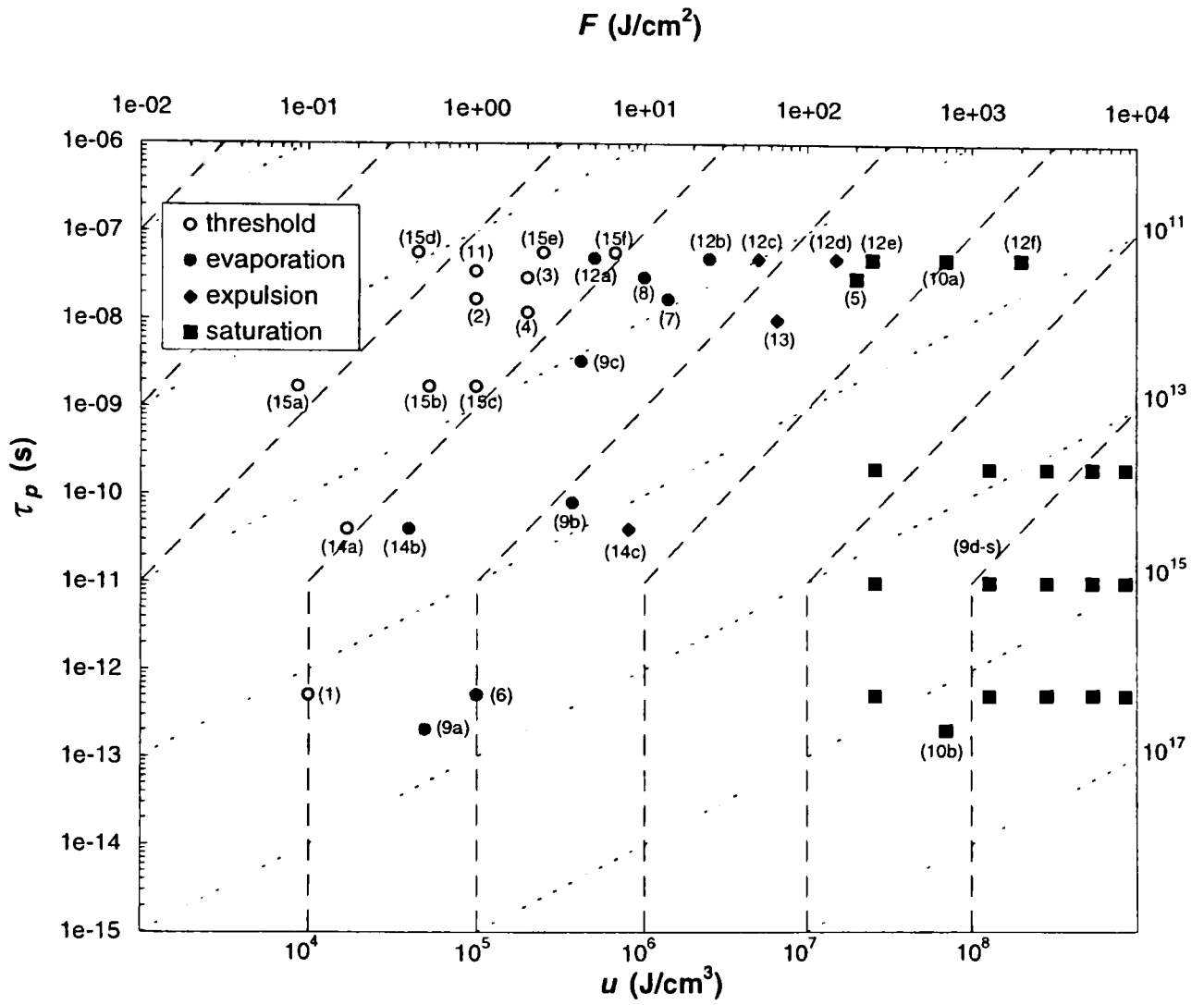


FIGURE 7.1: Map of pulsed laser ablation experiments, plotted against fluence F (top horizontal axis) and laser pulse duration τ_p (left vertical axis). Iso-intensity lines are indicated on the right (dotted lines with slope 1), while the dashed lines indicate lines of equal power deposition u (values on bottom axis), showing the turn-over point at 10 ps beyond which the diffusion depth D is independent of τ_p. Numbered references are listed in table XVIII.

point	laser (λ in nm)	ablation depth	reference
(1)	KrF (248)	threshold	(Preuss et al. 1995)
(2)	KrF (248)	threhold	(Timm et al. 1996)
(3)	KrF (248)	threshold	(Fähler & Krebs 1996)
(4)	KrF (248)	threshold	(Kelly & Rothenberg 1985)
(5)	ArF (193)/XeCl	5 μm	(Geertsen et al. 1994)
(6)	KrF (248)	20 nm	(Preuss et al. 1995)
(7)	KrF (248)	30 nm	(Timm et al. 1996)
(8)	KrF (248)	20 nm	(Fähler & Krebs 1996)
(9a-c)	Ti:Sapph (780)	10 nm	(Momma et al. 1996)
(9d-s)	Ti:Sapph (780)	1 -25 μm	(Momma et al. 1996)
(10a)	Ti:Sapph (780)	3 μm	(Luft et al. 1996)
(10b)	CVL	7 μm	(Luft et al. 1996)
(11)	CVL	surface structuring	present work
(12a-b)	CVL (511/578)	1 μm	(Körner et al. 1996)
(12c-d)	CVL (511/578)	10 microns	(Körner et al. 1996)
(12e-f)	CVL (511/578)	100 microns	(Körner et al. 1996)
(13)	Nd:YAG	few μm	(Xia et al. 1991)
(14a)	Nd:YAG	few nm	(Jandeleit et al. 1996)
(14b)	Nd:YAG	10 - 100 nm	(Jandeleit et al. 1996)
(14c)	Nd:YAG	100 - 300 nm	(Jandeleit et al. 1996)
(15a-c)	CO_2	threshold	(Figueira & Thomas 1982)
(15d-f)	CO_2	threshold	(Figueira & Thomas 1982)

TABLE XVIII: List of reported experiments and references used for the data-points in figure 1.

the smallest ablation depths of order of few monolayers have been reported. In the evaporation regime (solid circles •, 10^4 J/cm^3 $\lesssim u \lesssim$ 10^5 J/cm^3), the main mechanism for material removal is via surface evaporation/sublimation where the ablation depth per pulse increases with increasing pulse length: from $\sim$ 10 nm for a 0.5 ps pulse (Preuss et al. 1995) to $\sim$ 100 nm for 40 ps (Jandeleit et al. 1996), and $\sim$ 1 μm for 50 ns (Körner et al. 1996). In this evaporation regime the ablation rate is accurately described using a logarithmic scaling law with a well defined threshold fluence (Preuss et al. 1995). The transition to the onset of melt-expulsion (solid diamonds ♦, 10^5 J/cm^3 $\lesssim u \lesssim$ 10^6 J/cm^3) is marked with a sharp increase in mass-removal rates which can no longer be accounted for by a slow, surface evaporation process. Measured ablation depths of $10-100$ μm per pulse (Körner et al. 1996, Momma et al. 1996) are associated with volumetric material ejection due to the phase-explosion phenomenon described earlier (Miotello & Kelly 1995). At higher energies densities $u \gtrsim 10^6$ J/cm^3 (solid squares ■)the material removal rate eventually saturates. Increasing the energy deposition into this regime results in little to no increase in the ablation depth (Körner et al. 1996), while significant 'freezing' of molten material at the crater rims of drilled holes has been observed (Momma et al. 1996).

From figure 7.1 it is argued that a semi-quantitative classification of the pulsed laser ablation process can be made based on the energy density u. Similar to the line of reasoning presented by Figueira & Thomas (1982), Matthias et al. (1994), and Preuss et al. (1994), a critical energy density u is introduced

for each of the different ablation regimes, subsequently involving melting (threshold), vaporisation or explosive material with increasing u. In the case of pulsed nanosecond laser ablation (and also using longer pulses), such a concept of a critical energy density u is intuitively associated with the predominance of thermal diffusion where often the damage threshold is observed to follow $\sqrt{\tau_p}$. In the case of pulsed femtosecond ablation, the physical interpretation of thermal diffusion has remained more elusive, and only recent experiments by Matthias et al. (1994) and Preuss et al. (1994) on the damage thresholds of thin metal films have shown that even in the femtosecond regime the critical energy density is still essentially diffusion-dominated. In this case, due to the non-equilibrium heat transport the $\sqrt{\tau_p}$ scaling is replaced by a constant diffusion depth D_e, as argued by Corkum et al. (1988) and outlined above. Experiments on bulk silicon and gold (Pronko et al. 1995*a*), and bulk dielectrics (Stuart et al. 1995) have indeed shown a departure from the $\sqrt{\tau_p}$ dependence of the damage threshold for bulk materials, where for $\tau_p \lesssim 10$ ps the threshold fluence gradually approaches a constant value and becomes independent of τ_p.

Extending the concept further, figure 7.1 suggests that a similar critical energy density can be assigned to the transition from a slow surface evaporation process to fast, explosive volumetric mass removal. Equally, the transition into the regime where the material removal rates saturate can be associated with a critical value for $u \gtrsim 10^6$ J/cm^3. Thus, an empirically determined critical energy density can be determined for each ablation process (melting, evaporation, explosive ablation). Note, however, that the definition of such 'critical thresholds' will always remain somewhat arbitrary, and is dependent on the exact experimental method. In the case of determining the threshold for surface damage, data on indium from sensitive time-of-flight spectroscopy (Götz & Stuke 1997) are in good agreement with single-shot ablation rates and morphology studies (Preuss et al. 1995). However, a definition of a critical energy density threshold for 'evaporative' ablation is inherently tenuous on fundamental physical grounds, as will be discussed in more detail in section 7.2. Also, to arrive at a comprehensive definition for a critical energy density for explosive ablation one needs to account for the dynamic process of homogeneous nucleation (Miotello & Kelly 1995). The saturation of material removal rates in the explosive regime is possibly due to an proportional increase in the amount of molten material with increasing u, but only a disproportional, smaller increase in the ejection force associated with the phase explosion. However, to fully appreciate the complexity of the ablation process in this regime, a dynamic description of the phase transition problem is needed.

IV Nanosecond laser ablation within Compala The concept of a critical energy density u is now applied on the various experiments performed within the Compala programme, where only pulsed nanosecond lasers have been used. The results on ablation of stainless steel are shown in figure 7.2, alternatively using i) the fundamental output from a Q-switched flash-lamp pumped Nd:YAG laser (Philips); ii) the frequency tripled output from a diode-pumped Nd:YAG (DPSS Bosch); and iii) the copper vapour laser (CVL). The indicated ablation depths per pulse are averages calculated over multiple-shot experiments, and hence only provide estimates of the true single-shot ablation depths since shot-to-shot build-up and morphological effects are known to greatly influence ablation rates. Ablation with the Nd:YAG system (solid diamonds ♦) shows a continuing increase in the ablation depth per pulse with increasing energy deposition per unit volume u (equivalent to the increase in fluence F), while keeping the

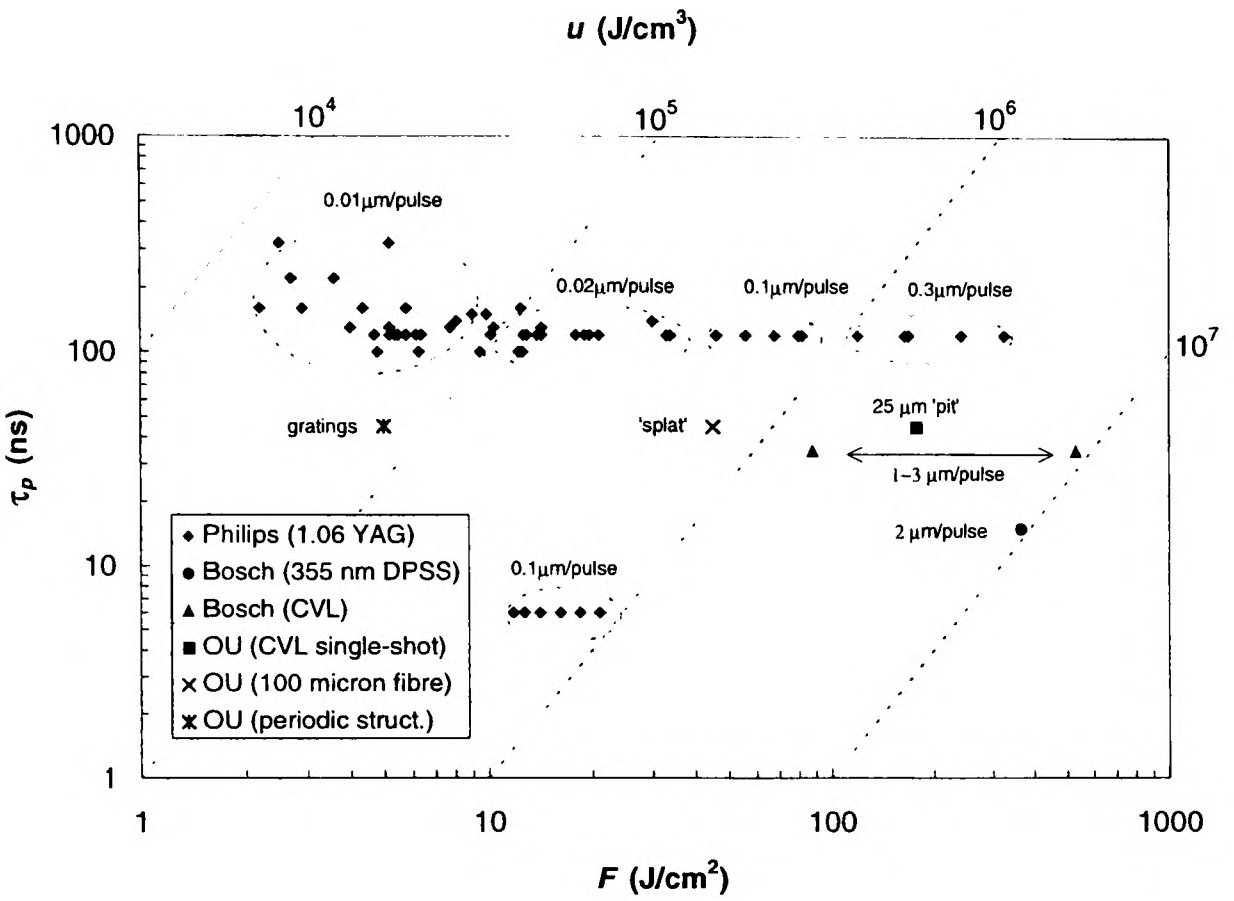


FIGURE 7.2: Classification of pulsed laser ablation experiments conducted within the Compala project, comparing fundamental Nd:YAG (1.06 YAG), diode-pumped frequency tripled Nd:YAG (DPSS), and CVL lasers.

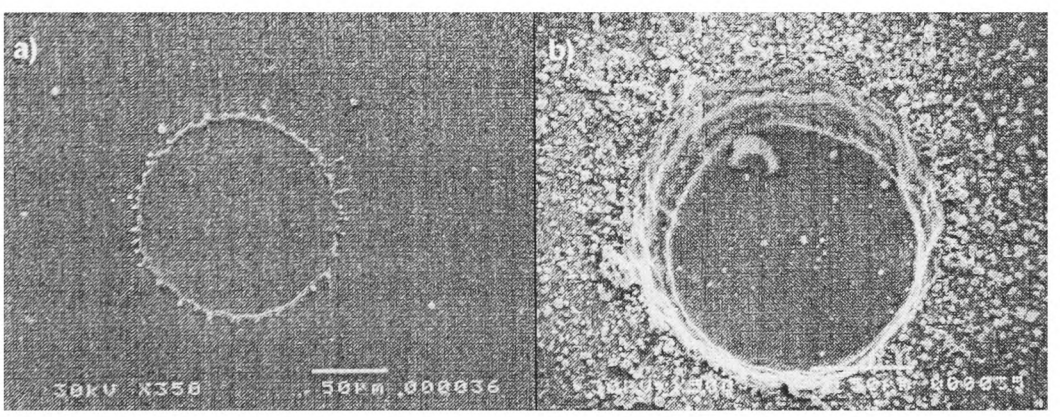


FIGURE 7.3: Ablation of stainless steel with the fibre- delivered output of a CVL (using a 100 μm core, multimode step-index fibre): **a)** single shot, 1.7 mJ; **b)** 100 shots, 6 kHz.

pulse duration constant at around 200 μs. For the same laser system comparable material removal rates are obtained by decreasing the pulse duration to 8 ns, whilst decreasing the fluence F to keep u constant in the range of $10^5 - 10^6$ J/cm^3. In the case of the CVL, the surface structuring experiments ($*$) performed in low energy regime (see following section), result in similar estimated material removal rates as the for the low fluence Nd:YAG experiments. The 'splat' ($\times$) produced by a single-shot pulse is identified with the intermediate regime where $u \simeq 10^5 - 10^6$ J/cm^3 (figure 7.3 **a**). Exposure over 100 shots (figure 7.3 b) shows a proportional increase in the ablation depth. For $u > 10^6$ J/cm^3, experiments performed on a large-scale MOPA system at Bosch resulted in ablation depths of order $2 - 5$ μm were obtained. Similar depths were achieved using the DPSS system with slightly shorter pulses of 15 ns, for which u approaches 10^7 J/cm^3. These results are to be compared with the deep pits produced aluminium with the high beam-quality MOPA system (solid square ■, see chapter 4), where due to the higher thermal conductivity (see table XVII) deeper pits are produced in aluminium compared to stainless steel.

V Discussion Based on the concept that different critical energy density thresholds define different laser ablation regimes, it has been argued in the above that the energy deposition per unit volume u is an important parameter in the characterisation of the ablation process. Despite the gross simplification by employing a static, kinetic description of the ablation process, it has been shown that both experimental results reported in literature, as well as experiments performed within Compala on different laser systems, are in line with this concept. The main advantage of using u as a single 'figure-of-merit' is that it combines the parameters of the incident laser beam (fluence F and pulse duration τ_p), and the thermal properties of the target material. However, it should be noted that the values for $u = F/D \simeq 10^5 - 10^7$ J/cm^3, as obtained by using the tabulated values for the thermal diffusivity of the material (see table XVII) and the experimental value of F, are one to two orders of magnitude larger than the calculated energy densities $10^4 - 10^5$ J/cm^3 required to vaporise one unit volume of material (table XVII). Yet, given the fact that losses due to the surface reflectivity have not been accounted for, nor power deposition in the plasma shock-wave which has been shown in chapter 4 to absorb up to 60% of the total incident energy, the main argument that the energy density per unit volume u provides a useful parameter for cross-system comparison holds true.

More importantly, the concept of a critical energy density shows that in essence the thermodynamics of the ablation mechanism is the same for both femtosecond and nanosecond lasers, thus refuting misleading claims which suggest that reduction of heat affected zones, or indeed establish melt-free laser machining of metals, can only be achieved using femtosecond lasers (Pronko et al. 1995*b*). Luft et al. (1996) concluded that by experimental comparison of holes drilled with a femtosecond CPA Ti:Sapphire and nanosecond CVL essentially show the same phenomenological characteristics in terms of heat affected zone, recast layers and ablation rates. The primary difference between femtosecond and nanosecond ablation is that for femtosecond ablation the thermal relaxation only occurs after the laser pulse. Yet the thermodynamics, and the mechanism of energy deposition in the bulk material, remain the same. Furthermore, theoretical studies by Körner (1997) on the non-equilibrium thermal transport problem have lead to the conclusion that melt-free laser processing of metals can *never* be achieved, not even when employing femtosecond lasers. Indeed, this has been independently confirmed experimentally in various reports (Luft et al. 1996, Simon & Ihlemann 1997). Therefore, in order to reduce heat affected zones, or

characterise the thermodynamic effects of the ablation process in general, it is more important to consider the regime of operation as defined by the energy deposition per unit volume u. As such, to optimise a certain processing strategy requires matching of the laser parameters to the physical properties of the target material. The two experimental studies presented below will provide additional substantiating evidence to this argument.

7.2 PRODUCTION OF SUB-MICRON PERIODIC SURFACE STRUCTURES

I INTRODUCTION The technological challenge to produce (sub-)micron periodic relief gratings on solid surfaces continues to receive much interest for applications such as generation of antireflection structures[5] (Glytis & Gaylord 1992, Motamedi et al. 1992, Raguin & Morris 1993), and patterning of low-dimensional semiconductor devices (Nebel et al. 1997, Shin et al. 1998). In this context, the universal phenomenon of laser-induced periodic surface structures (LIPSS) formed spontaneously during laser irradiation has been widely studied (van Driel et al. 1982, Siegman & Fauchet 1986), and many reports have demonstrated LIPSS in a wide variety of materials including polymers (Bolle et al. 1992, Dyer & Farley 1993, Bolle & Lazare 1993*a*, Bolle & Lazare 1993*b*, Bolle & Lazare 1993*c*, Hiraoka & Sendova 1994), semiconductors (Young et al. 1983, Lu et al. 1996, Giust & Sigmon 1997), fullerite (Milani & Manfredini 1996) and metals (Young et al. 1983, Dauscher et al. 1996).

From a technological viewpoint, however, the controlled production of *regular* surface relief gratings via direct writing/transfer of a modulated optical intensity pattern is more relevant, as has been demonstrated primarily for polymers (Philips et al. 1991*a*, Philips et al. 1991*b*, Dyer et al. 1994, Dyer et al. 1996) and semiconductors (Simon & Ihlemann 1996, Nebel et al. 1997, Shin et al. 1998). In the case of metals, which are of specific interest for applications in the area of microelectronics and micromechanics, controlled production of surface relief gratings with a well defined (sub-)micron periodicity is difficult due to the high thermal conductivity. Even when using short pulse (< 0.1 ns) lasers, significant melting of the metal has been observed (Simon & Ihlemann 1996), indicative of a fundamental thermal diffusion limit to the production of (sub-)micron feature sizes. Here the results of generation of regular sub-micron periodic relief gratings using a nanosecond pulsed copper vapour laser (CVL) are presented. A grating was produced on 316 stainless steel by direct writing of an interference pattern, where the grating spacing $d = \lambda/(2\sin(\Theta/2))$ was varied in the range $0.8 - 5$ μm by adjusting angle Θ between the two linearly polarised beams. This surface structuring mechanism in the threshold regime with fluences ≤ 1 J/cm^2 is tentatively identified as a slow, evaporative process. Finite element analysis of the 2D heat flow shows that a modulated lateral temperature distribution can be sustained at the target surface to establish selective surface evaporation on (sub-)micron scales, provided the thermal conductivity of the metal substrate is sufficiently low. The effect of multishot feedback, and possibly hydrodynamic processes which may enhance the production of regular surface relief gratings, are discussed.

II EXPERIMENTAL SETUP A MOPA system similar to that described in chapter 3 is used. Using only the green output an interference pattern was generated by overlapping two images of the near-field intensity distribution as shown in figure 7.4. For this purpose, the top-hat near-field beam profile naturally

[5] Because of their antireflection properties, spatial relief gratings have evolved on the eyes of various night-moth species via natural selection.

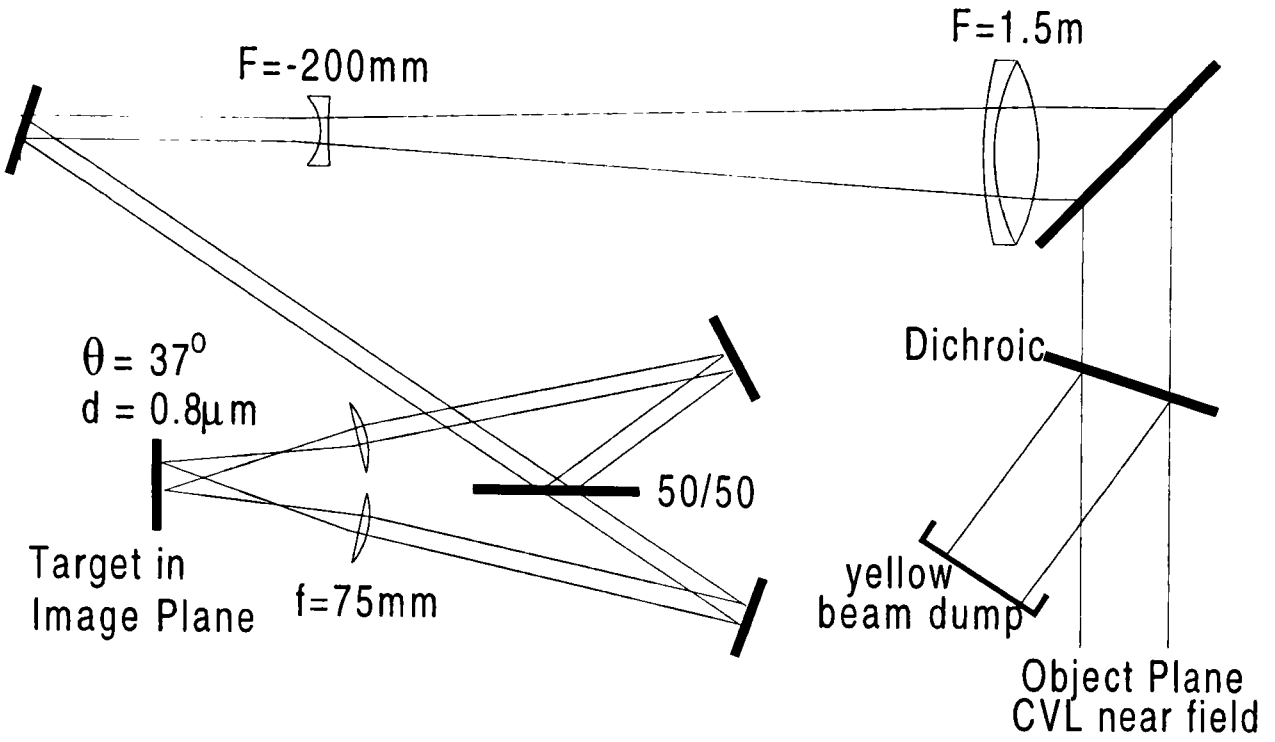


FIGURE 7.4: Experimental arrangement for direct writing of an interference pattern onto metal surfaces using the green output from a MOPA CVL system.

produced by CVLs (Coutts & Brown 1995*a*) facilitates the generation of a homogeneous, modulated intensity distribution, whereby the full spatial coherence allows the use of a flexible shearing interferometry arrangement. The choice for processing in the image plane rather than the focal plane was necessitated to reduce spurious diffraction in the intermediate field, and minimise the intensity variations over the full aperture of the beam. The main beam (25 mm diameter) was demagnified ($\times 7.5$) to minimise the numerical aperture of the imaging arrangement to give sufficiently large depth of field. Each of the two interfering beams was imaged separately for ease of alignment.

Optimisation of the processing strategy (schematically depicted in figure 7.5) was done as follows. First, the image size ($200 - 300$ μm diameter) was chosen such that the average fluence in one single beam (0.5 J/cm^2) was below threshold for surface modifications to occur. By interfering a second beam, the modulated peak fluences was increased by a factor of 4, sufficient to establish structuring of the metal surface, but still below the threshold for melt ejection or explosive ablation (Körner et al. 1996). Tests on varying the fringe visibility by changing the relative intensity of the two beams, whilst keeping the total average fluence constant, showed that even for relatively low contrast fringes (visibility $\simeq 0.3$) modulation of the metal surface profile could be achieved. This indicates that the *average* fluence on target is the most important parameter as this determines the average surface temperature, and for the current arrangement the optimum average fluence was determined to be 1.1 ± 0.1 J/cm^2. To obtain maximum image contrast required fringe visibilities > 0.8, which were readily obtained using a 50/50% beam splitter to ensure equal powers in each beam. Only a marginal difference was observed between using s or p polarised light, while for most experiments s polarised light (electric field perpendicular to plane of incidence) was used, in view of generating best visibility of the interference pattern.

The second important processing parameter involved the pulse train formatting of the CVL output.

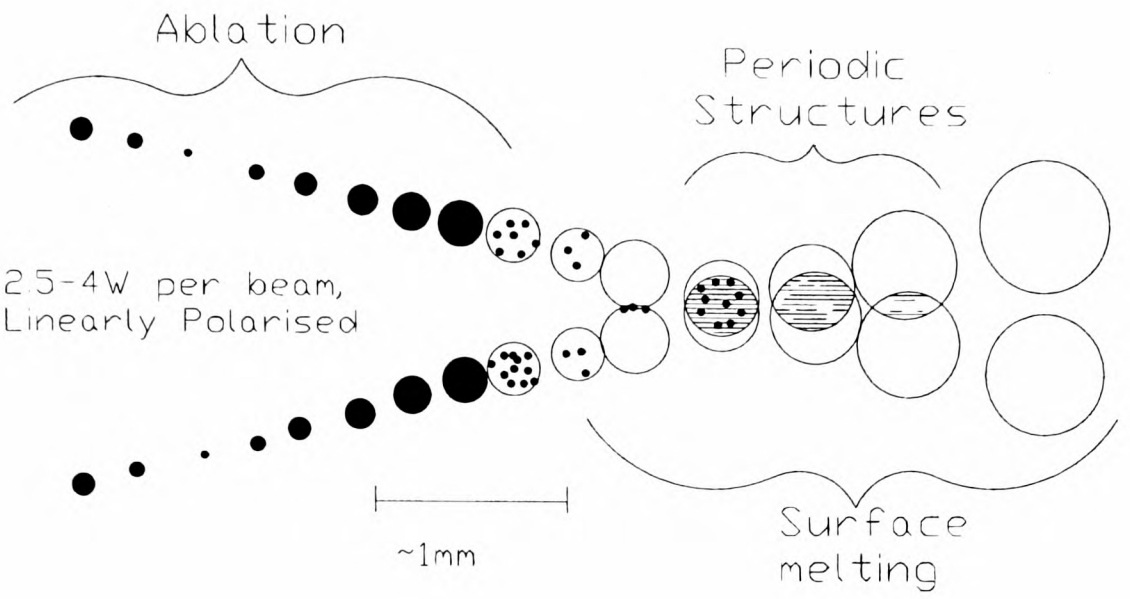


FIGURE 7.5: Schematic of optimisation of the processing strategy for producing the (sub-)micron periodic surface structures.

Using the time-delay shutter control of the MOPA (see chapter 3), bursts of n-pulses (n up to 255) at the fundamental 6.2 kHz pulse repetition frequency could be repeatedly delivered at slower burst-repetition frequencies of typically $1-10$ Hz. Thus, for a fixed number of pulses N, one could either opt for one continuous fast burst ($N = n$); one continuous slow burst ($n = 1$, N pulses repeated at $1-10$ Hz); or a burst-mode combination ($n = N/b, b$ bursts). The latter strategy was found to give the best surface modulation, where typically $n = 15-30$ pulses and $b = 7-10$ bursts. Beyond a certain number of pulses $N \simeq 100-1000$, the enhanced coupling at the structured surface resulted in increased power deposition, leading to the onset of explosive ablation. Prior to processing the substrate was polished to give an optical quality finish, where no significant scratches or surface irregularities could only be seen with an optical microscope. No additional pre-treatment or conditioning of the surface was done.

III RESULTS & CALCULATIONS An SEM image of a textured stainless steel surface is shown in figure 7.6. To illustrate the spatial transverse coherence of the CVL beam, an interferogram with a large period is shown in figure 7.7. The contour of the processed versus. unprocessed surface is clearly visible, where the unprocessed areas in the central part is due to the centre-hole mirror of the double-pass amplifier (see chapter 3). Where the surface has been modified, a regular periodic relief grating with a period of 0.8 μm is produced over the full aperture of the image. The presence of an initial surface defect on the left-hand side above the centre of the image, has caused an area to be above the damage threshold for ablation due to enhanced absorption (Jeong et al. 1996, Ang et al. 1997). The long-range undulating features (> 10 μm) are associated with spontaneous LIPSS formation (Clark & Emmony 1989). Enlarged pictures of typical sub-micron features are shown in figure 7.8 and figure 7.9, where a square 2D surface relief grating has been produced by sequential overlaying of two 1D line gratings, whose relative orientation has been rotated by 90°. Looking at figure 7.9 it is not completely clear whether the surface modulation is

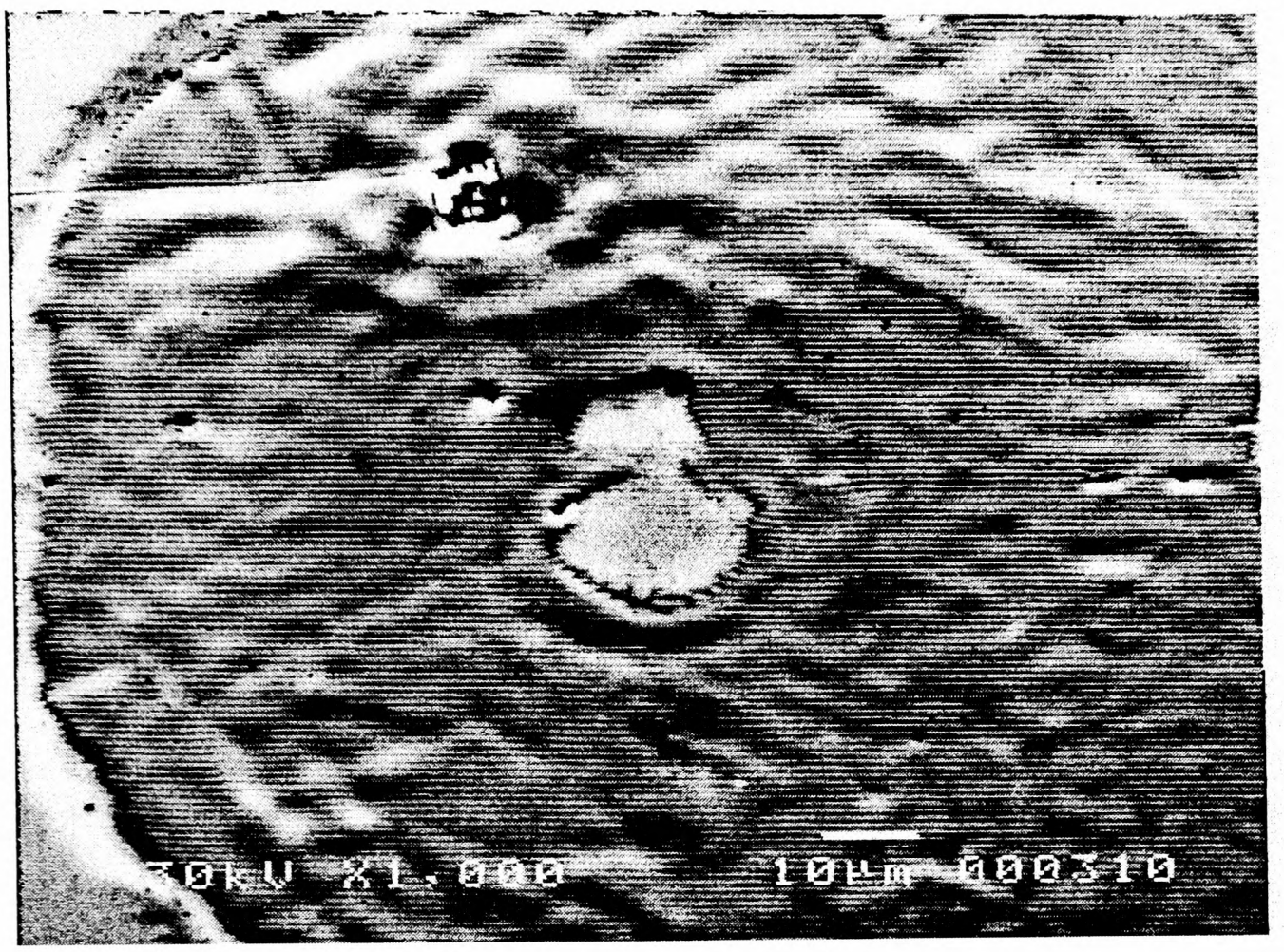


FIGURE 7.6: SEM micrograph of textured stainless steel surface with 0.8 μm periodic grating.



FIGURE 7.7: Intereferogram generated by shearing intereferometry of the CVL near-field profile, showing the full transverse coherence over the whole aperture.

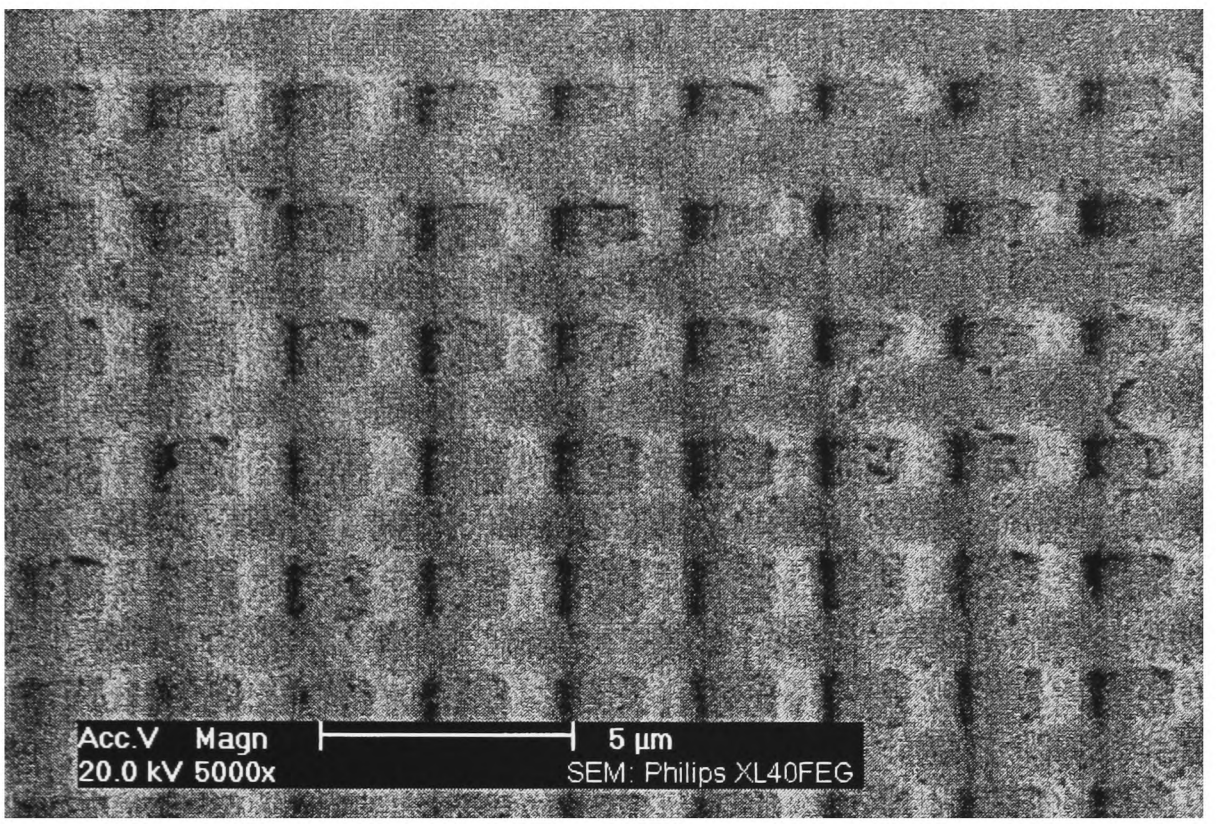


FIGURE 7.8: Two dimensional surface relief grating produced by repeated patterning of two orthogonal linear interference patterns rotated.

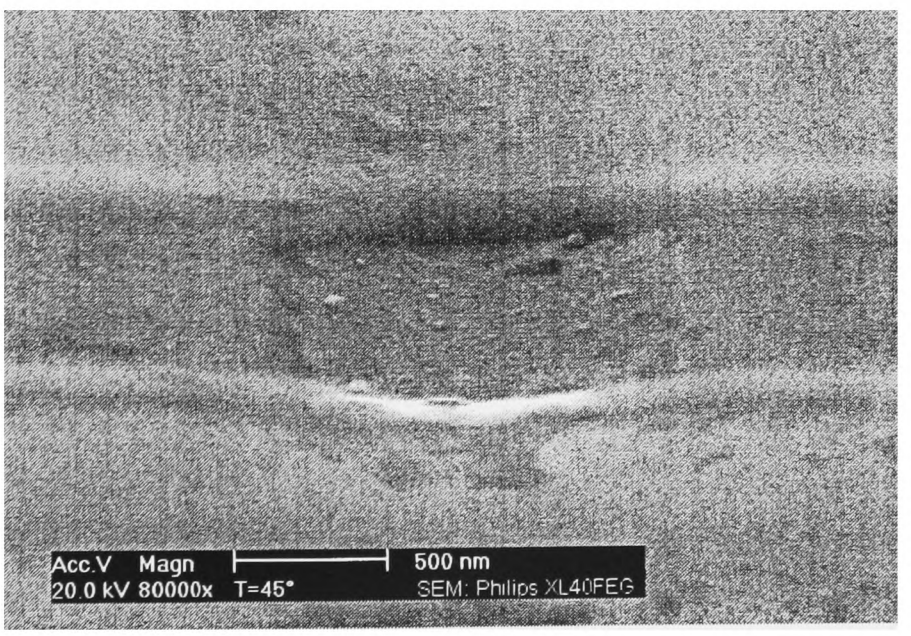


FIGURE 7.9: Typical view of a single period of the 2D surface relief grating.

created via localised material removal, or by redistribution of material towards areas of low temperature. The origin of the (recondensed?) droplets in the middle of the square is not clear, while the apparently bulging ridges seem to suggest motion of molten material has taken place.

To quantify the structuring process in terms of thermal diffusion, Coutts (1998) has performed a numerical simulation of the two dimensional heat-flow by employing a standard time-stepped staggered leap-frog finite-element analysis (Press et al. 1996). The surface was subjected to a modulated heat source with an approximate pulse-shape to reflect the temporal characteristics of the laser pulse, using an effective value for the reflectivity R to account for the energy deposition. The lateral heat flow across the surface was modeled, using periodic boundary conditions at the edges. Temperature-averaged values for the density $\rho = 7.8 \cdot 10^3$ kg/m^3 and heat capacity $c_p = 0.5$ kJ$\cdot$kg$^{-1}\cdot$K^{-1} of stainless steel were used, while the thermal conductivity $k = (14.5 + 0.015T)$ W$\cdot$m$^{-1}\cdot$K^{-1} was taken to increase linearly with temperature T. Thus, with the diffusion constant $\kappa = k/\rho c_p \simeq 5 \cdot 10^{-6}$ m^2/s, the thermal diffusion length $D \simeq 2\sqrt{\kappa \tau_p} = 0.9$ μm for $t_p = 40$ ns laser pulse.

Examining the calculated contour-plot of the surface temperature T_s as a function of time t and lateral dimension x along the surface (figure 7.10), a 300 K modulation of T_s can be observed throughout the laser pulse, while the overall average temperature is raised up to ~ 1600 K compared to the melting point $T_m = 1725$ K. The lateral modulation in surface temperature is only sustained for a surface layer < 1 μm deep, beyond which in the bulk of the metal the temperature distribution has been equilibrated. Once the laser pulse has stopped, the temperature modulation quickly decays on time-scales of few nanoseconds. Dissipation of heat into the bulk followed a classic exponential temperature decay, and causes the overall surface temperature to decrease rapidly. Given the interpulse period of around 0.1 ms, the overall residual from shot-to-shot is of order tens of degrees, which can be estimated by assuming that the total pulse energy (0.4 mJ) deposited in a volume determined by the spot-size on target and the diffusion depth $D \sim 50$ μm over such time-scales.. It is, therefore, to be expected that a cumulative effect over hundreds of shots will result in a significant increase of the surface temperature by few hundreds of degrees. This places an upper limit on the maximum number of shots n within one burst, as the average surface temperature needs to remain below a given maximum value at which point considerable melt-flow or explosive ablation will occur which is detrimental to the structuring process.

While the heat-flow simulations substantiate the assumption that a modulated surface temperature profile can be sustained for the duration of the laser pulse, it is more difficult to quantify to what extent thermal mechanisms, i.e. evaporation and melt-ejection, indeed can contribute to a differentiated material removal process to produce the resulting surface relief structure. By process of elimination, melt-ejection was first ruled out by performing experiments in vacuum with a close proximity window, which showed no significant of deposition of droplets. Since also all samples machined in either vacuum or air did not exhibit recondensation of melt-droplets, or significant hydrodynamic motion of molten material, melt ejection is unlikely to be a dominant process. Besides, the onset of such hydrodynamic processes is readily identified by the presence of surface features with larger dimensions, such as may occur at higher fluences, or due to enhanced coupling at surface irregularities.. Successful production of a two dimensional surface grating, as shown in figure 7.8, further indicates that the structuring process is reproducible, and the material response is faithful to the incident modulated intensity profile. Also noteworthy is the ability

metal	κ [cm^2/s]	T_m [K]	$\Delta H_{\rm m}$ [eV]	$\Delta H_{\rm v}$ [eV]
Fe	0.23	1811	0.14	3.1
Ni	0.23	1726	0.94	3.9
Ta	0.25	3269	0.38	7.6
Cr	0.29	2130	0.21	3.5

TABLE XIX: Metals exhibiting low diffusivities which are potentially suitable for production of (sub-)micron periodic surface relief gratings.

to 'add-on' structures on top of existing modulated surface profiles, and again the absence of melt-pool formation.

IV DISCUSSION These observations of 'near-threshold' ablation suggest that evaporation is the dominant material removal mechanism. However, in view of accounting for the observed ablation depths of order $1 - 10$ nm per pulse as estimated from SEM analysis, the ongoing debate regarding the 'thermal' nature of evaporative ablation in this threshold-regime (Bennett et al. 1996) emphasises that great care should be taken in applying equilibrium thermodynamic models to describe such pulsed laser ablation processes. Based on a classical evaporation process, the ablation depth per pulse is given by (Kelly & Miotello 1994)

$$\text{depth per pulse} = \frac{p_0}{n_c}\,(2\pi m k_B)^{1/2} \int_0^\infty T^{-1/2} \exp\left(\frac{-H_{\rm v}}{k_B T}\right) dt \qquad (7.2)$$

where p_0 is related to the equilibrium saturated vapour pressure, n_c is the density of the condensed (liquid) phase, $\Delta H_{\rm v}$ is the latent heat of vaporisation, T is the temperature, and m is the molecular weight of the species. Kelly & Miotello (1994) have shown that even by the most optimistic overestimates, evaporation rates of 1 nm/pulse (for 12 ns laser pulse) require temperatures well above the boiling temperatures of most materials. In addition, the observation of hyperthermal velocity distributions in the vapourised plume (Bennett et al. 1996) clearly points to the failure of a simple evaporative model based on classical thermodynamics. On the other hand, Bennet et al. (1995) have reported on experiments of near-threshold sputtering of gold using 12 ns KrF pulses in this context, and identified vaporisation as the main pathway for material removal for fluences < 1 J/cm^2, resulting in material removal rates of few monolayers (≤ 1 nm) per pulse. Beyond > 1 J/cm^2 the vaporisation rate is known to be self-limited due to the formation of Knudsen layers (Kelly & Rothenberg 1985), resulting in the predominance of hydrodynamic expulsion for fluences > 2 J/cm^2.

Despite these uncertainties, the experimental observations reported here favour an interpretation in terms of 'evaporative' ablation, i.e. a slow release of atoms one at a time, over other processes which are associated with violent ejections of clusters or particulates. Furthermore, given the thermal diffusivity of 316 stainless steel $\kappa = 0.05$ cm^2/s, the associated energy density $u = 2 \cdot 10^4$ J/cm^3 is within the regime of evaporative ablation as argued in the previous section, and below the threshold for explosive ablation $u \gtrsim 10^5$ J/cm^3. To account for the observed sharp contrast of localised evaporation, and the relatively deep modulation of the surface considering the peak surface temperatures are just above the melting temperature, suggests an explanation in terms of other (non-thermal) mechanisms which may well enhance the evaporation process. Recalling the observed multi-shot effects, clearly the cumulative modification of the surface structure affects the coupling efficiency (Bennet et al. 1995, Jeong

et al. 1996, Ang et al. 1997, Ang et al. 1998), providing a possible positive feedback the structuring process. While in the above melt-ejection processes have been ruled out, less violent hydrodynamic effects such as Marangoni convection due to the change in surface tension or quasi-steady capillary waves (Bostanjoglo & Nink 1996, Clark & Emmony 1989) may further enhancing the structuring process. Also, coherent excitation of surface waves or plasmons (Sipe et al. 1983) may play their part. The numerical simulations indicate that modulation of the surface temperature profiles on (sub-)micron scales can be achieved in metals which have sufficiently low thermal diffusivity κ. From a selection of pure metals (see below section 7.3), it is found that nickel, tantalum and chromium exhibit the lowest thermal diffusivity (table XIX) thus making them potential candidates for future trials. Besides the differences in the melting temperature, and the (bulk averaged) enthalphies of melting ΔH_{m} and vaporisation ΔH_{v}, the differences in the non-thermodynamic properties such as the tensile strength of the liquid phase and the microscopic crystal structure may further provide some degrees of freedom to increase the surface modulation. However, with values of $\kappa \simeq 0.23 - 0.29$ cm^2/s still a factor of four higher than the 316 stainless steel used in the experiments, it is expected that the smallest surface gratings which may possibly be produced in these metals is a factor of two larger than those produced here.

On the other hand, there are a number of mechanisms which equally put limits to the processing strategy described here. The numerical simulations indicated that if the overall average temperature is allowed to increase too much over the accumulation of pulses, the surface structures would be 'washed out'. Similar effects have been observed by externally heating the bulk material (Bennett et al. 1996) or via continuous irradiation (Clark & Emmony 1989, Bennet et al. 1995). Also, plasma formation, shock-waves or gas lensing in the accumulated vapour above the surface are likely to be detrimental. Finally, the maximum surface modulation which can be produced in the postulated evaporative regime is likely to be smaller in comparison with the deep modulation which can be obtained by operation in the hydrodynamic expulsion regime using femtosecond lasers (Simon & Ihlemann 1996).

In summary it is concluded that in order to produce surface features with dimensions approaching the thermal diffusion length, requires matching of the fluence regime to the thermophysical material properties to obtain the appropriate energy density regime for evaporative ablation. Using long (40 ns) laser pulses, a processing strategy has been identified where a modulated surface temperature profile can be sustained throughout the laser pulse to accommodate localised material removal. Via an as yet unidentified positive enhancement mechanism, modulation of the surface can be achieved over the cumulative effect of bursts of shots, whereby the pulse train format is adjusted to ensure that the overall average surface temperature does not reach the melting temperature to prevent 'washing out' of the surface structure. Sub-micron periodic surface structures can be produced in 316 stainless steel with sufficiently low thermal diffusivity $\kappa \simeq 0.05$ cm^2/s. While often materials processing of metals on (sub-)micron scale is thought of to be only possible using femtosecond lasers, these results show that there exist a (tight) processing window wherein it is possible to do so using nanosecond lasers. In first instance, this window is defined by the regime of low $u \lesssim 10^4$ J/cm^3 where effects which are detrimental to the surface structuring process, such as melting and explosive evaporation, are limited. Within this regime of u, further enhancement of the surface structuring process can be achieved by experimental optimisation of various secondary effects as has been discussed.

7.3 MOMENTUM TRANSFER DUE TO MELT EJECTION

I INTRODUCTION One of the major difficulties in describing the pulsed ablation process of metals regards the complex interplay of heat transport and phase transition of the solid substrate. One the one hand, for practical purposes one is often primarily interested in well-defined phenomenological aspects such as material removal rates, morphological studies of melt ejection and characterisation of heat affected zones. However, it is often difficult to translate these experimental observations to provide conclusive evidence on even the simplest theoretical descriptions of the ablation process. While the use of, for example, classical (quasi-)equilibrium kinetic heat diffusion models (von Allmen & Blatter 1995) can provide some background and order of magnitude estimates (sometimes sufficient from a practical perspective), it remains tenuous to arrive at more refined descriptions of the inherently non-stationary heat equation describing laser ablation (Arnold et al. 1998). From an academic viewpoint, a glance at the vast volume of existing body of literature illustrates the fact that it remains an arduous task to find conclusive experimental evidence for different proposed models which often result in the same phenomenology. Beyond considerations of the thermal aspects of the ablation process, it is even more difficult to probe into the nature of the phase transition which ultimately results in removal of material. Progress in this area has only been made recently, where the increased used of femtosecond lasers, combined with fast imaging and time-of-flight spectroscopy, has enabled time-resolved studies of the dynamics of short pulse laser ablation (von der Linde et al. 1997, Cavalleri et al. 1998, Sokolowski-Tinten et al. 1998*a*, Sokolowski-Tinten et al. 1998*b*). In the following section, a discussion of some of these issues will be presented based on the measurement of momentum transfer of various metals upon laser ablation in vacuum. In comparison with the previous section, which considered the evaporative ablation regime, the discussion will now focus on aspects of so-called 'explosive' ablation associated with the ejection of molten material. The relative effect of the physical properties of the target material on the liquid metal ejection mechanism for material removal will be studied using the ballistic pendulum.

Motion and ejection of liquid metal has been observed in many systems with varying pulse durations from in the millisecond regime, down to nanosecond and femtosecond pulses. The nature of the underlying physical mechanisms which drive the fluid motion, however, can differ significantly. When using relatively long pulse durations in the range of $0.1 - 1$ ms, such as CO_2 lasers (Armon et al. 1989*b*, Armon et al. 1989*a*, Basu & Debroy 1992) or Nd:YAG lasers (Phipps et al. 1988), it has been conjectured that motion and ejection of the molten metal are due to surface tension driven convection. Marangoni and buoyancy forces (Basu & Debroy 1992) have been shown to result in significant motion of the melt pool, which is of particular importance for laser welding applications (Matsunawa & Semak 1997, Semak & Matsunawa 1997). Knudsen layer formation is not only of importance to accurately describe evaporation rates and plume dynamics (as discussed in chapter 4 and 5), but also plays an important role to describe the recoil pressures generated which further causes motion of the vapour and melt-pool (Semak & Matsunawa 1997, Chan & Mazumder 1987). Numerical simulations have been performed by Chan & Mazumder (1987) and Aden et al. (1990) to describe the Knudsen layer formation and evolution of the ablation front. Even within a quasi-equilibrium surface evaporation model driven by these relatively long pulses, Anisimov et al. (1980) have shown that the evaporation front is inherently unstable.

By employing short pulses in the regime of $1 - 100$ ns, the window for slow, convective fluid motion is

reduced as typical time-scales for the liquid to perform damped oscillations are > 0.5 μs (Bostanjoglo & Nink 1996). Instead, in the nanosecond regime phenomena associated with superheated phase explosion becomes dominant, as was discussed earlier. Some controversy existed regarding the question whether the observation of violent ejection of metal is indeed caused by such a phase explosion, or whether an alternative mechanism of sub-surface heating (Dabby & Paek 1972, Gagliano & Paek 1974, Singh et al. 1990) plays a part. However, the convincing arguments put forward by Miotello & Kelly (1995) and Kelly et al. (1998) seem to favour the phase-explosion model. Stepping away from quasi-analytical approaches, Ho et al. (1995) have reported a numerical model which combines a one-dimensional transient heat transfer model for the description of the heat conduction in the solid, with a dynamical model for the plasma plume described using Euler's equations. While the approach taken by Ho et al. (1995) provides a significant advancement to describe the many physical aspects of the ablation process, including the surface recoil pressures (see also chapter 4) generated by the compressed vapour and its effect on the vapour/liquid interface, to date no progress has been made to simulate the phase transition problem and arrive at a comprehensive model which includes the explosive superheating phenomenon.

Going further into the femtosecond regime, the non-stationary and transient character of the phase transition becomes even more pronounced, where Sokolowski-Tinten et al. (1998*b*) and Sokolowski-Tinten et al. (1998*a*) have observed interference patterns between the expanding, dense vapour front and the metal surface provide insight into the dynamics occurring on time-scales of order 0.1 ps up to 1 ns. It is only by employing such short pulses laser that one can hope to resolve the dynamics of the phase transition and the fast (non-)equilibrium heating of the metal.

II Experiments & Results The experimental setup used for the measurement of momentum transfer has been described in chapter 4. For the current study, all measurements were performed in vacuum $\left(10^{-2}\text{ mbar}\right)$ to characterise the effect of different material properties on the piston recoil p_0. As the experiments involved frequent changing of target materials, the main issue to ensure reliable comparison of the measured recoil for different targets regards the calibration of the pendulum. Owing to the different densities of the targets, the pivot point of the pendulum was adjusted each time to yield a sufficiently long period of oscillation of around 1 s for ease of detection of the deflection angle; whilst maintaining the sensitivity of the pendulum in the $0.5 \cdot 10^{-8}$ Ns regime. An analysis of the experimental errors (see also chapter 4) showed that the overall precision of all the experiments were in the range of $\pm\ (0.3 - 2) \cdot 10^{-8}$ Ns. Apart from the systematic errors related to the calibration of the pendulum, it was found that the stochastic scatter of the recoil measurements varied greatly for the different materials. As will be shown below, this is related to the observed variations in the mechanism for momentum transfer.

The vacuum recoil was measured for about a dozen different pure metal foils ($> 99\%$ purity), with a typical thickness of $200 - 250$ μm. Choice of materials was primarily made on the basis of practical considerations (cost, availability), while also safety aspects precluded use of radioactive or highly toxic metals. The scope of material properties was sufficiently large to include light, low Z number metals such as aluminium, as well as dense, high Z number elements like tantalum and tungsten. Soft materials (tin, indium) were compared with hard metals (tungsten), and also metals with high thermal conductivity (copper, silver, aluminium) were measured against those of lower conductivity (titanium, vanadium). The focusing and detection arrangement was identical to that described earlier in chapters 3 & 4, using

a $f = 250$ mm focal length lens.

The vacuum recoil was measured as a function of focal position z as shown in figure 7.11.The first important observation is that for indium, and to a lesser degree silver, the maximum vacuum recoil p_0 does not occur at focus. Instead, p_0 exhibits a local minimum, and two approximately symmetric maxima around the focal position, which in the case of indium occurred for $3-4$ mm defocusing, and 1 mm for silver. With the $f/10$ focusing arrangement, these focal positions produced spotdiameters of approximately 300 μm and 100 μms, respectively, which was verified with an optical microscope. For other metals (aluminium, nickel and tungsten) the maximum value of p_0 does occur at focus. Furthermore, figure 7.11 shows that the range over which p_0 could be detected varied from metal to metal, where tungsten showed the sharpest cut-off as a function of defocusing, while for indium significant values for p_0 could be measured at relatively large distances away from focus.

In figure 7.12 the vacuum recoil p_0 is measured as a function of laser pulse energy E. Clearly, for each metal the value of $p_0 \propto E$, with slightly different slopes for different metals. The two data series for indium shown in figure 7.12 are the values of p_0 measured at two different focal positions, corresponding to the maximum (max) and minimum (focus) of figure 7.11. Note the sharp difference in the slope for the two measurements. Further shown in figure 7.13 is the (integrated) total recoil for a burst of n pulses ($1 \leq n \leq 10$). The vacuum recoil p_0 is found to be linear ($R = 0.998$) throughout, while in the presence of a background gas (atmospheric conditions) the onset of saturation of the total recoil momentum is observed for increasing n, possibly related to the shot-to-shot interaction of the nascent shock-wave plume (see also chapter 6).

The single-shot ablation craters where characterised *a posteriori* using an optical microscope, where typical images are shown in figure 7.14 and figure 7.15, for vanadium and indium respectively. The focal position is identified with the smallest diameter of the ablation crater, as seen in figure 7.14. An estimate of the incident fluence (or equivalent power density) can be obtained by considering the measured diameter of the ablation spot, or by calculating the waist of the spotsize on target given the focusing geometry of the CVL. Inevitably, these values differ slightly, indicative of the inherent uncertainty in determining the absolute value of the fluence. For the present discussion, the fluence at focus is estimated to be of order $0.1 - 0.3$ kJ/cm^2, while for defocused beams typical fluences are an order of magnitude lower $15 - 40$ J/cm^2. The most dramatic effect in this fluence range is illustrated in the photographs of indium (figure 7.15), where the incident pulse energy is changed whilst keeping the focal position fixed at focus. For the highest fluences (figure 7.15 a), deep craters ($\simeq 25 - 30$ μm) are produced, similar to the craters produced in aluminium (see chapter 4), characteristic of explosive ablation for fluence > 100 J/cm^2. Reducing the pulse energy from 3.1 to 2.1 mJ results in localised onset of explosive ablation (b), possibly caused by hot-spots in the laser beam or enhanced coupling due to initial defects present on the target surface, while other parts of the irradiated material only show signs of melting. At the lowest fluence (c) the threshold for explosive ablation is never reached. In comparison, the ablation crater produced by a defocused beam at maximum deflection (d) produces the same surface morphology as the low fluence experiment.

The key observations from these morphological studies seem to indicate that the ejection and/or motion of molten material produces a significant contribution to the measured vacuum recoil momentum

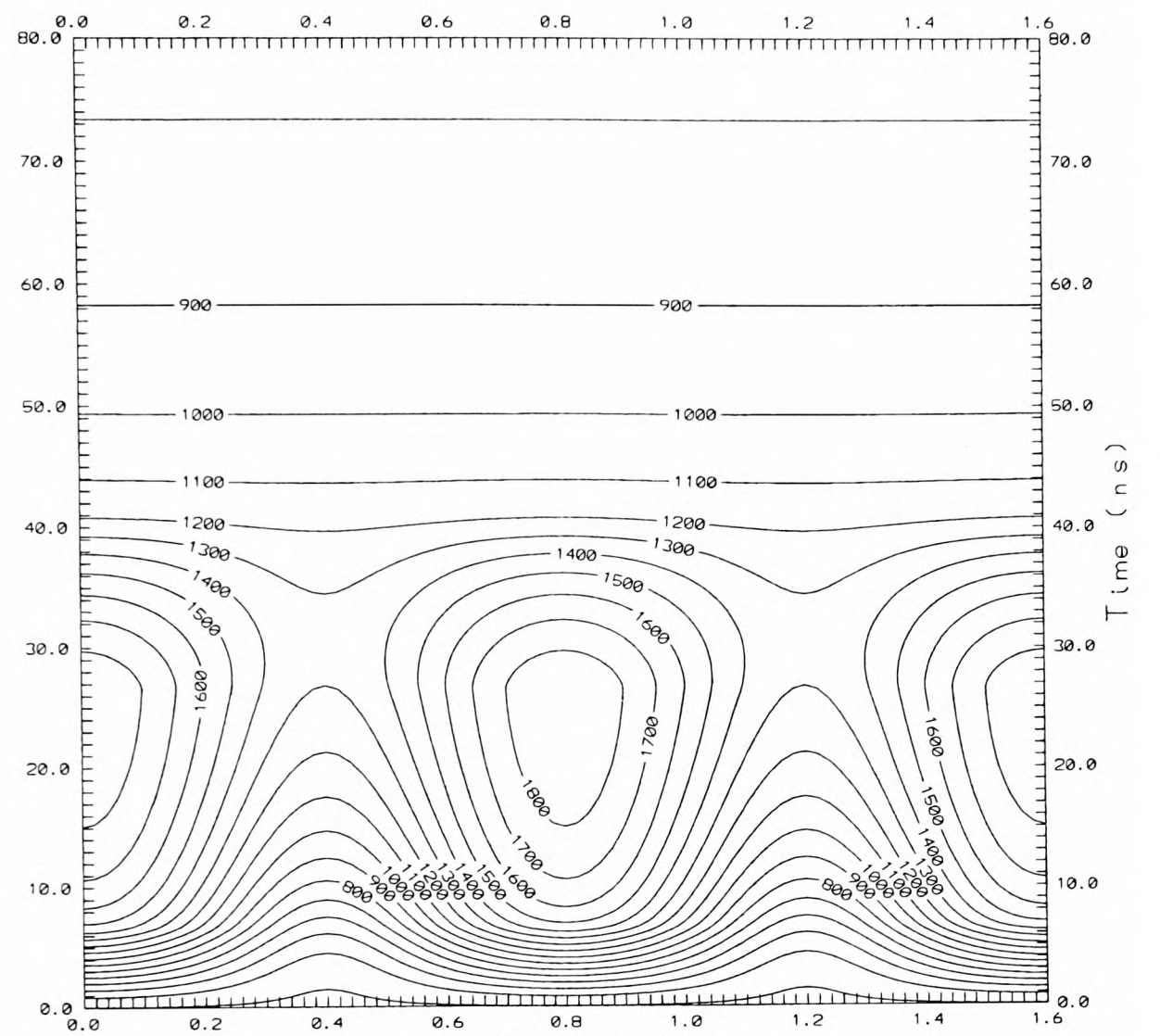


FIGURE 7.10: Contour plot of the simulated modulated surface temperature profile as a function of one lateral spatial coordinate (x-axis) and time (y-axis).

p_0 [10^{-8} Ns]	metals	T_m [K]	κ [cm^2/s]	u_{max} [J/cm^3]
20 – 25	Zn	693	0.42	$2 \cdot 10^4$
	In	430	0.48	
	Sn	505	0.43	
9 – 12	Ti	1933	0.39	$2 \cdot 10^5$
	V	2163	0.43	
	Mo	2869	0.59	
	Cu	1359	1.15	$1 \cdot 10^5$
	Ag	1235	1.77	
4	W	3695	0.67	$6 \cdot 10^5$

TABLE XX: Classification of a selection of metals into three groups according to the measured value of the vacuum recoil impulse p_0. The values of the energy density u_{max} are calculated for the fluence F which gave the largest vacuum recoil impulse p_0. Parameters used: $\tau_p = 40$ ns, $E = 2.5$ mJ.

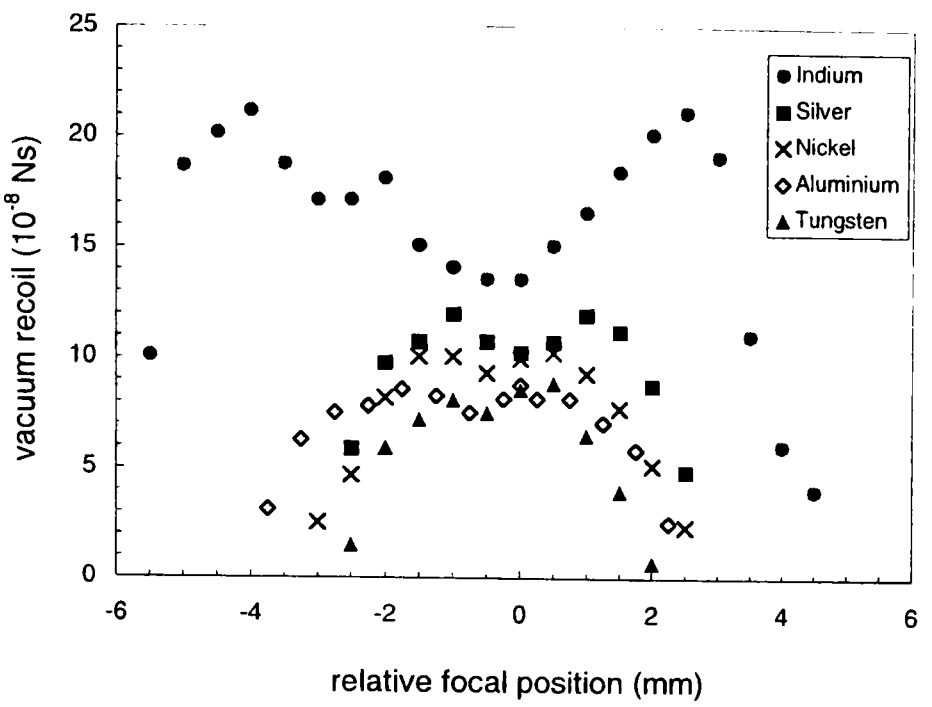


FIGURE 7.11: The vacuum recoil momentum measured for different metals as a function of focal position. Laser pulse energy $E = 3.1 - 3.3$ mJ.

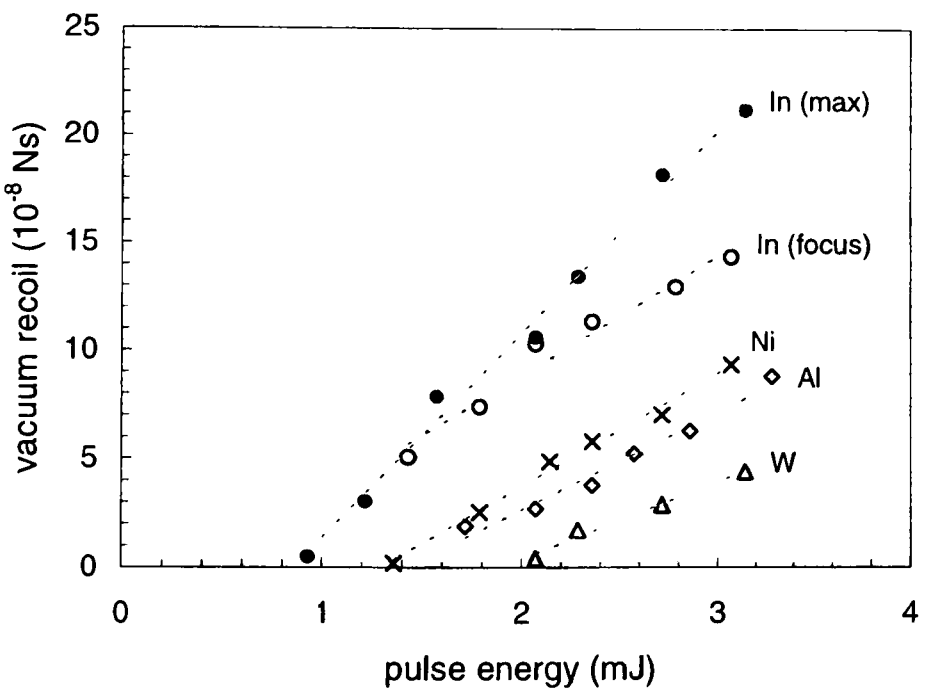


FIGURE 7.12: The vacuum recoil measured for different metals as a function of the laser pulse energy E. The two data series for indium correspond to two different focal positiions, one taken at the point of maximum deflection and one at focus where the deflection has a local minimum.

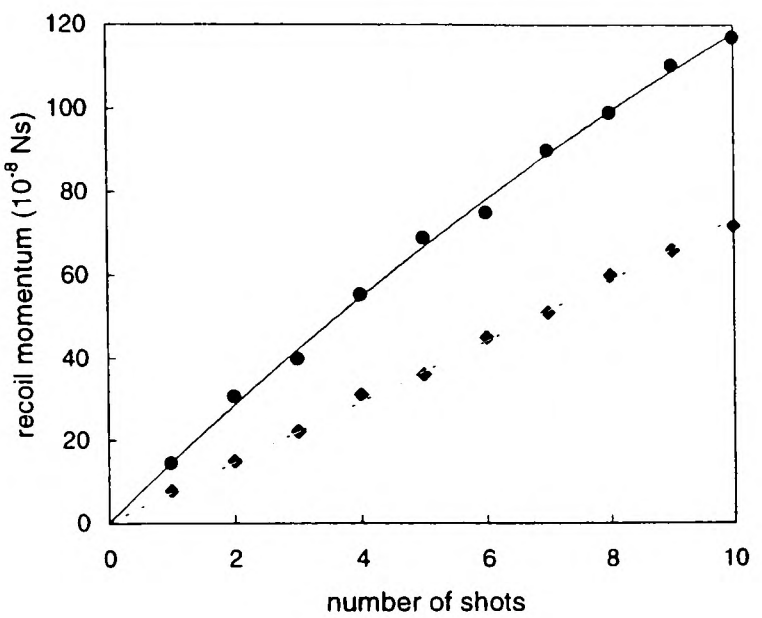


FIGURE 7.13: The recoil momentum measured as a function of the number of laser pulses for aluminium at focus, in vacuum (♦) and under atmospheric conditions (•) .

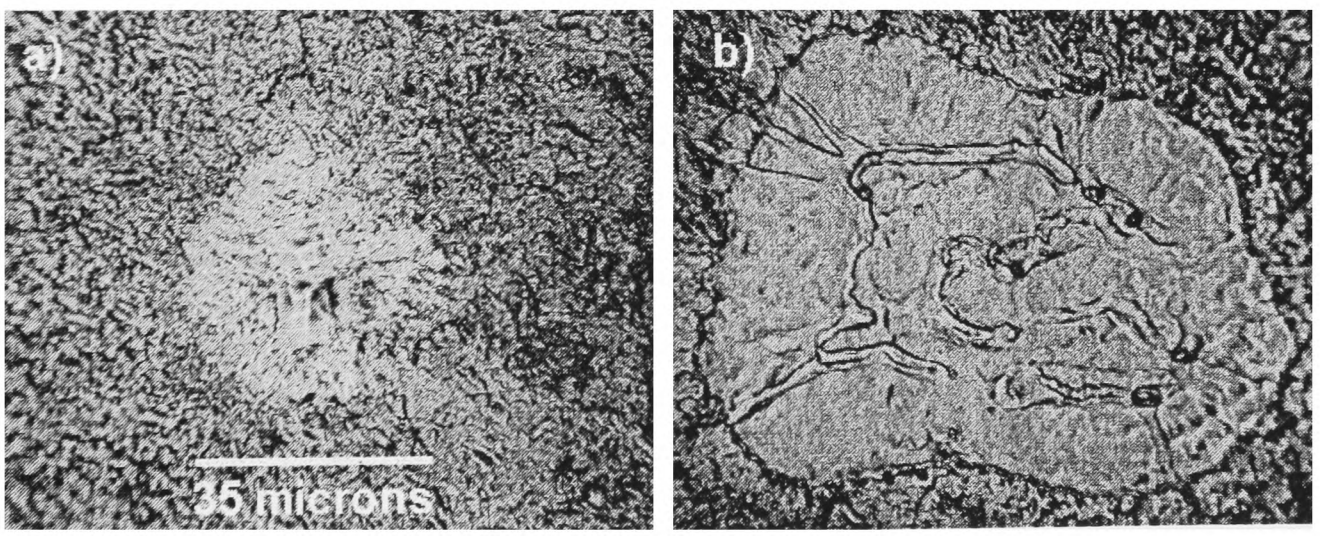


FIGURE 7.14: Single-shot ablation craters in vanadium **a)** at focus and **b)** defocused.

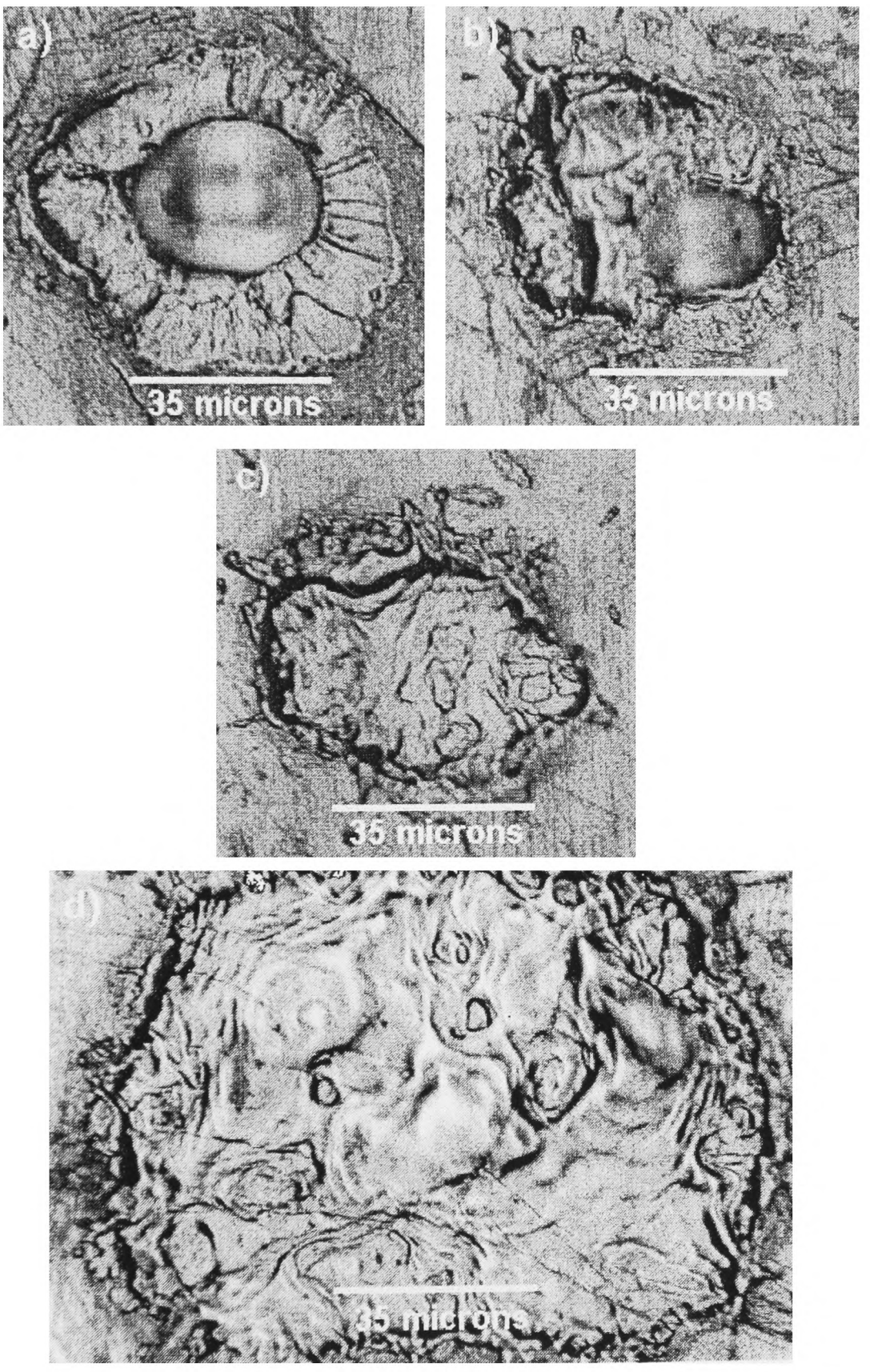


FIGURE 7.15: Single-shot ablation craters in indium at various fluences, varying from **a)** 3.1 mJ; **b)** 2.1 mJ; and **c)** 1.4 mJ. All craters were produced at focus, in comparison with a strongly defocused beam (maximum deflection) as shown in **d)**.

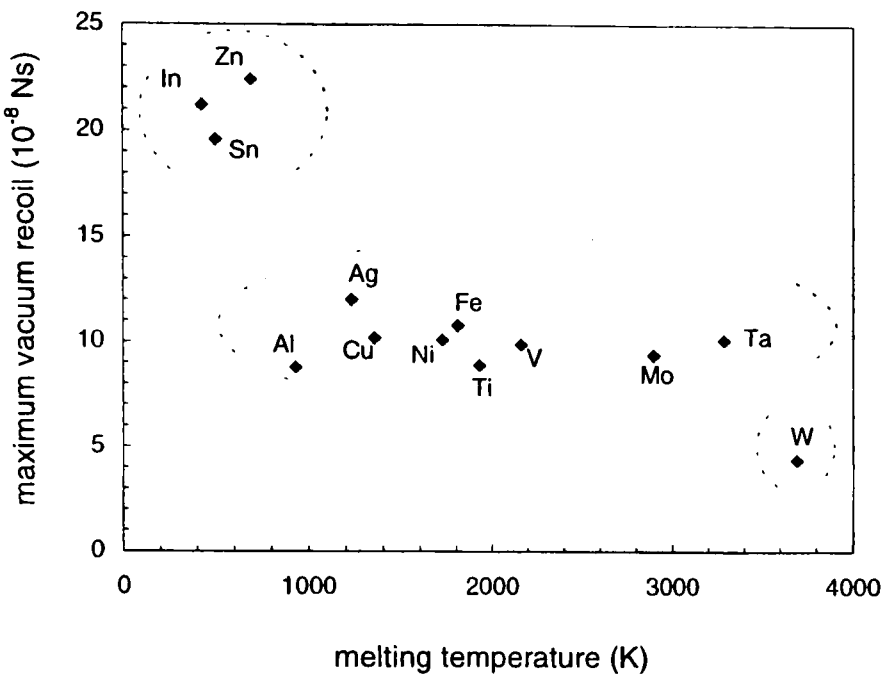


FIGURE 7.16: The maximum vacuum recoil momentum measured for various metals plotted against the melting temperature of material.

p_0. This hypothesis is further confirmed by comparing the maximum vacuum recoil impulses for different metals, as shown in figure 7.16. To illustrate this hypothesis, consider the maximum values of p_0 as a function of the melting temperature T_m to provide semi-qualitative comparison of the different materials. For the metals studied here, roughly three groups as listed in table XX can be distinguished. The first group consist of metals with low melting temperatures just a few hundred degrees above room temperature. Combined with intermediate thermal diffusivities κ of order 0.4 cm^2/s (compared to, for example, the low value of $\kappa \simeq 0.2$ cm^2/s as for the metals listed in table XIX, and good thermal conductors such as copper and silver with $\kappa > 1$ cm^2/s), the deposited energy density $u \simeq 10^4$ J/cm^3 is apparently sufficiently high to cause melting of a relatively large volume to result in the observed high vacuum recoil p_0. The second, and largest group of metals exhibit vacuum recoil momenta $p_0 \simeq (9-12) \cdot 10^{-8}$ Ns. In the case of, for example, titanium, vanadium and molybdenum, the decrease in p_0 is ascribed to the significantly higher (factor $4-5$) melting temperature T_m of around $(2-3) \cdot 10^3$ K. Finally, for tungsten the combination of a high value of T_m (the highest for all the metals considered here), combined with a relatively high κ results in the lowest measured p_0. Note, however, that the explanation given here remains somewhat tentative. For example, compared to the melting temperature of the first group of metals, the increase in T_m for copper and silver is only a factor of $2-3$. For copper and silver, however, it can be argued that the high thermal diffusivities κ of these metals results in low values of u whereby large volumes are heated but never attain sufficiently high temperatures to produce molten liquid to generate momentum. Alternatively, an explanation as proposed by Bergmann et al. (1996) can be given in terms of the hardness of the material, as characterised by the shear modulus G. Bergmann et al. (1996) observed

a decrease of the single-shot ablation depth for metals with increasing G. However, how this relates to a measured vacuum recoil p_0 remains as yet unclear.

III DISCUSSION The ballistic pendulum measurements have shown that the vacuum recoil p_0 varies for different materials. First experiments of this kind have been performed by Gregg & Thomas (1966), who also observed material dependent impulse coupling coefficients. Gregg & Thomas (1966) then already noted, however, that it remains difficult to deconvolve the combined effects of, for example, the optical properties (surface reflectivity), thermodynamic properties (thermal diffusivity, melting temperature, enthalphy of fusion and evaporation), or mechanical properties (hardness, tensile strength) of the material. Furthermore, the contribution of different modes of material removal result in greatly varying magnitudes of momentum transfer. Neuman (1964) observed marked differences in the momentum transfer during ablation of soft lead (melt drops) compared to other metals such as aluminium and silver. In the case of glazed porcelain Neuman (1964) measured large recoil momenta due to spalling and cracking of the target material.

In the present discussion it has been argued that thermodynamic processes are the most dominant aspect of the pulsed laser ablation of metals, particularly when using nanosecond lasers like the CVL. Therefore, the effect of the optical and mechanical properties of the material are assumed to be negligible.. In practice no direct evidence was found which suggested otherwise. The only exception in this, is that for iron a significant increase of p_0 was measured due to surface oxidation. While a clean, virgin surface would produce $p_0 \simeq 10^{-7}$ Ns, the oxidised sample would yield vacuum recoil momenta twice this value. This effect is ascribed to the blow-off of iron-oxide contributing to p_0.

As shown in figure 7.16, the main results indeed seem to indicate the predominant importance of the thermodynamic properties of the material. The morphology of the ablation craters further indicate that motion or ejection of molten material is the dominant contribution to p_0. Based on the melting temperature T_m and thermal diffusivity κ, a semi-quantitative comparison of different metals has been made which is in agreements with experiment within the resolution and systematics of the ballistic pendulum. These findings are in-line with the arguments put forward in the preceding sections pertaining the importance of the energy deposition per unit volume.

Beyond these observations, however, further conclusions or more detailed description of the momentum transfer mechanism remain tentative. For example, Anisimov & et al. (1984) have given estimates to calculate the effect of ejection of an incompressible fluid subjected to an external cylindrically symmetric pressure field, similar to the problem of a flat cylindrical plate colliding with and incompressible fluid (Yih 1974). Simulations like those presented by Ho et al. (1995), Ho et al. (1996), Chan & Mazumder (1987) and Lunney & Jordan (1998) provide an alternative avenue towards quantifying the contribution of molten metal to p_0. However, as mentioned earlier, most computational models to date only incorporate a description of the thermodynamic aspects of the ablation process with the fluid dynamics of the expansion of the vapour front, which is described using a classical (quasi-)equilibrium evaporation rate based on the Clausius-Clayperon equation. At the time of writing, a more comprehensive model accounting for the non-stationary characteristics of the phase-transition remains to be developed.

Arguably, only experimental studies can provide definite answers to these questions, as any comprehensive finite-element analysis or Monte-Carlo simulation will quickly approach current limits on

computation speed due to the large number of degrees of freedom. In view of the discussion pertaining to the effect of phase explosion (Kelly et al. 1998), the present results indicate there exists a threshold value for u beyond which explosive ejection of material becomes increasingly more dominant. While definition of 'ablation thresholds' always needs to be treated with great care, an experimental value can be determined beyond which the surface morphology shows evidence of explosive material removal (see figure 7.15), similar to the phenomenological definition of a melting threshold at lower fluences (Götz & Stuke 1997). These findings are in line with work reported by Götz & Stuke (1997) and Arnold et al. (1998) on determining the ablation threshold of indium using time-of-flight spectroscopy. Direct, in-situ measurement of single-shot ablation rates using a quartz crystal microbalance by Zhang et al. (1997) have shown mass removal rates which are two orders of magnitude larger than can be accounted within a simple surface vaporisation model. Zhang et al. (1997) therefore conclude that only hydrodynamical mechanisms such as the phase explosion can account for such high ablation rates.

7.4 Conclusion

In this chapter it has been argued that the parameter u as defined in equation (7.1) is a useful parameter for characterising the thermodynamic aspects of pulsed laser ablation of metals. Defined as the energy density per unit volume determined by the ratio of the incident laser fluence F, over the diffusion length of the target material D, the parameter u not only characterises the temporal aspects of the heat diffusion (as determined by the laser pulse duration τ_p) but also accounts for the absolute energy deposition in the material. For practical purposes, the value of u as defined by the laser parameters can be compared with the required energy density to remove one unit volume of material as calculated from simple thermodynamic considerations. In this fashion different ablation regimes can be identified, as substantiated by comparison of a large number of reported experiments. Furthermore, this picture allows for an intelligible assessment of the relative benefits of nanosecond versus femtosecond, which have led to the conclusion that the thermodynamic aspects of the ablation process are essentially the same for both systems.

Thus, in view of optimising different processes for a particular laser materials processing application, it is emphasised that the use of shorter femtosecond pulses does not necessarily lead to an improvement in phenomenological quality parameters, such as size of heat affected zones, capability to produce features with smaller critical dimensions, or increase material removal rates. This conclusion is in sharp contrast to the prevailing misconception that the performance of femtosecond lasers is superior to their nanosecond counterparts due to the reduction of thermal effects. Instead, it has been argued that both nanosecond and femtosecond systems share the same thermodynamic characteristics, which can be estimated by considering the value of u. Beyond these simple (but important) thermodynamic considerations lies a host of other effects and mechanisms, which are significantly different for laser with different pulse durations. Herein lies the scope for optimising the laser ablation process for different applications, where often femtosecond lasers can provide new enabling technologies, like for example the production of microcavities in the bulk of transparent materials as an application of self-focusing exhibited at these high optical intensities (Glezer & Mazur 1997, Ashkenasi et al. 1998).

As an example of the capabilities of nanosecond lasers, the production of sub-micron periodic surface relief gratings on stainless steel has been demonstrated via direct transfer of a modulated optical

intensity distribution. While ultimately the limiting critical dimension in this surface texturing process is set by the thermal diffusion length of the material at these pulse durations, the experimental results indicate that non-thermal mechanisms play an equally important role. The positive build-up effect over multiple (hundreds) shots and the possibility to add-on two 1D linear gratings to produce a 2D rectangular matrix hint at the possible effects of, for example, surface morphology to enhanced selective coupling of the optical field to the target surface. These experiments demonstrate that claims made on the unique capability of femtosecond lasers to produce sub-micron structures are misleading, or too naive at best. As a counter-example, machining on a sub-micron scale has been achieved using a cw laser source, where a sharp threshold for material removal is established by using reactive atmospheres (Mullenborn et al. 1996). Similarly, when operating in the threshold regime as demonstrated here, a host of different physical processes can be manipulated. Besides the fundamental thermodynamic aspects, which will always play their part, other effects regarding the energy coupling mechanism (surface roughness, lattice defects, plasmons), and different pathways of material removal (evaporation, expulsion, exfoliation) need to be considered specifically for a given application. However, as illustrated in the ballistic pendulum experiments, detailed studies on the exact nature of, for example, the phase transition associated with the laser ablation process still remains poorly understood. Future research hopefully will extend current understanding beyond the simple thermodynamic picture, by employing more detailed probing of for example the vibrational and rotational energy distribution of the ablated species via laser induced fluorescence studies (Dreyfus et al. 1986, Dreyfus et al. 1987, Geohegan 1994), or time-of-flight spectroscopy (Götz & Stuke 1997).

In conclusion, it is noted that from a practical point of view these subtle issues beyond the thermodynamic picture are likely to constitute the leverage and the determining factor to match the choice of laser to a required process. For example, Jandeleit et al. (1998) have shown that nanosecond ablation of ceramics and metals always results in higher material removal rates per pulse compared to picosecond pulses. Thus, nanosecond systems are preferred for application involving fast drilling, while Jandeleit et al. (1998) have also observed that the minimum ablation rates are smaller for shorter pulsed lasers making them more suitable for precise surface processing. Secondary effects, such as the observed variations of the ablation rates with varying background gas conditions (Kononenko et al. 1997), further provide degrees of freedom for process optimisation. Particularly in the case of the CVL, the advantage of operating at high pulse repetition frequencies (10 kHz) enables corresponding high throughputs, important from an economic perspective (Körner et al. 1996, Knowles 1996). Also, efficient drilling of transparent dielectric materials (silica, sapphire and diamond) can be achieved due to significant pulse-to-pulse interaction (Pini 1996), where in this case the formation of a plasma is actively used as an efficient intermediate for coupling of the optical field to the substrate (Ihlemann et al. 1995). Finally, the capability of fibre delivery make nanosecond devices a powerful and attractive tool in an industrial environment. The use of novel resonator designs have recently resulted in reliable delivery of 15 W CVL output through a 100 μm silica-silica multimode step-index fibre (Booth 1998, Booth et al. 1998), thus opening a window towards commercialisation of these devices.

Chapter 8
Conclusion

That which is complete is also dead
SALMAN RUSHDIE

8.1 Summary

In this thesis different aspects of the physics of laser ablation of metals with copper vapour lasers (CVLs) have been investigated. Four different topics have been covered, which respectively pertain to i) improvement of the beam-quality output from CVL systems; ii) the formation of shock-waves during the laser ablation process; iii) the spectroscopy of continuum radiation emitted at the cool, dense core during the early phase of the plasma plume evolution; and iv) investigations to the effect of material properties on laser ablation. Combining the findings from the various experimental studies, the following picture of laser ablation of metals with CVLs can be drawn.

Given the output characteristics of the CVL (chapter 2 & 3), delivering $\tau_p = 40$ ns long pulses with pulse energies of $E_0 = 2 - 5$ mJ, fluences in the range of $F = 0.1 - 10^3$ J/cm^2 can be generated on target from high beam-quality MOPA systems delivering tens of watts average output power. Due to thermal diffusion, characterised by the diffusion depth D, different ablation regimes can be associated with different degree of power deposition in terms of energy per unit volume $u = F/D$ which not only depends on the parameters of the incident radiation (F, τ_p) but also on the thermal diffusivity of the metal $\kappa = k/\rho c_p$, with k the thermal conductivity, ρ the solid target density, and c_p the bulk heat capacity. Qualitatively, in the regime of threshold machining $\left(u \lesssim 10^4 \text{ J/cm}^3\right)$, controlled surface structuring on sub-micron scale can be achieved, as has been demonstrated by production of regular surface relief gratings via direct transfer of a modulated optical interference pattern (chapter 7). Via optimisation of secondary, 'non-thermal' mechanisms, such as enhanced optical coupling due to surface morphology effects, surface structures can be produced in this threshold machining regime, with the minimal critical dimensions approaching the thermal diffusion length. By increasing the energy density u to $10^4 \lesssim u \lesssim 10^5$ J/cm^3, one enters the evaporative regime where accurate removal of surface layers (up to fractions of microns) can be achieved. With accurate control this process can be tailored for surface milling applications. Volumetric mass-removal, as associated with explosive ablation, is established for $u \geq 10^5$ J/cm^3. In this regime, (molten) material is ejected violently, resulting in efficient material removal ($1 - 10$ μm per shot) suitable for drilling and cutting of materials.

In the explosive ablation regime, a dense, cold plasma is formed directly above the target surface. The emission of continuum radiation (chapter 6) during the first stages of the plasma plume evolution ($t < 1$ μs) is ascribed to opacity broadening and collisional Stark broadening of the individual spectral

lines. The emission spectra are dominated by emission from resonance lines of the neutral atom, and lower lying transitions in the singly ionised ion. Due to the high densities of radiating species, particularly of the neutral ground state atoms, opacity broadening is dominant during the first $0.1-0.3$ μs of the plasma evolution. During this time, the continuum emission is approaches a blackbody-like continuum, as is concluded from the observation of self-reversal of the various opacity broadened resonance lines. As the plasma expands and the density decreases, collisional broadening becomes more dominant, producing broad quasi-continuous spectra where significant overlap of the wings of individual spectral lines is observed. The use of semi-empirical line broadening numerical codes provides an accurate means to calculate the electron temperature T_e and electron density n_e via multichannel analysis of the (parts of the) visible spectrum. At much larger delay times of few microseconds, the plasma is most readily characterised by monitoring individual spectral lines of the recombination emission whereby, for example, from time-integrated spectroscopy measurements similar to laser-induced breakdown spectroscopy techniques, trace species in the target materials can be detected.

The violently ejected material further acts as a driving piston to form shock-waves in the surrounding background gas. The kinetics of the shock-wave formation process has been characterised in vacuum for different target materials (chapter 7), and for different background gas conditions (chapter 4). Using a ballistic pendulum, the integrated recoil momentum is measured to consist of a vacuum component, associated with the direct recoil of the ejected material, and an integrated shock-wave recoil due to the overpressures generated by the shock-wave at the target surface. A modified Sedov-Taylor-von Neumann theory has been validated to accurately describe the characteristics of the shock-wave as a function of the background gas density, and ratio of heat capacities of the gas in the pressure range of $10^{-2}-10^{3}$ mbar. The transition from a vacuum free-flow phase, to the continuous propagation of the shock-wave is identified with the point at which the mass engulfed by the shock-wave becomes larger than the ablated piston mass. Eventually, the shock decays into an acoustic wave, signalling the end of the ablation process.

8.2 FUTURE WORK

With the ongoing work in the field of laser ablation, the primary (and sometimes tentative) findings of this work will undoubtedly be superseded. Indeed, in the case of the development of CVL technology, the results put forward in chapter 2 & 3 have already been surpassed with the discovery of kinetic enhancement techniques. The capability of single KE-CVL devices to deliver over 50 W from a medium-scale device similar to that described in chapter 2, or over 100 W from a 40 mm diameter, 1.5 m long, large-scale CVL (Withford et al. 1998*a*), have clearly pushed beyond the boundaries of conventional elemental CVL technology. In this light, the work reported here on the effects of total buffer gas pressure and thermal insulation on the characteristics of the radial gain profile, will probably only be of marginal relevance to future developments of KE-CVL technology. Nevertheless, other techniques relating to optimisation of the performance of elemental CVL MOPA systems, such as described in chapter 3, may still be applied successfully to KE-CVLs in the development of multi-100 W MOPA systems.

Looking towards parallel developments in competing laser technologies, the rise of KE-CVLs may also have significant impact on the commercialisation and industrialisation of copper vapour lasers. To date, the CVL remains the device of choice to produce high beam-quality (better than 2 times diffraction limited), high average output powers (up to 100 W) in the visible with high pulse repetition frequencies

(10 – 50 kHz), making them extremely suitable for industrial laser machining applications. However, with the continuing push and rapid improvement of the high-power performance of diode-pumped frequency doubled solid-state lasers (Nd:YAG and Nd:YLF), research in CVL technology needs to continue in order to keep this competitive edge. The potential of KE-CVLs may be the key factor in making these lasers more attractive and accepted in an industrial environment.

On another front, the relative advantages of femtosecond-nanosecond for laser materials processing will continue to be explored. As outlined in chapter 7, both type of lasers are capable of producing comparable results, provided optimum processing conditions and strategies are employed. While femtosecond lasers may provide some advantages for enabling technologies which make specific use of the short pulse duration, from an economic perspective nanosecond lasers are more readily implemented in an industrial production environment because of their capital costs, and potentially high production throughputs related to the high average power. For many materials processing applications, such as bulk drilling, milling and cutting of materials with accuracies of order 1 μm, nanosecond lasers remain the most practical laser technology solution.

Besides the continuing technology push in laser materials processing, there also remains enough scope for further fundamental research into the physics of laser ablation. To date, no practical model exists which can accurately quantify the non-stationary phase transition associated with the phase explosion phenomenon. While the low energy (threshold and evaporative) regime has been quantified accurately, many challenges remain to synthesise a comprehensive model which combines a description of the heat flow in the material, the non-stationary phase transition, together with the dynamics of the vapour directly above the target material. Further research into this area is readily justified given the importance of the explosive ablation regime in many applications. Undoubtedly, time-resolved studies with (sub-)picosecond resolution using pulsed femtosecond lasers will provide new insights into the problem.

Turning towards the phenomena occurring above the target surface, presently a good understanding of the fluid dynamics of the plasma plume seems to be at hand. Particularly the description of the strong shock regime (chapter 4) has been verified against experiment, while also already a lot of work has been presented in the past few years on the rarefied flows relevant to pulsed laser deposition. Instead, academic challenges are to be sought in the area of plasma spectroscopy and diagnostic techniques. For example, spectroscopic studies may be applied to resolve the chemical interaction of the ablated material with a reactive background gas (chapter 5), relevant to the development of mass-spectrometer laser ablation microprobes. Along other lines, interest in the physics of cool, dense plasmas (chapter 6) will continue to motivate experimental work on the spectroscopy of laser generated plasmas as a test-bed for theoretical models which may subsequently be applied to described astrophysical plasmas. In view of using high pulse repetition frequencies lasers with short interpulse blanking periods $10^{-4} - 10^{-8}$ s (from 10 – 50 kHz CVLs, up to 100 MHz cw modelocked solid-state laser), the study of multi-shot interactions with quasi-continuous plasmas is also of interest. During some of the experiments described in this work, it was accidentally observed that two consecutive pulses from a strongly defocused beam (focus few millimetres above the target surface) would produce a radiating bright red plasma on the second pulse, provided the pulses are not separated by more than one millisecond. Inspection of the target surface showed no significant signs of ablation, thus indicating that the effect can be ascribed to thermionic emission of

electrons inducing optical breakdown in the ambient atmosphere by subsequent pulses. A recent report by Rode et al. (1998) have started studying these effects towards producing more homogeneous plasmas for pulsed laser deposition applications.

Clearly, the many aspects of the physics of laser ablation will continue to be researched for some time, be it for purely academic reasons, or for more industrially oriented incentives of new technological challenges. While the fundamental characteristics across the breadth of the field are now reasonably well understood, many subtle but significant details remain to be addressed for any particular application of laser ablation. As these aspects will continue to be investigated, laser technology will undoubtedly also continue to make an impact in research, manufacturing and industry well into the 21st century.

Daniel Kapitan, Oxford, Michaelmas 1998.

List of Publications

Journal papers

- D. Kapitan, D.W. Coutts and C.E. Webb, 'Efficient generation of near-diffraction limited beam-quality output from medium-scale copper vapour lasers', IEEE J. Quantum electronics **34** (1998), 419-426.
- E.D. Young, D.W Coutts and D. Kapitan, 'UV laser ablation and irm-GCMS microanalysis of $^{18}O/^{16}O$ and $^{17}O/^{16}O$ with application to a calcium-aluminium-rich inclusion from the Allende meteorite', Geochemica Cosmichemica Acta **62** (1998).
- D. Kapitan and D.W. Coutts, 'Effect of background gas properties and the piston-mass on shock-wave formation during laser ablation', in preparation.
- D.W. Coutts, D. Kapitan and C.E.Webb, 'Controlled production of sub-micron surface relief gratings on stainless steel with a copper vapour laser', in preparation.

Conference papers

- D Kapitan, 'Issues in the characterisation of metallic plasmas generated with copper vapour lasers', Symposium on Lasers in Manufacturing, organised by the Rank Prize Fund, March 1996, Grasmere, England.
- D. Kapitan, D.W. Coutts and C.E. Webb, 'Time-resolved spectroscopy of plasmas generated by copper vapour laser ablation of metals', 13th National Quantum Electronics Conference (QE-13) 1997, Cardiff, Wales.
- D. Kapitan, D.W. Coutts and C.E. Webb, 'Gasdynamical studies of laser generated plasmas using a ballistic pendulum (CMF8)' and 'On pulsed laser ablation of metals: the relative importance of thermal diffusion in the nanosecond-femtosecond regime (CThH75)', European Conference on Lasers and Electro-Optics (E-CLEO) 1998, Glasgow, Scotland.
- M.R.H. Knowles, G. Rutterford, A.I. Bell, A.J. Andrews, G. Foster-Turner, A.J. Kearsley, D.W. Coutts, D. Kapitan and C.E. Webb, 'Sub-micron and high precision micro-machining using nanosecond lasers', International Conference on Laser Applications and Electro-Optics (ICALEO) 1998, Orlando, Florida, USA, Planet Earth, Sol system, Western Spiral Arm, Milky Way, Local Group, Chiral Universe.

Other work

- D. Kapitan, H.J. Booth, G.J. Murray, G.P.Hogan and C.E. Webb, 'High-gain double-pass pulsed dye amplifiers for laser guide stars', Proceedings XI International Symposium on Gas Flow and Chemical Lasers & High-Power Laser Conference GCL/HPL 1996, Edinburgh, Scotland (SPIE 3092), 732-735.
- D. Kapitan, D.W. Coutts and C.E. Webb, 'High-gain double-pass pulsed dye amplifiers for laser guide stars (CThI63)', European Conference on Lasers and Electro-Optics (E-CLEO) 1996, Hamburg, Germany.

Appendix A
The Ballistic Pendulum

A.1 Dynamics of a Compound or Physical Pendulum

Equation of motion The equation of motion for a physical pendulum with a total moment of inertia I and total mass M

$$I\ddot{\Theta} + Mgl\sin\Theta = 0 \tag{A.1}$$

where l is the length between the centre of mass and the point of suspension, and Θ is the angular amplitude of the motion. The well-known solution in the small-angle approximation yields the eigenfrequency ω_0 for the system

$$\omega_0 = \sqrt{\frac{Mgl}{I}}. \tag{A.2}$$

Integration of (A.1) with respect to time yields and expression for the total energy of the system

$$H = \frac{1}{2}I\dot{\Theta}^2 + Mgl(1-\cos\Theta). \tag{A.3}$$

Upon impact of an (recoil) impulse p_0 at a distance L from the point of suspension, the maximum angle of deflection Θ_{max} can be calculated as follows. Using the relationship for conservation of energy

$$\frac{1}{2}I\dot{\Theta}^2 = Mgl(1-\cos\Theta) \tag{A.4}$$

and the conservation of angular momentum

$$I\dot{\Theta} = p_0 L \tag{A.5}$$

yields

$$p_0^2 = 4\frac{MI}{L^2}gl\sin^2\frac{1}{2}\Theta_{\mathrm{max}}. \tag{A.6}$$

For $\Theta \ll 1$, and rearranging equation (A.2) and (A.6) finally results in

$$p_0 = 2\pi\frac{I}{TL}\Theta_{\mathrm{max}} \tag{A.7}$$

Calibration of the pendulum is achieved by measuring the period T and the position of the point of impact L directly from experiment. Furthermore, the total moment of inertia I is calculated assuming

a homogeneous mass distribution of the various parts. To this purpose the pendulum was designed to consist of simple geometric shaped parts, for which the moment of inertia could be calculated assuming a homogeneous mass distribution. Using the parallel-axis theorem

$$I = I_0 + mr^2 \tag{A.8}$$

where I_0 is the moment of inertia of the individual parts relative to its centre of mass, and with mass m and r is the distance to the pivot point. The total moment of inertia is simply

$$I = \sum I_{0i} + m_i l_i^2 \quad . \tag{A.9}$$

For future reference, the moment of inertia for a parallelepiped with sides a, b and an axis of rotation through the centre of mass parallel to one side c,

$$I_0 = \frac{a^2 + b^2}{12} m \quad ; \tag{A.10}$$

and the moment of inertia for a thin circular disc of radius a and the axis of rotation through the centre and in the plane of the disc,

$$I_0 = \frac{a^2}{4} m \quad ; \tag{A.11}$$

which will be used in calculating the total moment of inertia of the pendulum.

Note also that given the geometry and mass of the pendulum the momentum transfer due to a recoil impulse can be considered truely elastic. To illustrate this, consider a simplified geometry where a small mass M_s (representing the ablated material) impinges on one end of a bar of length $2L$ (the pendulum). Given the conservation of angular momentum (A.5), and that the linear momentum of the pendulum centre of mass is simply p_0/M, the conservation of energy is can be rewritten to obtain an expression for the outgoing impulse $\widetilde{p}$ after the impact

$$\widetilde{p}^2 = p_0^2 \left(1 - \frac{M_s}{M} - \frac{M_s L^2}{I}\right) \tag{A.12}$$

Thus, provided that the conditions

$$\begin{aligned} M_s &\ll M \\ M_s &\ll \frac{I}{L^2} \end{aligned} \tag{A.13}$$

are met, the collision can be considered elastic. Considering that from experiment $M, I/L^2$ are of order of one gram, and that the single shot ablation mass is less that a milligram, this is indeed the case.

NONLINEAR CORRECTION To ensure the pendulum is operating in the linear regime, consider the

first order nonlinear correction to the equation of motion for a simple harmonic oscillator

$$I\ddot{\Theta} + Mgl\left(\Theta - \frac{1}{6}\Theta^3\right) = 0 \tag{A.14}$$

Solutions to this equation are found by considering that the motion should be periodic, and symmetric under time-reversal, and that the restoring force is symmetric around the origin. Hence, solutions in terms of a cosine Fourier-series consisting of odd harmonics are found

$$\Theta(t) = \Theta_{\max}\left(\cos\omega_f t + \epsilon\cos 3\omega_f t + \ldots\right) \tag{A.15}$$

where the fundamental frequency ω_f is a function of the amplitude of the angular deflection $\Theta_{\max}$. Retaining only terms up to first order in ϵ yields

$$\begin{aligned} \omega_f &= \omega_0\left(1 - \frac{1}{16}\Theta_{\max}^2\right) \\ \epsilon &= \frac{1}{192}\Theta_{\max}^2 \end{aligned} \tag{A.16}$$

Equation (A.14) is valid beyond the standard small-angle approximation, and accurately describes the motion of the pendulum up to angular deflections of approximately 140°. However, only for sufficiently high deflection angles $\Theta_{\max} \sim 20°$ does the nonlinear correction constitute a significant frequency correction $\sim 1\%$. In practice, the maximum deflections are of order 10 mrad, resulting in insignificant corrections of $1 : 10^5$.

DAMPING The presence of damping constitutes another systematic correction. In the underdamped regime, the equation of motion for damped oscillations

$$m\ddot{\Theta} + c\dot{\Theta} + k\Theta = 0 \tag{A.17}$$

has solutions of the form

$$\Theta(t) = Ae^{-\gamma t}\cos\omega_D t \quad , \tag{A.18}$$

where the damped frequency ω_D is dependant on the quality Q of the oscillation

$$\omega_D = \omega_0\left(1 - \frac{1}{8Q^2}\right) \tag{A.19}$$

where

$$Q = \frac{\omega_D}{2\gamma} \quad . \tag{A.20}$$

Thus corrections due to damping are found to be insignificant for sufficiently high Q-factors (~ 150), with corresponding frequency correction of $1 : 10^5$ as has been experimentally verified in chapter 4.

Appendix B
'Einstein's' shock-condition

Following Freiwald & Axford (1975), the transition radius R^* for a spherical shock-wave taking into account the source mass is defined by

$$R^* = R_s \left(\frac{\rho_s}{\rho_1} \right)^{1/3} \tag{B.1}$$

where R_s is the radius of the crater, and ρ_s the density of the target material and ρ_1 the density of the undisturbed gas. The maximum radius R_0 signalling the onset of decay of the shock into an acoustic wave is defined by the condition

$$R_0 = \left(\frac{E_0}{P_1} \right)^{1/3} \tag{B.2}$$

with E_0 the laser pulse energy, and P_1 the initial pressure of the ambient atmosphere. Comparing these two length scales, it is concluded that only when

$$R^* > R_0 \tag{B.3}$$

a Sedov-Taylor-von Neumann shock-wave can be sustained. Given that the sound velocity for any (ideal) gas c_0

$$c_0 = \sqrt{\frac{\gamma P_1}{\rho_1}} \tag{B.4}$$

with γ is the ratio of heat capacities of the background gas, substitution of equation (B.4) in (B.1), and (B.1)-(B.2) in (B.3) yields

$$E_0 > \rho_s R_s^3 c_0^2 \tag{B.5}$$

But since $\rho_s R_s^3 = M_s$ for an approximately hemispherical ablation crater, one finally arrives at

$$E_0 > M_s c_0^2 \tag{B.6}$$

Appendix C
Heat Capacities of Real Gases

C.1 Equilibrium Thermodynamics

Consider the first law of thermodynamics (for a more thorough introduction see for example Adkins (1983)) describing the change in the internal energy $d\overline{U}$ due to non-adiabatic heat exchange $d\overline{Q}$ and amount of work $d\overline{W}$ performed by the system

$$d\overline{U} = d\overline{Q} + d\overline{W} \tag{C.1}$$

The classic example, $d\overline{W} = PdV$ describing volumetric expansion dV against a static background pressure P. In order to relate this to the intrinsic properties of the substance, introduce the heat capacities C_P, C_V

$$C_P = \frac{d\overline{Q}_P}{dT} = \left(\frac{\partial U}{\partial T}\right)_P \tag{C.2}$$

$$C_V = \frac{d\overline{Q}_V}{dT} = \left(\frac{\partial U}{\partial T}\right)_V$$

describing the change in internal energy at constant pressure and volume, respectively. Substituting equation (C.1) into (C.2) yields

$$C_P\, dT = C_V\, dT + P\, dV \tag{C.3}$$

For any homogeneous substance this can be rewritten as

$$C_P - C_V = T\left(\frac{\partial P}{\partial T}\right)_V \left(\frac{\partial V}{\partial T}\right)_P \tag{C.4}$$

which can be further rearranged using the relation

$$dV = \left(\frac{\partial V}{\partial T}\right)_P dT + \left(\frac{\partial V}{\partial P}\right)_T dP \tag{C.5}$$

to yield the following expression for volumetric changes

$$C_P - C_V = -T\left(\frac{\partial V}{\partial T}\right)_P^2 \Big/ \left(\frac{\partial V}{\partial P}\right)_T \tag{C.6}$$

showing that the difference in heat capacities is proportional to the square of the coefficient of (volumetric) thermal expansion $(\partial V/\partial T)_P/V$, and the bulk modulus $-V/(\partial V/\partial P)_T$.

C.2 IDEAL & V.D. WAALS GASES

Now consider the equation of state for n mole of an ideal gas

$$PV = nRT \tag{C.7}$$

and that for a van der Waals gas

$$\left(P + \frac{n^2 a}{V^2}\right)(V - nb) = nRT \tag{C.8}$$

The coefficient a relates to the degree of liquefaction of the gas, while the constant b account for the finite size of the molecules. The origin of the van der Waals equation is that when the temperature, volume and pressure are written in the reduced units π, ϕ, θ relative to the critical point

$$\begin{aligned} P &= \pi P_c \\ V &= \phi V_c \\ T &= \theta T_c \end{aligned} \tag{C.9}$$

the equation

$$\left(\pi + \frac{3}{\phi^2}\right)(3\phi - 1) = 8\theta \tag{C.10}$$

holds true for all normal gases. Thus, the critical pressure P_c, volume V_c, and temperature T_c are related to the van der Waals constants a, b

$$\begin{aligned} P_c &= \frac{a}{27b^2} \\ V_c &= 3b \\ T_c &= \frac{8a}{27Rb} \end{aligned} \tag{C.11}$$

as listed in table XXI for the gases used in chapter 4. The difference in the heat capacities for a van der Waals gas can then be expressed as

$$C_P - C_V = R + \frac{2a^2}{RT^2}P - \frac{3ab}{R^2T^3}P^2 \tag{C.12}$$

while for an ideal gas $a = b = 0$ only the first terms on the right-hand side remains.

gas	a [litre atm^2 mole^{-1}]	b [litre mole^{-1}]
He	0.03	2.38
Ar	1.35	3.23
N_2	1.39	3.23
CO_2	3.60	4.28

TABLE XXI: v.d. Waals-constants for four different inert gases used in the experiments of chapter 4.

C.3 RATIO OF HEAT CAPACITIES FOR ADIABATIC PROCESSES

In the mathematical description of strong shocks, the ratio of heat capacities γ

$$\gamma \equiv \frac{C_P}{C_V} \tag{C.13}$$

enters the jump conditions as a dimensionless parameter describing the change in the internal energies of the system under the adiabatic expansion due to the shock-wave. To arrive at the analytical solutions of the STN theory the medium is assumed to obey the ideal gas law (with sufficient accuracy), in which case γ is independent of pressure and temperature. In practice, a constant value for γ is used where an effective number of internal degrees of freedom f of the gas is assumed to be accessible, and using

$$\gamma = 1 + \frac{2}{f} \tag{C.14}$$

derived from first principles based on equipartition. Thus, for system with infinitely large degrees of freedom (a large bath) $\gamma \to 1$, while the maximum value of γ is determined by the value for a perfect gas with the smallest amount degrees of freedom $f = 3, \gamma = 5/3$.

The validity of such an approximation will be considered here. For real gases C_P varies with pressure, and C_V varies with volume, while both C_P, C_V change with temperature. In the case of shock-wave formation, where significant changes in the thermodynamic properties occur, it is not known *ab initio* whether an intelligible assumption of constant γ can be maintained at all. Phenomenologically the change of C_V with volume is small compared to the change of C_P with pressure. Evaluation of the van der Waals equation yields $(\partial C_V/\partial V)_T \equiv 0$, and hence the variation of $C_P - C_V$ with pressure and temperature is dominated by the changes in C_P. As seen in equation (C.12), significant changes in γ are expected in the limit $P \to \infty, T \to 0$, in which case considerable liquefaction due to compression or condensation, respectively.

However, for adiabatic processes the following relations hold true

$$\begin{aligned} \frac{T_2}{T_1} &= \left(\frac{V_1}{V_2}\right)^{\gamma-1} \Rightarrow TV^{\gamma-1} = \text{constant} \\ \frac{T_2}{T_1} &= \left(\frac{P_2}{P_1}\right)^{(\gamma-1)/\gamma} \Rightarrow TP^{-(\gamma-1)/\gamma} = \text{constant} \end{aligned} \tag{C.15}$$

Specifically, during the expansion of shock-waves, the pressure and temperature of the shocked atmosphere

increase simultaneously in an adiabatic fashion. Upon inspection of the constants a, b it can be confirmed from equation (C.12) that the approximation $C_P - C_V \simeq R$ holds with sufficient accuracy (better than 5%) for the experiments considered here. Note, however, that the argument given above only holds when the molecular structure of the gas is not altered significantly, i.e. in the absence of dissociation or ionisation. As is discussed in chapter 4, the effect of radiation transport can lead to significant changes in the ratio of heat capacities.

Appendix D
Elements of Classical Plasma Theory

D.1 A Classical Lorentz Plasma

The Langmuir plasma frequency Consider a simplified model of a plasma in which it is assumed that the electrons interact with each other only through collective space-charge forces while the heavy positive ions (and neutral) atoms are at rest. In this picture, collisional processes are mediated and dominated by the electron density n_e [cm^{-3}], moving in a relatively stationary, viscous fluid formed by the ions n_{ion} [cm^{-3}]. Note that the plasma as a whole may have a net drift velocity in a particular direction, as in the case of an expanding laser ablation plasma, but in the reference frame of the plasma only the electrons have a significant thermal motion at the electron temperature T_e. It is a well known result from classical electrodynamics that such a plasma can sustain electron plasma oscillations, often referred to in the form of a specific plasma frequency ω_p [rad s^{-1}]. A short outline of the derivation shall be given, following Heald & Wharton (1965). If in an initially uniform, neutral Lorentz plasma a group of the electrons are displaced over a small (one-dimensional) distance dx by some means of perturbation, an electric field will be generated locally. Due to this net space-charge the electrons will start on oscillatory motion around the equilibrium position. In the absence of friction, the oscillation would be undamped. However, via collisions with the heavy ions in which momentum is transferred, the electrons are slowed down at a rate proportional to the collision frequency ν_{ei} [s^{-1}]. The equation of motion then becomes

$$\ddot{\mathbf{x}} + v_{ei}\dot{\mathbf{x}} + \frac{n_e e^2}{\epsilon_0 m_e}\mathbf{x} = 0. \tag{D.1}$$

Solving this equation, by substitution of $\partial/\partial t \rightarrow i\omega$, and defining the current density

$$\mathbf{J} = -n_e e\dot{\mathbf{x}} = \sigma\mathbf{E}, \tag{D.2}$$

where the second equality states Ohm's law, results in the following expression for the complex Lorentz conductivity σ

$$\sigma = \frac{n_e e^2}{m_e}\frac{\nu_{ei} - i\omega}{\nu_{ei}^2 + \omega^2}. \tag{D.3}$$

The complex dielectric constant $\tilde{\epsilon}_m$ is then given by

$$\tilde{\epsilon}_m = \left(1 - \frac{\omega_p^2}{\nu_{ei}^2 + \omega^2}\right) - i\left(\frac{\nu_{ei}}{\omega}\frac{\omega_p^2}{\nu_{ei}^2 + \omega^2}\right) \tag{D.4}$$

with the Langmuir angular plasma frequency ω_p

$$\omega_p^2 = \frac{n_e e^2}{\epsilon_0 m_e} \tag{D.5}$$

THE DEBYE RADIUS The Debye radius, originally derived by Debye for an electrolyte (see for example Thorne (1988)), provides a measure for the characteristic length over which shielding occurs, and thus the plasma can be considered (globally) neutral. By solving Poisson's equation for the ions and electrons in thermal equilibrium, under the approximation that

$$eV \ll k_B T_e \tag{D.6}$$

the potential around a particle of charge q can be shown to decay exponentially

$$V = \frac{q}{4\pi\epsilon_0 r} \exp\left(-\frac{r}{\rho_D}\right) \tag{D.7}$$

with

$$\rho_D^2 = \frac{\epsilon_0 k_B T_e}{2e^2 n_e} \tag{D.8}$$

The Debye criterion (D.6) effectively states that the density of charged particles is sufficiently large to cause smooth decay of the potential V, i.e. Debye plasmas should contain large numbers of particles within ρ_D. The Debye length can also be considered as the skin depth for external fields penetrating the plasma, which increases as $\sqrt{T_e}$. Comparison of the Debye length ρ_D and the plasma frequency ω_p given in equation (D.5) yields

$$(\rho_D \omega_p)^2 = \frac{k_B T_e}{m_e} \tag{D.9}$$

The Debye length (D.8) further provides a measure for the effect of ionisation depression in classical plasmas. When the mean distance $\langle r \rangle$ of the valence electron from the nucleas is of order of ρ_D, the electron is effectively free to move in the plasma. The associated energy potential with this radius $\langle r \rangle$ often lies below the ionisation potential of for the isolated atom (or ion) in question, thus resulting in ionisation depression.

LOCAL THERMODYNAMIC EQUILIBRIUM One of the main characteristics of a plasma is its temperature. Whether such a thing as 'the' temperature can be defined at all, depends on the assumption as regards what type of thermodynamic equilibrium is achieved. In the most general case, four independent energy distributions can be distinguished (Thorne 1988), associated with the radiative, kinetic, (internal) excitation and ionisation energy of the individual atoms and ions constituting the plasma. When in thermal equilibrium, these distributions respectively obey the Planck, Maxwell, Boltzmann and Saha distribution, each involving a different temperature T. Only in the specific situation of thermodynamic equilibrium can a singly value of T be assigned, in which case the principle of detailed balance, or micro-

scopic reversibility, holds. The form of energy most likely to be out of equilibrium involves the radiation temperature, which is often the case in plasmas. To arrive at a useful concept of a plasma temperature, the definition of local thermodynamic equilibrium (LTE) requires only the temperatures defined by the kinetic, excitation and ionisation energy distributions to be equal. Explicitly, the temperature defined by the Boltzmann equation

$$\frac{n_2}{n_1} = \frac{g_2}{g_1} \exp\left(-\frac{E_2 - E_1}{k_B T}\right) \tag{D.10}$$

for the ratio of population densities n_1, n_2 of two energy states E_1, E_2 with degeneracies g_1, g_2, should be equal to Saha temperature defined by the fraction of the two sequential ionisation stages n_j, n_{j+1} separated by the ionisation potential $\Delta E_{j+1 \to j}$

$$\frac{n_{j+1}}{n_j} = 2\frac{g_{j+1}}{g_j}\frac{\Lambda^{-3}}{n_e} \exp\left(\frac{-\Delta E_{j+1 \to j}}{k_B T}\right) \tag{D.11}$$

where Λ is the thermal de Broglie wavelength

$$\Lambda = \frac{h}{\sqrt{2\pi m_e k_B T}} \tag{D.12}$$

and g_{j+1} and g_j the statistical weights of the ionisation stages under consideration. Further, the temperature defined in (D.10) and (D.11) should be equal to the kinetic temperature of the Maxwell velocity distribution of the electrons T_e

$$\frac{dn_e(\mathbf{v})}{n_e} = 4\pi \mathbf{v}^2 \left(\frac{m_e}{2\pi k_B T_e}\right)^{3/2} \exp\left(\frac{m\mathbf{v}^2}{2k_B T_e}\right) \tag{D.13}$$

The underlying criterion for LTE assumes that collisional processes must dominate over radiative processes. Thus, (D.10) and (D.11) are clamped at the electron temperature T_e, neglecting ion-ion encounters due to the relatively low mobility of the ions. The definition of LTE given above is sometimes referred to as the *weak* LTE (Bowers & Deeming 1984). In the definition of Bowers & Deeming (1984), the *strong* LTE condition requires the radiation field to be Planckian locally at the electron temperature. This is similar to the condition of complete thermodynamic equilibrium, with the extension to allow local (spatial) variations in temperature. The *moderate* LTE condition only requires the local source function of the radiation field to be Planckian, which effectively neglects scattering processes.

The importance of LTE is that the relative ionisation fractions and atomic populations can be found without any knowledge of cross-sections and transition probabilities. However, for the assumption of LTE to be valid between any two energy levels, McWhirter (Huddlestone & Leonard 1965, chapter 5) has shown that the electron density should obey

$$n_e \geq 10^{12} \sqrt{T_e} \Delta E_{ij}^3 \, \mathrm{cm}^{-3} \tag{D.14}$$

where ΔE_{ij} is the energy difference between the pair of levels in electronvolts. Given an approximately hydrogenic distribution of energy levels $\Delta E \propto 1/n^3$ where n is the principle quantum number, it is quite

possible that the populations of the higher states are in LTE, while the lower states are not. In this case, the definition of coronal equilibrium is useful to describe the population distribution of those levels for which upward transitions are dominated by electron collisions while downward transitions occur by spontaneous emission.

D.2 SPECTRAL LINE BROADENING

The study of spectral line broadening has long since been used to characterise the state of plasmas over a wide range of temperatures and densities (Griem 1974). In order to asses the usefulness of any spectroscopic technique, an estimate needs to be made as to which effects are likely do dominate. For a simple two-level transition with frequency ω_{12} for a radiator with mass m_r, the following line-broadening mechanisms will be considered.

NATURAL LINE BROADENING The natural line width $\Delta\omega_n$ is associated with the fundamental quantum mechanical limit relating the minimal uncertainty, resulting in the natural homogeneous Lorentzian line width for a transition with a spontaneous emission coefficient A_{21}

$$\Delta\omega_n \simeq A_{21} \tag{D.15}$$

Typically for an optical transition the frequency spread is of order 10^8 rad s^{-1}.

DOPPLER BROADENING The Doppler width $\Delta\omega_D$ is associated with the thermal motion of the radiators within the plasma, whereby the stochastic frequency shift due to the Doppler effects results in an averaged inhomogeneous line width

$$\Delta\omega_D \simeq \left(\frac{k_B T}{m_r c^2}\right)\omega_{21} \tag{D.16}$$

The relation

$$\Delta\omega_D = 7.16 \cdot 10^{-7}\omega_{12}\sqrt{\frac{T}{m_r}}$$

is useful for calculating the Doppler width for a medium at temperature T (in Kelvin) and atomic mass m_a (in atomic units).

COLLISIONAL OR PRESSURE BROADENING The homogeneous collisional broadened line width $\Delta\omega_c$ finds it origin in the finite emission duration of an atomic radiator which is dephased due to collisions on timescales τ_c

$$\Delta\omega_c \simeq \frac{1}{\tau_c} \tag{D.17}$$

In the case of collisional broadening due to collisions with charged particles, such as perturbing electrons in a plasma, this is often referred to as Stark broadening. Particularly for electron-ion encounters, where due to the Coulomb interaction the collisional cross-section is significantly larger compared to for example electron-neutral collisions, the Stark width of ionic spectral lines is easily of order 0.1 – 1 nm. For high principal quantum numbers n the Stark broadening will become sufficient to merge

the levels, referred to as the Inglis-Teller limit. Actual derivation of the contribution of different types of perturbation to pressure broadening (e.g. resonance interactions between identical atoms, ion-ion encounters) often require different additional approximations to render the mathematics tractable. The impact approximation is often used to describe the interaction during the 'fly-by' of a light perturber (the electron) near a radiator (ion). Within the impact approximation, only binary encounters are accounted for, with additional assumptions that the perturber follows a classical path (a straight line for uncharged encounters, or hyperbolic trajectories for charged particles), and that within the adiabatic approximation the perturbers do not induce transitions between, or mix up, different close-lying states of the emitting atom. In the case of the quasi-static approximation, often employed to calculate broadening due to ion-ion interactions, the perturbation is almost stationary and assumed nearly constant over the whole time for which the atom is radiating. For the discussion presented in chapter 6, the impact approximation is used, which can be shown to be valid for the dense, cool plasmas considered here (Griem 1997).

OPACITY BROADENING Opacity effects such as self-reversal and opacity broadening are caused by repeated self-absorption of photons by surrounding atoms/ions occupying the lower state of the relevant transition. Due to the higher probability of absorption at line centre by radiators with thermal velocities perpendicular to the propagation path of the photon, and the subsequent redistribution of re-emission over the whole line shape of the transition, the relative intensity of emission in the wings is increased as the optical density of the transition is increased. This results in opacity broadening of the spectral line, as is most commonly observed for resonance transitions which terminate on the ground state, or transitions which end on metastable state. Owing to the nature of the opacity broadening process, the line profiles no longer exhibit Gaussian or Lorentzian line shapes, but are described such that in the limit of infinite optical thickness the blackbody luminance L_{BB} is produced

$$L(\omega, T) = L_{BB}(\omega, T)\left(1 - \exp\left(-k(\omega, T)\, l\right)\right) \tag{D.18}$$

where l is the optical path, and $k(\omega, T)$ the spectral absorption coefficient, determined by the atomic properties of the transition. In order to obtain rough estimates of the optical absorption coefficient averaged over the spectral line profile, an atomic cross-section $\sigma(\omega)$ is often defined as (Thorne 1988)

$$\sigma(\omega) = \frac{k(\omega, T)}{n_1} \tag{D.19}$$

which is related to the Einstein A_{21} coefficient of the transition

$$\sigma(\omega) = \frac{g_2}{g_1}\frac{\pi^2 c^2}{\omega_{12}^2} A_{21} g(\omega - \omega_{12}) \tag{D.20}$$

where g_1, g_2 are the degeneracies of the lower and upper level, respectively, $g(\omega - \omega_{12})$ is the normalised line shape, and $\Delta\omega$ is the line width of the transition. In effect, equation. (D.20) states that the optical cross-section of a transition proportional to the ratio of its natural width (A_{21}), and its actual (broadened)

line width ($g(\omega - \omega_{12})$). To arrive at a reasonable numerical estimate of the optical cross-section of any transition, the definition of the emission oscillator strength f_{21}, and associated absorption oscillator strength f_{12}

$$A_{21} \equiv -3 f_{21} \gamma_{\rm cl} \tag{D.21}$$

$$g_1 f_{12} = -g_2 f_{21} \tag{D.22}$$

relates the semi-classical value for the Einstein A_{21}-coefficient to the lifetime of a classical radiation dipole $\gamma_{\rm cl}$

$$\gamma_{\rm cl} = \frac{e^2 \omega_{12}^2}{6\pi\epsilon_0 m_e c^3} \qquad \text{[SI units]} \tag{D.23}$$

Rearranging equation. (D.20) then yields

$$\sigma(\omega) = \frac{3}{4} \lambda_{12}^2 f_{12} \gamma_{\rm cl} g(\omega - \omega_{12}) \tag{D.24}$$

Assuming that the (Lorentzian) collisional broadened line width $\Delta\omega_L$ is much larger than the (Gaussian) Doppler width $\Delta\omega_D$ in the plasmas of interest, the optical cross-section at line centre σ_{12} [in cm^2] is given by

$$\sigma_{12} = 5.6 \cdot 10^{-20} \frac{\lambda_{12}^2}{\Delta\lambda} f_{12} \tag{D.25}$$

where the transition wavelength λ_{12}, and line width $\Delta\lambda$ are both given in nanometers. Thus, for a typical optical transition $\lambda_{12} = 400$ nm, $f_{12} = 0.1$, and collisional Stark widths of order $\Delta\lambda = 0.1$ nm, the optical cross-section at line centre $\sigma_{12} = 10^{-14} - 10^{-15}$ cm^2. These estimates will be used in chapter 6 to estimate the relative contributions of opacity effects versus collisional Stark broadening to the observed emission of continuous spectra.

Appendix E
Heat Transport During Pulsed Laser Ablation

E.1 Classical Equilibrium Heat Flow

From classical elementary kinetic theory the heat transport equation describing thermal conduction in any medium is given by

$$\nabla \cdot (k \nabla T) + Q^* = \rho c_p \frac{\partial T}{\partial t} \tag{E.1}$$

where $Q^*$is the heat generated or deposited within the volume, with k [W·cm^{-1}·K^{-1}] the thermal conductivity of the material, ρ [g·cm^{-3}]the density and c_p [J·g^{-1}·K^{-1}] the heat capacity at constant pressure of the solid. Upon absorption of laser radiation, the excess energy deposited in the target substrate via excitation of electrons within the lattice is thermalised and transformed into thermal energy. Due to the generated temperature gradients, heat will be transported and distributed within the solid. Following von Allmen & Blatter (1995), elements from heat-transport theory will be given below.

In order to quantify the importance of heat transport in the target substrate during the laser pulse (i.e. $t \leq t_p$), the (inverse of the) absorption coefficient α_{bulk} [cm^{-1}] at the wavelength of the incident optical field needs to be compared with the heat diffusivity κ, which is given by

$$\kappa = \frac{k}{\rho c_p} \quad [\mathrm{cm}^2/\mathrm{s}] \tag{E.2}$$

The heat diffusion length D is given by

$$D = 2\sqrt{\kappa t} \quad [\mathrm{cm}]\,, \tag{E.3}$$

and similarly a diffusion length during the laser pulse D_p can be defined by taking $t = t_p$ in ((E.3)).

In the case $\alpha_{bulk}^{-1} \gg D_p$ the energy of the laser light will be deposited over a large depth, and negligible heat flow occurs. The temperature rise profile obeys an exponential law, and decays as the beam penetrates deeper into the material

$$\Delta T(z) = \frac{(1-R)\, F\alpha \exp(-\alpha z)}{\rho c_p} \tag{E.4}$$

where F [J·cm^{-2}] is the fluence of the incoming optical pulse.

For $\alpha_{bulk}^{-1} \ll \delta_p$ the absorption will occur in a relatively small surface layer (of approximately α_{bulk}^{-1}

deep), while the maximum surface temperature is limited by diffusion. Depending on the geometry of the set-up, the heat-diffusion equation needs to be solved to derive an expression for the surface temperature T_s. In the case of ablation using excimer lasers the focal spotsize is sufficiently large (of order 1 mm) compared to the absorption and diffusion length, that a 1D approach is justified. In the case of near-diffraction limited focal spotsizes of few microns diameter, either a cylindrical or spherical geometry needs to be used.

E.2 Non-Equilibrium Two Temperature Heat Flow

In the case of laser ablation using fast (femtosecond) pulses, the heat-flow in the target material can no longer be described within a classical equilibrium heat flow (E.1). Instead, a two-temperature model needs to be employed, where the electron temperature T_e and the lattice (ion) temperature T_i are decoupled. Thus, following (Corkum et al. 1988)

$$\begin{aligned} \nabla \cdot (k \nabla T_e) - g\,(T_e - T_i) + Q^* &= \rho_e c_e \frac{\partial T_e}{\partial t} \\ g\,(T_e - T_i) &= \rho_i c_i \frac{\partial T_i}{\partial t} \end{aligned} \tag{E.5}$$

the heat-flow in the lattice is determined by the electron-phonon coupling constant g, which for metals typically is of order 10^{16} W/m^3·K. (Corkum et al. 1988) have shown that this results in significant modifications from equilibrium heat-flow, where for laser pulse durations < 1 ns the thermal diffusion length D deviates from the square-root law (E.3). Instead, (Corkum et al. 1988) showed that the for each material D approaches a constant minimal value, associated with the electron-phonon coupling g. The time-scale τ_c on which this transition occurs lies in the regime of $10 - 100$ ps, as has been experimentally determined for different metals. These findings form the basis of the discussion presented in chapter 7.

BIBLIOGRAPHY

Aden, M., E. Beyer & G. Herziger (1990), 'Laser-induced vaporisation of metal as a Riemann problem', *J. Appl. Phys. D: Appl. Phys.* **23** pp. 655–661.

Aden, M., E.W. Kreutz, H. Schlüter & K. Wissenbach (1997), 'The applicability of the Sedov-Taylor scaling during material removal of metals and oxide layers with pulsed CO_2 and excimer and laser radiation', *J. Phys. D: Appl. Phys.* **30** pp. 980–989.

Adkins, C.J. (1983), *Equilibrium Thermodynamics* (third edition), Cambridge University Press.

Agostini, P., G. Barjot, G. Mainfray, C. Manus & J. Thebault (1970), 'Multiphoton ionisation of rare gases at 1.06 μm and 0.53 μm', *IEEE J. Quantum Electron.* **6** pp. 782–788.

Alcock, A.J., K. Kato & M.C. Richardson (1972), 'New features of laser-induced gas breakdown in the ultraviolet', *Optics Comm.* **6** pp. 342–344.

Alexander, M.L., M.R. Smith, J.S. Hartman, A. Mendoza & D.W. Koppenaal (1998), 'Laser ablation inductively coupled plasma mass spectrometry', *Appl. Surf. Sci.* **127-129** pp. 255–261.

André, N., C. Geertsen, J.-L. Lacour, P. Mauchien & S. Sjöström (1994), 'UV laser ablation optical emission spectrometry on aluminium alloys in air at atmospheric pressure', *Spectrochimica Acta* **49B** pp. 1363–1372.

Ang, L.K., Y.Y. Lau, R.M. Gilgenbach & H.L. Spindler (1997), 'Analysis of laser absorption on a rough metal surface', *Appl. Phys. Lett.* **70** pp. 696–698.

Ang, L.K., Y.Y. Lau, R.M. Gilgenbach, H.L. Spindler, J.S. Lash & S.D. Kovaleski (1998), 'Surface instability of multipulse laser ablation on a metallic target', *J. Appl. Phys.* **83** pp. 4466–4471.

Anisimov, S.I., M.I. Tribel'skiĭ & Ya.G. Épel'baum (1980), 'Instability of plane evaporation front in interaction of laser radiation with a medium', *Sov. Phys. JETP.* **51** pp. 802–806.

Anisimov, V.N. & et al. (1984), 'Materials processing by high-repetition-rate pulsed excimer and carbon dioxide lasers', *Appl. Opt.* **23** pp. 18–25.

Arad, B., S. Eliezer, S. Jackel, A. Krumbein, H.M. Loebenstein, D. Salzmann, A. Zigler, H. Zmora & S. Zweigenbaum (1980), 'Effect of pulse duration and polarisation on momentum and energy transfer to laser-irradiated targets', *Phys. Rev. Lett.* **44** pp. 326–329.

Arad, B., S. Eliezer, Y. Gazit, H.M. Loebenstein, A. Zigler, H. Zmora & S. Zweigenbaum (1979), 'Burn-through of thin aluminium foils by laser-driven ablation', *J. Appl. Phys.* **50** pp. 6817–6821.

Armon, E., M. Hill, I.J. Spalding & Y. Zvirin (1989), 'Metal drilling with a CO_2 laser beam. II. Analysis of aluminium drilling experiments', *J. Appl. Phys.* **65** pp. 5003–5006.

Armon, E., Y. Zvirin, G. Laufer & A. Solan (1989), 'Metal drilling with a CO_2 laser beam. I. Theory', *J. Appl. Phys.* **65** pp. 4995–5002.

Arnold, N., B. Luk'yanchuk, N. Bityurin & D. Bäuerle (1998), 'Non-stationary effects in laser ablation of indium: calculations based on spatial moments technique', *Laser Physics* **8** pp. 47–55.

Arrowsmith, P. (1987), 'Laser ablation of solids for elemental analysis by inductively coupled plasma mass spectrometry', *Anal. Chem.* **59** pp. 1437–1444.

Ashkenasi, D., H. Varel, A. Rosenfeld, S. Henz, J. Hermann & E.E.B. Cambell (1998), 'Application of self-focusing of ps laser pulses for three-dimensional microstructuring of transparent materials', *Appl. Phys. Lett.* **72** pp. 1442–1444.

Asprey, L.B. (1976), 'The preparation of very pure fluorine gas', *J. Fluor. Chem.* **7** pp. 359–361.

Astadjov, D.N., K.D. Dimitrov, D.R. Jones, V. Kirkov, L. Little, C.E. Little, N.V. Sabotinov & V.K. Vuchkov (1997), 'Influence on operating characteristics of scaling sealed-off CuBr lasers in active length', *Optics Comm.* **135** pp. 289–294.

Astadjov, D.N., N.V. Sabotinov & N.K. Vuchkov (1985), 'Effect of hydrogen on CuBr laser power and efficiency', *Optics Comm.* **56** pp. 279–282.

Atkins, P.W. (1994), *Physical Chemistry* (fifth edition), Oxford University Press.

Autin, M., A. Briand, P. Mauchien & J.M. Mermet (1993), 'Characterisation by emission spectrometry of a laser-produced plasma from a copper target in air at atmospheric pressure', *Spectrochimica Acta* **48B** pp. 851–862.

Bach, G.G. & J.H.S. Lee (1970), 'An analytical solution for blast waves', *AIAA J.* **8** pp. 271–275.

Banishev, A.F., V.S. Golubev & V.D. Dubrov (1996), 'Influence of an external pressure and of the type of gas on the mechanism and rate of breakdown of metals by Nd:YAG laser pulses', *Sov. J. Quantum Electron.* **26** pp. 1003–1006.

Barbinin, R., F. Colao, R. Fantoni, A. Palucci, S. Ribezzo, H.J.L. van der Steen & M. Angelone (1997), 'Semi-quantitative time resolved LIBS measurements', *Appl. Phys. B* **65** pp. 101–107.

Bashkin, S. & J.O. Stoner Jr. (1975), *Atomic Energy Levels and Grotrian Diagrams*, North-Holland Publishing Company.

Basu, S. & T. Debroy (1992), 'Liquid metal expulsion during laser ablation', *J. Appl. Phys.* **72** pp. 3317–3322.

Bates, D.R. (1962), *Atomic and Molecular Processes*, Academic Press.

Bäuerle, D. (1996), *Laser Processing and Chemistry* (second edition), Springer.

Bélanger, P.A., Y. Champagne & C. Paré (1994), 'Beam propagation factor of diffraction limited beams', *Optics Comm.* **105** pp. 233–242.

Bennet, G.R., J.S. Wark, D.J. Heading, N.C. Woolsey, H. He, R. Cauble, R.W. Lee & P. Young (1994), 'Production of strongly coupled plasmas by the laser irradiation of thin metallic films confined within micrometer-scale gaps by transparent insulators', *Phys. Rev. E* **50** pp. 3935–3942.

Bennet, T.D., C.P. Grigoropoulos & D.J. Krajnovich (1995), 'Near-threshold laser sputtering of gold', *J. Appl. Phys.* **77** pp. 849–864.

Bennett, T.D., D.J. Krajnovich & C.P. Grigoropoulos (1996), 'Seperating thermal, electronic, and topographic effects in pulse laser melting and sputtering of gold', *Phys. Rev. Lett.* **76** pp. 1659–1662.

Bergmann, H.W., C. Körner, M. Hartmann & R. Mayerhofer (1996), 'Precission machining with copper vapour lasers', in *'Pulsed Metal Vapour Lasers'*, C.E. Little & N.V. Sabotinov (editors), Kluwer Academic Publishers.

Bettis, J.R. (1992), 'Correlation among the laser-induced breakdown thresholds in solids, liquids, and gases', *Appl. Optics* **31** pp. 3448–3452.

Bigeleisen, J. (1965), 'Chemistry of isotopes', *Science* **147** pp. 463–471.

Blau, P. (1994), 'Analysis of the impedance of a coaxial, large-bore copper vapour laser', *IEEE J. Quantum Electron.* **30** pp. 763–769.

Bobin, J.L., Y.A. Durand, P.P. Langer & G. Tonon (1968), 'Shock-wave generation in rarefied gases by laser impact on beryllium targets', *J. Appl. Phys.* **39** pp. 4184–4189.

Bollanti, S., P. Di Lazzaro & D. Murra (1997), 'How many times is a laser beam diffraction limited?', *Optics Comm.* **134** pp. 503–513.

Bolle, M. & S. Lazare (1993*a*), 'Characterisation of submicrometer periodic structures produced on polymer surfaces with low-fluence ultraviolet laser radiation', *J. Appl. Phys.* **73** pp. 3516–3524.

Bolle, M. & S. Lazare (1993*b*), 'Large scale excimer laser production of submicron periodic structures on polymer surfaces', *Appl. Surf. Sci.* **69** pp. 31–37.

Bolle, M. & S. Lazare (1993*c*), 'Submicron periodic structures produced on polymer surfaces with polarised excimer laser ultraviolet radiation', *Appl. Surf. Sci.* **65** pp. 349–354.

Bolle, M., S. Lazare, M. Le Blanc & A. Wilmes (1992), 'Submicron periodic structures produced on polymer surfaces with polarised excimer ultraviolet radiation', *Appl. Phys. Lett.* **60** pp. 674–676.

Booth, H.J. (1998), *Guide Star Lasers*, PhD thesis, University of Oxford.

Booth, H.J., C.E Webb & A. Whybrew (1998), 'High power fibre optic laser beam delivery (CWN7)', in *CLEO/Europe-EQEC* 1998 Glasgow, Scotland.

Borets-Pervak, I.Yu. & V.S. Vorob'ev (1991), 'Plasma formation threshold in a vapour-gas mixture on the surface of a laser heated metal', *Sov. J. Quantum Electron.* **21** pp. 905–908.

Bostanjoglo, O. & T. Nink (1996), 'Hydrodynamic instabilities in laser pulse-produced melts of metal films', *J. Appl. Phys.* **79** pp. 8725–8729.

Boulmer-Leborgne, C., J. Herann & B. Dubreuil (1992), 'Spectroscopic observation of the plasma produced by a CO_2 laser beam interacting with titanium target under helium and/or argon atmosphere', *Appl. Phys. A* **55** pp. 340–346.

Bowers, R.L. & T. Deeming (1984), *Astrophysics I & II*, Jones and Bartlett Publishers.

Brand, W.A. (1996), 'High-precision isotope ratio monitorin techniques in mass-spectrometry', *J. Mass Spectrometry* **31** pp. 225–235.

Brauers, T., U. Aschmutat, U. Brandenburger, H.-P. Dorn, M. Hausmann, M. Heßling, A. Hofzumahaus, F. Holland, C. Plass-Dülmer & D.H. Ehhalt (1996), 'Intercomparison of tropospheric OH radical measurements by multiple folded long-path laser-absorption and laser-induced fluorescence', *Geophys. Res. Lett.* **23** pp. 2545–2548.

Brode, H.L. (1955), 'Numerical solutions of spherical blast waves', *J. Appl. Phys.* **26** pp. 766–775.

Brown, D.J.W. & D.W. Coutts (1994), 'Efficient high beam quality coper vapour laser mopa system with miniature master oscillator (CFD2)', in *CLEO* 1994 Annaheim, USA.

Brown, D.J.W. & D.W. Coutts (1996), 'Beam-quality issues in copper vapour lasers', in *'Pulsed Metal Vapour Lasers'*, C.E. Little & N.V. Sabotinov (editors), Kluwer Academic Publishers.

Brown, D.J.W., M.J. Withford, R.P. Mildren & J.A. Piper (1995), 'The effects of impurities on metal vapour laser performance', in *'Pulsed Metal Vapour Lasers'*, C.E. Little & N.V. Sabotinov (editors), Kluwer Academic Publishers.

Brown, D.J.W., R. Künnemeyer & A.I. McIntosh (1990), 'Time-resolved measurements of excited state densities in a copper vapour laser', *IEEE J. Quantum Electron.* **26** pp. 1609–1619.

Brown, D.J.W., R.Künnemeyer & A.I. MacIntosh (1989), 'Radial excited-state density effects in a small-bore copper vapour laser', in Proc. SPIE vol. **1041**: *Metal Vapour, Deep Blue, and Ultraviolet Lasers*, pp. 25–33.

Buchkremer, F. (1997), *Particle Image Velocimetry in Intensly Radiating Plasma Ttorches*, Master's thesis, University of Oxford.

Buscher, H.T., R.G. Tomlinson & E.K. Damon (1965), 'Frequency dependence of optically induced gas breakdown', *Phys. Rev. Lett.* **15** pp. 847–849.

Callies, G., P. Berger & H. Hügel (1996), 'Time-resolved observation of gas-dynamic discontinuities arising during excimer laser ablation and their interpretation', *J. Phys. D: Appl. Phys.* **28** pp. 794–806.

Carman, R.J. (1995), 'Modelling of intracavity optical fields in a copper vapour laser', *Optics Comm.* **119** pp. 415–423.

Carman, R.J. (1997), 'Modelling of the kinetics and parametric behaviour of a copper vapour laser: output power limitation issues', *J. Appl. Phys.* **82** pp. 71–83.

Carman, R.J., D.J.W. Brown & J.A. Piper (1994), 'A self-consistent model for the discharge kinetics in a high-repetition-rate copper vapour laser', *IEEE J. Quantum Electron.* **30** pp. 1876–1895.

Casti, J. (1997), 'Flight over Wall St', *New Scientist* **2078** pp. 38–41.

Cavalleri, A., K. Sokolowski-Tinten, J. Bialowski & D. von der Linde (1998), 'Femtosecond laser ablation of gallium arsenide investigated with time-of-flight mass spectroscopy', *Appl. Phys. Lett.* **72** pp. 2385–2387.

Chan, C.L. & J. Mazumder (1987), 'One-dimensional steady-state model for damage by vaporisation and liquid expulsion due to laser-material interaction', *J. Appl. Phys.* **62** pp. 4579–4586.

Chang, J.J. (1993), 'Pressure dependence of copper laser output characteristics', *Appl. Optics* **32** pp. 5230–5235.

Chang, J.J. (1994), 'Time-resolved beam-quality characterisation of copper vapour lasers with unstable resonators', *Appl. Optics* **33** pp. 2255–2265.

Chang, J.J. (1995), 'Copper laser oscillator with adjoint-coupled self-filtering injection', *Optics Lett.* **20** pp. 575–577.

Chang, J.J. & B.E. Warner (1996), 'Laser-plasma interaction during visible-laser ablation of metals', *Appl. Phys. Lett.* **69** pp. 473–475.

Chang, J.J., B.E. Warner, C.D. Boley & E.P. Dragon (1996), 'High-power copper vapour lasers and applications', in *'Pulsed Metal Vapour Lasers'* C.E. Little & N.V. Sabotinov (editors), Kluwer Academic Publishers.

Chang, J.J., M.W. Martinez, B.E. Warner, E.P. Dragon, G. Huete & M.E. Solarski (1994), 'Precision micro drilling with copper vapour lasers', *Proceedings of the Laser Material Processing Conference, ICALEO '94, Orlando, Florida, USA* p. 323.

Chang, J.J., P.A. Arnold & B.E. Warner (1997), 'Improvement of high-current large-volume discharge with profiled hollow-cathode electrodes', *IEEE Trans. Plasma Sci.* **25** pp. 392–399.

Chase, M.W., Jr, C.A. Davies, Jr J.R. Downey, D.J. Frurip, R.A. MacDonald & A.N. Syverud (1985), 'JANAF Thermochemical tables', *J. Phys. Chem. Ref. Data 14, Suppl. 1* .

Chen, K.R., J.N. Leboeuf, R.F. Wood, D.B. Geohegan, J.M. Donato, C.L. Liu & A.A. Puretzky (1995), 'Accelerated expansion of laser-ablated materials near a solid surface', *Phys. Rev. Lett.* **75** pp. 4706–4709.

Cheng, H.K. & J.W. Kirsch (1969), 'On the gas dynamics of an intense explosion with an expanding contact surface', *J. Fluid Mech.* **39** pp. 289–305.

Chichkov, B.N., C. Momma, S. Nolte, F. von Alvensleben & A. Tünnermann (1996), 'Femtosecond, picosecond and nanosecond laser ablation of solids', *Appl. Phys. A* **63** pp. 109–115.

Clark, S.E. & D.C. Emmony (1989), 'Ultraviolet-laser-induced periodic surface structures', *Phys. Rev. B* **40** pp. 2031–2041.

Clayton, R.N. (19993), 'Oxygen istopes in meteorites', *Ann. Rev. Earth Planet. Sci.* **21** pp. 115–149.

Clayton, R.N. & T.K. Mayeda (1963), 'The use of bromine pentafluoride in the extraction of oxygen from oxides and silicates for isotopic analysis', *Geochim. Cosmochim. Acta* **27** pp. 43–52.

Cobb, J.K. & J.J. Murray (1965), 'Laser beam-induced electron and ion emission from metal foils', *Brit. J. Appl. Phys.* **16** pp. 271–273.

Combis, P., B. Cazalis, J. David, A. Froger, M. Louis-Jacquet, B. Meyer, G. Nierat, A. Saleres, G. Sibille, G. Thiell & F. Wagon (1991), 'Low-fluence laser-target coupling', *Laser and Particle Beams* **9** pp. 403–420.

Corkum, P.B., F. Brunel, N.K. Sherman & T. Srinivasan-Rao (1988), 'Thermal response of metals to ultra-short laser excitation', *Phys. Rev. Lett.* **25** pp. 2886–2889.

Coutance, P., G. Naylor & J.P. Pique (1995), 'A copper HyBrID laser of high beam-quality using an axial unstable cavity', *IEEE J. Quantum Electron.* **31** pp. 1747–1752.

Coutts, D.W. (1994), 'Influence of off-axis unstable resonator alignment on copper vapour laser ouput divergence', *Optics Comm.* **113** pp. 283–291.

Coutts, D.W. (1995*a*), 'Optimisation of line-focusing geometry for efficient nonlinear frequency conversion from copper vapour lasers', *IEEE J. Quantum Electron.* **31** pp. 2208–2214.

Coutts, D.W. (1995*b*), 'Time resolved beam divergence from a copper vapour laser with unstable resonator', *IEEE J. Quantum Electron.* **31** pp. 330–342.

Coutts, D.W. (1998), 'UV cerium doped fluoride lasers pumped by frequency doubled copper vapour lasers at kHz pulse repetition rates (ThE3)', in *International Quantum Electronics Conference*, 1996 OSA Technical Digest Series, pp. 204–205.

Coutts, D.W. (1998), private communication.

Coutts, D.W. & D.J.W. Brown (1995*a*), 'Formation of output in copper vapour lasers', *Appl. Optics* **34** pp. 1502–1512.

Coutts, D.W. & D.J.W. Brown (1995*b*), 'Production of high average power UV by second harmonic and sum frequency generation of copper vapour lasers', *IEEE J. Sel. Topics Quantum Electron.* **1** pp. 768–778.

Coutts, D.W. & J.A. Piper (1992), 'One watt average power by second harmonic and sum frequency generation from a single scale copper vapour laser', *IEEE J. Quantum Electron.* **28** pp. 1761–64.

Coutts, D.W., M.D. Ainsworth & J.A. Piper (1990), 'Enhanced efficiency of UV second harmonic and sum frequency generation from copper vapour lasers', *IEEE J. Quantum Electron.* **26** pp. 1555–1558.

Coutts, D.W., W.J. Wadsworth & C.E. Webb (1998), 'High average power blue generation from a copper vapour laser pumped titanium sapphire laser', *J. Mod. Optics* **45** pp. 1185–1197.

Dabby, F.W. & U.-C. Paek (1972), 'High-intensity laser-induced vaporisation and explosion of solid metals', *IEEE J. Quantum Electron.* **8** pp. 106–111.

Dauscher, A., V. Feregotto, P. Cordier & A. Thomy (1996), 'Laser induced periodic surface structures on iron', *Appl. Surf. Sci.* **96-98** pp. 410–414.

Deguchi, H., T. Hatakeyama, E. Murata, Y. Izawa & C. Yamanaka (1994), 'Efficient design of multistage magnetic pulse compression', *IEEE J. Quantum Electron.* **30** pp. 2934–2938.

DeMichelis, C. (1970), 'Laser interaction with solids - a bibliographical review', *IEEE J. Quantum Electron.* **6** pp. 630–641.

Dolgaev, S.I., A.A. Lyalin, A.V. Simakin & G.A. Shafeev (1996*a*), 'Etching of sapphire assisted by copper vapour laser radiation', *Quantum Electron.* **26** pp. 65–68.

Dolgaev, S.I., A.A. Lyalin, A.V. Simakin & G.A. Shafeev (1996*b*), 'Fast etching of sapphire by a visible range quasi-cw laser radiation', *Appl. Surf. Sci.* **96-98** pp. 491–495.

Dresner, L. (1970), 'Variation of shock overpressure with the distance in a shock tube driven by an exploding gas mixture', *J. Appl. Phys.* **41** pp. 797–801.

Dreyfus, R.W. (1991), 'Cu^0, Cu^+ and Cu_2 from excimer-ablated copper', *J. Appl. Phys.* **69** pp. 1721–1729.

Dreyfus, R.W., R. Kelly & R.E. Walkup (1986), 'Laser-induced fluorescence studies of excimer laser ablation of Al_2O_3', *Appl. Phys. Lett.* **49** pp. 1478–1480.

Dreyfus, R.W, R. Kelly & R.E. Walkup (1987), 'Laser-induced fluorescence study of laser sputtering of graphite', *Nucl. Instr. and Meth.* **B23** pp. 557–561.

Duff, R.E. & A.N. Blackwell (1966), 'Explosive driven shock tubes', *Rev. Sci. Intrum.* **37** pp. 579–586.

Duley, W.W. (1996), *UV Lasers: Effects & Applications in Materials Science*, Cambridge University Press.

Dyer, P.E., A. Issa & P.H. Key (1990), 'Dynamics of excimer laser ablation of superconductors in an oxygen environment', *Appl. Phys. Lett.* **57** pp. 186–188.

Dyer, P.E. & J. Sidhu (1988), 'Spectroscopic and fast photographic studies of excimer laser polymer ablation', *J. Appl. Phys.* **64** pp. 4657–4663.

Dyer, P.E. & R. Srinivasan (1986), 'Nanosecond photoacoustic studies on ultraviolet laser ablation of organic polymers', *Appl. Phys. Lett.* **48** pp. 445–447.

Dyer, P.E., R.D. Greenough, A. Issa & P.H. Key (1988), 'Spectroscopic and ion probe measurements of KrF laser ablated Y-Ba-Cu-O bulk samples', *Appl. Phys. Lett.* **53** pp. 534–536.

Dyer, P.E. & R.J. Farley (1993), 'Dynamics of laser-induced periodic surface structures in excimer laser ablation of polymers', *J. Appl. Phys.* **74** pp. 1442–1444.

Dyer, P.E., R.J. Farley & R. Giedl (1996), 'Analysis and application of a 0/1 order Talbot interferometer for 193 nm laser grating formation', *Optics Comm.* **129** pp. 98–108.

Dyer, P.E., R.J. Farley, R. Giedl, C. Ragdale & D. Reid (1994), 'Study and analysis of submicron-periodic grating formation on polymers ablated using a KrF laser irradiated mask', *Appl. Phys. Lett.* **64** pp. 3389–3391.

Dyer, P.E., S. Farrar & P.H. Key (1992*a*), 'Investigation of excimer laser ablation of ceramic and thin film Y-Ba-Cu-O using nanosecond photoacoustic techniques', *Appl. Phys. Lett.* **60** pp. 1890–1892.

Dyer, P.E., S.R. Farrar & P.H. Key (1992*b*), 'Fast time-response photoacoustic studies and modelling of KrF laser ablated $YBa_2Cu_3O_7$', *Appl. Surf. Sci.* **54** pp. 255–263.

Eggins, S.M., L.P.J. Kinsley & J.M.G. Shelley (1998), 'Deposition and element fractionation processes during atmospheric pressure laser sampling for analysis by ICP-MS', *Appl. Surf. Sci.* **127-29** pp. 278–286.

Elsenheimer, D. & J.W. Valley (1992), 'In situ oxygen isotope analysis of feldspar and quartz by Nd:YAG laser microprobe', *Chem. Geology* **101** pp. 21–42.

Engst, P., P. Kubát, P. Boháček & J. Wild (1994), 'Time-resolved emission spectra of plasma produced by excimer laser ablation of Bi-Sr-Ca-Cu-O and Y-Ba-Cu-O superconductors in air', *Appl. Phys. Lett.* **64** pp. 2025–2027.

Evans, I.J. & C.E. Webb (1994), 'A 10-kHz pusled tunable laser source at 308-nm for tropospheric OH detection', *Chem. Phys. Lett.* **230** pp. 127–130.

Fähler, S. & H.U. Krebs (1996), 'Calculations and experiments of materials removal and kinetic energy during pulsed laser ablation of metals', *Appl. Surf. Sci.* **96-98** pp. 61–65.

Figg, D.J., J.B. Cross & C. Brink (1998), 'More investigations into elemental fractionation resulting from laser ablation-inductively coupled plasma-mass spectrometry on glass samples', *Appl. Surf. Sci.* **127-129** pp. 287–291.

Figueira, J.F. & S.J. Thomas (1982), 'Damage thresholds at metal surfaces for short pulse IR lasers', *IEEE J. Quantum Electron.* **18** pp. 1381–1386.

Fortier, S.M., D.R. Cole, D.L. Wesolowski, L.R. Riciputi, B.A. Paterson, J.W. Valley & J. Horita (1995), 'Determination of the magnetite-water equilibrium oxygen-isotope fractionation factor at 350-degrees-Celsius: a comparison of ion microprobe and laser fluorination techniques', *Geochim. Cosmochim. Acta* **59** pp. 3871–3875.

Fournier, J., P. Ballard, P. Merrien, J. Barralis, L. Castex & R. Fabbro (1991), 'Mechanial effects induced by shock waves generated by high energy laser pulses', *J. Phys. III France* **1** pp. 1467–1480.

Freiwald, D.A. (1972), 'Approximate blast wave theory and experimental data for shock trajectories in linear explosive-driven shock tubes', *J. Appl. Phys.* **43** pp. 2224–2226.

Freiwald, D.A. & R.A. Axford (1975), 'Approximate spherical blast wave theory including source mass', *J. Appl. Phys.* **46** pp. 1171–1174.

Fried, D. & G.P. Reck (1991), 'Time-resolved emission spectra follwing the 93-nm photoablation of CuO, BaO_2, Y_2O_3, and $YBa_2Cu_3O_{7-x}$ in vacuum and oxygen', *J. Appl. Phys.* **70** pp. 2337–2342.

Fujimoto, J.G., J.M. Liu, E.P. Ippen & N. Bloembergen (1984), 'Femtosecond laser interactioin with metallic tungsten and nonequilibrium electron and lattice temperature', *Phys. Rev. Lett.* **53** pp. 1837–1840.

Gagliano, F.P. & U.C. Paek (1974), 'Observation of laser-induced explosion of solid materials and correlation with theory', *Appl. Optics* **13** pp. 274–279.

Garrelie, F., J. Aubreton & A. Catherinot (1998), 'Monte Carlo simulation of the laser-induced plasma plume expansion under vacuum: comparison with experiments', *J. Appl. Phys.* **83** pp. 5075–5082.

Geertsen, C., A. Briand, F. Chartier, J.-L. Lacour, P. Mauchien & S. Sjöström (1994), 'Comparison between infrared and ultraviolet laser ablation at atmospheric pressure - Implications for solid sampling inductively coupled plasma spectrometry', *J. Anal. Atom. Spectrom.* **9** pp. 17–22.

Geohegan, D.B. (1992), 'Fast intensified-CCD photography of $YBa_2Cu_3O_{7-x}$ laser ablation in vacuum and ambient oxygen', *Appl. Phys. Lett.* **60** pp. 2732–2734.

Geohegan, D.B. (1994), 'Diagnostics and characterisation of pulsed laser deposition laser plasmas', in *'Pulsed Laser Deposition of Thin Films'*, D.Chrisey & G.Hubler (editors), John Wiley & Sons, chapter 5, pp. 115–165.

Geohegan, D.B. & A.A. Puretzky (1995), 'Dynamics of laser ablation plume penetration through low pressure background gases', *Appl. Phys. Lett.* **67** pp. 197–199.

Geohegan, D.B. & D.N. Mashburn (1989), 'Characterisation of ground-state neutral and ion transport during laser ablation of $Y_1Ba_2Cu_3O_{7-x}$ using transient optical absorption', *Appl. Phys. Lett.* **55** pp. 2345–2347.

Gilgenbach, R.M. & P.L.G. Ventzek (1991), 'Dynamics of excimer laser-ablated aluminium neutral atom plume measured by dye laser resonance absorption photography', *Appl. Phys. Lett.* **58** pp. 1597–1599.

Giori, F., L.A. MacKenzie & E.J. McKinney (1963), 'Laser-induced thermionic emission', *Appl. Phys. Lett.* **3** pp. 25–27.

Girard, J.-P., D. Razanadranorosoa & P. Freyssinet (1997), 'Laser oxygen isotope analysis of weathering goethite from the lateritic profile of Yaou, French Guiana: paleoweathering and paleoclimatic implications', *Appl. Geochem.* **12** pp. 163–174.

Giust, G.K. & T.W. Sigmon (1997), 'New ripple patterns observed in excimer-laser irradiated SiO_2/polycrystalline silicon/SiO_2 structures', *Appl. Phys. Lett.* **70** pp. 3552–3554.

Glenn, H.D. & B.K. Crowley (1971), 'Analysis of a high-explosive shock-tube experiment', *J. Appl. Phys.* **42** pp. 2099–2105.

Glezer, E.N. & E. Mazur (1997), 'Ultrafast-laser driven micro-explosions in transparent materials', *Appl. Phys. Lett.* **71** pp. 882–884.

Glover, A.C.J., D.W. Coutts, D.J. Ramsay, D.F. Karabaic & D.J.W. Brown (1993), 'The frequency-doubled copper vapour laser - an alternative source for high repetition rate micro-machining', in *ICALEO* 1993 Orlando, USA.

Glover, A.J.C., E.K. Illy & J.A. Piper (1995), 'High-speed UV machining of polymers with frequency-doubled copper vapour lasers', *IEEE J. Sel. Topics in Quantum Electron.* **1** pp. 830–835.

Glytis, E.N. & T.K. Gaylord (1992), 'High-spatial-frequency binary and multilevel stairstep gratings: polarisation-selective mirrors and broadband antireflection surfaces', *Appl. Optics* **31** pp. 4459–4470.

Goldstine, H.H. & J. Von Neumann (1955), 'Blast wave calculation', *Comm. Pure Appl. Math. 8* pp. 327–354.

Gonzalo, J., C.N. Afonso, F. Vega, D. Martinéz García & J. Perrière (1995), 'Plasma properties and stoichiometry of laser-deposited BiSrCaCuO thin films', *Appl. Surf. Sci.* **86** pp. 40–44.

Gonzalo, J., R. Goméz San Romaín, J. Perriére, C.N. Afonso & R. Pérez Casero (1998), 'Pressure effects during pulsed-laser deposition of barium titanate thin films', *Appl. Phys. A* **66** pp. 487–491.

Gorchakov, L.V., G.S. Evtushenko, A.G. Filonov & N.A. Filonova (1994), 'Investigation of spectrum width and emission divergence of a gold-vapour laser ($\lambda\lambda$ 312.2 and 627.8 nm)', *J. Russian Laser Research* **15** pp. 25–27.

Götz, T. & M. Stuke (1997), 'Short-pulse UV laser ablation of solid and liquid metals: indium', *Appl. Phys. A* **64** pp. 539–543.

Gray, A.L. (1985), 'Solid sample introduction by laser ablation for inductively coupled plasma mass spectrometry', *Analyst* **110** pp. 551–556.

Greenspan, H.P. & D.S. Butler (1962), 'On the expansion of a gas into vacuum', *J. Fluid Mech.* **13** pp. 101–119.

Gregg, D.W. & S.J. Thomas (1966), 'Momentum transfer produced by focused laser giant pulses', *J. Appl. Phys. 37* pp. 2787–2789.

Griem, H.R. (1974), *Spectral Line Broadening in Plasmas*, Academic Press.

Griem, H.R. (1997), *Principles of Plasma Spectroscopy*, Cambridge University Press.

Griffith, W., D. Brickl & V. Blackman (1956), 'Structure of shock waves in polyatomic gases', *Phys. Rev.* **102** pp. 1209–1216.

Grun, J. & B.H. Ripin (1982), 'Ballistic pendula for measuring the momentum of a laser-produced plasma', *Rev. Sci. Instrum.* **53** pp. 1878–1881.

Grun, J., J. Stamper, C. Manka, J. Resnick, R. Burris, J. Crawford & B.H. Ripin (1991), 'Instability of Taylor-Sedov blast waves propagating through a uniform gas', *Phys. Rev. Lett.* **66** pp. 2738–2741.

Grun, J., R. Decoste, B.H. Ripin & J. Gardner (1981), 'Characteristics of ablation plasma from planar, laser-driven targets', *Appl. Phys. Lett.* **39** pp. 545–547.

Gupta, A., B. Braren, K.G. Casey, B.W. Hussey & R. Kelly (1991), 'Direct imaging of the fragments produced during excimer laser ablation of $YBa_2Cu_3O_{7-\delta}$', *Appl. Phys. Lett.* **59** pp. 1302–1304.

Harilal, S.S., C.V. Bindhu, V.P.N. Nampoori & C.P.G. Vallabhan (1998), 'Influence of ambient gas on the temperature and density of laser produced carbon plasma', *Appl. Phys. Lett.* **72** pp. 167–169.

Harilal, S.S., C.V. Bindhu, R.C. Issac, V.P.N. Nampoori & C.P.G. Vallabhan (1997*a*), 'Electron density and temperature measurements in a laser produced carbon plasma', *J. Appl. Phys.* **82** pp. 2140–2146.

Harilal, S.S., R.C. Issac, C.V. Bindhu, V.P.N. Nampoori & C.P.G. Vallabhan (1997*b*), 'Time resolved analysis of C_2 emission from laser induced graphite plasma in helium atmosphere', *Jpn. J. Appl. Phys.* **36** pp. 134–138.

Harilal, S.S., R.C. Issac, V.P.N. Nampoori & C.P.G. Vallabhan (1997*c*), 'Emission characteristics and dynamics of C_2 from laser produced graphite plasma', *J. Appl. Phys.* **81** pp. 3637–3643.

Harrison, G.R. (1969), *MIT Wavelength Tables*, MIT Press.

Heading, D.J., A. Machacek, L.C. Whitford, A.J. Varney, J.S. Wark, R.W. Lee, R. Stamm & B. Talin (1997), 'Rapid generation of approximate optical spectra of dense cool plasmas', *J. Quant. Spectrosc. Radiat. Transfer* **58** pp. 619–626.

Heading, D.J., J.S. Wark, R.W. Lee, R. Stamm & B. Talin (1997), 'Comparison of the semiclassical and modified semiemperical method of spectral calculation', *Phys. Rev. E* **56** pp. 936–946.

Heading, D.J., G.R. Bennett, J.S. Wark & R.W. Lee (1995), 'Novel plasma source for dense plasma effects', *Phys. Rev. Lett.* **74** pp. 3616–3619.

Heading, D.J., J.S. Wark, G.R. Bennet & R.W. Lee (1995), 'Simulations of spectra from dense aluminium plasmas', *J. Quant. Spectrosc. Radiat. Transfer* **54** pp. 167–180.

Heald, M.A. & C.B. Wharton (1965), *Plasma Diagnostics with Microwaves*, John Wiley & Sons.

Hecht, E. (1987), *Optics* (second edition), Addison-Wesley.

Heidenreich, J.E. & M.H. Thiemens (1983), 'A non-mass-dependent isotope effect in the production of ozone from molecular oxygen', *J. Chem. Phys.* **78** pp. 892–895.

Heidenreich, J.E. & M.H. Thiemens (1985), 'The non-mass-dependent oxygen isotope effect in the electro dissociation of carbon dioxide: a step towards understanding NoMaD chemistry', *Geochim. Cosmochim. Acta* **49** pp. 1303–1306.

Hermann, J., A.L. Thomann, C. Boulmer-Leborgne, B. Dubreuil, M.L. De Giorgi, A. Perrone, A. Luches & I.N. Mihailescu (1995), 'Plasma diagnostics in pulsed laser TiN layer deposition', *J. Appl. Phys.* **77** pp. 2928–2936.

Hermann, J., C. Boulmer-Leborgne & D. Hong (1998), 'Diagnostics of the early phase of an ultraviolet laser induced plasma by spectral line analysis considering self-absorption', *J. Appl. Phys.* **83** pp. 691–696.

Herzberg, G. (1950), *Molecular Spectra and Molecular Structure: I. Spectra of Diatomic Molecules* (second edition), Van Nostrand Reinhold Company.

Hettche, L.R., J.T. Schriempf & R.L. Stegman (1973), 'Impulse reaction resulting from the in-air irradiation of aluminium by a pulse CO_2 laser', *J. Appl. Phys.* **44** pp. 4079–4085.

Hettche, L.R., T.R. Tucker, J.T. Schriempf, R.L. Stegman & S.A. Metz (1976), 'Mechanical response and thermal coupling of metallic targets to high-intensity 1.06-μ laser radiation', *J. Appl. Phys.* **47** pp. 1415–1421.

Hiraoka, H. & M. Sendova (1994), 'Laser-induced sub-half-micrometer periodic structure on polymer surfaces', *Appl. Phys. Lett.* **64** pp. 563–565.

Hirata, T. & R.W. Nesbitt (1995), 'U-Pb isotope geochronology of zircon: evaluation of the laser probe-inductively coupled plasma mass spectrometry technique', *Geochim. Cosmochim. Acta* **59** pp. 2491–2500.

Hnilo, A.A. & O.E. Martínez (1987), 'On the design of pulsed dye laser amplifiers', *IEEE J. Quantum Electron.* **23** pp. 593–598.

Ho, J.R., C.P. Grigoropoulos & J.A.C. Humphrey (1995), 'Computational study of heat transfer and gas dynamics in the pulsed laser evaporation of metals', *J. Appl. Phys.* **78** pp. 4696–4709.

Ho, J.R., C.P. Grigoropoulos & J.A.C. Humphrey (1996), 'Gas dynamics and radiation heat transfer in the vapour plume produced by pulsed laser irradiation of aluminum', *J. Appl. Phys.* **79** pp. 7205–7215.

Hoefs, J. (1996), *Stable Isotope Geochemistry* (fourth edition), Springer, Berlin.

Hofzumahaus, A., U. Aschmutat, M. Heßling, F. Holland & D.H. Ehhalt (1996), 'The measurement of tropospheric OH radials by laser-induced fluorescence spectroscopy during the POPCORN field campaign', *Geophys. Res. Lett.* **23** pp. 2541–2544.

Hogan, G.P., C.E. Webb, C.G. Whyte & C.E. Little (1995), 'Experimental studies of CVL kinetics', in *'Pulsed Metal Vapour Lasers'*, C.E. Little & N.V. Sabotinov (editors), Kluwer Academic Publishers.

Honig, R.E (1963), 'Laser-induced emission of electrons and positive ions from metals and semiconductors', *Appl. Phys. Lett.* **3** pp. 8–11.

Honig, R.E. & J.R. Woolston (1963), 'Laser-induced emission of electrons, ions, and neutral atoms from solid surfaces', *Appl. Phys. Lett.* **2** pp. 138–139.

Huang, Z.G., K. Namba & F. Shimizu (1986), 'Influence of molecular gases on the output characteristics of a copper vapour laser', *Jpn. J. Appl. Phys.* **25** pp. 1677–1679.

Huddlestone, R.H. & S.L. Leonard (1965), *Plasma diagnostic techniques*, Academic Press.

Hutchens, G.J. (1995), 'Approximate cylindrical blast theory: near-field solutions', *J. Appl. Phys.* **77** pp. 2912–2915.

Hutcherson, R.K. & A.W. DeSilva (1997), 'Stark broadening observations for a cool, dense plasma', *Phys. Rev. E* **55** pp. 4820–4821.

Hutchinson, I.H. (1987), *Principles of plasma diagnostics*, Cambridge University Press.

Ihlemann, J., A. Scholl, H. Schmidt & B. Wolff-Rottke (1995), 'Nanosecond and femtosecond excimer-laser ablation of oxide ceramics', *Appl. Phys. A* **60** pp. 411–417.

Ihlemann, J., B. Wolff & P. Simon (1992), 'Nanosecond and femtosecond excimer laser ablation of fused silica', *Appl. Phys. A* **54** pp. 363–368.

ISO/DIS11146 (1995), 'Test methods for laser beam parameters: Beam widths, divergence angle and beam propagation factor', Technical report, International Organisation for Standarisation.

Itina, T.E., A.A. Katassonov, W. Marine & M. Autric (1998), 'Numerical study of the role of a background gas and system geometry in pulsed laser deposition', *J. Appl. Phys.* **83** pp. 6050–6054.

Itina, T.E., W. Marine & M. Autric (1997), 'Monte Carlo simulation of pulsed laser ablation from two-component target into diluted gas', *J. Appl. Phys.* **82** pp. 3536–3542.

Itoh, N., T. Shimizu-Iwayama & T. Fujita (1994), 'Excitons in crystalline and amorphous SiO_2: formation, relaxation and conversion to Frenkel pairs', *J. Non-Cryst. Solids* **179** pp. 194–201.

Jandeleit, J., A. Horn, R. Weichenhain, E.W. Kreutz & R. Poprawe (1998), 'Fundamental investigations of micromachining by nano- and picosecond laser radiation', *Appl. Surf. Sci.* **127-129** pp. 885–891.

Jandeleit, J, G. Urbasch, H.D. Hoffmann, H.-G. Treusch & E.W. Kreutz (1996), 'Picosecond laser ablation of thin copper films', *Appl. Phys. A* **63** pp. 117–121.

Jeong, S.H., R. Greif & R.E. Russo (1996), 'Laser heating of a cavity versus plane surface for metal targets utilizing photothermal deflection measurements', *J. Appl. Phys.* **80** pp. 1996–2002.

Jeong, S.H., R. Greif & R.E. Russo (1998), 'Propagation of the shock wave generated from excimer laser heating of aluminium targets in comparison with theory', *Appl. Surf. Sci.* **127-129** pp. 1029–1034.

Kapitan, D. (1995), *'Experiments Towards an Artificial Guide Star: Copper Vapour Laser Pumped Dye Amplifiers'*, Master's thesis, University of Leiden.

Karman, G.P., M.W. Beijersbergen, A. van Duijl, D. Bouwmeester & J.P. Woerdman (1998), 'Airy pattern reorganisation and sub-wavelength structure in a focus', *J. Opt. Soc. Am. A* **15** pp. 884–899.

Kearsley, A.J., G.A. Naylor & R.R. Lewis (1987), 'Optimisation of resonator design for large-volume, short-pulse copper vapour lasers (MG1)', in *CLEO* 1987 Baltimore, USA.

Keller, J.B. (1948), 'On the solution of the Boltzmann equation for rarefied gases', *Comm. Pure Appl. Math.* **1** pp. 275–285.

Kelley, S.P. & A.E. Fallick (1990), 'High precision spatially resolved analysis of $\delta^{34}S$ in sulphides using a laser extraction technique', *Geochim. Cosmochim. Acta* **54** pp. 883–888.

Kelly, R. (1990), 'On the dual role of the Knudsen later and unsteady, adiabatic expansion in pulse sputtering phenomena', *J. Chem. Phys.* **92** pp. 5047–5056.

Kelly, R. & A. Miotello (1994), 'Mechanisms of pulsed laser sputtering', in *Pulsed Laser Deposition of Thin Films*, John Wiley & Sons, chapter 3, pp. 55–113.

Kelly, R., A. Miotello, A. Mele, A. Giardini Guidoni, J.W. Hastie, P.K. Schenck & H. Okabe (1998), 'Gas-dynamic effects in the laser-pulse sputtering of AlN: is there evidence for phase explosion?', *Appl. Surf. Sci.* **133** pp. 251–269.

Kelly, R. & J.E. Rothenberg (1985), 'Laser sputtering part III. The mechanism of sputtering of metals at low energy densities', *Nucl. Instr. and Meth.* **B7/8** pp. 755–763.

Kelly, R. & R.W. Dreyfus (1988), 'Reconsidering the mechanisms of laser sputtering with Knudsen-layer formation taken into account', *Nucl. Instr. and Meth.* **B32** pp. 341–348.

Kittel, C. (1996), *Introduction to Solid State Physics* (seventh edition), Wiley.

Knowles, D.S. & D.J.W. Brown (1995*b*), 'Compact 24 kHz CVL-pumped Ti:sapphire laser', *Optics Lett.* **20** pp. 569–571.

Knowles, M. (1996), 'Micromachining with copper lasers (CFA7)', in *CLEO/Europe-EQEC* 1996 Hamburg, Germany.

Knowles, M. & C. Webb (1995), 'Copper lasers show their mettle', *Physics World, May* pp. 41–44.

Knowles, M., J. Evans, R. Foster-Turner & A. Kearsley (1994), 'Multi-wavelength copper vapour laser for novel materials processing application', *Proc. 6th Int. Symp. on Adv. Nucl. Energy Research* pp. 236–245.

Knowles, M.R.H. & C.E. Webb (1993), 'Efficient high-power copper vapour laser pumped Ti:Al_2O_3 laser', *Optics Lett.* **18** pp. 607–609.

Knudtson, J.T., W.B. Green & D.G. Sutton (1987), 'The UV-visible spectroscopy of laser-produced aluminium plasmas', *J. Appl. Phys.* **61** pp. 4771–4780.

Koechner, W. (1996), *Solid-State Laser Engineering*, Springer-Verlag.

Kohn, M.J., M.J. Schoeninger & J.W. Valley (1996), 'Herbivore tooth oxygen isotope compositions: Effect of diet and physiology', *Geochim. Comsochim. Acta* **60** pp. 3889–3896.

Kononenko, T.V., S.V. Garnov, S.M. Klimentov, V.I. Konov, E.N. Loubin, F. Dausinger, A. Raiber & C. Taut (1997), 'Laser ablation of metals and ceramics in picosecond-nanosecond pulsewidths in the presence of different ambient atmospheres', *Appl. Surf. Sci.* **109/110** pp. 48–51.

Kools, J.C.S. (1993), 'Monte Carlo simulations of the transport of laser-ablated atoms in a diluted gas', *J. Appl. Phys.* **74** pp. 6401–6406.

Körner, C. (1997), *Theoretical Study of the Interaction of Ultrashort Laserpulses with Metals* (in German), PhD thesis, University of Erlangen-Nürnberg.

Körner, C., R. Mayerhofer, M. Hartmann & H.W. Bergmann (1996), 'Physical and material aspects in using visible laser pulses of nanosecond duration for ablation', *Appl. Phys. A* **63** pp. 123–131.

Kumar, V. & R.K. Thareja (1992*a*), 'Laser-induced breakdown of argon gas near a metal surface', *Laser and Particle Beams* **10** pp. 109–116.

Kumar, V. & R.K. Thareja (1992*b*), 'Laser-induced gas breakdown and its application to switching', *Appl. Optics* **31** pp. 3460–3462.

Kuznetsov, L.I., & V.Yu. Savichev, &N.N. Tikhonov (1998), 'Laser-reactive protection of spacecraft from fine debris', *Quantum Electron.* **28** pp. 361–365.

Lacroix, D., G. Jeandel & C. Boudot (1997), 'Spectroscopic characterisation of laser-induced plasma created during welding with a pulsed Nd:YAG laser', *J. Appl. Phys.* **81** pp. 6599–6606.

Landau, L.D. & E.M. Lifshitz (1987), *Fluid mechanics* (second edition), Butterworth Heinemann.

Lash, J.S. & R.M. Gilgenbach (1993), 'Copper vapour laser drilling of copper, iron and titanium foils in atmospheric pressure air and argon', *Rev. Sci. Instrum.* **64** pp. 3308–3313.

Leisz, F., W. Sdorra, J.B. Ko & K. Niemax (1989), 'Basic investigation for laser microanalysis: I. Optical emission spectrometry of laser-produced sample plumes', *Mikrochim. Acta* **II** pp. 185–199.

Leonard, T.A. & P. Hammerling (1980), 'Spherical shock development near laser-heated microshell® targets', *J. Appl. Phys.* **51** pp. 6130–6133.

Lichtman, D., & J.F. Ready (1963), 'Laser beam induced electron emission', *Appl. Phys. Lett.* **10** pp. 342–345.

Lide, D.R. (1995), *Handbook of Chemistry and Physics*, CRC Press.

Lindl, J. (1995), 'Development of the indirect-drive approach to inertial confinement fusion and the target phsysics basis for ignition and gain', *Phys. Plasmas* **2** pp. 3933–4024.

Little, C.E., D.R. Jones, S.A. Fairlie & C.G. Whyte (1995), 'Metal hybrid lasers', in *'Pulsed Metal Vapour Lasers'*, C.E. Little & N.V. Sabotinov (editors), Kluwer Academic Publishers.

Little, C.E. & N.V. Sabotinov (editors) (1995), *Pulsed Metal Vapour Lasers*, NATO Advanced Research Workshop, Kluwer Academic Publishers.

Liu, X., D. Du & G. Mourou (1997), 'Laser ablation and micromachining with ultrashort laser pulses', *IEEE J. Quantum Electron.* **33** pp. 1706–1716.

Lowder, J.E., D.E. Lencioni, T.W Hilton & R.J. Hull (1973), 'High-energy pulsed CO_2-laser-target interactions in air', *J. Appl. Phys.* **44** pp. 2759–2762.

Lowder, J.E. & L.C. Pettinghill (1974), 'Measurement of CO_2-laser-generated impulse and pressure', *Appl. Phys. Lett.* **24** pp. 204–207.

Lowndes, D.H., M. DeSilva, M.J. Godbole, A.J. Pedraza & D.B. Geohegan (1993), 'Ablation, melting and smoothing of polycrystalline alumina by pulsed laser ablation', *Mat. Res. Soc. Symp. Proc.* **285** pp. 191–214.

Lu, Y.F., W.K. Choi, Y. Aoyagi, A. Kinomura & K. Fujii (1996), 'Controllable laser-induced periodic structures at silicon-dioxide/silicon interface by excimer laser irradiation', *J. Appl. Phys.* **80** pp. 7052–7056.

Luft, A., U. Franz, A. Emsermann & J. Kaspar (1996), 'A study of thermal and mechanical effects on materials induced by pulsed laser drilling', *Appl. Phys. A* **63** pp. 93–101.

Lunney, J.G. & R. Jordan (1998), 'Pulsed laser ablation of metals', *Appl. Surf. Sci.* **127-129** pp. 941–946.

MacPherson, C.G. & D.P. Mattey (1998), 'Oxygen isotope variations in Lau Basin lavas', *Chem. Geology* **144** pp. 177–194.

Manka, C., J. Grun, J. Stamper, J. Resnick, R. Burris, J. Crawford & B.H. Rippin (1996), 'Images of unstable Taylor-Sedov blast waves propagating through a uniform gas', *IEEE Trans. Plasma Sci.* **24** pp. 35–36.

Marine, W., V. Tokarev, M. Gerri, M. Sentis & E. Fogarassy (1994), 'Ablation dynamics of silicon based targets in oxygen and nitrogen atmospheres', *Thin Solid Films* **241** pp. 103–108.

Martynyuk, M.M. (1974), 'Vapourisation and boiling of liquid metal in an exploding wire', *Sov. Phys. Tech. Phys.* **19** pp. 793–797.

Matsunawa, A. & V. Semak (1997), 'The simulation of front keyhole wall dynamics during laser welding', *J. Phys. D: Appl. Phys.* **30** pp. 798–809.

Matsuo, Y., T. Nakajima, T. Kobayashi & M. Takami (1997), 'Formation and laser-induced-fluorescence study of SiO^+ ions produced by laser ablation of Si in oxygen gas', *Appl. Phys. Lett.* **71** pp. 996–998.

Mattey, D. & C. MacPherson (1993), 'High-precision oxygen mineral isotope microanalysis of ferromagnesian minerals by laser fluorination', *Chem. Geology* **105** pp. 305–318.

Matthias, E., M. Reichling, J. Siegel, O.W. Käding, S. Petzoldt, H. Skurk, P. Bizenberger & E. Neske (1994), 'The influence of thermal diffusion on laser ablation of metal films', *Appl. Phys. A* **58** pp. 129–136.

McGonigle, A.J.S., D.W. Coutts & C.E. Webb (1998), 'A 530 mW Cerium LiCAF laser pumped by the sum frequency mixed output of a copper vapour laser', *Optics Lett., in press.*

Melville, W.S. (1951), 'The use of saturable reactors as discharge devices for pulse generators', *Proc. IEE* **98** pp. 185–207.

Metz, S.A. (1973), 'Impulse loading of targets by subnanosecond laser pulses', *Appl. Phys. Lett.* **22** pp. 211–213.

Metz, S.A., L.R. Hettche, R.L. Stegman & J.T. Schriempf (1975), 'Effect of beam intensity on target response to high-intensity pulsed co_2 laser radiation', *J. Appl. Phys.* **46** pp. 1634–1642.

Meyer, R.J. (1990), *Gmelin Handbook of Inorganic and Organometallic Chemistry*, Fluorine, Suppl. Vol. 2, Springer-Verlag.

Meyer, R.J. (1991), *Gmelin Handbook of Inorganic and Organometallic Chemistry*, Bromine, Suppl. Vol. B3, Springer-Verlag.

Milani, P. & M. Manfredini (1996), 'Surface periodic structures induced by pulsed laser radiation of fullerite', *Appl. Phys. Lett.* **68** pp. 1769–1771.

Mildren, R.P., D.J.W. Brown & J.A. Piper (1997 *a*), 'Evolution of excited and ground-state species during burst-mode excitation of a barium vapour laser', *IEEE J. Quantum Electron.* **33** pp. 1717–1726.

Mildren, R.P., D.J.W. Brown & J.A. Piper (1997 *b*), 'Ground-state depletion mechanisms in pulsed barium vapor lasers', *J. Appl. Phys.* **82** pp. 2039–2048.

Mildren, R.P., D.J.W. Brown & J.A. Piper (1997 *c*), 'Ground-state depletion mechanisms in pulsed barium vapour lasers', *J. Appl. Phys.* **82** pp. 2039–2048.

Mildren, R.P., D.J.W. Brown, R.J. Carman & J.A. Piper (1995), 'The effect of hydrogen additive on population densities in the afterglow of barium vapour lasers', *Optics Comm.* **120** pp. 112–120.

Miotello, A. & R. Kelly (1995), 'Critical assessment of thermal models for laser sputtering at high fluences', *Appl. Phys. Lett.* **67** pp. 3535–3537.

Molmud, P. (1960), 'Expansion of a rarefied gas cloud into a vacuum', *Phys. Fluids* **3** pp. 362–366.

Momma, C., B.N. Chichkov, S. Nolte, F. von Alvensleben, A. Tünnerman, H. Welling & B. Wellegehausen (1996), 'Short-pulse laser ablation of solid targets', *Optics Comm.* **129** pp. 134–142.

Moore, C.E. (1971), *Atomic energy levels*, NSRDS.

Morrow, T., H.F. Sakeek, A. El Astal, W.G. Graham & D.G. Walmsley (1994), 'Absorption and emission spectra of the YBCO laser plume', *J. Superconductivity* **7** pp. 823–827.

Motamedi, M.E., W.H. Southwell & W.J. Gunning (1992), 'Antireflection surfaces in silicon using binary optics technology', *Appl. Optics* **31** pp. 4371–4376.

Mott-Smith, H.M. (1951), 'The solution of the Boltzmann equation for a shock wave', *Phys. Rev.* **82** pp. 885–892.

Mukherjee, P., J.B. Cuff & S. Witanachchi (1998), 'Plume expansion and stoichiometry in the growth of multi-component thin films using dual-laser ablation', *Appl. Surf. Sci.* **127-129** pp. 620–625.

Mullenborn, M., H. Dirac & F. Grey (1996), 'Nanostructures by direct etching of silicon', in *CLEO/Europe-EQEC* 1996 Hamburg, Germany.

Naylor, G.A., A.J. Kearsley & H. Shaw (1986), 'High-power low-divergence injection-locked copper vapour laser (WE2)', in *CLEO* 1986 San Francisco, USA.

Naylor, G.A., R.R. Lewis & A.J. Kearsley (1988), Performance of high power copper vapour lasers in an injection-controlled oscillator-amplifier configuration, in Proc. SPIE vol. **894** - *Gas Laser Technology*, pp. 110–117.

Neal, C.R, J.P. Davidson & K.D. McKeegan (1995), 'Geochemical analysis of small samples: Micro-analytical techniques for the nineties and beyond', *Reviews of Geophysics* **33**, Supplement Part 1 pp. 25–32.

Nebel, C.E., J. Rogg, M.K. Kelly, B. Dahlheimer, M. Rother, M. Bichler, W. Wegschneider & M. Stutzmann (1997), 'Realisation of AlGaAs antidot arrays by pulsed laser interference gratings', *J. Appl. Phys.* **82** pp. 1497–1499.

Nehmadi, M., Z. Kramer, Y. Ifrah & E. Miron (1989), 'Magnetic pulse compression for a copper vapour laser', *J. Phys. D: Appl. Phys.* **22** pp. 29–34.

Német, B. & L. Kozma (1995), 'Time-resolved optical emission spectrometry of Q-switched Nd:YAG laser-induced plasmas from copper targets in air at atmospheric pressure', *Spectrochim. Acta Part B* **48** pp. 1869–1888.

Német, B. & L. Kozma (1996), 'Time-resolved line shape studies of Nd:YAG laser-induced microplasmas arising from gold surfaces', *Fresenius J. Anal. Chem.* **355** pp. 904–908.

Neogi, A., A. Mishra & R.K. Thareja (1998), 'Dynamics of laser produced carbon plasma expanding in low pressure ambient atmosphere', *J. Appl. Phys.* **83** pp. 2831–2834.

Nerheim, N.M. (1977), 'A parametric study of the copper chloride laser', *J. Appl. Phys.* **48** pp. 1186–1190.

Neuman, F. (1964), 'Momentum transfer and cratering effects produced by giant laser pulses', *Appl. Phys. Lett.* **4** pp. 167–169.

Neumann, J. Von & R.D. Richtmeyer (1950), 'A method for the numerical calculation of hydrodynamic shocks', *J. Appl. Phys.* **21** pp. 232–237.

Nielsen, P.E. (1975), 'Hydrodynamic calculations of surface response in the presence of laser-supported detonation waves', *J. Appl. Phys.* **46** pp. 4501–4505.

Nier, A.O., E.P. Ney & M.G. Inghram (1947), 'A null method for the comparison of two ion currents in a mass spectrometer', *Rev. Sci. Instrum.* **18** p. 294.

Nolte, S., C. Momma, H. Jacobs, A. Tünnermann, B.N. Chichkov, B. Wellegehausen & H. Welling (1997), 'Ablation of metals by ultrashort laser pulses', *J. Opt. Soc. Am. B* **14** pp. 2716–2722.

O'Hanlon, J.F. (1989), *A User's Guide to Vacuum Technology*, John Wiley.

Olmes, A., S. Lohmann, H. Lubatschowski & W. Ertmer (1997), 'An improved method of measuring laser induced pressure transients', *Appl. Phys. B* **64** pp. 677–682.

Petrash, G.G. (1995), 'Kinetics of metal vapour and metal halide lasers', in *'Pulsed Metal Vapour Lasers'*, C.E. Little & N.V. Sabotinov (editors), Kluwer Academic Publishers.

Peyre, P. & R. Fabbro (1995), 'Laser shock processing: a review of the physics and applications', *Opt. Quantum Electron.* **27** pp. 1213–1229.

Philips, H.M., D.L. Callahan, R. Sauerbrey, G. Szabo & Z. Bor (1991*a*), 'Direct laser ablation of sub-100 nm line structures into polyimide', *Appl. Phys. A* **54** pp. 158–165.

Philips, H.M., D.L. Callahan, R. Sauerbrey, G. Szabo & Z. Bor (1991*b*), 'Sub-100 nm lines produces by direct laser ablation in polyimide', *Appl. Phys. Lett.* **58** pp. 2761–2763.

Phipps, C.R. & J.P. Reilly (1996), ORION: Cleaning near-Earth space debris in two years using a 30-kW repetitively-pulsed laser, in *Proceedings XI International Symposium GCL/HPL* 1996 Edinburgh, Scotland, SPIE vol. **3092**, pp. 728–731.

Phipps, C.R., T.P. Turner, R.F. Harrison, G.W. York, W.Z. Osborne, G.K. Anderson, X.F. Corlis, L.C. Haynes, H.S. Steele, K.C. Spicochi & T.R. King (1988), 'Impulse coupling to targets in vacuum by KrF, HF, and CO_2 single-pulse lasers', *J. Appl. Phys.* **64** pp. 1083–1096.

Pichahchy, A.E., D.A. Cremers & M.J. Ferris (1997), 'Elemental analysis of metals under water using laser-induced breakdown spectroscopy', *Spectrochim. Acta Part B* **52** pp. 25–39.

Pini, R. (1996), 'Drilling and cutting transparent substrates with copper vapour lasers', in *'Pulsed Metal Vapour Lasers'*, C.E. Little & N.V. Sabotinov (editors), Kluwer Academic Publishers.

Pini, R., R. Salimbeni, G. Toci & M. Vannini (1990), 'High efficiency diffraction limited operation of a copper vapour laser', *Optics Comm.* **81** pp. 138–144.

Pirri, A.N. (1973), 'Theory for momentum transfer with a high-power laser', *Phys. Fluids* **16** pp. 1435–1440.

Pirri, A.N., R. Schlier & D. Northam (1972), 'Momentum transfer and plasma formation above a surface with a high-power CO_2 laser', *Appl. Phys. Lett.* **21** pp. 79–81.

Press, W.H., S.A. Teukolsky, W.T. Vetterling & B.P. Flannery (1996), *Numerical Recipes in C: the Art of Scientific Computing* (second edition), Cambridge University Press.

Preuss, S., A. Demchuk & M. Stuke (1995), 'Sub-picosecond UV laser ablation of metals', *Appl. Phys. A* **61** pp. 33–37.

Preuss, S., E. Matthias & M. Stuke (1994), 'Sub-picosecond UV-laser ablation of Ni films: strong fluence reduction and thickness-independent removal', *Appl. Phys. A* **59** pp. 79–82.

Pronko, P.P., S.K. Dutta, D. Du & R.K. Singh (1995), 'Thermophysical effects in laser processing of materials with picosecond and femtosecond pulses', *J. Appl. Phys.* **78** pp. 6233–6240.

Pronko, P.P., S.K. Dutta, J. Squier, J.V. Rudd, D. Du & G. Mourou (1995), 'Machining of sub-micron holes using a femtosecond laser at 800 nm', *Opt. Comm.* **114** pp. 106–110.

Raguin, D.H. & G.M. Morris (1993), 'Antireflection structured surfaces for the infrared spectral region', *Appl. Optics* **32** pp. 1154–1167.

Reid, R.C., J.M. Prausnitz & B.E. Poling (1987), *The Properties of Gases and Liquids*, McGraw-Hill.

Rode, A.V., B. Luther-Davies & E.G. Gamaly (1998), 'Laser ablation of carbon with high-pulse-rate nanosecond and picosecond lasers (CMF2)', in *CLEO/Europe-EQEC* 1998 Glasgow, Scotland.

Rothenberg, J.E. & R. Kelly (1984), 'Laser sputtering part II. The mechanism of the sputtering of al_2o_3', *Nucl. Instr. and Meth.* **B1** pp. 291–300.

Rumble, D. III, D. Rumble, J. Farquhar, E.D. Young & C.P. Christensen (1997), 'In situ oxygen isotope analysis with an excimer laser using F_2 and BrF_5 reagents and O_2 gas as analyte', *Geochim. Cosmochim. Acta* **61** pp. 4229–4234.

Rumble, D. III, & T.C. Hoering (1994), 'Analysis of oxygen and sulfur isotope ratios in oxide and sulfide minerals by spot heating witha carbon dioxide laser in a fluorine atmosphere', *Acc. Chem. Res.* **27** pp. 237–241.

Ryu, D. & E.T. Vishniac (1987), 'The growth of linear perturbations of adiabatic shock waves', *Astrophys. J.* **313** pp. 820–841.

Sabotinov, N.V. (1995), 'Copper bromide lasers', in *'Pulsed Metal Vapour Lasers'*, C.E. Little & N.V. Sabotinov (editors), Kluwer Academic Publishers.

Sabotinov, N.V., N.K. Vuchkov & D.N. Astadjov (1993), 'Effect of hydrogen in the CuBr- and CuCl-vapor lasers', *Optics Comm.* **95** pp. 55–56.

Schellhorn, M. & A. Eichhorn (1996), 'Spectroscopic comparison of aluminium welding plasmas produced by high power CO and CO_2 lasers', *Optics and Laser Technology* **28** pp. 405–407.

Schilling, A., O. Yavaş, J. Bischof, J. Boneberg & P. Leiderer (1996), 'Absolute pressure measurements on a nanosecond time scale using surface plasmons', *Appl. Phys. Lett.* **69** pp. 4159–4161.

Schittenhelm, H., G. Callies, P. Berger & H. Hügel (1997), 'Time-resolved interferometric investigations of the KrF-laser-induced interaction zone', *Appl. Surf. Sci.* **109/110** pp. 493–497.

Sdorra, W., A. Quentmeier & K. Niemax (1989), 'Basic investigations for laser microanalysis: II. Laser-induced fluorescence in laser-produced sample plumes', *Mikrochim. Acta* **II** pp. 201–218.

Seaton, M.J. (1995), *The Opacity Project*, Institute of Physics Publishing.

Sedov, L.I. (1993), *Similarity and dimensional analysis in mechanics* (tenth edition), CRC Press, Florida.

Seki, H. & et al. (1994), 'Development of a pulsed power supply for a large-bore copper vapour laser', *Rev. Sci. Instrum.* **65** pp. 323–326.

Semak, V. & A. Matsunawa (1997), 'The role of recoil pressure in energy balance during laser materials processing', *J. Phys. D: Appl. Phys.* **30** pp. 2541–2552.

Sharp, Z.D. (1992), 'In situ laser microprobe techniques for stable isotope analysis', *Chem. Geology* **101** pp. 3–19.

Sharp, Z.D. & T.E. Cerling (1998), 'Fossil isotope records of seasonal climate and ecology: Straight form the horse's mouth', *Geology* **26** pp. 219–222.

Shin, J.-J., S. Gurtler, Y. Chang & C.C. Yang (1998), 'Gratinglike modulation of GaAs/AlGaAs quantum well intermixing fabricated with laser interference', *Appl. Phys. Lett.* **72** pp. 2808–2810.

Shui, V.H., L.A. Young & J.P. Reilly (1978), 'Impulse transfer from pulsed CO_2 laser irradiation at reduced ambient pressures', *AIAA J.* **16** pp. 649–650.

Siano, S., R. Pini, R. Salimbeni & M. Vannini (1996), 'A diagnostic set-up for time-resolved imaging of laser-induced ablation', *Optics and Lasers in Engineering* **25** pp. 1–12.

Sibold, D. & H.M. Urbassek (1991), 'Kinetic study of pulsed desorption flows into vacuum', *Phys. Rev. A* **43** pp. 6722–6734.

Siegman, A.E. (1986), *Lasers*, University Science Books.

Siegman, A.E. & P.M. Fauchet (1986), 'Stimulated Wood's anomalies on laser-illuminated surfaces', *IEEE J. Qantum Electron.* **22** pp. 1384–1403.

Simon, P. & J. Ihlemann (1996), 'Machining of submicron structures on metals and semiconductors by ultrashort UV-laser pulses', *Appl. Phys. A* **63** pp. 505–508.

Simon, P. & J. Ihlemann (1997), 'Ablation of submicron structures on metals and semiconductors by femtosecond UV-laser pulses', *Appl. Surf. Sci.* **109/110** pp. 25–29.

Singh, R.K., D. Bhattacharya & J. Narayan (1990), 'Subsurface heating effects during pulsed laser evaporation of metals', *Appl. Phys. Lett.* **57** pp. 2022–2024.

Sipe, J.E., J.F. Young, J.S. Preston & H.M. van Driel (1983), 'Laser-induced periodic surface structure. I. Theory', *Phys. Rev. B* **27** pp. 1141–1154.

Slemrod, M. (1996), 'Resolution fo the spherical piston problem for compressible isentropic gas dynamics via a self-similar viscous limit', *Proc. Royal Soc. Edinburgh* **126A** pp. 1309–1340.

Sokolowski-Tinten, K., J. Bialkowski, A. Cavalleri & D. von der Linde (1998*a*), 'Observation of a transient insulating phase of metals and semiconductors during short-pulse laser ablation', *Appl. Surf. Sci.* **127-129** pp. 755–760.

Sokolowski-Tinten, K., J. Bialkowski, A. Cavalleri & D. von der Linde (1998*b*), 'Transient states of matter during short pulse laser ablation', *Phys. Rev. Lett.* **81** pp. 224–227.

Spicuzza, M.J., J.W. Valley, M.J. Kohn, J.P. Girard & A.M. Fouillac (1998), 'The rapid heating, defocused beam technique: a CO_2-laser-based method for highly precise and accurate determination of $\delta^{18}O$ values of quartz', *Chem. Geology* **144** pp. 195–203.

Steen, W.M. (1991), *Laser Materials Processing*, Springer-Verlag.

Stuart, B.C., M.D. Feit, A.M. Rubenshik, B.W. Shore & M.D. Perry (1995), 'Laser-induced damage in dielectrics with nanosecond to subpicosecond pulses', *Phys. Rev. Lett.* **74** pp. 2248–2251.

Stuart, B.C., M.D. Feit, S. Herman, A.M. Rubenshik, B.W. Shore & M.D. Perry (1996), 'Nanosecond-to-femtosecond laser-induced breakdown in dielectrics', *Phys. Rev. B* **53** pp. 1749–1761.

Tambay, R., R. Singh & R.K. Thareja (1992), 'Studies on recombining Al-plasma using 1.06, 0.532, 0.355 and 0.266 μm laser radiation', *J. Appl. Phys.* **72** pp. 1197–99.

Tas, G., S.A. Hambir, J. Franken, D.E. Hare & D.D. Dlott (1997), 'Coherent Raman spectroscopy of nanoshocks', *J. Appl. Phys.* **82** pp. 1080–1087.

Taylor, G. (1949), 'The formation of a blast wave by a very intense explosion', *Proc. Roy. Soc.* **201 A** pp. 159–174.

Thiem, T.L., R.H. Salter, J.A. Gardner, Y.I. Lee & J. Sneddon (1994), 'Quantitative simultaneous elemental determinations in alloys using laser-induced breakdown spectroscopy (LIBS) in an ultra-high vacuum', *Appl. Spectrosc.* **48** pp. 58–64.

Thorne, A.P. (1988), *Spectrophysics* (second edition), Chapman and Hall.

Timm, R., P.R. Willmott & J.R. Huber (1996), 'Ablation and blow-off characteristics at 248 nm Al, Sn, and Ti targets used for thin film pulsed laser deposition', *J. Appl. Phys.* **80** pp. 1794–1802.

Turcu, I.C.E., M.C. Gower & P. Huntington (1997), 'Measurement of KrF laser breakdown threshold in gases', *Optics Comm.* **134** pp. 66–68.

Uger, J. Kr¨& W. Kautek (1996), 'Femtosecond-pulse visible laser processing of transparent materials', *Appl. Surf. Sci.* **96-98** pp. 430–438.

Urbassek, H.M. & D. Sibold (1993), 'Gas-phase segragation effects in pulsed laser desorption from binary targets', *Phys. Rev. Lett.* **70** pp. 1886–1889.

Urey, H.C. (1947), 'The thermodynamic properties of isotopic substances', *J. Chem. Soc.* **1947** p. 562.

Valley, J.W., N. Kitchen, M.J. Kohn, C.R. Niendorf & M.J. Spicuzza (1995), 'UWG-2, a garnet standard for oxygen isotope ratios: Strategies for high precision and accuracy with laser heating', *Geochim. Cosmochim. Acta* **59** pp. 5223–5231.

van Driel, H.M., J.E. Sipe & J.F. Young (1982), 'Laser-induced periodic surface structure on solids: a universal phenomenon', *Phys. Rev. Lett.* **49** pp. 1955–1958.

Ventzek, P.L.G., R.M. Gilgenbach, C.H. Ching & R.A. Lindley (1992), 'Schlieren and dye laser resonance absorption photographic investigations of Krf excimer laser-ablated atoms and molecules from polyimide, polyethyleneterephtalate, and aluminium', *J. Appl. Phys.* **72** pp. 1696–1706.

Ventzek, P.L.G., R.M. Gilgenbach, C.H. Ching, R.A. Lindley & W.B. McColl (1992), 'Copper vapour laser machining of polyimide and polymethylmethacrylate in atmospheric pressure air', *J. Appl. Phys.* **72** pp. 3080–83.

Ventzek, P.L.G., R.M. Gilgenbach, J.A. Sell & D.M. Heffelfinger (1990), 'Schlieren measurements of the hydrodynamics of excimer laser ablation of polymers in atmospheric gases', *J. Appl. Phys.* **68** pp. 965–968.

Vetter, A.A. & N.M. Nerheim (1977), 'Addition of HCl to the double-pulse copper chloride laser', *Appl. Phys. Lett.* **30** pp. 405–407.

von Allmen, M. & A. Blatter (1995), *Laser-Beam Interaction with Materials* (second edition), Springer.

von der Linde, D., K .Sokolowski-Tinten & J. Bialkowski (1997), 'Laser-solid interaction in the femtosecond time regime', *Appl. Surf. Sci.* **109/110** pp. 1–10.

von Neumann, J. (1944), 'Shock hydrodynamics and blast waves', *Los Alomos Scientifc Laboratory Report* pp. AECD–2860.

Wadsworth, W.J. (1997), *Copper vapour laser pumped Ti:sapphire lasers*, PhD thesis, University of Oxford.

Wang, H., A.P Salzberg & B.R. Weiner (1991), 'Laser ablation of aluminium at 193, 248 and 351 nm', *Appl. Phys. Lett.* **59** pp. 935–937.

Warner, B.E. (1986), 'Injection locking of a copper vapour lasers oscillator (WE1)', in *CLEO San Francisco*, USA.

Webb, C.E. (1991), 'High-power dye lasers pumped by copper vapour lasers', in *High-Power Dye Lasers*, Springer-Verlag.

Webb, C.E. & G.P. Hogan (1995), 'Copper laser kinetics - a comparative study', in *'Pulsed Metal Vapour Lasers'*, C.E. Little & N.V. Sabotinov (editors), Kluwer Academic Publishers.

Weyl, G.M. & D. Rosen (1985), 'Laser-induced breakdwon in argon at 0.35 μm: Theory and experiments', *Phys. Rev. A* **31** pp. 2300–2313.

Weyl, G.M., D.I. Rosen, J. Wilson & W. Seka (1982), 'Laser-induced breakdown of argon at 0.35 μm', *Phys. Rev. A* **26** pp. 1164–1167.

Wiechert, U. & J. Hoefs (1995), 'An excimer laser-based micro analytical preparation technique for in-situ oxygen isotope analysis of silicate and oxide materials', *Geochim. Cosmochim Acta* **59** pp. 4093–4101.

Withford, M.J., D.J.W. Brown & J.A. Piper (1994*a*), 'Effect of H_2 buffer gas additive on repetitiion rate scaling of a copper vapour laser', *Optics and Quantum Electron.* **26** pp. 1089–1100.

Withford, M.J., D.J.W. Brown & J.A. Piper (1994*b*), 'Investigation of the effects of hydrogen and deuterium on copper vapour laser performance', *Optics Comm.* **110** pp. 699–707.

Withford, M.J. (1995), *Investigations of the Effects of Trace Impurities on Copper Vapour Laser Performance*, PhD thesis, Macquarie University, Sydney, Australia.

Withford, M.J., D.J. Brown, D.W. Coutts & J.A. Piper (1995), 'Increased efficiency of high-beam quality extraction from a copper vapour laser with H_2-Ne admixtures', *IEEE J. Quantum Electron.* **31** pp. 898–902.

Withford, M.J. & D.J.W. Brown (1995), 'Improved ultraviolet second-harmonic generation at elevated repetition rates from amedium-scale copper vapour laser', *IEEE J. Sel. Topics Quantum Electron.* **1** pp. 779–783.

Withford, M.J., D.J.W. Brown & J.A. Piper (1996a), 'Optimisation of H_2-Ne buffer gas mixtures for copper vapour lasers', *IEEE J. Quantum Electron.* **32** pp. 1310–1315.

Withford, M.J., D.J.W. Brown, R.J. Carman & J.A. Piper (1996*b*), 'Boosted laser output by kinetic enhancement in copper vapour lasers (CTuC3)', in *CLEO/Europe-EQEC* 1996 Hamburg, Germany.

Withford, M.J., D.J.W. Brown, R.J. Carman & J.A. Piper (1996*c*), 'Performance enhancement of elemental copper vapour lasers by bromine and hydrogenated bromine additives', in *XI International Symposium GCL/HPL* 1996, Edinburgh, Scotland, Proc. SPIE vol. **3092** pp. 68–71.

Withford, M.J., D.J.W. Brown, R.J. Carman & J.A. Piper (1997), 'Investigation of the effects of bromine and hydrogen bromide additives on copper vapour laser performance', *Optics Comm.* **135** pp. 164–170.

Withford, M.J., D.J.W. Brown & J.A. Piper (1998*a*), 'Enhanced performance of elemental copper-vapor lasers by use of H_2-HCl-Ne buffer-gas mixtures', *Optics Lett.* **23** .

Withford, M.J., D.J.W. Brown & J.A. Piper (1998*b*), 'Repetition rate scaling of a kinetically enhanced copper vapour laser', *Optics Lett.* (in press).

Withford, M.J., D.J.W. Brown, R.J. Carman & J.A. Piper (1998c), 'Kinetically enhanced copper vapour lasers employing H_2-HCl-Ne buffer gas mixtures', *Optics Comm.* (in press).

Wood, R.F., K.R. Chen, J.N. Leboeuf, A.A. Puretzky & D.B. Geohegan (1997), 'Dynamics of plume propagation and splitting during pulsed-laser ablation', *Phys. Rev. Lett.* **79** pp. 1571–1574.

Wu, S.T. & T.S. Fu (1970), 'Structure of the blast wave with ionization', *J. Appl. Phys.* **41** pp. 791–797.

Xia, Y., L. Mei, C. Tan, X. Lu, Q. Wang & S. Yue (1991), 'Laser ablation of copper and aluminium in air', *Appl. Phys. A* **52** pp. 425–432.

Yabe, T., H. Hoshino & T. Tsuchiya (1991), 'Two- and three dimensiona behaviour of Rayleigh-Taylor and Kelvin-Helmholtz instabilities', *Phys. Rev. A* **44** pp. 2756–2758.

Yavaş, O., E.L. Maddocks, M.R. Papantonakis & R.F. Haglund Jr. (1997), 'Shock-wave generation during rear- and front-side ablation of calcite', *Appl. Phys. Lett.* **71** pp. 1287–1289.

Yih, C.-S. (1974), 'Fluid mechanics of colliding plates', *Phys. Fluids* **17** pp. 1936–1940.

Young, E.D., A.J. Andrews & D.W. Coutts (1996), 'Oxygen isotope ratio analysis of silicate and oxide materials by uv ablation with frequency-doubled copper vapour laser (CWF71)', in *CLEO/Europe-EQEC* 1996 Hamburg, Germany.

Young, E.D., D.W. Coutts & D. Kapitan (1998), 'UV laser ablation and irm-GCMS microanalysis of $^{18}O/^{16}O$ and $^{17}O/^{16}O$ with application to a calcium-aluminium-rich inclusion from the Allende meteorite', *Geochim. et Cosmochim. Acta* **62** .

Young, E.D. & S.S. Russell (1998), 'Oxygen reservoirs in the early solar nebula inferred from an Allende CAI', *Science* **282** pp. 452–455.

Young, J.F., J.S. Preston, H.M. van Driel & J.E. Sipe (1983), 'Laser-induced periodic surface structure. II. Experiments on Ge, Si, Al, and brass', *Phys. Rev. B* **27** pp. 1155–1172.

Zel'dovich, Ya.B. & Yu.P. Raizer (1966), *Physics of shock waves and high-temperature hydrodynamic phenomena*, Academic Press.

Zerkle, D.K. & A.D. Sappey (1996), 'Time-resolved PLIF imaging of Cu in a laser-ablated copper plasma plume', *IEEE Trans. Plasma Sci.* **24** pp. 37–38.

Zhang, X., S.S. Chu, J.R. Ho & C.P. Grigoropoulos (1997), 'Excimer laser ablation of thin gold films on a quartz crystal microbalance at various argon background pressures', *Appl. Phys. A* **64** pp. 545–552.

The essence of true freedom
lies in the ability to accept change
Oxford, September 1994 - January 1999

... so tonight I'm going to party like it's 1999
the artist formerly known as Prince